

# Magnonic crystals with reconfigurable magnetic defects for spin-based microwave electronics

Présentée le 24 mars 2021

Faculté des sciences et techniques de l'ingénieur  
Laboratoire des matériaux magnétiques nanostructurés et magnoniques  
Programme doctoral en science et génie des matériaux

pour l'obtention du grade de Docteur ès Sciences

par

**Korbinian BAUMGÄRTL**

Acceptée sur proposition du jury

Prof. K. Scrivener, présidente du jury  
Prof. D. Grundler, directeur de thèse  
Prof. A. Chumak, rapporteur  
Dr G. Gubbiotti, rapporteur  
Prof. D. Damjanovic, rapporteur





If we knew what it was we were doing,  
it would not be called research, would it?  
— Albert Einstein

To my parents, who encouraged me to be curious.



# Acknowledgements

I would like to express my gratitude to everyone who supported me scientifically as well as on a personal level. During my time at EPFL I had innumerable positive encounters, so the following list is not (nor can it be) extensive. In particular I would like to thank:

**Prof. Dirk Grundler** who supervised this PhD thesis. Thank you for the continuous support, fruitful discussions and your optimism. Your feedback was always encouraging and of tremendous help. Thank you for the rigorous proofreading of all my scientific works, which not only improved the works itself, but was also invaluable for improving my scientific writing.

**Prof. Andrii Chumak**, **Prof. Dragan Damjanovic** and **Dr. Gianluca Gubbiotti** for taking the time to evaluate my thesis, **Prof. Karen Scrivener** for accepting to preside the examination committee.

I would like to thank and acknowledge all **external collaborators**, in particular: **Dr. Joachim Gräfe** and co-workers from the MPI Stuttgart for the fruitful collaboration on X-ray based nanoimaging of magnonic grating coupler modes. **Dr. Carsten Dubs** for providing high quality YIG films essential for parts of this thesis. **Dr. V. E. Demidov** and **Prof. S.O. Demokritov** for the support and hands-on training regarding Brillouin light scattering. **Mingran Xu** from **Prof. Yoshichika Otani's group** for the fruitful collaboration on magnon-phonon interactions and the good time we spent working together in the lab. **Dr. Joe Bailey** for the exciting collaboration on Bose-Einstein condensation.

The **CMI team** for maintaining a first-class cleanroom facility. A particular thank you goes to **Zdenek Benes** and **Joffrey Pernollet** for the crucial support concerning electron-beam lithography, to **Rémy Juttin** for the support concerning wet etching and to **Patrick Alain Madliger**, who ensured a safe and a cheerful working environment in the cleanroom. To **Corradini Giancarlo** for electrically bonding even the most challenging samples with the patients and seriousness of a bomb disposal expert. Thank you for saving several of my experiments.

**Prof. Anna Fontcuberta i Morral** and the **LMSC group** for the warm welcome at EPFL. After having the pleasure to spent part of my Master's Thesis in your group, the decision to go for a PhD at EPFL was an easy one. I am thankful for the granted asylum in your group during the first month of my PhD when LMGN had only a few members. You are an inspiring person and I hope I can copy some of your organization skills for my future career.

To **all members and former members of LMGN**. Thank you for the many good moments we

## Acknowledgements

---

shared. To **Sho Watanabe** and **Maria Carmen**, with whom I enjoyed four amazing years confined in the same office. Thank you for plenty of scientific and non-scientific discussion and especially for the discussions in between. One day, spin waves will propagate to Napoli! Thank you as well for the fruitful scientific collaborations. Arigato Sho for the on-site programming support and the epic struggle for good MFM images. **Ping Che** for the successful collaboration on magnetic CPWs and the great time we had. Thank you for your positive "Yes-we-can" mentality and pushing projects constantly forwards. **Andrea Muccietto** thank you for being always willing to help, e.g. thanks for your great support at Bessy. It was a pleasure to work with you! **Mohammad Hamdi** for all the interesting scientific and non-scientific discussions. Thank you for your help concerning MuMax3, theoretical questions and supporting the maintenance of the BLS setup. **Bin Lu** thank you for the good working atmosphere during your Master's thesis project and your dedication. Thank you to **Anna Kúkol'ová**, **Dr. Jilei Chen**, **Dr. Kyongmo An** and **Dr. Vinayak Bhat** for the fruitful scientific collaborations and good times spent. Merci **Yuko Kagata** for the warm and friendly organizational support.

I would like to thank the **Swiss National Science Foundation** for funding this PhD project via grant **No. 163016**. More generally I would like to thank all Swiss tax payers for their indirect financial support to scientific research, which makes projects like this only possible.

Finally I would like to thank **my family and friends** for their unconditional support. A big thank you to **Lorena Molnar** for her constant love and support, to my parents **Ingrid** and **Helmut**, and my siblings **Magdalena** and **Martin**.

*Lausanne, December 4, 2020*

K. B.

# Abstract

Collective spin excitations can propagate in magnetically ordered materials in the form of waves. These so-called spin waves (SWs) or magnons are promising for low-power beyond-CMOS information processing, which does not rely anymore on the lossy movement of electric charges. SWs in the few GHz frequency regime possess nanoscale wavelengths about five orders of magnitude smaller than electromagnetic waves of the same frequency. This property makes SWs ideally suited for application in microwave technology, essential for on-chip processing of wireless telecommunication signals. In this thesis, three crucial challenges relevant for the technological application of SWs are addressed:

First, to functionalize SWs and exploit their small wavelengths, it is necessary to control them at the nanoscale. Here, periodically nanostructured materials, denoted magnonic crystals, are promising, as they allow to tailor the band structure of SWs. We report on SWs propagating in a prototypical one-dimensional magnonic crystal consisting of dipolarly coupled magnetic nanostripes. The remanent magnetization of individual stripes was designed to be bistable along the long axis. By magnetizing an individual stripe in opposite direction to the others, we created a magnetic defect. We measured by means of all-electrical spin wave spectroscopy and Brillouin light scattering microscopy phase and amplitude of SWs trespassing the defect. We found that spin wave phases and amplitudes were modified at the nanoscale, and phase shifts could be tuned by an applied bias magnetic field. Using micromagnetic simulations, we identified specific bias fields for which phase shifts of  $\pi$  are achieved without suppressing SW amplitudes. This result is highly relevant for the implementation of logic gates based on interference of phase-controlled SWs. We further measured propagation of short-waved SWs in an antiferromagnetically ordered one-dimensional magnonic crystal, where every second stripe was magnetized in opposite direction. We found a band gap closing at the Brillouin zone boundary when no magnetic bias field was applied. Our observations are promising for reprogrammable microwave filters capable of adjusting stop- and passband.

Second, we address how long-waved electromagnetic waves can be coupled efficiently to nanoscale SWs. We demonstrate by space- and time-resolved scanning X-ray transmission measurements, that excited nanogratings allow to transfer their reciprocal lattice vector and multiple of it to an underlying magnetic thin film, in which nanoscale propagating SWs are launched. Additionally, we discovered a second method for short-waved spin wave generation based on magnetic microwave guides. This approach is easy to fabricate and relies on the adaption of the SW wavelength to a changing effective magnetic field. Efficient coupling of electromagnetic waves to nanoscale SWs promises an unprecedented miniaturization of

## Abstract

---

microwave components.

Third, we found that the magnetization direction of bistable nanomagnets can be switched by propagating SWs in an underlying magnetic thin film when a threshold amplitude is reached. This discovery is promising for the realization of a non-volatile magnonic memory, which stores spin wave amplitudes. A possible application are spin wave logic gates, which encode the outcome of a logic operation in the output spin wave amplitude. Magnonic memory would allow for storing these amplitudes directly, without requiring lossy conversion into the electrical domain.

**Key words:** *Magnonics, Spin waves, Magnonic crystals, Microwave electronics, Grating coupler, Phase shifting, Microwave characterization*

# Zusammenfassung

Kollektive Spin-Anregungen können sich in magnetisch geordneten Materialien in Form von Welle ausbreiten. Diese sogenannten Spinwellen oder Magnonen sind vielversprechend für niederenergetische Datenverarbeitung, die im Gegensatz zur CMOS-Technologie nicht auf den verlustreichen bewegten elektrischen Ladungen beruht. Spinwellen im Frequenzbereich von einigen GHz besitzen nanoskalige Wellenlängen, die etwa fünf Größenordnungen kleiner sind als die von elektromagnetischen Wellen gleicher Frequenz. Diese Eigenschaft prädestiniert Spinwellen für die Anwendung in der Mikrowellentechnologie, welche essentiell für das Verarbeiten von drahtlosen Kommunikationssignalen ist. Im Verlauf dieser Doktorarbeit werden drei entscheidende Herausforderungen auf dem Weg zur technischen Anwendbarkeit von Spinwellen adressiert: Erstens, um Spinwellen zu funktionalisieren und von den kleinen Wellenlängen zu profitieren ist es notwendig, sie auf der nanoskaligen Ebene manipulieren zu können. Periodisch nanostrukturierte magnetische Gitter, sogenannte magnonische Kristalle, sind hierbei vielversprechend, da sie es erlauben, die Bandstruktur von Spinwellen maßzuschneidern. Wir berichten über propagierende Spinwellen in einem prototypischem eindimensionalen magnetischen Kristall, der aus dipolar gekoppelten magnetischen Nanostreifen besteht. Die remanente Magnetisierung von einzelnen magnetischen Streifen ist bistabil entlang ihrer langen Achse. Durch das Magnetisieren eines einzelnen Streifens in entgegengesetzte Richtung zu den Anderen, erzeugen wir einen magnetischen Defekt. Wir zeigen durch Mikrowellenspektroskopie und Brillouin-Mikroskopie, dass ein solcher Defekt dazu geeignet ist die Phase und Amplitude von Spinwellen nanoskalig zu manipulieren. Wir identifizieren in mikromagnetischen Simulationen Parameter unter welchen ein  $\pi$  Phasenversatz erreicht wird, ohne dabei die Amplitude zu reduzieren. Dieses Ergebnis ist hochrelevant für die Implementierung von Logikgatter, die auf der Interferenz von phasenkontrollierten SW beruhen. Des Weiteren adressieren wir kurzwellige propagierende Spinwellen in einem antiferromagnetisch geordneten eindimensionalen magnetischen Kristall, indem jeder zweite Streifen entgegengesetzt magnetisiert ist. Für Spinwellen mit einem Wellenvektor an der Brillouin-Zonengrenze schloss sich die gemessene Bandlücke, wenn kein magnetisches Feld angelegt war. Unsere Beobachtungen sind vielversprechend für programmierbare Mikrowellenfilter, die dazu fähig ihren Sperr- und Durchlassbereich anzupassen.

Zweitens adressieren wir, wie langwellige elektromagnetisch Wellen effizient mit nanoskaligen Spinwellen gekoppelt werden können. Wir zeigen durch orts- und zeitaufgelöste Röntgenmikroskopie, dass angeregte Nanogitter ihren reziproken Gittervektor und Vielfache davon auf einen unterliegenden magnetischen Dünnschicht übertragen können, indem dann propagie-

rende nanoskalig Spinwellen angeregt werden. Außerdem schlagen wir eine zweite Methode basierend auf magnetischen Mikrowellenleitern vor, welche einfach in der Herstellung ist, und auf der Anpassung der Wellenlänge von Spinwellen an ein sich änderndes effektives magnetisches Feld beruht. Effiziente Kopplung von elektromagnetischen Wellen und nanoskaligen Spinwellen verspricht eine beispiellose Miniaturisierung von Mikrowellenkomponenten.

Drittens zeigen wir, dass die Magnetisierungsrichtung von bistabilen Nanomagneten durch propagierende Spinwellen in einem unterliegenden Dünnsfilm geschaltet werden kann, wenn die Amplitude der Spinwellen einen gewissen Schwellenwert überschreitet. Diese Entdeckung ist vielversprechend für die Realisierung eines nichtflüchtig magnonischen Speichers, der die Amplituden von Spinwellen aufzeichnet. Eine mögliche Anwendung sind Logikgatter, die das Ergebnis einer logischen Operation in der ausgegebenen Spinwellenamplitude kodieren. Magnonischer Speicher würde es erlauben diese Amplituden direkt zu speichern, ohne eine verlustreiche Konvertierung in die elektrische Domäne zu erfordern.

**Stichwörter:** *Magnonics, Spinwellen, magnonische Kristalle, Mikrowellenelektronik, Gitterkoppler, Phasenschieber, Mikrowellen-Charakterisierung*



# Résumé

Les excitations collectives de spin peuvent se propager dans des matériaux magnétiquement ordonnés sous la forme de vagues. Les appelées ondes de spin ou magnons sont prometteurs pour le traitement de l'information à une faible puissance, qui, au contraire que la technologie CMOS, ne repose plus sur le mouvement des charges électriques. Les ondes de spin dans le régime de fréquences de quelques GHz possèdent des longueurs d'onde nanométriques d'environ cinq ordres de grandeur plus petits que ceux des ondes électromagnétiques de même fréquence. Cette propriété rend les ondes de spin parfaitement adaptées à une application dans la technologie micro-ondes, essentielle pour le traitement sur puce des télécommunications sans fil. Dans cette thèse, trois défis cruciaux pertinents pour la l'application technologique des ondes de spin sont abordés :

Premièrement, pour fonctionnaliser les ondes de spin et exploiter leurs petites longueurs d'onde, il est nécessaire de les contrôler à l'échelle nanométrique. Ici, les matériaux périodiquement nanostructurés, appelés cristaux magnoniques, sont prometteurs, car ils permettent d'adapter la structure de bande des ondes de spin. Nous rapportons des ondes de spin se propageant dans un cristal magnonique unidimensionnel prototypique composé de nanorayures magnétiques couplées dipolairement. L'aimantation rémanente des bandes individuelles a été conçue pour être bistable le long du grand axe. En magnétisant une bande individuelle dans la direction opposée des autres, nous avons créé un défaut magnétique.

Nous avons mesuré la phase et l'amplitude des ondes de spin qui ont transgressé le défaut au moyen de la spectroscopie d'onde de spin entièrement électrique et de la microscopie à diffusion de lumière Brillouin. Nous avons constaté que les phases et amplitudes des ondes de spin étaient modifiées à l'échelle nanométrique et que les déphasages pouvaient être réglés par un champ magnétique appliqué. En utilisant des simulations micromagnétiques, nous avons identifié des champs spécifiques pour lesquels des déphasages de  $\pi$  sont obtenus sans réduire les amplitudes des ondes de spin.

Ce résultat est très pertinent pour la mise en oeuvre de portes logiques basées sur l'interférence d'ondes de spin commandées en phase. Nous avons en outre mesuré la propagation des ondes de spin à ondes courtes dans un cristal magnonique unidimensionnel à ordre antiferromagnétique, où chaque seconde nanorayure était magnétisée dans la direction opposée. Nous avons trouvé une bande interdite se fermant à la limite de la zone Brillouin lorsqu'aucun champ magnétique n'était appliqué. Nos observations sont prometteuses pour des filtres micro-ondes reprogrammables capables d'ajuster les bandes d'arrêt et passantes.

Deuxièmement, nous examinons comment les ondes électromagnétiques à ondes longues

peuvent être couplées efficacement aux ondes de spin à l'échelle nanométrique. Nous démontrons par des mesures de microscopie en transmission par rayons X à balayage résolu dans l'espace et dans le temps que les nanoréseaux excités permettent de transférer leur vecteur de réseau réciproque et son multiple vers un mince film magnétique sous-jacent, dans lequel des ondes de spin se propageant à l'échelle nanométrique sont lancées. De plus, nous avons découvert une deuxième méthode de génération d'ondes de spin à ondes courtes basée sur des guides magnétiques à micro-ondes. Cette approche est facile à fabriquer et repose sur l'adaptation de la longueur d'onde des ondes à spin à un champ magnétique efficace changeant. Le couplage efficace des ondes électromagnétiques aux ondes à spin à l'échelle nanométrique promet une miniaturisation sans précédent des composants micro-ondes.

Troisièmement, nous avons constaté que la direction de magnétisation des nanomagnets bistables peut être commutée en propageant des ondes de spin dans un mince film magnétique sous-jacent lorsqu'une amplitude de seuil est atteinte. Cette découverte est prometteuse pour la réalisation d'une mémoire magnonique non volatile, qui stocke les amplitudes des ondes de spin. Une application possible est les portes logiques des ondes de spin, qui codent le résultat d'une opération logique dans l'amplitude de l'onde de spin de sortie. La mémoire magnétique permettrait de stocker ces amplitudes directement, sans nécessiter de conversion avec perte dans le domaine électrique.

**Mots clés :** *Magnonique, ondes de spin, cristaux magnoniques, électronique micro-ondes, coupleur de réseau, déphasage, caractérisation micro-ondes*

# Contents

<b>Acknowledgements</b>	<b>i</b>
<b>Abstract (English/Français/Deutsch)</b>	<b>iii</b>
<b>List of publications</b>	<b>1</b>
<b>I Introductory chapters</b>	<b>3</b>
<b>1 Motivation and context</b>	<b>5</b>
1.1 Magnonic crystals: Controlling spin waves on the nanoscale . . . . .	6
1.2 Efficient excitation of short magnons . . . . .	7
1.3 Magnonic memory: How to store spin waves? . . . . .	8
<b>2 Theoretical background</b>	<b>9</b>
2.1 Introduction to Magnetism . . . . .	9
2.2 Static micromagnetics . . . . .	11
2.3 Magnetization dynamics . . . . .	13
2.3.1 Landau-Lifshitz-Gilbert Equation . . . . .	13
2.3.2 Ferromagnetic resonance . . . . .	14
2.3.3 Spin wave dispersion . . . . .	16
2.3.4 Bloch's theorem applied to magnonic crystals . . . . .	18
2.3.5 Micromagnetic Simulations . . . . .	18
<b>3 Methods</b>	<b>21</b>
3.1 All-electrical spin wave spectroscopy . . . . .	21
3.1.1 Experimental setup and measurement technique . . . . .	22
3.1.2 Spin wave excitation and detection with a coplanar waveguide . . . . .	23
3.1.3 Spectrum analysis and group velocity of propagating spin waves . . . . .	26
3.1.4 Data processing . . . . .	27
3.2 Brillouin light spectroscopy . . . . .	29
3.2.1 Magnon-photon scattering . . . . .	29
3.2.2 Brillouin light scattering microscopy . . . . .	31
3.3 Sample fabrication . . . . .	35

ix

<b>II Results and Discussion</b>	<b>39</b>
<b>4 Magnetic defects in 1D magnonic crystals</b>	<b>41</b>
4.1 Phase control of spin waves based on a magnetic defect in a one-dimensional magnonic crystal . . . . .	41
4.2 Microscopic observation of phase shifts at a magnetic defect . . . . .	49
4.3 Low-loss nanoscale $\pi$ -phase shifting observed in micromagnetic simulations .	52
4.4 Reprogramming the band structure: Propagating spin waves in the antiferromagnetically ordered state . . . . .	57
<b>5 Coupling microwaves to short-waved spin waves</b>	<b>61</b>
5.1 Nanoimaging of Ultrashort Magnon Emission by Ferromagnetic Grating Couplers at GHz Frequencies . . . . .	61
5.2 Efficient wavelength conversion of exchange magnons below 100 nm by magnetic coplanar waveguides . . . . .	69
<b>6 Magnonic memory</b>	<b>85</b>
6.1 Switching of Py stripes with propagating spin waves . . . . .	85
6.1.1 Introduction . . . . .	85
6.1.2 Switching by spin waves - magnetic force microscopy and spin-wave spectroscopy . . . . .	86
<b>7 Summary and Outlook</b>	<b>95</b>
<b>Appendix</b>	<b>99</b>
<b>A Supporting Information</b>	<b>101</b>
A.1 SI – Phase control of spin waves based on a magnetic defect in a one-dimensional magnonic crystal . . . . .	101
A.1.1 Spin wave spectra for increasing $H$ of MC2 . . . . .	101
A.2 SI – Nanoimaging of Ultrashort Magnon Emission by Ferromagnetic Grating Couplers at GHz Frequencies . . . . .	101
A.2.1 Sample fabrication. . . . .	102
A.2.2 Time-resolved STXM. . . . .	102
A.2.3 Processing of TR-STXM raw data . . . . .	102
A.2.4 All electric broadband spin wave spectroscopy. . . . .	103
A.2.5 Magnon dispersion relation. . . . .	103
A.3 SI – Efficient wavelength conversion of exchange magnons below 100 nm by magnetic coplanar waveguides . . . . .	107
A.4 SI – Chapter 6: Magnonic memory . . . . .	111
A.4.1 Estimation of spin wave decay . . . . .	112
<b>B Sample fabrication: Detailed steps</b>	<b>115</b>

B.1	Fabrication of NiFe gratings on YIG . . . . .	115
<b>C</b>	<b>Scripts</b>	<b>117</b>
C.1	Numerical calculation of the CPW excitation profile . . . . .	117
	<b>Bibliography</b>	<b>121</b>
	<b>Curriculum Vitae</b>	<b>139</b>



# List of publications

## First-Authored Publications

1. K. Baumgaertl, J. Gräfe, P. Che, A. Mucchietto, J. Förster, N. Träger, M. Bechtel, M. Weigand, G. Schütz and D. Grundler. Nanoimaging of Ultrashort Magnon Emission by Ferromagnetic Grating Couplers at GHz Frequencies. *ACS Nano Letters* **20**, 7281–7286 (2020). DOI: 10.1021/acs.nanolett.0c02645
2. P. Che\*, K. Baumgaertl\*, A. Kúkol'ová, C. Dubs and D. Grundler. Efficient wavelength conversion of exchange magnons below 100 nm by magnetic coplanar waveguides. *Nature Communications* **11**, 1445 (2020). DOI: 10.1038/s41467-020-15265-1  
\*equal contributions
3. K. Baumgaertl, S. Watanabe and D. Grundler. Phase control of spin waves based on a magnetic defect in a one-dimensional magnonic crystal. *Applied Physics Letters* **112**, 142405 (2018). DOI: 10.1063/1.5024541

## Co-Authored Publications

1. V. S. Bhat, S. Watanabe, K. Baumgaertl, A. Kleibert, M. A. W. Schoen, C. A. F. Vaz, and D. Grundler. Magnon Modes of Microstates and Microwave-Induced Avalanche in Kagome Artificial Spin Ice with Topological Defects. *Physical Review Letters* **125**, 117208 (2020). DOI: 10.1103/PhysRevLett.125.117208
2. M. C. Giordano, K. Baumgaertl, S. R. Steinvall, J. Gay, M. Vuichard, A. Fontcuberta i Morral and D. Grundler. Plasma-Enhanced Atomic Layer Deposition of Nickel Nanotubes with Low Resistivity and Coherent Magnetization Dynamics for 3D Spintronics. *ACS Applied Materials & Interfaces* **12**, 40443-40452 (2020). DOI: 10.1021/acsami.0c06879
3. S. Watanabe, V. S. Bhat, K. Baumgaertl and D. Grundler. Direct Observation of Worm-Like Nanochannels and Emergent Magnon Motifs in Artificial Ferromagnetic Quasicrystals. *Advanced Functional Materials* **30**, 2001388 (2020). DOI: 10.1002/adfm.202001388
4. M. Xu, K. Yamamoto, J. Puebla, K. Baumgaertl, B. Rana, K. Miura, H. Takahashi, D. Grundler, S. Maekawa and Y. Otani. Nonreciprocal surface acoustic wave propagation via

## List of publications

---

- magneto-rotation coupling. *Science Advances* **6**, 32 (2020) DOI: 10.1126/sciadv.abb1724
5. N. Träger, F. Groß, J. Förster, K. Baumgaertl, H. Stoll, M. Weigand, G. Schütz, D. Grundler and J. Gräfe. Single shot acquisition of spatially resolved spin wave dispersion relations using X-ray microscopy. *Scientific Reports* **10**, 18146 (2020). DOI: 10.1038/s41598-020-74785-4
6. H. Wang, J. Chen, T. Liu, J. Zhang, K. Baumgaertl, C. Guo, Y. Li, C. Liu, P. Che, S. Tu, S. Liu, P. Gao, X. Han, D. Yu, M. Wu, D. Grundler and H. Yu. Chiral spin-wave velocities induced by all-garnet interfacial Dzyaloshinskii-Moriya Interaction in ultrathin yttrium iron garnet films. *Physical Review Letters* **124**, 027203 (2020). DOI: 10.1103/PhysRevLett.124.027203



# **Introductory chapters**

## **Part I**



# 1 Motivation and context

Magnetic materials play an important role in modern technologies. Applications exploit for instance bulk materials as permanent magnets in energy-harvesting windmills, ferrimagnetic spheres in microwave components and ferromagnetic thin films in non-volatile data storage. Current research efforts aim at optimizing the microwave properties of ferro- and ferrimagnetic materials to advance and miniaturize microwave electronics. Here, nanostructured materials with tailored and optimized spin wave (SW) properties are important [1–3]. Spin waves (magnons) are collective spin excitations that exhibit a specific wavelength [4] and allow for information transport and processing without moving electric charges. They are excited in the technologically relevant GHz regime, where electromagnetic waves in air have wavelengths on the order of centimeter or larger. At the same frequencies spin waves exhibit significantly shorter wavelengths down to a few 10 nm [5]. The gigantic wavelength reduction is at the core of a magnonics-based technology [6, 7].

Our society heavily relies on the wireless exchange of information. Currently we are undergoing a digital transformation towards an internet of things (IoT) [8], where a growing number of devices are wirelessly interconnected and share information in real time. By end of 2019 about 8 billion of active IoT devices were estimated and a tripling within the next 10 years is expected [9]. Key challenges include miniaturization, power consumption and receiver flexibility. Energy efficiency determines the life cycle of IoT devices with non-chargeable battery cells [10]. Microwave receivers are required to operate at several frequency bands and today's fixed filter technology adds considerable to the fabrication cost, size and energy footprint [11]. Here, magnonic devices promise unprecedented down-scaling, low energy consumption by circumventing Joule heating, and flexibility, as magnonic band structures are reprogrammable. Analog signal processing with spin waves has attracted ongoing research interest for several decades [12–15]. However, most of the pioneering works addressed long-waved SWs in the millimeter and micrometer range. Only in the recent decade advances in the field of magnonics and in technology in general have led to the study of SWs at the nanoscale [16]. At small wavelengths, SWs become interesting for beyond-CMOS computation [3, 17–19] as well. This thesis addresses three challenges towards technological applicability of SWs at the nanoscale, which are contextualized in the following:

### 1.1 Magnonic crystals: Controlling spin waves on the nanoscale

To control electromagnetic waves in solids periodic modulation of material properties has been used to create man-made band structures and engineer material properties not found in nature. A prominent example are so-called photonic crystals. Here the dielectric constant is periodically modulated which gives rise to an artificial band structure for photons [20, 21]. Other prominent examples are plasmonic and phononic crystals [22, 23].

To functionalize magnetic materials for microwave applications, we aim at enhanced control of their SW properties on the nanoscale. Nowadays, state of the art lithography allows one to nanopattern magnetic materials on the length scale of the SW wavelength. It was shown that periodic modulation of magnetic parameters modifies the dispersion relation of SWs and leads to artificial band structures, giving rise to so-called magnonic crystals (MCs) [24–26]. Thereby magnetic metamaterials with tailored SW properties are created.

Magnonic crystals have been realized in various ways and in up to three dimensions [27]. Common approaches for MCs included periodic structuring of magnetic thin films by introducing partial grooves [28–31] or complete air gaps [32–34], and the alternation between different magnetic materials [35–37]. MC were further realized by periodic ion-implantation [38], optical heating [39] and spatially modulated magnetic fields [40–42].

In the course of this thesis we focus on one-dimensional (1D) MCs consisting of ferromagnetic nanostripes separated by small air gaps. Individual ferromagnetic nanostripes confine standing SWs with quantized wavelengths [43, 44]. Gubbiotti *et al.* [32, 33] demonstrated that, if spaced close enough together, magnetic nanostripes dipolarly couple and a band structure is formed allowing for propagating SWs.

Ferromagnetic nanostripes itself exhibit a bistable magnetic ground state and are therefore ideal building blocks for reconfigurable MCs, that feature different stable magnetic configurations at remanence. By periodic modification of the magnetic order, the band structure of such a MC can be reprogrammed [34, 45–48]. This is one of the main advantages of MCs compared to their equivalents in photonics, plasmonics and other fields of physics.

In 2013, R. Huber *et al.* [49] reported SW scattering, when an individual nanostripe in a 1D MC was magnetized antiparallel to the others. The introduced magnetic defect reduced measured SW transmission between two coplanar waveguides by about 30 %. In Chapter 4 we build on this pioneering work and investigate a magnetic defect in an metallic 1D MCs by means of all-electrical spin wave spectroscopy and space- and phase-resolved Brillouin light scattering. Our findings show that phase and amplitude of SWs are modified by an individual magnetic defect depending on the application of a magnetic bias field. In our experiments large phase shifts were concomitant with a reduction in amplitude. Using micromagnetic simulations, we identify specific bias fields at which a  $\pi$  phase shift and occurs while maintaining a large SW amplitude. We note that part of Chapter 4 (Section 4.1) was published in Applied Physics Letters [50] and was reproduced with the permission of the publisher.

## 1.2 Efficient excitation of short magnons

To exploit the short wave lengths of SWs for applications in microwave technology, it is essential to efficiently couple them to electromagnetic waves. The severe mismatch in wave vector makes effective inter-conversion challenging. To excite propagating SWs, commonly planar microwave transmission lines, e.g. microstrips or coplanar waveguides (CPWs), are fabricated on top of a magnetic thin film [51], which serves as the SW medium. When a microwave current is applied to the transmission line, a dynamic magnetic field is created in the vicinity of transmission line. The dynamic field provides an oscillating torque on the magnetic moments in the thin film and propagating SWs are excited. Details of the excitation efficiency of CPWs will be provided in Chapter 3 (Methods). Importantly, the SW wavelength is governed by the spatial variation of the microwave field and is on the length scale of the transmission line width [52]. While the width of waveguides can be downsized to a certain extend [53], Ohmic resistance increase becomes a limiting factor on the nanoscale. In 2013, H. Yu *et al.* showed that by introducing a periodic grating of nanomagnets between CPW and a magnetic thin film, several additional high frequency modes appeared in all-electrical spin wave spectroscopy measurements. The modes were attributed to reciprocal lattice vectors of the grating and multiple of it. This so-called grating coupler effect was addressed by several later studies [5, 54–56], however due to a lack of spatial and temporal resolution of the used measurement techniques, wavelengths and amplitudes of the grating coupler modes were not quantified. In the first part of Chapter 5 we report on time-resolved scanning X-ray transmission microscopy on a 1D grating coupler fabricated out of periodically arranged permalloy (Py) nanostripes on a thin Yttrium iron garnet (YIG) film. We measured efficient emission of SWs with wavelengths down to 100 nm at 8 GHz, which is two orders of magnitude smaller than the SW wavelength provided by the geometrical size of the CPW and 375000 times smaller than the wavelength of electromagnetic waves at the same frequency. Additional to the anticipated grating coupler effect, we found a further wavelength conversion at the interface between grating coupler and bare YIG film. Our observations were published in ACS Nano Letters [57] and reprinted with the permission of the journal.

In the second part of Chapter 5 we report on an alternative approach for short-waved SW generation, which does not require nanotechnology. Our method is based on wavelength conversion of SWs in an inhomogeneous magnetic field [58]. By fabricating magnetic CPWs (mCPWs), we introduce a stray field in the underlying SW medium. The stray field increased the resonance frequency of SWs in the vicinity of the mCPW. SWs which propagated away from a mCPW were exposed to a lower effective magnetic field and their wavelength took smaller values in accordance to their dispersion relation. We found propagating SWs with wavelengths down to 100 nm, and showed with micromagnetic simulations that wavelengths down to few tens of nanometers are expected in an optimized sample. This research was done in close collaboration with Ping Che, whose contributions are explicitly acknowledged here. The work was published with us as equally contributing Co-authors in Nature Communications [59]. Reprint was granted due to a Creative Commons licensing of the publisher.

### 1.3 Magnonic memory: How to store spin waves?

Magnons are quasiparticles with a life-time of few hundred nanoseconds in optimized materials [3]. Proposed computation schemes with SWs often encode the outcome of a logic operation in the output SW amplitude. To have the computed information accessible, it is thus important to store SW amplitudes in a non-volatile manner. While it is possible to electrically detect SWs and then store outcome amplitudes in conventional memories, magneto-electric conversion losses were identified as the main factor limiting the energy efficiency of magnonic devices [60]. Recently J. Han *et al.* [61] reported the displacement of a domain wall exposed to propagating spin waves. The results are promising in that volatile SWs induced a non-volatile change in the static magnetization. However the required microwave powers were in the milliwatt scale. In Chapter 6 we report on remote switching of the static magnetization of nanomagnets by propagating SWs excited at few tens of microwatt. Our results are promising for the realization of a *magnonic memory*, which stores SW signals directly, without converting them to electrical signals first.

## 2 Theoretical background

This chapter is intended to introduce essential theoretical concepts required in the course of this thesis. In Sec. 2.1 we provide a brief introduction to magnetism and magnetically ordered materials. In Sec. 2.2 we introduce relevant micromagnetic energy terms, which allow for computation of the static magnetization configuration. Section 2.3 addresses magnetization dynamics of ferromagnets. Thereby first the Landau-Lifshitz-Gilbert equation (Sec. 2.3.1), which constitutes the equation of motion for magnetic moments, and the effective magnetic field are introduced. Then we discuss the special case of ferromagnetic resonance (Sec 2.3.2). Finally we address the dispersion relation of spin waves in magnetic thin films (Sec. 2.3.3) and in magnonic crystals (Sec. 2.3.4). In Sec. 2.3.5 the theoretical foundations for micromagnetic simulations are provided.

### 2.1 Introduction to Magnetism

Magnetic phenomena fascinated people for a long time. More than 2500 years ago, Thales of Miletus described the attraction between natural occurring  $\text{Fe}_3\text{O}_4$  (known as "loadstone") and iron [62]. However for the most time of human history, the origin of magnetism stayed a mystery. Fundamental understanding of magnetism was only achieved with the established of quantum mechanics during the first half of the 20th century [63]. Following quantum electrodynamics, an microscopic magnetic moment  $\boldsymbol{\mu}_i$  is attributed to the spin and orbital angular momenta of electrons. The total magnetic moment  $\boldsymbol{m} = \sum_i \boldsymbol{\mu}_i$  is directly proportional to the total angular momentum  $\boldsymbol{J}$  (summation rules for  $\boldsymbol{J}$  are found in Ref. [63]) via

$$\boldsymbol{m} = \gamma \boldsymbol{J}, \quad (2.1)$$

where  $\gamma = g\mu_0 \frac{|e_0|}{2m_e}$  is called the gyromagnetic ratio [64, 65]. Here  $\mu_0 = 4\pi \cdot 10^{-7} \text{ N/A}^2$  is the vacuum permeability,  $e_0$  and  $m_e$  are the electron mass and charge respectively and  $g$  is the Landé factor. Metallic ferromagnets are typically governed by the spin angular momentum with  $\boldsymbol{J} \approx \boldsymbol{S}$  and  $g \approx 2$ . For an electron the spin angular momentum projected along any given direction amounts to  $\frac{1}{2}\hbar$ , where  $\hbar$  is the reduced Planck constant. Thus the associated mag-

netic moment of an electron calculates to  $\mu_B = \frac{\hbar e_0}{2m_e} = 9.274 \cdot 10^{-24} \text{ J} \cdot \text{T}^{-1}$  and is denoted Bohr magneton.

Despite the quantized nature, a classical continuum approach can be used to describe most of the magnetic properties of solids. We note that this still holds true for the magnetic nanostructures discussed in this thesis, as all structural dimensions are still large compared to the interatomic lattice constant, i.e. to the spacing of atomic magnetic moments.

The magnetization  $\mathbf{M} = \mathbf{m}/V$  is a measure of the magnetic moments per volume  $V$  and treated as continuous variable. The magnetic property of a materials is classified based on the response of its magnetization to an applied magnetic field  $\mathbf{H}$ , given by the relationship

$$\mathbf{M} = \chi \mathbf{H}, \quad (2.2)$$

where  $\chi$  is termed magnetic susceptibility. In general,  $\mathbf{M}$  and  $\mathbf{H}$  are not necessarily parallel and the susceptibility is then expressed as a tensor  $\hat{\chi}$ . Magnetic materials can be classified as follows [66]:

*Diamagnetic* materials possess no permanent magnetic moments  $\mu_i$ . For applied  $\mathbf{H}$ , a weak magnetic flux density is induced pointing against the external magnetic field.  $\chi$  is negative and very small on the magnitude of  $10^{-5}$ .

*Paramagnetic materials* possess magnetic moments which are not ordered. By application of an increasing external field the moments are gradually aligned into the same direction, resulting in a macroscopic magnetization.  $\chi$  is positive and on the order of  $10^{-4}$ .

*Ferromagnetic, ferrimagnetic and antiferromagnetic* materials possess permanent magnetic moments which are ordered also without the application of an external magnetic field. The ordering is due to the quantum-mechanical exchange interaction between neighboring permanent moments. The energy of the exchange interaction is on the scale of 10 to 100 meV and exceeds by far the energy of the classical dipolar interaction amounting to about 0.1 meV [65]. In *antiferromagnetic* materials the exchange interaction favors an anti-parallel orientation of magnetic moments resulting in a vanishing macroscopic magnetization. The susceptibility of antiferromagnetic materials is positive but very small, as an external field has to act against the exchange-interaction.

In contrast for *ferromagnetic* materials a parallel alignment of neighboring magnetic moments is favored by the exchange interaction. Due to further interactions discussed in the next section, on the macroscopic scale magnetic domains are formed. Within each domain magnetic moments are aligned parallel. The magnetization of a ferromagnetic material depends on it's magnetic history. For a random alignment of the magnetic domains the remanent magnetization without external field (so-called *remanence*) is zero and the magnetization increases significantly with an applied field. The relative susceptibility of a strong ferromagnet is on the order of  $10^6$ . When all magnetic moments are aligned in the same direction, the magnitude of the magnetization  $|\mathbf{M}|$  reaches the saturation magnetization  $M_s$  of the material.  $M_s$  depends on the temperature  $T$ . For low temperatures  $M_s(T)$  can be described via Bloch's  $T^{2/3}$  law, given by [67, 68],

$$M_s(T) = M_s(T = 0) [1 - a(T/T_C)^{2/3}]. \quad (2.3)$$



Here  $a$  is a constant depending on the exchange energy.  $T_C$  is the so-called Curie temperature. Above  $T_C$  a ferromagnetic material loses its permanent magnetization and becomes paramagnetic. From the elements only iron (Fe), nickel (Ni) and cobalt (Co) are ferromagnetic at room temperature (RT).

*Ferrimagnetic* materials possess two different magnetic sublattices. Neighboring magnetic moments are antiferromagnetically aligned, however their magnitude is different. Hence ferrimagnets show a spontaneous magnetization and their macroscopic magnetic behavior is similar to ferromagnets. Due to the partial cancelling of magnetic moments the saturation magnetization of ferrimagnets is typically smaller than for ferromagnets.

Besides the magnetization  $\mathbf{M}$  and the magnetic field  $\mathbf{H}$ , another important quantity is the magnetic flux density  $\mathbf{B}$ , defined as

$$\mathbf{B} = \mu_0 (\mathbf{M} + \mathbf{H}) = \mu_0 (\hat{\chi} + 1) \mathbf{H}. \quad (2.4)$$

The term  $\mu_0 (\hat{\chi} + 1)$  is denoted permeability  $\hat{\mu}$ . In literature often the relative permeability  $\mu_r = \mu / \mu_0$  is found.

## 2.2 Static micromagnetics

Ferromagnets often exhibit complex domain patterns due to the interplay of various short- and long-range magnetic interactions. The equilibrium state of a system can be computed by minimizing the total energy resulting from all interactions. Due to computational limitations, this so-called micromagnetic approach [69] is most successful on the micron and sub-micron length scale. Still, an important assumption for micromagnetics is that the direction of neighboring magnetic moments changes only by small angles, such that the magnetization can be approximated as a continuous vector. In the following relevant energy terms are introduced.

### Exchange energy

Ordering of magnetic moments is fundamentally driven by the quantum mechanical exchange energy. Qualitatively it can be understood as a consequence of the Coulomb energy, Heisenberg's uncertainty principle and the Pauli exclusion principle [65]. Following the Pauli exclusion principle, the wave functions of two electrons can only overlap, if their spins  $\mathbf{S}_i$  and  $\mathbf{S}_j$  are aligned antiparallel. Overlapping wave functions allow for more spatial delocalization  $\Delta x$  of the electrons, which reduced the uncertainty of their momenta  $\Delta p$  and thus the kinetic energy proportional to  $(\Delta p)^2$ . On the other hand side, for  $\mathbf{S}_i \parallel \mathbf{S}_j$ , the electrons have to be separated apart in space, which lowers the repulsive electrostatic Coulomb energy. Depending on which of the two energies is larger, either a antiferromagnetic or a ferromagnetic coupling

## Chapter 2. Theoretical background

---

is preferred. In a system with  $N$  electrons the exchange energy can be formulated via

$$E_{\text{ex}} = - \sum_{i,j}^N J_{i,j} \mathbf{S}_i \cdot \mathbf{S}_j = - \sum_{i < j}^N 2J_{i,j} \mathbf{S}_i \cdot \mathbf{S}_j, \quad (2.5)$$

where  $2J_{i,j}$  characterizes the energy difference between parallel and antiparallel spin orientation of electrons  $i$  and  $j$ . In a continuum approach the exchange energy is calculated by [70, 71]

$$E_{\text{ex}} = \frac{A_{\text{ex}}}{M_S^2} \int (\nabla \mathbf{M})^2 dV. \quad (2.6)$$

The parameter  $A_{\text{ex}}$  is the material specific exchange stiffness. Typical values are on the order of  $10^{-11} \text{ J} \cdot \text{m}^{-1}$ . The exchange energy can take large values when the magnetization direction changes on a short length scale. This explains for example why domain walls, in which  $\mathbf{M}$  is rotated by  $180^\circ$  are not abrupt, but possess typically a width in the range of tens of nanometers [66], such that on the atomistic scale neighboring magnetic moments are only tilted slightly against each other and the exchange energy is small.

### Zeeman energy

The potential energy of magnetic moments in an external field  $H_{\text{ext}}$  is named after Pieter Zeeman and calculated via

$$E_z = -\mu_0 \int_V \mathbf{H}_{\text{ext}} \cdot \mathbf{M} dV. \quad (2.7)$$

The Zeeman energy is minimized when the magnetization is aligned with the external field.

### Demagnetization field energy

From Eq. 2.4 and Maxwell's equation  $\nabla \cdot \mathbf{B} = 0$ , we find  $\nabla \cdot \mathbf{M} = -\nabla \cdot \mathbf{H}$ , i.e. a discontinuity in the magnetization is a source or sink of a magnetic field. The field created from a magnetic body itself is often called *stray field* in the region outside the body and *demagnetization field*  $\mathbf{H}_d$  inside the body. The demagnetization field acts on the magnetization and is responsible for a magnetostatic self energy given by

$$E_d = \frac{\mu_0}{2} \int_V \mathbf{H}_d \cdot \mathbf{M} dV. \quad (2.8)$$

In general the demagnetization field is inhomogeneous and often solved numerically in micromagnetic simulations. For the special case of uniformly magnetized elliptical bodies the demagnetization field is uniform and can be analytically calculated by

$$\mathbf{H}_d = -\hat{N}\mathbf{M} = - \begin{pmatrix} N_x & 0 & 0 \\ 0 & N_y & 0 \\ 0 & 0 & N_z \end{pmatrix} \mathbf{M} \quad (2.9)$$

where  $\hat{N}$  is denoted demagnetization tensor. The parameters on its diagonal are called demagnetization factors. They fulfill  $N_x + N_y + N_z = 1$ . In the case of a sphere we find  $N_x = N_y = N_z = \frac{1}{3}$ . The formalism of Eq. 2.9 can still be applied to non-ellipsoidal magnetic bodies, if a uniform magnetization is assumed [72]. The demagnetization field of a magnetic thin film with a large width and length compared to its thickness is well approximated by  $N_x = N_y = 0$  and  $N_z = 1$  for  $z$  being the out-of-plane direction [73].

### Anisotropy Energy

Due to spin-orbit coupling, crystalline magnetic materials are often magnetized preferably into certain high symmetry axis. This leads to an additional anisotropy energy  $E_{\text{ani}}$ . A detailed discussion on magnetocrystalline anisotropy can be found e.g. in Ref. [74]. For the materials used in the course of this thesis  $E_{\text{ani}}$  plays a minor role. In the case of Py the stoichiometry of Fe and Ni was specially optimized to suppress magnetocrystalline anisotropy [75]. CoFeB is amorphous and for YIG the magnetocrystalline anisotropy is relatively small [76].

### Total energy and effective magnetic field

By summing up all relevant energy terms the total energy of a system is computed according to:

$$E_{\text{tot}} = E_{\text{ex}} + E_{\text{d}} + E_{\text{ani}} + E_z. \quad (2.10)$$

To reach an equilibrium state of the static magnetization, the energy landscape can be minimized using an gradient method. From the energy landscape it is possible to define an effective magnetic field via [71]

$$\mathbf{H}_{\text{eff}} = -\frac{1}{\mu_0} \frac{\text{d}}{\text{d}\mathbf{M}} \frac{\text{d}E_{\text{tot}}}{\text{d}V}. \quad (2.11)$$

A metastable magnetic configuration is reached when  $\mathbf{M} \parallel \mathbf{H}_{\text{eff}}$ .

## 2.3 Magnetization dynamics

### 2.3.1 Landau-Lifshitz-Gilbert Equation

In the previous section effective magnetic field  $\mathbf{H}_{\text{eff}}$  was introduced. In the static limit  $\mathbf{M}$  is aligned with  $\mathbf{H}_{\text{eff}}$  to minimize the total energy. In this section we discuss the dynamic response if  $\mathbf{M}$  and  $\mathbf{H}_{\text{eff}}$  are not parallel. Magnetic moments in a field  $\mathbf{H}$  exhibit a torque  $\mathbf{T} = \mu_0 \mathbf{m} \times \mathbf{H}$ . In classical Newtonian mechanics a torque describes the rate of change of an angular momentum  $\mathbf{L}$  via  $\mathbf{T} = \frac{\text{d}\mathbf{L}}{\text{d}t}$ . Quantum mechanics directly links magnetic moments to an angular momentum (Eq. 2.1). This leads to the equation of motion proposed by Landau and Lifschitz (LL) [77] in 1935:

$$\frac{\text{d}\mathbf{M}}{\text{d}t} = -\gamma \mu_0 \mathbf{M} \times \mathbf{H}_{\text{eff}}. \quad (2.12)$$

The LL equation describes a precession of the magnetization around the effective field with an angular frequency  $\omega_H = \gamma\mu_0 \mathbf{H}_{\text{eff}}$ . This is valid for a ferromagnet which is infinitely large. Experimental observations show that eventually the precession amplitude decays and  $\mathbf{M} \parallel \mathbf{H}_{\text{eff}}$  in the static limit. To attribute for the damping Landau and Lifshitz included a phenomenological term, which was later redefined by Gilbert, leading to the Landau–Lifshitz–Gilbert equation (LGG)[78]:

$$\frac{d\mathbf{M}}{dt} = -\gamma\mu_0 \mathbf{M} \times \mathbf{H}_{\text{eff}} - \frac{\gamma\mu_0\alpha}{M_s(1+\alpha^2)} \mathbf{M} \times (\mathbf{M} \times \mathbf{H}_{\text{eff}}). \quad (2.13)$$

The parameter  $\alpha$  can take values from 0 to 1 and is termed Gilbert damping parameter. For magnonic applications materials with small  $\alpha$  are considered to avoid damping losses. In optimized YIG values of  $\alpha$  in the order of  $10^{-5}$  can be achieved. The quadratic term of  $\alpha$  in Eq. 2.13 is hence often neglected. The LLG equation is the standard equation of motion and solved numerically in most micromagnetic simulation programs. For small precession amplitudes the equation can be linearized and analytically solved. An extensive overview of analytic solutions can be found in Ref. [64].

### 2.3.2 Ferromagnetic resonance

In this section we sketch a general approach for solving the LLG equation following Ref. [64] and provide the most relevant analytic solutions.

For simplicity we start with the LL without damping. We assume a uniform precession of all magnetic moments. The magnetization and the magnetic field are written as the sums of stationary components  $\mathbf{M}_0$  and  $\mathbf{H}_0$  and dynamic components  $\tilde{\mathbf{m}}$  and  $\tilde{\mathbf{h}}$ , respectively.  $\mathbf{M}_0$  and  $\mathbf{H}_0$  are assumed to be parallel, consequently  $\mathbf{M}_0 \times \mathbf{H}_0 = 0$ . Further we assume that the dynamic components are much smaller than the static ones ( $\tilde{m} \ll M_0$  and  $\tilde{h} \ll H_0$ ). Accordingly the term  $\tilde{\mathbf{m}} \times \tilde{\mathbf{h}} \approx 0$  can be neglected. Inserting  $\mathbf{M} = \mathbf{M}_0 + \tilde{\mathbf{m}}$  and  $\mathbf{H}_{\text{eff}} = \mathbf{H}_0 + \tilde{\mathbf{h}}$  into Eq. 2.12 leads to the linearized equation of motion

$$\frac{d\tilde{\mathbf{m}}}{dt} = -\gamma\mu_0 (\tilde{\mathbf{m}} \times \mathbf{H}_0 + \mathbf{M}_0 \times \tilde{\mathbf{m}}). \quad (2.14)$$

We assume a sinusoidal time dependence of  $\tilde{\mathbf{m}}$  and  $\tilde{\mathbf{h}}$  and use a complex notation with  $\tilde{\mathbf{m}} = \mathbf{m} \exp(i\omega t)$  and  $\tilde{\mathbf{h}} = \mathbf{h} \exp(i\omega t)$ , leading to

$$i\omega \mathbf{m} + \gamma\mu_0 \mathbf{m} \times \mathbf{H}_0 = -\gamma\mu_0 \mathbf{M}_0 \times \mathbf{h}. \quad (2.15)$$

In a Cartesian coordinate system with  $\mathbf{M}_0$  and  $\mathbf{H}_0$  pointing in  $x$ -direction, we obtain

$$\begin{aligned} i\omega m_x &= 0 \\ i\omega m_y + \gamma\mu_0 m_z H_0 &= \gamma\mu_0 M_0 h_z \\ i\omega m_z - \gamma\mu_0 m_y H_0 &= -\gamma\mu_0 M_0 h_y \end{aligned} \quad (2.16)$$

The set of equations is solved by  $m_x = 0$ ,  $m_y = \chi h_y + i\chi_a h_z$  and  $m_z = -i\chi_a h_y + \chi h_z$ . Here  $\chi$  and  $\chi_a$  are the diagonal and off-diagonal elements of a susceptibility tensor  $\hat{\chi}$  introduced by Polder [79]. We find

$$\chi = \frac{\gamma\mu_0 M_0 \omega_H}{\omega_H^2 - \omega^2}, \quad \chi_a = \frac{\gamma\mu_0 M_0 \omega}{\omega_H^2 - \omega^2} \quad (2.17)$$

with  $\omega_H = \gamma\mu_0 H_0$ . The dynamic magnetization  $\mathbf{m}$  can be written as  $\mathbf{m} = \hat{\chi}\mathbf{h}$  with the Polder tensor given by

$$\hat{\chi} = \begin{pmatrix} 0 & 0 & 0 \\ 0 & \chi & i\chi_a \\ 0 & -i\chi_a & \chi \end{pmatrix}. \quad (2.18)$$

In the simplified case of a lossless ferromagnet the susceptibility diverges to  $\pm\infty$  for  $\omega$  approaching  $\omega_H$ . For a more realistic solution the LLG-equation with damping term has to be considered. Further it is necessary to include dynamic demagnetization fields  $\tilde{\mathbf{h}}_{\text{dem}} = \hat{N}\tilde{\mathbf{m}}$ . Such a treatment was first conducted by Charles Kittel [80], leading to the well known Kittel formula:

$$\omega_{\text{res}} = 2\pi f_{\text{res}} = \gamma\mu_0 \sqrt{[H_0 + (N_y - N_x)M_S][H_0 + (N_z - N_x)M_S]} \quad (2.19)$$

with  $f_{\text{res}}$  being the frequency of the ferromagnetic resonance (FMR) and  $H_0$  pointing in the  $x$ -direction. Figure 2.1a shows the calculated FMR frequency for a YIG thin film in the  $x$ - $y$

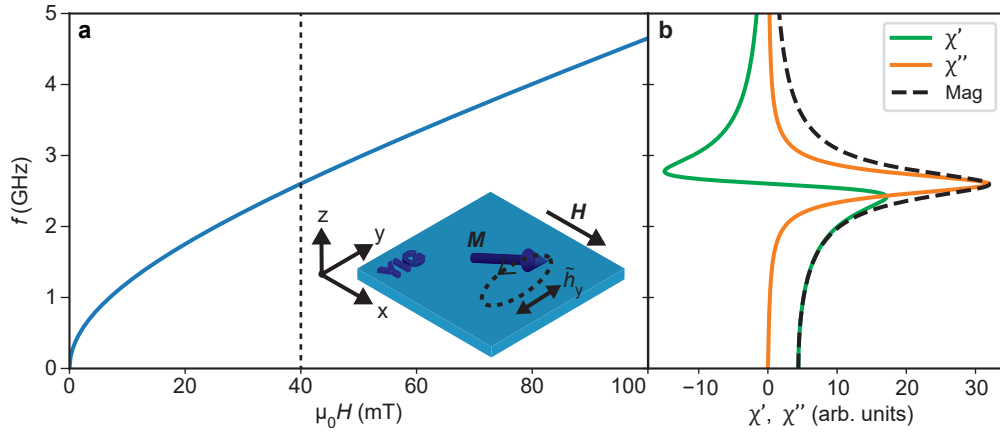


Figure 2.1 – **a** FMR frequency of a YIG thin film with a magnetic field applied in-plane following Kittel's formula. **b** Susceptibility at 40 mT (indicated by a dashed line in **a**) calculated for  $\alpha = 0.05$ . At resonance the real part of the susceptibility  $\chi'$  goes to zero and the imaginary part  $\chi''$  is at its maximum.

plane with  $N_x = N_y = 0$  and  $N_z = 1$  (YIG parameters:  $\frac{\gamma\mu_0}{2\pi} = 28 \text{ GHz T}^{-1}$  and  $\mu M_S = 0.176 \text{ T}$ ). In a typical experimental configuration, the FMR is excited by a small  $\tilde{h}_y$  applied perpendicular to  $\mathbf{H}_0$ . The relevant susceptibility in  $y$ -direction calculates to [81–83]:

$$\text{Re}(\chi_{yy}) = \chi'_{yy} = \frac{\omega_M(\omega_H + \omega_M)(\omega_{\text{res}}^2 - \omega^2)}{(\omega_{\text{res}}^2 - \omega^2)^2 + \alpha^2 \omega^2 (2\omega_H + \omega_M)^2} \quad (2.20)$$

$$\text{Im}(\chi_{yy}) = \chi''_{yy} = \frac{\alpha \omega \omega_M [\omega^2 + (\omega_M + \omega_H)^2]}{(\omega_{\text{res}}^2 - \omega^2)^2 + \alpha^2 \omega^2 (2\omega_H + \omega_M)^2} \quad (2.21)$$

Here, we use  $\omega_M = \mu_0 \gamma M_S$  and  $\omega_H = \mu_0 \gamma H_0$ . Figure 2.1b depicts  $\chi'_{yy}$  and  $\chi''_{yy}$  for  $\mu_0 H_0 = 40$  mT and an exemplary Gilbert damping parameter  $\alpha = 0.05$ . At resonance the real part of the susceptibility goes through zero and the imaginary part is at its maximum. This corresponds to a  $90^\circ$  phase-delay of the precessional amplitude with respect to the driving  $\tilde{h}_y$ . The line shape of  $\chi''$  can be approximated by an Lorentzian function. The linewidth of  $\chi''$  is a measure of the Gilbert damping. To extract  $\alpha$  of a magnetic thin film typically the sample is saturated in out-of-plane direction to avoid two-magnon scattering. In this case the linewidth  $\Delta f_{\text{res}}$  (full width at half maximum) depends on  $\alpha$  via [84, 85]

$$\Delta f_{\text{res}} = \frac{|\gamma|}{2\pi} \mu_0 \Delta H + 2\alpha f_{\text{res}}. \quad (2.22)$$

Here  $\Delta H$  is a linewidth broadening attributed to extrinsic mechanisms and film inhomogeneities. To extract  $\alpha$  the lineshape is measured for different magnetic field values and the slope of  $\Delta f_{\text{res}}$  plotted over  $f_{\text{res}}$  is evaluated.

### 2.3.3 Spin wave dispersion

So far, we introduced the special case of uniform magnetization precession of all magnetic moments in phase, called ferromagnetic resonance. The FMR response is typically probed in experiments in which a uniform driving field  $\tilde{h}$  is applied to the whole sample. In contrast, when magnetic moments are excited locally with a confined  $\tilde{h}$ , the dipolar and exchange couplings between neighboring magnetic moments lead to a spread of the oscillation throughout the sample. Thereby the precession of neighboring moments possess a certain phase difference, giving rise to spin waves (SWs) with a finite wavelength  $\lambda$  and a non-zero wave

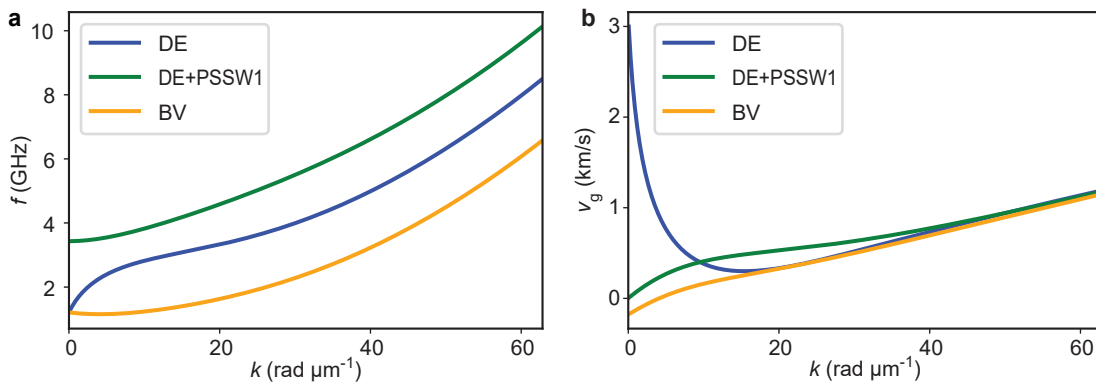


Figure 2.2 – **a** SW dispersion relations of a 100 nm thick YIG film magnetized in-plane with  $\mu H = 10$  mT. The blue curve shows DE SWs with  $\mathbf{k} \perp \mathbf{M}$ , the orange curve BV SWs with  $\mathbf{k} \parallel \mathbf{M}$ . The green curve shows the first PSSW ( $n = 1$ ) in DE configuration. **b** Related group velocities for the dispersion relations depicted in **a**.

vector  $k = \frac{2\pi}{\lambda}$ . To compute the dispersion relation of such SWs, exchange and dipolar energies need to be considered. A comprehensive analytical treatment was done by Kalinkos and Slavin (K.S.) [86] in 1986. Here we provide their solution for an in-plane magnetized magnetic thin film with unpinned surface spins. The wave vector is split into an in-plane component  $\mathbf{k}$  and an out-of-plane component  $\mathbf{\kappa}_n$ . The wave vector  $\mathbf{\kappa}_n$  represents perpendicular standing spin waves (PSSWs). The wave vector of PSSWs is quantized with  $\kappa_n = n\pi/t$ , where  $n$  is an integer number ( $n = 0, 1, 2, \dots$ ) and  $t$  is the thickness of the magnetic film. The magnitude of the full wave vector is calculated by  $k_n = \sqrt{k^2 + \kappa_n^2}$ . The dispersion relation of SWs in a thin film with in-plane magnetization is anisotropic and depends on the angle  $\varphi$  defined between  $\mathbf{M}$  and  $\mathbf{k}$ . The K.S. formalism reads:

$$\omega_{\text{res}} = \sqrt{(\omega_H + \omega_M l_{\text{ex}}^2 k_n^2)(\omega_H + \omega_M l_{\text{ex}}^2 k_n^2 + \omega_M F_n)} \quad (2.23)$$

with

$$F_n = 1 - P_n \cos^2(\varphi) + \frac{\omega_M P_n (1 - P_n) \sin^2(\varphi)}{\omega_H + \omega_M l_{\text{ex}}^2 k_n^2} \quad (2.24)$$

and

$$P_n = \frac{k^2}{k_n^2} + \frac{2k^3}{k_n^4 L} \left[ 1 - (-1)^n e^{-kt} \right] \frac{1}{[(1 + \delta_{0n})(1 + \delta_{0n})]}.$$

Further terms are  $\omega_H = \gamma\mu_0 H$ ,  $\omega_M = \gamma\mu_0 M_S$  and  $l_{\text{ex}} = \sqrt{2A_{\text{ex}}/(\mu_0 M_S^2)}$ , which defines the magnetic exchange length [87, 88]. Figure 2.2a shows exemplary dispersion relations calculated for a 100 nm thick YIG film with  $\mu_0 M_S = 176$  mT, an exchange stiffness of  $A_{\text{ex}} = 3.75$  pJ/m and a gyromagnetic ratio of  $\gamma = 28.0$  GHz/T at  $\mu_0 H = 10$  mT. Figure 2.2b depicts the related group velocities calculated by

$$v_g = \partial\omega_{\text{res}}/\partial k. \quad (2.25)$$

SWs with  $\mathbf{k} \perp \mathbf{M}$  are called Damon–Eshbach (DE) waves (blue curves in Fig.2.2a,b), SWs with  $\mathbf{k} \parallel \mathbf{M}$  are denoted backward-volume (BV) waves (orange curves in Fig.2.2a,b). The green curves in Fig. 2.2a,b depict the dispersion and group velocity of a DE SW with  $n = 1$ , i.e. with the first perpendicular quantization in out-of-plane direction, denoted as PSSW1. For large in-plane wave vectors the dispersion is dominated by the exchange interaction, which is isotropic. We find  $\omega_{\text{res}} \propto k^2$  and  $v_g \propto k$ , independent of the angle  $\varphi$  between  $\mathbf{M}$  and  $\mathbf{k}$ . In contrast, for small wave vectors with  $l_{\text{ex}}k \ll 1$  the exchange interaction can be neglected and the dispersion relation is governed by the dipolar interaction, which depends on the relative orientation of magnetic moments. Consequently the dispersion relation is highly anisotropic. The part of the dispersion relation where the exchange interaction can be neglected is often called dipolar regime. At low  $k$ , BV SWs exhibit a small negative group velocity. PSSW modes start with a group velocity of zero, which makes them unfavorable for transmitting information. SWs in DE configuration feature the largest group velocity for small  $k$  and thus the DE configuration is typically preferred in transmission experiments.

### 2.3.4 Bloch's theorem applied to magnonic crystals

The K.S. formalism is valid for SWs in a homogeneous magnetic thin film with in-plane translational invariance of magnetic properties. In magnonic crystals one or several relevant magnetic properties are periodically modulated, which gives rise to a novel artificial band structure [1, 2]. Similar to the calculation of an electronic band structure for electrons in the periodic potential of a crystal lattice, for magnonic crystals an ansatz based on Bloch's theorem can be chosen. The spatially dependent magnetic moment is expressed as a Bloch wave  $\mathbf{m}(\mathbf{r}) = e^{i\mathbf{k}\cdot\mathbf{r}} \mathbf{m}_{\mathbf{k}}(\mathbf{r})$  where  $\mathbf{r} = (x, y, z)$  is the position vector and  $\mathbf{m}_{\mathbf{k}}(\mathbf{r}) = \mathbf{m}_{\mathbf{k}}(\mathbf{r} + \mathbf{R})$  is a periodic function with the period  $\mathbf{R}$ . Due to the periodic properties, Bloch waves are often expressed as Fourier series, defined as:

$$\mathbf{m}(\mathbf{r}) = \sum_{\mathbf{G}} \mathbf{m}_{\mathbf{k}}(\mathbf{G}) e^{i(\mathbf{k}+\mathbf{G})\cdot\mathbf{r}} \quad (2.26)$$

Here  $\mathbf{G}$  denotes reciprocal lattice vectors fulfilling  $\mathbf{G} \cdot \mathbf{R} = 2\pi N$  with  $N \in \mathbb{Z}$  and  $\mathbf{k}$  is a wave vector within the first Brillouin zone (BZ) of the modulated quantity. In the exemplary case of a 1D magnonic crystals with magnetic stripes arranged with a lattice constant  $p$ , the BZ boundary is at  $k_{\text{BZ}} = \frac{\pi}{p}$ . In a first approximation the K.S. dispersion of a plane-film can be taken and back-folded into the first BZ. For a given  $k$  within the first BZ, the dispersion  $f_n(k)$  has multiple solutions characterized by the miniband number  $q$  with  $q \in \mathbb{N}$ . Depending on the modulation strength, band gaps are opened at the BZ boundary. The size of the band gaps and the precise  $f_q(k)$  can be calculated analytically by the plane wave method introduced in Refs. [24, 89]. Band structures presented in this thesis are extracted from micromagnetic simulations, which solve the LLG equation numerically.

### 2.3.5 Micromagnetic Simulations

Computing the magnetic behavior of a system is a challenging problem as both short and long range interactions need to be considered. Due to the substantial increase of computational power in the last decades and the shift of research focus towards smaller magnetic structures on the micron and nanoscale, micromagnetic simulations have become a viable tool, employed by a vast number of research groups [90].

In the course of this thesis we utilize the open-source simulation program MuMax3 [91]. The program uses a finite-difference discretization of the space into a 2D or 3D grid of orthorhombic cells. Different material parameters can be attributed to regions of the simulated space. Each cell represents a microscopic magnetic moment  $\mathbf{m}$ . The volume integrals used in Eqs. 2.6-2.8 are replaced by a summation over cells. For example, the exchange field  $\mathbf{H}_{\text{eff}}$  of a cell with magnetization  $\mathbf{m}$  is calculated by a next-neighbor approximation, as follows:

$$\mathbf{H}_{\text{eff}} = \frac{2A_{\text{ex}}}{\mu_0 M_S} \sum_i \frac{\mathbf{m}_i - \mathbf{m}}{\Delta_i^2}. \quad (2.27)$$



Here  $\Delta_i$  is the center-to-center distance of the evaluated cell to its next-neighbor  $i$  with  $i$  ranging from 1 to 6. Due to the short-range nature of the exchange interaction, it is the limiting factor when choosing the cell size. Equation 2.27 provides an accurate approximation of  $\mathbf{H}_{\text{eff}}$  only if the angle of  $\mathbf{m}$  between neighboring cells is below  $20^\circ$  [91]. Hence the cell size should be small enough to avoid larger deviations between neighboring cells. Generally it is advised to use cells, where each dimension is smaller than the magnetic exchange length  $l_{\text{ex}}$  of the simulated material [92]. For metallic ferromagnets  $l_{\text{ex}}$  is typically on in the range of few nanometers.

MuMax3 calculates the time evolution of the magnetization of each cell by integrating the LLG equation (Eq. 2.13) using a Runge-Kutta method. To relax the magnetic configuration to a state of minimized energy, only the damping torque in the LLG equation is considered. The time evolution is computed until the torque acting on every cell falls below a threshold value. To compute the dispersion relation of a structure along direction  $x$ , we use the following approach: First the magnetization is relaxed to its static equilibrium state. Then a spatial and temporally varying excitation signal [92] is applied, as follows:

$$h_{\text{rf},x}(x, t) = A_0 \cdot \text{sinc}(2\pi f_c(t - t_{\text{off}})) \cdot \text{sinc}(k_c(x - x_{\text{off}})). \quad (2.28)$$

Here, we use the unnormalized sinc function given by  $\text{sinc}(x) = \sin(x)/x$ . The parameter  $t$  represents the time in the simulation. Typically we simulated for 10 ns. A time offset  $t_{\text{off}} = 5$  ns shifted the peak of the sinc function to the center of the simulated time span. Parameters  $f_c$  and  $k_c$  represent the cut-off frequency and wave vector of the sinc excitation, respectively, which is illustrated in Fig. 2.3 exemplary for  $f_c$ .

Figure 2.3a shows the time evolution of  $h_{\text{rf},x}$  at  $x = 0$  with  $f_c = 40$  GHz and the peak amplitude  $A_0 = 1$  mT. The fast Fourier transform (FFT) of the signal is depicted in Fig. 2.3b and shows a rectangular function which is constant between  $-f_c$  and  $f_c$ . I.e. the sinc function provides an equal excitation strength for all frequencies up to  $\pm f_c$ . Similarly, a FFT in space results in a rectangular function spanning from  $-k_c$  to  $k_c$  (not shown). In the case of an infinite

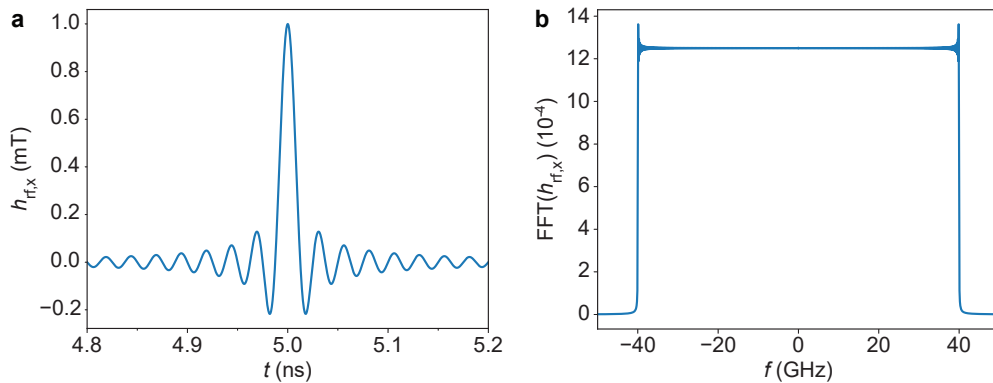


Figure 2.3 – **a** Time evolution of the exciting signal  $h_{\text{rf},x}$  at  $x = 0$ . **b** The FFT of  $h_{\text{rf},x}$  is given by a rectangular function with cut-off frequencies  $\pm f_c = 40$  GHz. I.e., the sinc function provides an equal excitation strength for frequencies in the window between  $-f_c$  and  $+f_c$ .

magnetic plane film, where  $\chi$  is translationally invariant, all wave vectors between  $-k_c$  to  $k_c$  are excited with equal strength. For finite or structured films with standing mode profiles, the situation is more involved. When simulating 1D MCs we shifted the center of the sinc function by  $x_{\text{off}} = 100$  nm with respect to the center of the stripe in the middle of the 1D MC, in order to break the symmetry and allow for more efficient excitation of modes with odd miniband number  $q$ . This approach was sufficient enough to excite all minibands in the studied frequency window and extract relevant mode frequencies, however mode amplitudes were not interpreted.

During the simulation the magnetization  $\mathbf{m}(t, x)$  is recorded in small time steps of 10 ps. Then the FFT of  $\mathbf{m}(t, x)$  is computed in time and space to find excited frequencies  $f$  and wave vectors  $k_x$  and reconstruct the band structure.

## 3 Methods

This chapter starts with two prominent experimental techniques in magnonics: Section 3.1 introduces the excitation and detection of SWs by all-electrical spin wave spectroscopy (AESWS). In Section 3.2 measurement methods based on Brillouin light scattering (BLS) are presented. Both techniques were available on-site in the laboratories of LMGN and essential for most of the studies presented in this thesis. Special attention is given to experimental details, which go beyond existing literature.

Further relevant characterization techniques included magnetic force microscopy (MFM) and scanning transmission X-ray microscope (STXM), where details can be found in Refs. [93, 94] and Refs. [95–97], respectively.

In the last Section, Sec. 3.3, the fabrication process for 1D MCs is described.

### 3.1 All-electrical spin wave spectroscopy

Electromagnetic (EM) waves interact with magnetic moments via the magnetic field component  $\mathbf{h}_{\text{rf}}$  exerting a torque on  $\mathbf{M}$ . Historically ferromagnetic resonance was studied by placing a magnetic sample into a microwave cavity and measuring its microwave absorption as function of an applied external field [80, 98, 99]. When the resonance condition was met and the magnetic susceptibility became large, increased absorption was detected due to energy transfer from the EM field in the cavity to magnetization precession in the sample. Such cavity FMR offers a very high sensitivity, which is due to the resonant enhanced of the EM field in a cavity with a high quality factor. The limitations of such a measurement technique are that the probing frequencies are constrained to the resonance modes of the cavity and that due to the uniform  $\mathbf{h}_{\text{rf}}$  mainly the FMR mode with  $k = 0$  is efficiently excited.

In the course of this thesis, we use a measurement method where  $\mathbf{h}_{\text{rf}}$  is locally applied by coplanar waveguides (CPWs), and absorption is measured by a broadband vector network analyzer (VNA). Such an approach allows to probe SWs with finite wave vector in a broad frequency range. We will refer to this method thus as *all-electrical spin wave spectroscopy* (AESWS) to distinguish this technique from the light and X-ray based spectroscopy techniques. We note that in literature also other terms are found, e.g. *propagating spin wave spectroscopy*

(PSWS) [100, 101], used to describe AESWS experiments in which propagating SWs are probed. This section is structured as follows: In Sec. 3.1.1 we introduce the experimental setup for AESWS. In Sec. 3.1.2 the excitation and detection of SWs with CPWs is discussed. In Sec. 3.1.3 we discuss the line shape analysis of propagating SWs. Sec. 3.1.4 provides an overview of different post-processing techniques relevant for AESWS data.

### 3.1.1 Experimental setup and measurement technique

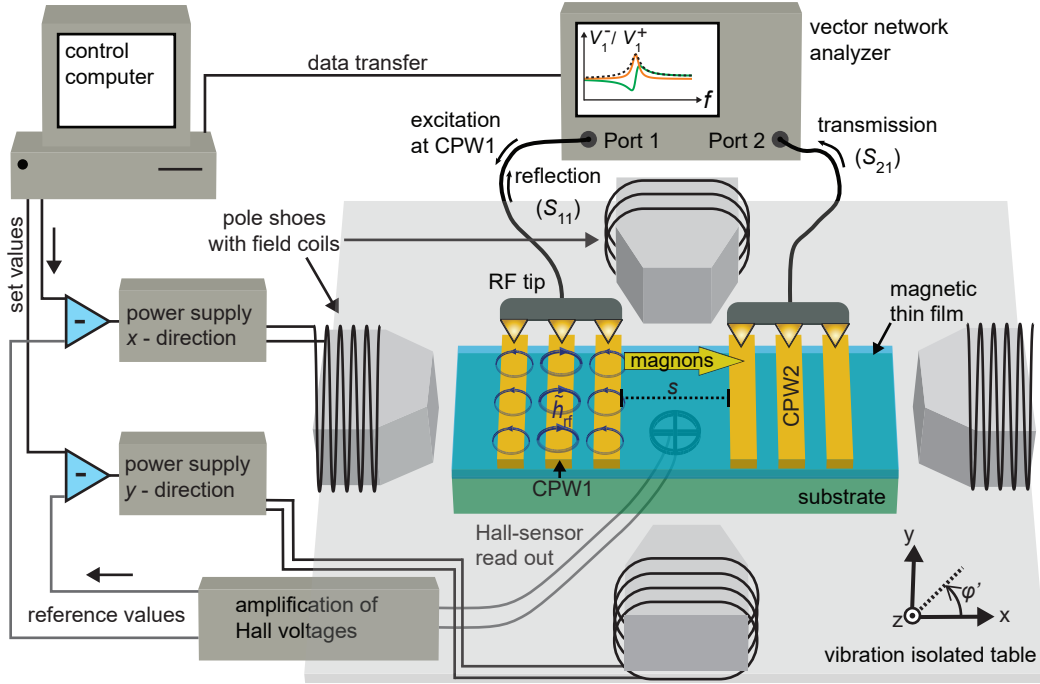


Figure 3.1 – Sketch of the AESWS setup in a typical measurement configuration. Port 1 and 2 of a VNA are connected with RF tips to CPWs integrated on a sample. Microwave absorption at CPW1 and transmission from CPW1 to CPW2 are characterized by measuring scattering parameters  $S_{11}$  and  $S_{21}$ , respectively, with the VNA. A magnetic field  $\mu_0 \mathbf{H}$  can be applied in any in-plane direction by using a two-axis electromagnet system. The field is monitored by a Hall-sensor placed directly below the sample positions. The magnet system regulates its output currents to the field coils until the Hall-voltages match set voltages sent by a control computer. Field sweeps and data acquisition from the VNA is automated by a software on the control computer.

Figure 3.1 depicts a sketch of the AESWS measurement setup present at LMGN. The heart of the setup is a Agilent PNA-X N-5242A vector network analyzer. At its two RF ports, microwaves in the frequency range from 10 MHz up to 26.5 GHz can be applied. At the same time incoming signals are detected with high sensitivity and phase resolution. The system dynamic range of the VNA, which is defined as the difference between maximum source output and detection noise floor, reaches typically values above 120 dB. The VNA measures scattering (S) parameters between port 1 and port 2. The S-parameters are defined by a scattering matrix, which can be

formulated for a two-port network by [102]:

$$\begin{pmatrix} V_1^- \\ V_2^- \end{pmatrix} = \begin{pmatrix} S_{11} & S_{12} \\ S_{21} & S_{22} \end{pmatrix} \begin{pmatrix} V_1^+ \\ V_2^+ \end{pmatrix} \quad (3.1)$$

$V_1^+$  ( $V_2^+$ ) represents voltages applied by the VNA at port 1 (port 2), while  $V_1^-$  ( $V_2^-$ ) represents voltages detected at port 1 (port 2). If the output at port 2 is switched off ( $V_2^+ = 0$ ), Eq. 3.1 leads to  $S_{11} = V_1^- / V_1^+$  and  $S_{21} = V_2^- / V_1^+$ . We note that S-parameters are unitless complex numbers and are either described by magnitude  $\text{Mag}(S_{ij})$  and phase  $\Phi(S_{ij})$ , or by a real part  $\text{Re}(S_{ij})$  and an imaginary part  $\text{Im}(S_{ij})$ .

In a typical measurement configuration, both ports are connected via microwave cables and RF tips to CPWs integrated on the sample surface. When microwaves are applied to CPW1, the microwave current creates a dynamic  $\mathbf{h}_{\text{rf}}$  in its vicinity, which exerts a torque on the sample magnetization. In a resonant condition increased absorption is measured in  $S_{11}$ . SWs which propagate to CPW2 induce a voltage, which is registered in the  $S_{21}$  parameter.

Essential for AESWS measurements is the precise control of an apply external field  $\mu_o \mathbf{H}$ . The magnet system is comprised by two perpendicularly mounted electromagnets, allowing for field application in all in-plane directions  $\varphi'$  (see Figure 3.1). Each of the two field axis is driven by a Kepco bipolar power supply, respectively. The power supplies support a smooth zero crossing of their output currents applied to the field coils, i.e. the magnetic field can be swept from positive to negative values without intermission. The applied magnetic field is monitored by a two-axis Hall-sensor mounted directly below the sample position. The Hall voltages are amplified and fed back to the power supplies as reference values. The power supplies receive a set voltage from the control computer, which encodes the intended  $\mu_o \mathbf{H}$ . The power output is adjusted such that set values and reference values are leveled. The Hall-sensor feedback ensures a precise field control and prevents nonlinearities, e.g. due to hysteretic effects of the pole shoes.

The control computer allows to program automatic field sweeps and reads the measured S-parameters from the VNA. The probe station is mounted on an optical table designed for vibration isolation. The magnet system supports a maximum field of  $|\mu_o \mathbf{H}_{\text{max}}| = 90 \text{ mT}$ .

#### 3.1.2 Spin wave excitation and detection with a coplanar waveguide

CPWs are comprised by a conducting signal line and two shielding ground lines (cf. sketch in Fig. 3.1.1). The geometrical parameters of a CPW are optimized to match the EM wave impedance of the measurement system, which is  $Z_0 = 50 \Omega$  in the case of the VNA. Details on the analytical calculation of  $Z_0$  of a CPW can be found in Refs. [85, 103]. We use CPW designs similar to Refs. [104–107], in which impedance matching was further optimized by 3D-EM simulations.

The length of CPWs used in this is thesis about  $120 \mu\text{m}$ , which is much smaller than the EM wavelengths for the relevant GHz frequencies. Hence,  $\mathbf{i}_{\text{rf}}$ , and consequently  $\mathbf{h}_{\text{rf}}$ , are approximately constant along the CPW lengths ( $y$ -direction). We will thus discuss the spatial

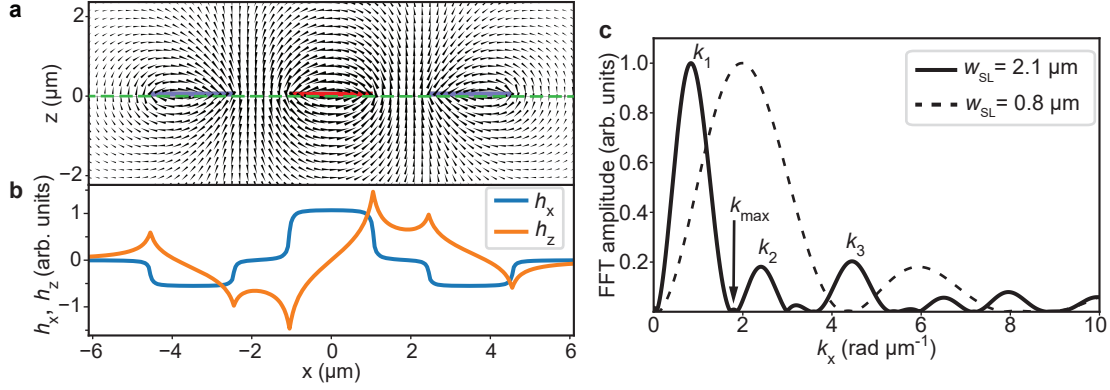


Figure 3.2 – **a** Cross-section of a CPW in the  $x$ - $z$ -plane.  $\mathbf{h}_{\text{rf}}(x, z)$  is represented by black arrows, the size of the arrows is logarithmically scaled with  $|\mathbf{h}_{\text{rf}}|$ . The current in the signal line (red) is flowing out of the sketched plane, in the ground lines the current flow (blue) is in opposite direction. **b** Line-plot of the  $x$  and  $z$  component of  $\mathbf{h}_{\text{rf}}$  at  $z = 0$   $\mu\text{m}$  at the bottom of the CPW (indicated by green dashed line in **a**). **c** FFT amplitude of  $h_x(x)$  at  $z = 0$   $\mu\text{m}$  for a CPW with  $w_{\text{SL}} = 2.1$   $\mu\text{m}$  (solid line) and  $w_{\text{SL}} = 0.8$   $\mu\text{m}$  (dashed line).

distribution of  $\mathbf{h}_{\text{rf}}$  in the  $x - z$ -plane. The VNA injects a microwave current  $\mathbf{i}_{\text{rf}}$  to the signal line and  $-0.5\mathbf{i}_{\text{rf}}$  to each of the ground lines. Due to the counterflowing current in the ground lines, the net current on a CPW is zero. With sufficient distances from the CPW, the field contributions from signal and ground lines cancels each other. This shielding effect ensures that the EM cross-talk between two neighboring CPWs is minimal [107], which is a substantial advantage compared to microstripe transmission lines without such shielding.

Figure 3.2a shows a cross-sectional view of  $\mathbf{h}_{\text{rf}}$  of a CPW simulated with Comsol Multiphysics® for microwave currents at 6 GHz. The signal line width, ground line width and gap width of the CPW amounted to  $w_{\text{SL}} = w_{\text{GL}} = 2.1$   $\mu\text{m}$  and  $w_{\text{G}} = 1.4$   $\mu\text{m}$ , respectively. The simulated CPW was out of gold (Au) and  $t = 0.115$   $\mu\text{m}$  thick. Figure 3.2b shows the in-plane and out-of-plane components  $h_{\text{rf},x}$  and  $h_{\text{rf},z}$  extracted below the CPW, i.e. at the typical sample position (green dashed line in Fig. 3.2a). The in-plane field is large below signal and ground lines, the out-of-plane component takes large values in the gap regions. Outside of the CPW both field components decay rapidly. The spatial distribution of  $\mathbf{h}_{\text{rf}}$  determines the SW wave vectors, which are excited and detected by the CPW. The voltage  $V_{\text{ind}}$  induced by a SW below the CPW calculates following refs. [81, 108] via

$$V_{\text{ind}}(t) = \frac{d\Phi_{\text{CPW}}}{dt} = \frac{\mu_0}{2} \int_{V_s} \mathbf{h}_{\text{rf}} \cdot \frac{d\mathbf{M}}{dt} dV, \quad (3.2)$$

where  $\Phi_{\text{CPW}}$  is the flux in the CPW and  $V_s$  is the sample volume. The temporal change in  $\mathbf{M}$  due to SWs can be expressed by

$$\frac{d\mathbf{M}}{dt} = i\omega \mathbf{m} \exp[i(\omega t - \mathbf{k} \cdot \mathbf{r})]. \quad (3.3)$$

Following Eqs. 3.2 and 3.3, the induced voltage is proportional to the spatial convolution of  $\mathbf{h}_{\text{rf}}$  and the SW wave function. As  $\mathbf{h}_{\text{rf}}$  is constant in  $y$ -direction, only SWs with  $k_y = 0$  result in a non-zero  $V_{\text{ind}}$ . For thin films with a thickness much smaller than the CPW width,  $\mathbf{h}_{\text{rf}}$  is approximately constant along the film thickness, i.e. mainly SWs with  $\kappa = 0$  are excited. Additionally, there is a small contribution for PSSWs with odd quantization numbers  $n$ . For SWs propagating in  $x$ -direction, the induced voltage is proportional to  $\int \mathbf{h}_{\text{rf}}(x) \exp(-ik_x \cdot x) dx$ , i.e. to the Fourier transform of  $\mathbf{h}_{\text{rf}}$  in  $x$ -direction. The solid line in Fig. 3.2c shows the amplitude of the Fast Fourier transform (FFT) computed for the CPW shown in Fig. 3.2a. We note that the FFT amplitudes of  $h_{x,\text{rf}}$  and  $h_{y,\text{rf}}$  (Fig. 3.2b) are identical. In the FFT spectrum we find a prominent peak at  $k_1 = 0.85 \text{ rad } \mu\text{m}^{-1}$  and several small side peaks  $k_i$  with  $i = 2, 3, \dots$  located at larger wave vectors. The  $k_1$  peak covers the region from  $k_x = 0$  to  $k_{\text{max}} = 1.8 \text{ rad } \mu\text{m}^{-1}$ . Following Ref. [52] the value of  $k_{\text{max}}$  can be roughly approximated by  $2\pi/(w_{\text{SL}} + 2w_{\text{G}})$ , which would amount to  $1.3 \text{ rad } \mu\text{m}^{-1}$  for our example. To excite and detect SWs in a larger wave vector range, the width of the CPW has to be shrunk down. The dashed line in Fig. 3.2c represents the FFT amplitude for a CPW with  $w_{\text{SL}} = w_{\text{GL}} = 0.8 \text{ } \mu\text{m}$  and  $w_{\text{G}} = 0.64 \text{ } \mu\text{m}$  and identical thickness  $t = 0.115 \text{ } \mu\text{m}$ . Here we find  $k_1 = 2.0 \text{ rad } \mu\text{m}^{-1}$  and  $k_{\text{max}} = 4.35 \text{ rad } \mu\text{m}^{-1}$ . I.e. both the peak wave vector  $k_1$  as well as the peak width increased for a smaller CPW width. We note that width reduction of the CPW decreases the spatial overlap of  $\mathbf{h}_{\text{rf}}$  with  $\mathbf{M}$  and hence limits  $V_{\text{ind}}(t)$ . Additionally, it is challenging to obtain broadband impedance matching for sub-micrometer CPWs. In Chapter 5 and Chapter 5.2 we will present two approaches, how EM waves can be interfaced with nanoscale SWs without shrinking the CPW size. We further note that strictly speaking  $\mathbf{h}_{\text{rf}}$  depends also on the frequency of the microwave current. Due to the skin effect microwave current densities are largest on the surface of a conductor and decay exponentially characterised by the skin depth  $\delta$ , calculated by:

$$\delta = \sqrt{\frac{2\rho}{\omega\mu_r\mu_0}}. \quad (3.4)$$

Here,  $\rho$  is the resistivity of the conductor. Using parameters for Au ( $\rho = 22.14 \text{ n}\Omega \cdot \text{m}$  and  $\mu_r \approx 1$  [109]), we find  $\delta = 0.46 \text{ } \mu\text{m}$  at  $26.5 \text{ GHz}$ , which is the largest frequency provided by the VNA. The thickness of CPWs used in this thesis is around  $110 \text{ nm}$ , i.e. considerable smaller than the skin depth for all measurement frequencies. The microwave current density inside signal and ground lines can thus be assumed homogeneous and frequency independent. This assumption simplifies the calculation of  $\mathbf{h}_{\text{rf}}$ . In Supplement Sec. C.1 we provide a Python 3 [110] script, by which  $\mathbf{h}_{\text{rf}}$  is numerically calculated by approximating signal and ground lines by a series of infinite current carrying wires and using the superposition principle. The obtained  $\mathbf{h}_{\text{rf}}$  is in excellent agreement with the more involved field simulations by Comsol Multiphysics®, where the Skin effect was considered.

As a concluding remark, we note that wave vectors, extracted from the FFT amplitude of  $\mathbf{h}_{\text{rf}}$ , were also evidenced experimentally. Fallarino *et al.* [111] measured the  $k_1$  and  $k_2$  excitation of a CPW with phase-resolved  $\mu\text{BLS}$  and found a good agreement between theory and experiment. Maendl *et al.* [55] found in AESWS measurements on low-damping YIG multiple side peaks,

which matched well to calculated  $k_i$  with up to  $i = 11$ .

### 3.1.3 Spectrum analysis and group velocity of propagating spin waves

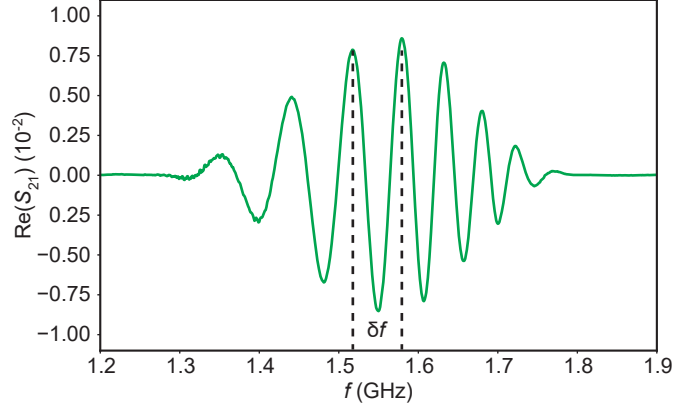


Figure 3.3 – Line plot of  $\text{Re}(S_{21})$  showing the induced signal by SWs in a frequency regime that corresponds to wave vectors around  $k_1$  of the used CPW. The CPW was integrated to a YIG film. SWs were studied in the DE configuration. An oscillatory line is observed due to the phase accumulation of propagating SWs with varying wave vectors. The width  $\delta f$  of a single oscillation period is used to extract the SW group velocity.

As shown in previous section, excited wave vectors possess a certain distribution in  $k$ -space. Considering the dispersion relation (Sec. 2.3.3) this consequently translates to a certain peak width in the frequency domain. Figure 3.3 shows exemplary a line plot of  $\text{Re}(S_{21})$  in the vicinity of the  $k_1$  excitation. The data<sup>1</sup> was taken at 10 mT in DE configuration on a 100 nm thick YIG film with two integrated CPWs with  $w_{\text{SL}} = w_{\text{GL}} = 2.1 \mu\text{m}$  and  $w_g = 1.4 \mu\text{m}$ . The center-to-center distance of the CPWs amounted to  $s_{\text{cc}} = 35 \mu\text{m}$ . We find that the signal spans from about 1.3 to 1.8 GHz.  $\text{Re}(S_{21})$  shows about 8 full oscillation periods. These oscillations are attribute to a frequency dependent phase accumulation  $\Phi$  of propagating SWs, following [101, 113]

$$\Phi = k \cdot s_{\text{eff}}, \quad (3.5)$$

where  $s_{\text{eff}}$  is the effective phase accumulation distance. For CPWs,  $s_{\text{eff}}$  is approximately equivalent to  $s_{\text{cc}}$  [113]. The  $k_1$  peak covers a region from  $k = 0$  to  $k_{\text{max}}$ , which by Eq. 3.5 leads to a phase accumulation from  $\Phi_{\text{min}} = 0$  to  $\Phi_{\text{max}} = k_{\text{max}} s_{\text{eff}} = 63 \text{ rad}$  (for  $k_{\text{max}} = 1.8 \text{ rad}$  and  $s_{\text{eff}} \approx s_{\text{cc}}$ ). I.e. the calculated  $\Phi$  varies by  $63 \text{ rad}/2\pi = 10.0$  periods, which is in good agreement with the experimental observation. For a single oscillation period the change in wave vector  $\delta k$  calculates to  $\delta k = 2\pi/s_{\text{eff}}$  (Eq. 3.5). The corresponding change in frequency  $\Delta f$  can be extracted from the  $S_{21}$  data. This allows to approximate the group velocity of SWs following [114]

$$v_g = \frac{\partial \omega}{\partial k} \approx \frac{2\pi \delta f}{\delta k} = \delta f \cdot s_{\text{eff}}. \quad (3.6)$$

<sup>1</sup>Data taken by Andrea Mucchietto during his Master thesis project at LMGN [112].



We note that the oscillating period in Fig. 3.3 decreases with increasing  $f$ , indicating a gradual decrease in the group velocity. This is the expected behavior for DE SWs in the dipolar regime (cf. Fig. 2.2).

#### 3.1.4 Data processing

This section provides an overview of different data processing methods used for isolating the magnetic signal in AESWS measurements. Ideally, the measured VNA signal would contain  $V_{\text{ind}}$  only originating from SW precession. However microwave cables, tips and CPWs are not ideal wave guides and cause a frequency dependent microwave absorption and reflection. We use a calibration routine with known on-wafer calibration standards to correct for the microwave properties of cables and microwaves probes [115]. Still, the microwave response of CPWs integrated on the sample surface is not corrected for by such a calibration. Further, temporal drifts of the non-magnetic background signal are often observed during long measurements. Such drifts might be caused by temperature changes, translating in thermal expansion and possible mechanical forces. Especially the connection of microwave tips to integrated CPWs are expected to be very sensitive to mechanical stress.

To reduce the non-magnetic background, different post-processing routines are applied in the course of this thesis, which are demonstrated in Fig. 3.4 on an exemplary data set. We display  $\text{Mag}(S_{21}) = \sqrt{\text{Re}(S_{21})^2 + \text{Im}(S_{21})^2}$  taken between two CPWs with grating couplers (GCs) on a YIG film. The field was applied parallel to the CPW. Details on the involved SW modes are discussed in Chapter 5.1.

In Fig. 3.4a the raw data without additional processing is plotted. At frequencies above  $\sim 5$  GHz non-magnetic background is dominant and obscures the observation of additional SW modes. In Fig. 3.4b a reference dataset (RM) was subtracted from the real and imaginary part of  $S_{21}$ , before the magnitude was calculated [106]. The RM was taken at  $\mu_0 H = 90$  mT applied perpendicular to the CPW. The reference subtraction removes field-independent background. However, unwanted traces appear (marked by orange arrows in Fig. 3.4b). They originate from SW resonances contained in RM. Ideally, these resonances occur outside of the interesting frequency window of the measurement data. We use reference subtraction in Chapter 4, when we focus at the  $k_1$  mode of MCs at low fields. At 90 mT, the lowest resonance in the RM is well above the interesting frequency window and does not interfere with the interpretation of the data. In contrast, for measurements with GCs on YIG, we want to utilize the whole frequency range offered by the VNA (i.e. from 0 to 26.5 GHz). To push the FMR frequency of YIG above 26.5 GHz, a field of about 1 T is required (Eq. 2.19), which is not reachable in the used probe station. Consequently other post-processing methods are preferable.

In Fig. 3.4c we calculated the median values of  $\text{Re}(S_{21})(H)$  and  $\text{Im}(S_{21})(H)$  for all measured field values. The median values were then used for reference subtraction. This method removes the field-independent background similarly to the subtraction of a RM taken at a single field value, however the unwanted traces are circumvented. Median values are generally insensitive to extrema in the data set. This method works particularly well, if for each frequency, the majority of data points are taken at field values for which the resonance condition

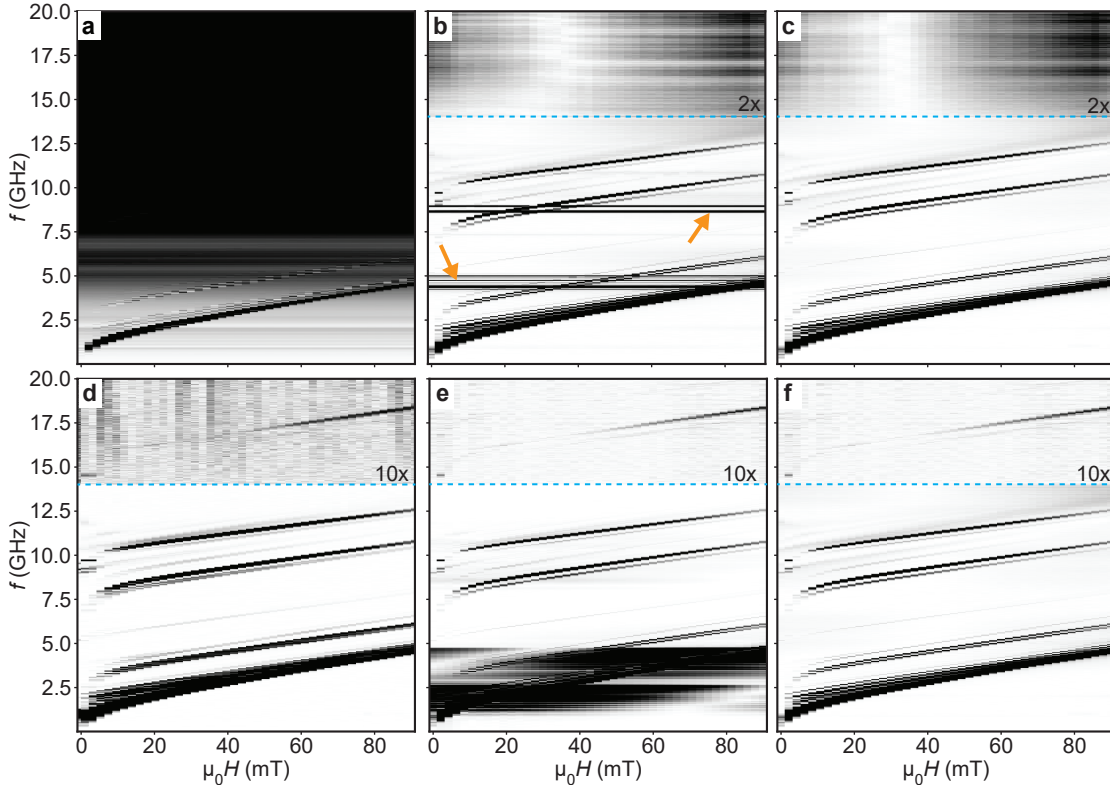


Figure 3.4 – Example of different post-processing methods for Mag(S<sub>21</sub>) measurement on a YIG film with GCs in DE configuration. **a** Raw data of a calibrated VNA. **b** Reference measurement taken at 90 mT in BV configuration subtracted. Traces due to resonances in the RM are marked with orange arrows. **c** Median of measurements for all field values is subtracted as reference. **d** Next-neighbor subtraction of spectra at sequential field values. **e** FFT filter based on predicted line shapes. **f** Combined image using median subtraction up to 14 GHz and FFT filtering from 14 to 20 GHz.

is not met. Instead, for data sets with a small number of field values, or SWs modes which are not sufficiently shifted in frequency with the applied  $H$ , the method is not suitable.

An limitation of both methods discussed so far is that only the constant background is removed. Temporal changes of the background during a measurement are not corrected for.

An useful approach to suppress temporal drifts is next-neighbor subtraction of spectra taken at sequential field values, as demonstrated in Fig. 3.4d. An additional mode is observed above 15 GHz, which was not apparent in Fig. 3.4b, c. Due to the small temporal difference of successive field measurements, temporal drifts are effectively suppressed. We use next-neighbor subtraction in some AESWS spectra in Sec. 5.2. A downside of the method is that mode amplitudes are difficult to interpret. As discussed in the previous section, peaks in  $\text{Re}(S_{21})$  and  $\text{Im}(S_{21})$  have oscillating line shapes with periods  $\delta f(k)$  (cf. Fig. 3.3). For a discrete field step  $\Delta H$ , SW modes shift by a certain  $\Delta_H f$ . If  $\Delta_H f$  matches  $\frac{1}{2}\delta f$ , next-neighbor subtraction provides large amplitudes. However, for  $\Delta_H f = \delta f$  two successive peaks are subtracted and amplitudes are small. As  $\delta f$  depends on the wave vector, the relative peak amplitudes of

modes with different  $k$  can be misleading in next-neighbor subtracted data. The spectra further depend on the used field step  $\Delta H$ .

The phase oscillations in  $S_{21}$  can be purposely utilized in post-processing by applying Fourier filtering. When the dispersion relation of a material is well known,  $v_g(k)$  (Eq. 2.25) and hence expected  $\delta f(k)$  (Eq. 3.4) can be calculated. In Fig. 3.4e we applied a FFT filtering on  $\text{Re}(S_{21})(f)$  and  $\text{Im}(S_{21})(f)$ , which removed frequency components below  $\Delta f = 0.0125$  GHz and above  $\Delta f = 0.2$  GHz (selecting for SWs with  $0.44 \text{ km s}^{-1} < v_g < 7 \text{ km s}^{-1}$ ). Additionally a high-pass FFT filter was applied along the field-direction of the data, to remove temporal drifts of the background. In the filtered data (Fig.3.4e) the mode above 15 GHz is clearly observable and the noise is reduced. Around the  $k_1$  mode (frequency window up to about 5 GHz) artefacts are observed, which we attribute to a ringing effect of the FFT [116]. We note that the ringing is relatively small and only apparent due to a severe clipping of the maximum intensity (black) in Fig. 3.4, chosen to improve visibility of weaker modes.

For optimized mode visibility, it is sometimes useful to use different post-processing methods depending on the frequency regime. In Fig. 3.4f, median subtraction was applied in the frequency range up to 14 GHz. Above 14 GHz FFT filtering was used and the data was multiplied by a factor of 10 to improve visibility.

## 3.2 Brillouin light spectroscopy

Brillouin light spectroscopy (BLS), sometimes also called Brillouin-Mandelstam scattering, is an optical spectroscopy technique. It is named after Brillouin [117] and Mandelstam [118], who in the 1920s independently predicted light scattering from acoustic phonons. Commonly BLS is differentiated from Raman scattering by the addressed frequency range [119]. While Raman grating spectrometers measure shifts of the photon energy in the THz regime, BLS refers to the detection of inelastically scattered light with energy shifts in the GHz regime [119]. Due to the small spectral separation of GHz-shifted light from elastically scattered Rayleigh light, spectrometers with high frequency resolution and high contrast are required for BLS. J. Sandercock [120] developed an optimized multipass Fabry-Pérot interferometer which made BLS on magnons feasible. Details on the interferometer can be found in Refs [121, 122]. In 1973, Sandercock and Wettling [123] reported for the first time Brillouin scattering on thermal magnons in YIG. Since then BLS based techniques have been widely used for research in magnonics. In Sec. 3.2.1 we introduce the basic working principle of inelastic magnon-photon scattering and discuss the wave vector transfer for plane film measurements. In Sec. 3.2.2 we introduce the BLS microscopy setup used in LMGN.

### 3.2.1 Magnon-photon scattering

In a semiclassical picture, scattering of photons with magnons can be understood as follows: Due to spin-orbit-coupling, magnetic oscillations cause a variation of the dielectric permittivity  $\epsilon$ . Propagating SWs give rise to a periodic, traveling perturbation of  $\epsilon$ , which

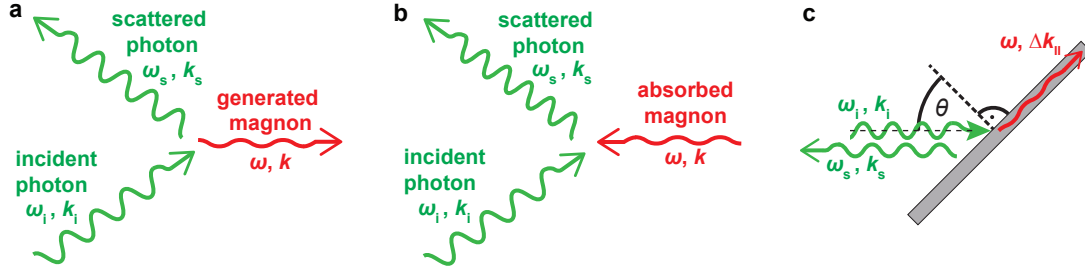


Figure 3.5 – Illustration of **a** the Stokes scattering process, in which a magnon is generated **b** and the anti-Stokes scattering process, in which a magnon is absorbed. **c** Sketch of the employed measurement configuration for wave vector resolved BLS on reflective magnetic plane films. Laser light impinges on the sample surface with an incident angle  $\theta$ . Back-reflected light with  $\mathbf{k}_s \parallel \mathbf{k}_i$  is guided to the interferometer and analyzed. In the scattering process, the photon wave vector parallel to the sample surface was changed by  $\Delta k_{\parallel}$ , which is transferred to the generated magnon.  $\Delta k_{\parallel}$  can be adjusted by changing  $\theta$  and reaches maximally two times the photon momentum for  $\theta = 90^\circ$ .

acts as a moving Bragg grating for incoming photons. The frequency of reflected photons is consequently Doppler-shifted by the SW frequency. In a quantum mechanical framework, the scattering process is described as the interaction of quasi-particles as sketched in Fig. 3.5. An incident photon with energy  $\hbar\omega_i$  and wave vector  $\mathbf{k}_i$  either generates (Fig. 3.5a) or absorbs (Fig. 3.5b) a magnon with energy  $\hbar\omega$  and wave vector  $\mathbf{k}$ . The generation process, in which the energy of the scattered photon is decreased, is denoted Stokes scattering; the absorption process, in which the scattered photon gains energy, is denoted anti-Stokes scattering. The energy  $\hbar\omega_s$  and wave vector  $\mathbf{k}_s$  of the scattered photon is given by

$$\hbar\omega_s = \hbar\omega_i \pm \hbar\omega \quad (3.7)$$

$$\mathbf{k}_s = \mathbf{k}_i \pm \mathbf{k}. \quad (3.8)$$

The wave vector conservation stated in Eq. 3.8 applies in the presence of translational invariance. In the course of the thesis we study magnetic thin films. Here only the wave vector component parallel to the film surface is conserved. Figure 3.5c shows a typical measurement configuration for wave-vector resolved BLS on a reflective thin film sample. Monochromatic laser light is focused on the sample with an incident angle  $\theta$  defined in respect to the surface normal of the film. According to the law of reflections, elastically scattered light is reflected on the opposing side of the surface normal. The angle between incident and elastically reflected beam amounts to  $2\theta$ . Instead, in the used measurement configuration, light reflected with  $\mathbf{k}_s \parallel \mathbf{k}_i$  is collected and analyzed. Here the photon wave vector parallel to the sample surface  $k_{\parallel}$  was changed during the scattering process. The change  $\Delta k_{\parallel}$  is given by [124]

$$\Delta k_{\parallel} = 2k_i \cdot \sin\theta. \quad (3.9)$$

$\Delta k_{\parallel}$  is either absorbed or transferred by a magnon depending on whether Stokes or anti-Stokes process is considered. The magnitude of the wave vector of the incident light is given

by  $k_i = 2\pi/\lambda_L$ , where  $\lambda_L$  is the laser wave length. Measurements in this thesis were conducted with solid-state lasers with  $\lambda_L = 473$  nm. Photons can maximally transfer two times their wave vector which amounts to  $k_{\max} = 26.6 \text{ rad } \mu\text{m}^{-1}$  for the used laser wave length. For the artificial band structures of MCs with lattice constants on the order of some hundred nanometers instead,  $k_{\max}$  covers several times the Brillouin zone boundary. This makes BLS an ideal tool for mapping out the tailored band structures of MCs.

#### 3.2.2 Brillouin light scattering microscopy

With the growing focus on magnetic micro- and nanostructures in magnonic research, Brillouin microscopy ( $\mu\text{BLS}$ ) techniques have been developed. A comprehensive overview of  $\mu\text{BLS}$  implementations and their applications is provided in Refs. [124–126]. Here we introduce the  $\mu\text{BLS}$  setup operated at LMGN. Special attention is given to a modified phase-resolved  $\mu\text{BLS}$  technique, which I implemented while working at LMGN.

Figure 3.6 shows a sketch of the  $\mu\text{BLS}$  setup. We first go through the basic components for spatially-resolved  $\mu\text{BLS}$  measurements. Additional components for time- and phase- resolution are introduced later.

A monochromatic solid-state laser with  $\lambda_L = 473$  nm generates a linearly polarized laser beam. The laser polarization is horizontal in the beginning. The laser beam is focused to a spot size of around 300 nm diameter on the surface of a sample. We note that for measurements shown in the course of this thesis a laser power of 1 mW or below was used to avoid heating effects such as the reduction of  $M_s$  (c.f. Eq. 2.3).

The sample is mounted on a  $x, y, z$  nanopositioning stage, i.e. it can be moved with respect to the laser spot position. An external magnetic field is applied in  $y$ -direction by means of a pair of permanent magnets mounted on a translation stage. The magnitude of the magnetic field is adjusted by changing the distance between magnets and sample.

The used objective lens (Olympus LCPLFLN100xLCD) features a large numerical aperture of  $\text{NA} = 0.85$ , which allows to collect photons scattered in a broad range of angles from the sample surface. The light which is back-reflected is composed of elastically scattered photons and a small fraction of inelastically scattered photons, which generated or absorbed magnons. In the magnon-photon scattering process, the light polarization is rotated by  $90^\circ$ . The back-reflected light is passed through a Glan-Taylor prism. Horizontally polarized photons pass the prism in a straight trajectory. They are guided via beam splitters partially to a CCD camera, which monitors the laser spot on the sample. A diffuse white light source is used to illuminate the sample, such that structures on the sample surface are observable by the camera. The optical feedback is used to focus and stabilize the laser spot on the sample surface.

The inelastically scattered photons which possess a vertical polarization are reflected in the Glan-Taylor prism and leave it at a side window. This signal carrying light is then guided into a six-pass tandem Fabry-Pérot interferometer (Table Stable TFP-2). Photons with the matching frequency are transmitted by the interferometer and registered by a silicon avalanche photodiode detector. Each detected photon generates an electrical pulse, which is read out

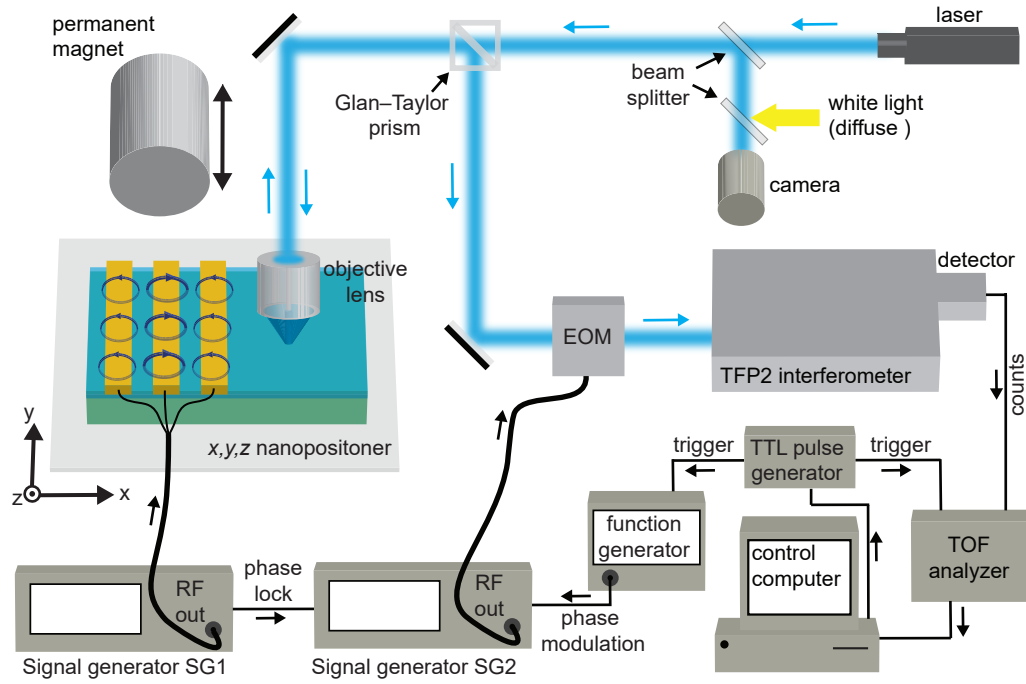


Figure 3.6 – Sketch of a  $\mu$ BLS setup with phase-resolved measurement capability. The optical beam (blue) is focuses on the sample surface with an objective lens. The sample is mounted on a nanopositioner and a magnetic field can be applied with a moveable permanent magnet. The position of the laser spot on the sample is monitored with a camera. The light scattered from the sample is guided to the interferometer, where its energy shift is analyzed. Coherent SWs are excited by applying a microwave current with signal generator SG1 to a CPW integrated on the sample surface. Signal generator SG2 is used to apply microwave power to an electro-optical modulator (EOM), which generates a reference signal relevant for phase-resolved measurements. A time-of-flight (TOF) analyzer allows for registering the time of incoming photon counts. The setup is controlled with a software package running on the control computer.

by a time-of-flight (TOF) analyzer (Fast ComTec MCS6A), described later. The TOF analyzer passes the information of an incoming photon count to the control computer. A software package [126] on the computer controls the interferometer. It matches the received counts to the frequency measured by the interferometer at the time of detection.

In  $\mu$ BLS typically SWs are excited by an microwave antenna, in order to increase the signal strength and investigate propagating wave fronts. A CPW integrated on the sample is wire-bonded to a macroscopic CPW (not shown in Fig. 3.6), which is connected via an end launch connector and microwave cable to the signal generator SG1. For coherent SWs the measured BLS counts are proportional to the square of the spin wave amplitude [127]. SWs propagating away from the CPW decay exponentially and the measured BLS intensity  $I(x)$  as function to

the distance  $x$  from the CPW can be described by [128]

$$I(x) = I_0 \exp\left(-\frac{2x}{\delta}\right) + b. \quad (3.10)$$

Here  $\delta$  is the amplitude decay length,  $I_0$  is the intensity at  $x = 0$  and  $b$  is a offset due to the noise floor of the setup.

While BLS analyzes magnetic oscillations in frequency domain, sometimes it is of interest to measure the evolution of wave packets in time and space. We generate SW wave packets by pulsing the microwave excitation provided by the CPW. This is done by opening and closing of microwave switches (not shown). The TOF analyzer allows to register incoming photon counts with a time resolution of 0.8 ns. By measuring the time delay  $\Delta t$  between microwave excitation and signal detection at laser spot position  $x$ , the group velocity of the wave front can be calculated as  $v_g = x/\Delta t$ . To measure  $\Delta t$  correctly, the switch opening and the starting time for the TOF analyzer need to be synchronized. We use a pulse generator (DG645) to trigger microwave switch and TOF analyzer simultaneously. Typically the measurements are repeated with a cycle of about 1  $\mu$ s to allow for integration of the measurement signal over a longer time period.

In the following we introduce phase-resolved  $\mu$ BLS, which was first demonstrated by Serga *et al.* [129] in 2006. While the phase is conserved during the inelastic scattering process, the photon detector is only sensitive to the energy quanta provided by the photon and phase information is lost in a standard  $\mu$ BLS measurement. To access the phase information, interference with a reference beam is utilized. A broadband electro-optical modulator (EOM) is used to modulate part of the laser light at the frequency of SW excitation. The inelastically scattered light with intensity  $I_{SW}$  interferes with the modulated light with intensity  $I_{EOM}$  and the combined intensity  $I_{tot}$  is given by [130]

$$I_{tot} = I_{SW} + I_{EOM} + 2 \cos(\Theta(x) - \Theta') \sqrt{I_{SW} I_{EOM}}. \quad (3.11)$$

Here  $\Theta(x)$  is the SW phase at the position of the measurement spot.  $\Theta'$  is the phase of the modulated reference beam. Typically CPW and EOM are driven by the same signal generator in parallel and  $\Delta\Theta = \Theta - \Theta'$  is constant in time. By using microwave switches one can measure  $I_{SW}$ ,  $I_{EOM}$  and  $I_{tot}$  separately by applying microwave power only to the CPW, only to the EOM, and then to CPW and EOM together, respectively [130]. With this information  $\cos(\Theta - \Theta')$  can be calculated by rearranging Eq. 3.11 as follows

$$\cos(\Theta - \Theta') = \frac{I_{tot} - I_{SW} - I_{EOM}}{2\sqrt{I_{SW} I_{EOM}}}. \quad (3.12)$$

This method was used e.g. for BLS measurements presented in Sec. 4.2. If a propagating plane wave is sampled at enough spatial positions,  $\cos(\Delta\Theta(x))$  is sufficient to extract the SW wave length by sinusoidal fitting. However, we note that for a single measurement point, it is not possible to retrieve  $\Delta\Theta$  in the full angle interval from 0 to  $2\pi$ . Due to the symmetry of the cosine function, its inverse function provides values only from 0 to  $\pi$ . In the worst case,

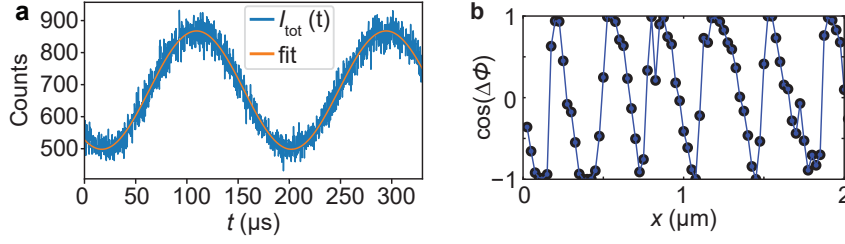


Figure 3.7 – **a**  $I_{\text{tot}}(t)$  measured for a fixed position as a function of time  $t$ , when the reference phase  $\Delta\Theta'$  of light modulated with an EOM was swept linearly by about  $3\pi$ . **b** Measured phase signal for SWs with a wave length of 340 nm propagating in a thin YIG film. The measured wave length was close to the optical detection limit of the setup. Figure **b** is adapted from Ref. [59] published under Creative Commons licensing.

one might imagine a scenario in which the SW phase at measurement position  $x'$  is such that  $\cos(\Delta\Theta(x')) = 0$ . When the SW phase is now phase shifted by  $\pm\pi$  the measured  $\cos(\Delta\Theta(x') \pm \pi)$  is still zero, and thus the phase shift would go unnoticed.

To solve this issue, in literature  $\cos(\Delta\Theta(x))$  was sometimes measured a second time, with a phase shift applied to  $\Theta'$  [111, 129, 131]. When  $\Theta'$  is shifted by  $\pi/2$  in a second measurement,  $\Delta\Theta$  can be reconstructed in the full angle interval (0 to  $2\pi$ ) [129]. Still, for the calculation of  $\Delta\Theta$  [129], it is necessary to measure  $I_{\text{SW}}$  and  $I_{\text{EOM}}$  individually.

I implemented a measurement routine, in which the  $\Delta\Theta$  was extracted without requiring the measurement of  $I_{\text{SW}}$  and  $I_{\text{EOM}}$ . For every spot position, the phase of the reference beam  $\Theta'(t)$  was changed linearly as a function of time. While the reference phase was swept,  $I_{\text{tot}}(t)$  was recorded in a time-resolved manner by the TOF analyzer. Figure 3.7a shows exemplarily a measured time trace. During the measured time window of 330  $\mu\text{s}$ , the reference phase was swept by about  $3\pi$ . As expected following Eq. 3.11, the recorded  $I_{\text{tot}}(t)$  showed a sinusoidal oscillation and a constant offset. The oscillation is given by  $2 \cos(\Delta\Theta(t)) \sqrt{I_{\text{SW}} I_{\text{EOM}}}$ . By sinusoidal fitting (orange line in Fig. 3.7) the phase offset  $\Delta(\Theta)(t=0)$  can be evaluate in the range from 0 to  $2\pi$ . The amplitude of the oscillation is given by  $2\sqrt{I_{\text{SW}} I_{\text{EOM}}}$ . We note that even for weak SW signals,  $I_{\text{EOM}}$  can be chosen sufficiently large such that  $2\sqrt{I_{\text{SW}} I_{\text{EOM}}}$  is above the noise floor of the instrument. With this method we measured the phase of SWs with small  $I_{\text{SW}}$  at wave lengths close to the optical detection limit of the instrument. Figure 3.7 shows  $\cos(\Delta\Theta)$  measured for SWs with a wave length of  $\sim 340$  nm. The figure is adapted from the supplementary information of our publication Ref. [59].

Technically the method was implemented by using two Anritsu MG 3692C signal generators which were phase-locked together by connecting the 10 MHz reference output of generator SG1 to the reference input of signal generator SG2. SG1 applies microwave current to the CPW, while SG2 applies microwaves to the EOM as sketched in Fig. 3.6. Both signal generators operate at the same frequency. The output phase of SG2 can be shifted with respect to SG1. The phase shift is externally controlled and is proportional to a input voltage applied at the rear panel of SG2. We use a function generator (Tektronix AFG3152C) to apply a linearly increasing voltage ramp, which translates to a linear phase sweep. The start of the voltage ramp and of the time acquisition by the TOF analyzer was simultaneously triggered by the pulse generator.



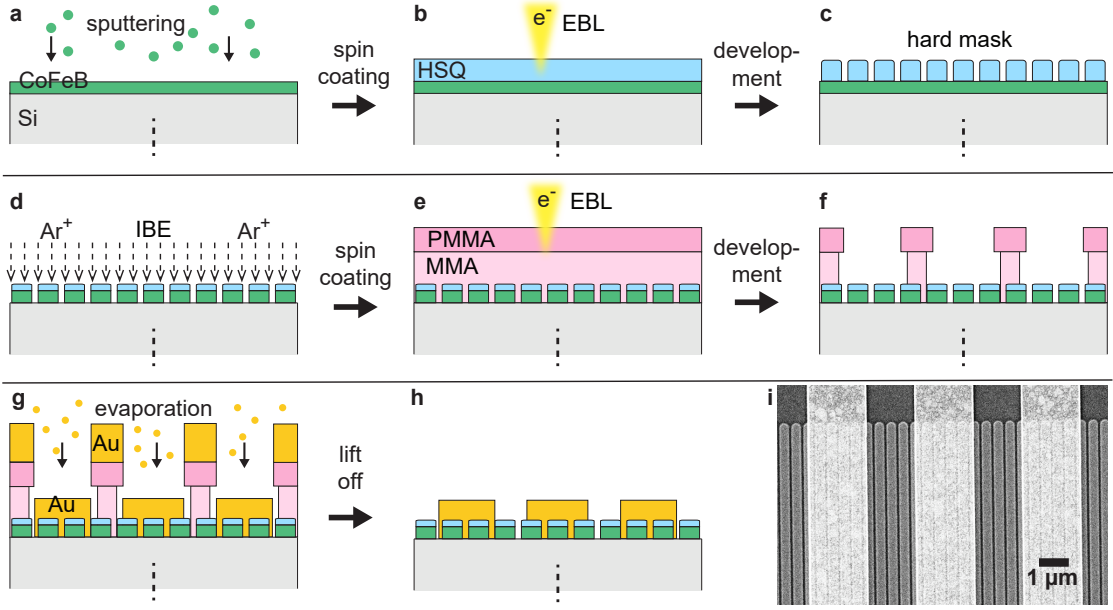


Figure 3.8 – Schematic (cross-sectional view) of the fabrication process for 1D MCs. **a** RF-magnetron sputtering of CoFeB thin film (green) on Si substrate (gray). **b** EBL exposure of a spin-coated HSQ resist (blue). **c** After development the exposed HSQ remains and forms an etching mask. **d** Transfer of the mask into the CoFeB film by IBE with  $\text{Ar}^+$  ions. **e** Definition of CPW structures by EBL exposure of a spin-coated MMA/PMMA double layer resist. **f** Resist profile after development. **g** Deposition of 4 nm Cr and 120 nm Au by electron beam evaporation. **h** Lift-off processing of the CPW. **i** SEM image (top view) of a fully prepared sample after lift-off processing. Signal and ground lines of a CPW are visible in light gray in the SEM image.

### 3.3 Sample fabrication

In this thesis 1D MCs consisting out of closely spaced ferromagnetic nanostripes arranged with submicrometer periodicity are addressed. The sample preparation relied on nanofabrication techniques [132] which were optimized thoroughly in the course of this thesis and was conducted in the cleanroom of the EPFL *Center of MicroNanotechnology* (CMi). In the following the relevant steps for preparing 1D MCs out of CoFeB is outlined.

Samples were fabricated on a 4 inch boron-doped Si wafer in [100] orientation and with a resistivity in the range of  $(0.1 - 100) \Omega\text{cm}$ . The wafer was cleaned by acetone and isopropyl alcohol (IPA) rinsing, blown dry with nitrogen and baked for 10 min on a hotplate at  $180^\circ\text{C}$ . A CoFeB thin film with a thickness of  $(19 \pm 2) \text{ nm}$  was RF-magnetron sputtered (Alliance-Concept DP 650) from a  $\text{Co}_{20}\text{Fe}_{60}\text{B}_{20}$  target in argon (Ar) atmosphere at a pressure of  $5 \cdot 10^{-5} \text{ mbar}$  (Fig. 3.8a). The deposition rate amounted to  $0.3 \text{ Å s}^{-1}$ .

To define the 1D MC stripe patterns electron-beam lithography (EBL) was employed (Fig. 3.8b). First a hydrogen silsesquioxane (HSQ) EBL resist (Dow Corning® XR-1541-002) was spun for 1 min at 4500 rpm to form a thin film with a thickness of  $\sim 40 \text{ nm}$ . Then the resist was exposed with a Raith EBPG5000ES EBL system operated at 100 keV acceleration voltage. A

beam current of 5 nA and a base dose of  $6200 \mu\text{C cm}^{-2}$  were used.

After development exposed areas of the negative HSQ resist cross-linked [133] and remained on top of the CoFeB film as an etching mask (Fig. 3.8c). For the development we immersed the wafer for 2 min in a salty TMAH/NaCl (0.25/ 0.7N) solution. The preparation of the solution is described in Ref. [134]. We found that the prepared solution offered a better contrast compared to standard developers.

The HSQ hard mask was transferred into the CoFeB thin film via ion beam etching (IBE) (Fig. 3.8d). A Veeco Nexus IBE350 system with argon ion source was employed. The wafer was mounted with a slight -3 deg tilt angle between the surface normal and the trajectory of the  $\text{Ar}^+$  ions and was rotated during the IBE process. The etch time amounted to 85 s using the 'Low\_IBE' program (500 mA beam current, 300 V beam voltage). After the IBE step, the CoFeB film was fully removed in regions which were not protected by the HSQ hard mask. On the protected CoFeB structures still a thin HSQ layer ( $\sim 20$  nm thickness) remained.

For the fabrication of CPWs a standard lift-off process with a MMA/PMMA double layer resist was used [82]. MMA EL9 resist was spun for 1 min at 4000 rpm ( $\sim 320$  nm film thickness) and baked for 5 min on a hotplate at  $180^\circ\text{C}$ . After 1 min cool down time, PMMA 495K A4 resist was spun for 1 min at 4000 rpm ( $\sim 150$  nm film thickness) and baked for 5 min at  $180^\circ\text{C}$  as well. CPW structures were defined by EBL with a beam current of 150 nA and a base dose of  $6200 \mu\text{C cm}^{-2}$  (Fig. 3.8e).

The exposed sample was developed for 1 min in 1:3 MIBK/IPA developer [135], followed by immediate transfer into an IPA bath, where it was kept for 1 min and then dry blown with nitrogen. Due to a lower critical dose the MMA resist layer dissolved more widely than the PMMA layer, resulting in an undercut profile as sketched in Fig. 3.8f.

For the CPW structures 4 nm Cr and 120 nm Au were deposited in a electron beam evaporator (Leybold Optics LAB 600H) with a 1 m working distance between source and substrate (Fig. 3.8g). Lift-off was conducted by soaking the wafer in an acetone bath for 48 h and subsequent ultrasonic cleaning (Fig. 3.8h). Figure 3.8i depicts an exemplary scanning electron beam (SEM) image of a fully prepared 1D MC with CPW.

We note that in order to ensure a correct alignment between the 1D MC pattern and the CPWs during the EBL writing process, Au alignment markers were used. The alignment markers were fabricated on the Si wafer already before CoFeB deposition. Therefore the same lift-off process as outlined for the CPW structures was employed.

A key challenge for the EBL fabrication of 1D MCs was to obtain a uniform resist exposure of center and edge regions. Due to the high filling factor of 1D MCs, backscattered electrons increased significantly the effective dose in the center region of the pattern and led locally to an overexposure, when a uniform exposure dose was used (Fig. 3.9a). To counteract this effect, we used the proximity effect correction software Layout Beamer [136]. The software required two electron scattering coefficients ( $\beta$  and  $\eta$ ), which are substrate and resist specific. We used visual inspection of fabricated reference patterns [137] to find optimized parameters. A uniform exposure was achieved for  $\beta = 33 \mu\text{m}$  and  $\eta = 1.7$  as exemplarily shown in Fig. 3.9b. For the fabrication of  $\text{Ni}_{81}\text{Fe}_{19}$  grating couplers on YIG a similar process flow was used. Details on the fabrication parameters are provided in the Supplement Sec. B.1.

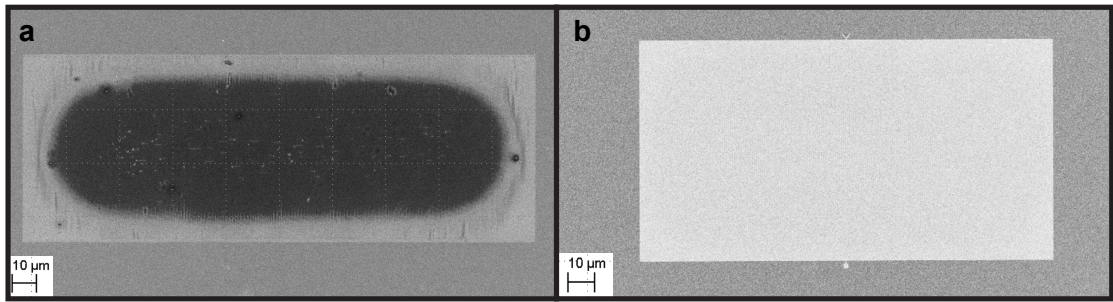


Figure 3.9 – **a** SEM image of a 1D MC exposed with a uniform beam dose during the EBL writing. Strong overexposure is observed in the central region due to electrons which were backreflected due to scattering in the substrate and exposed the resist twice. **b** Non-uniform electron beam dose based on proximity effect calculations led to a uniform exposure of the HSQ resist. The magnification does not allow one to identify the individual 325 nm wide nanowires.



## **Results and Discussion Part II**



## 4 Magnetic defects in 1D magnonic crystals

This chapter constitutes a substantial part of my thesis, namely the investigation of magnetic defects in one-dimensional magnonic crystals. In Sec. 4.1 we report on AESWS measurements of SWs trespassing an individual magnetic defect. Phase shifts and amplitude variations were evidenced as a function of an applied bias field. The results have been published in Applied Physics Letters [50] and are reproduced with permission of the journal. Section 4.2 goes beyond the published work in that we present spatially resolved measurements of SW amplitudes and phases in the vicinity of a magnetic defect. These  $\mu$ BLS data suggests that measured phase shifts originated from the tailored magnetic defect. Section 4.3 provides micromagnetic simulations in a wider parameter space, not accessible in the experiments. The results are very promising in that  $\pi$  phase shifts and low amplitude attenuation were found, once the SW modes in the defect were shifted to the second miniband. Section 4.4 demonstrates that the band structure of a 1D MC is reprogrammable. By magnetizing neighboring stripes antiparallelly (AP), acoustic and optical modes were created. We report on propagating SWs in the AP state and report the disappearance of a band gap between acoustic and optical modes at zero field, when wave vectors are excited at the Brillouin zone boundary.

### 4.1 Phase control of spin waves based on a magnetic defect in a one-dimensional magnonic crystal

K. Baumgaertl, S. Watanabe and D. Grundler  
Appl. Phys. Lett. **112**, 142405 (2018)  
doi: 10.1063/1.5024541

*Reproduced from Appl. Phys. Lett. **112**, 142405 (2018) with permission of AIP Publishing. For uniformity the layout was reformatted and the references were integrated into the thesis' bibliography.*

My contribution to this paper included the fabrication of samples, the AESWS and Macro-BLS

measurements and data analysis. MFM measurements were conducted with the help of S. Watanabe. I wrote the draft of the manuscript.

### Abstract

Magnonic crystals are interesting for spin-wave based data processing. We investigate one-dimensional magnonic crystals (1D MCs) consisting of bistable CoFeB nanostripes separated by 75 nm wide air gaps. By adjusting the magnetic history, we program a single stripe of opposed magnetization in an otherwise saturated 1D MC. Its influence on propagating spin waves is studied via broadband microwave spectroscopy. Depending on an in-plane bias magnetic field, we observe spin wave phase shifts of up to almost  $\pi$  and field-controlled attenuation attributed to the reversed nanostripe. Our findings are of importance for magnetologics, where the control of spin wave phases is essential.

### Main part

Information encoded in spin waves (SWs) can be transmitted and processed without moving electrical charge. This feature makes SWs promising for low power consumption in future logic devices [18, 138]. Here magnonic crystals play an important role [3]. A specific approach is to encode data in the phase of SWs and use Mach-Zehnder-type interferometers as logic gates [139–141]. For this, the controlled manipulation of SW phases is essential.  $360^\circ$  domain walls were predicted to provide the relevant SW phase shift  $\Delta\Theta$  of  $\pi$  [Ref. [139]]. This concept has however not yet been realized due to experimental challenges. Instead the magnetic field of a current carrying wire [140, 141] was used to create an inhomogeneous effective field  $H_{\text{eff}}$  in a ferromagnet and shift the phase of backward volume spin waves [142]. The required current might however cause local heating. Recently, magnonic crystals with magnetic defects were thoroughly investigated [45, 49, 143, 144], but defect-induced phase shifts for propagating SWs were not reported.

In this Letter, we explore a magnetic defect in one-dimensional (1D) magnonic crystals (MCs) as a phase shifter. The MCs consisted of bistable  $\text{Co}_{20}\text{Fe}_{60}\text{B}_{20}$  (CoFeB) stripes separated by air gaps. By reversing the magnetization of a specific stripe in an otherwise ordered MC we find phase shifts of Damon-Eshbach-type (DE) SWs of close to  $\pi$ , depending on an applied magnetic field  $H$ . Also the SW amplitude is varied. Because of their high group velocities [84] and non-reciprocity [145] DE-type SWs are favorable for future magnonic applications.

The MCs [Fig. 4.1 (a)] were fabricated from magnetron-sputtered CoFeB with a thickness of  $(19 \pm 2)$  nm deposited on an oxidized silicon substrate. The nanostripes were defined via electron beam lithography (EBL) using the negative resist hydrogen silsesquioxane (HSQ) and transferred into the magnetic film via ion beam etching. After the etching, a layer of  $\sim 20$  nm thick HSQ remained as an isolation layer. We present data on two 1D MCs with periods  $p = 400$  nm (sample MC1) and  $p = 600$  nm (MC2). In both cases the air gap between stripes amounted to  $g = (75 \pm 10)$  nm [Fig. 4.1 (a)], and the overall outer dimensions were  $160 \mu\text{m}$  in  $x$ -direction and  $80 \mu\text{m}$  in  $y$ -direction. The saturation magnetization  $\mu_0 M_s = 1.8$  T



#### 4.1. Phase control of spin waves based on a magnetic defect in a one-dimensional magnonic crystal

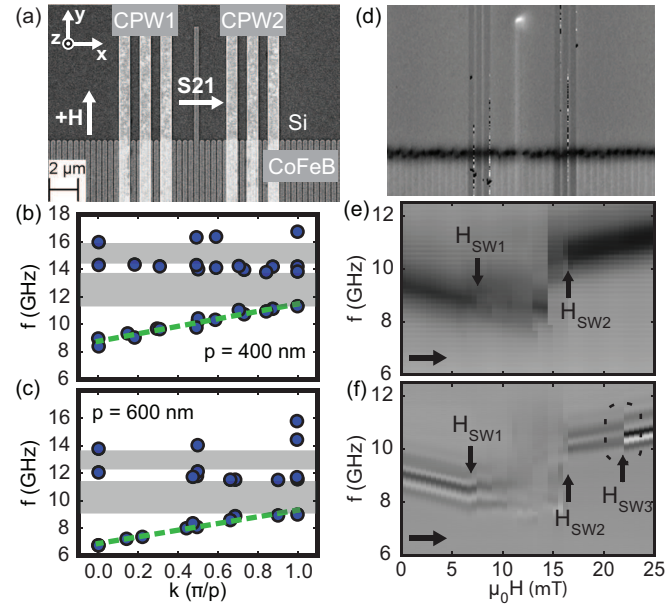


Figure 4.1 – (a) Scanning electron microscopy image of the central region of MC1. Dispersion relations measured via wavevector resolved BLS (symbols) on saturated 1D MCs with  $p$  of (b) 400 and (c) 600 nm (plotted in the reduced zone scheme) at  $H = 0$ . Grey colors indicate stopbands. The dashed lines in (c) and (d) indicate fitted linear functions that evaluate the averaged slopes, i.e., the averaged group velocities. (d) MFM performed on a reference MC1 at  $\mu_0 H = +18$  mT after saturation at  $-90$  mT. Black (white) signals indicate stray fields, i.e., orientations of magnetization vectors along (opposite) to the applied field. Grey-scaled plot of (e)  $a_{11}(H)$  and (f)  $a_{21}(H)$  of MC1 for increasing  $H$  (indicated by arrows), after saturation at  $\mu_0 H = -90$  mT. In (f) between  $H_{SW2}$  and  $H_{SW3}$  we assume the presence of a single magnetic defect. At  $H_{SW3}$  the SW signal undergoes an abrupt phase jump.

was extracted from ferromagnetic resonance measurements on a reference film (not shown). Dispersion relations  $f(k)$  were studied on reference samples that were similar to MC1 [Fig. 4.1 (b)] and MC2 [Fig. 4.1 (c)] ( $f$  is the frequency,  $k$  is the wavevector). For this, we applied  $k$ -resolved Brillouin light scattering (BLS) on MCs in backscattering configuration following Refs. [33, 146]. The laser had a wavelength 473 nm. A lens with focal length of 50 mm and f-number 2.8 was used to focus the laser to a spot diameter of few tens of micrometers. Figure 4.1 (b) and 4.1 (c) shows the resonance frequencies  $f$  (BLS peaks) recorded as a function of transferred in-plane wavevector  $k$ . The measured dispersion relations  $f(k)$  consist of allowed minibands and SW stopbands (shaded in gray color), similar to magnonic bandstructures reported in Ref. [33]. For  $p = 400$  nm ( $p = 600$  nm) we attribute the first allowed miniband to a frequency regime ranging from 8.4 GHz to 11.3 GHz (6.7 GHz to 9.0 GHz). The second one ranges from 13.9 GHz to 14.4 GHz (11.5 GHz to 12.1 GHz).

We patterned coplanar waveguides (CPWs) on top of the MC1 and MC2 via EBL and lift-off processing of 4 nm thick evaporated Cr and 120 nm thick Au. Intentionally, a single CoFeB stripe in the center between CPW1 and CPW2 was longer by 8 μm [Fig. 4.1 (a)]. The CPWs allowed for excitation and detection of propagating SWs [147]. The center-to-center separation

between CPW1 and CPW2 amounted to  $s = 7.5 \mu\text{m}$ . The width of the signal and ground lines of the CPWs were  $w = 0.8 \mu\text{m}$ . Using a vector network analyser we applied a radiofrequency signal with a power of  $\leq -5 \text{ dBm}$  at CPW1. The spatial profile of the exciting magnetic field of the CPW was simulated in COMSOL Multiphysics. Fast Fourier analysis of the in-plane field component showed a peak in SW excitation at  $k_1 = 2.0 \cdot 10^4 \text{ rad/cm}$ , which is below the wavevector  $k_{\text{BZ}} = \frac{\pi}{p}$  of the first Brillouin zone (BZ) boundary, amounting to  $7.9 \cdot 10^4 \text{ rad/cm}$  ( $5.2 \cdot 10^4 \text{ rad/cm}$ ) for MC1 (MC2). Scattering parameters  $S_{11}(H)$  ( $S_{21}(H)$ ) were recorded at CPW1 (CPW2), while a magnetic field  $H$  was applied in  $y$ -direction. In this work we discuss the magnitude of the scattering parameters. To extract the magnon-induced signal contribution  $a_{ij} = S_{ij}(H) - S_{ij}(H_\perp)$  ( $i, j = 1, 2$ ), we subtracted the reference spectrum  $S_{ij}(H_\perp)$  taken at  $\mu_0 H_\perp = 90 \text{ mT}$  applied in  $x$ -direction, where SW excitation was negligible. We performed magnetic force microscopy (MFM) [Fig. 4.1 (d)] on a reference MC1 to estimate the reversal fields of the bistable nanostripes. The sample was first saturated at  $-90 \text{ mT}$  with  $H$  collinear to the  $y$ -axis. Then the field was increased in steps of  $1 \text{ mT}$ . The short stripes forming the MC were found to reverse their magnetization direction between  $5$  and  $15 \text{ mT}$ . The long stripe switched at a larger field of  $19 \text{ mT}$  which we attributed to the modified shape anisotropy compared to the short stripes.

Figure 4.1 (e) shows  $a_{11}(H)$  of MC1 for increasing  $H$  after it was saturated at  $\mu_0 H = -90 \text{ mT}$ . The prominent dark branch indicates the SW resonance at  $k_1$ . Its frequency  $f_{\text{res}}$  (dark) linearly decreases with increasing  $H$  until  $\mu_0 H_{\text{SW1}} = 6 \pm 1 \text{ mT}$ . Here, the intensity of the branch reduces and its linewidth increases. The signal strength recovers at  $\mu_0 H_{\text{SW2}} = 16 \pm 1 \text{ mT}$ . Beyond  $\mu_0 H_{\text{SW2}}$ ,  $f_{\text{res}}$  increases with  $H$ . We attribute the field regime between  $H_{\text{SW1}}$  and  $H_{\text{SW2}}$  to the switching fields of stripes in close vicinity of CPW1. In Fig. 4.1 (f) field-dependent transmission signals  $a_{21}(H)$  are summarized.  $a_{21}$  shows pronounced oscillations (black-white-black contrast) which we attribute to the interference of the spin-precession induced voltage and direct electromagnetic crosstalk between CPW1 and CPW2 following Ref. [113]. The crosstalk showed a stable phase, and the interference pattern allowed us to analyse phase differences  $\Delta\Theta$  of transmitted SWs as will be presented later.

Increasing  $H$  from  $0 \text{ mT}$  in Fig. 4.1 (f), the oscillations in  $a_{21}$  become weak at  $H_{\text{SW1}}$ . At  $H_{\text{SW2}}$  the oscillating signature regains a pronounced signal strength. Beyond  $\mu_0 H_{\text{SW3}} = 23 \pm 1 \text{ mT}$  in Fig. 4.1 (f) the signal is found to be even stronger than at  $H = 0$ . We attribute the regime between  $H_{\text{SW2}}$  and  $H_{\text{SW3}}$  to the configuration where all short stripes are aligned to the external field, but the long stripe is oppositely magnetized similar to Fig. 4.1 (d). Strikingly, at  $H_{\text{SW3}}$  not only the amplitude changes, but also a clear phase jump is seen in the oscillations, indicating an abrupt SW phase variation. We attribute this observation to the reversal of the long nanostripe. Similar characteristics were observed for MC2. Only the switching of stripes occurred at smaller field values of  $\mu_0 H'_{\text{SW1}} = 3 \text{ mT}$ ,  $\mu_0 H'_{\text{SW2}} = 8.5 \text{ mT}$  and  $\mu_0 H'_{\text{SW3}} = 12.5 \text{ mT}$  [see Fig. A.1 in the supplementary material].

Based on Fig. 4.2 we now discuss in detail the effect of an individual magnetic defect on SW transmission in the 1D MCs. It is instructive to first present field-dependent transmission signals  $a_{21,\text{SAT}}(H)$  for the saturated array (SAT). For Fig. 4.2 (a) we saturated MC1 at  $+90 \text{ mT}$  and then decreased  $H$  in a stepwise manner down to  $\mu_0 H = -4 \text{ mT} > -\mu_0 H_{\text{SW1}}$  without inducing

#### 4.1. Phase control of spin waves based on a magnetic defect in a one-dimensional magnonic crystal

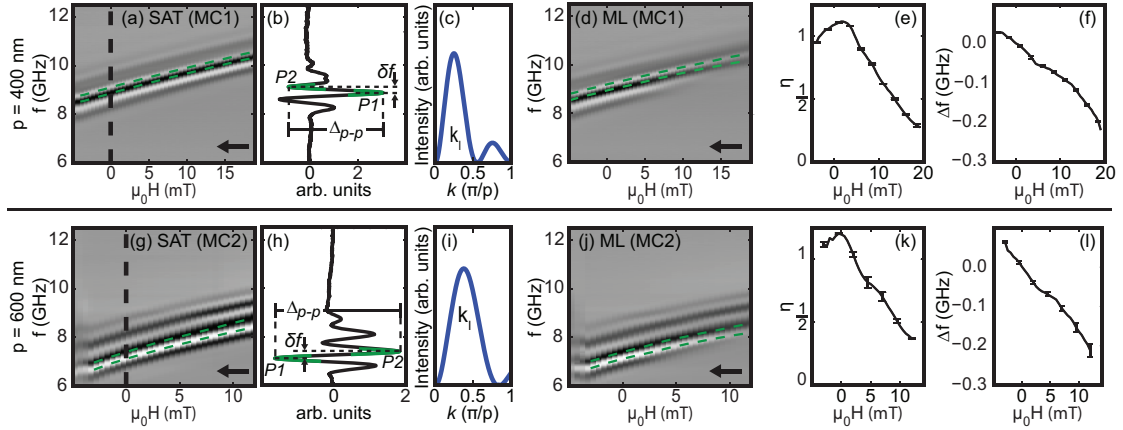


Figure 4.2 – (a) Grey scale plot (SAT) of  $a_{21}(H)$  of MC1 for decreasing  $H$  (indicated by arrows) after  $\mu_0 H = 90\text{mT}$  was applied. Green dashed lines indicate extrema  $P1$  and  $P2$  defined in (b). (b) Line plot of  $a_{21}$  at  $H = 0$ .  $P1$  and  $P2$  are used to extract  $\delta f$  and  $\Delta_{p-p}$ . (c) Excitation spectrum of the CPW where  $k$  is in units of  $\pi/p$ . (d)  $a_{21}(H)$  obtained in a minor loop (ML) assuming the presence of a magnetic defect.  $H$  was decreased starting from  $\mu_0 H^* = 19\text{mT}$  after saturation at  $\mu_0 H = -90\text{mT}$ . (e) Relative signal  $\eta(H)$  of spectra ML compared to spectra SAT. (f) Frequency shift  $\Delta f$  between peaks  $P1$  of SAT and ML datasets. (g) to (l) Corresponding data obtained on MC2.  $\mu_0 H^*$  amounted to  $-12\text{mT}$  indicating a smaller coercive field of MC2. Green dashed lines in datasets (a), (d), (g) and (j) indicate the frequencies of extrema  $P1$  and  $P2$  as they are defined in (b).

a reversal. We find a branch containing pronounced oscillations over the full depicted field regime. Frequencies of local extrema  $P1$  and  $P2$  [Fig. 4.2 (b)] systematically shift with  $H$  as highlighted by broken lines. The envelope of the oscillating signal of Fig. 4.2 (b) reflects the excitation spectrum of the CPW which is displayed in the reduced zone scheme in Fig. 4.2 (c) ( $k \leq k_{BZ}$ ). For the following analysis we refer to Fig. 4.2 (b), define the peak-to-peak amplitude  $\Delta_{p-p}$  (signal strength) between neighbouring extrema  $P1$  and  $P2$ , and introduce the frequency difference  $\delta f$ . According to Ref. [114] we calculate the group velocity following  $v_g = \frac{\partial \omega}{\partial k} = \frac{4\pi \delta f}{2\pi/s} = 2\delta f \times s$ . At  $H = 0$  we find  $\delta f = 0.244\text{ GHz}$  corresponding to  $v_g = 3.7\text{ km/s}$ . This value represents the upper limit of  $v_g$ , considering Ref. [113] where a reduced phase accumulation length was encountered.

The effect of the defect was probed via a minor loop (ML) starting at a field  $H^*$  located between  $H_{SW2}$  and  $H_{SW3}$ . For the spectra displayed in Fig. 4.2 (d) we first saturated MC1 at  $-90\text{ mT}$ , and then applied  $\mu_0 H^* = +19\text{ mT}$  to reverse the short stripes but keep the long stripe oriented along the negative field direction. Thereby we programmed the magnetic defect. We highlight three discrepancies found in Fig. 4.2 (d) compared to (a): (i) between 12 and 19 mT less oscillations are present, (ii) the oscillation amplitudes are weaker over a broad field range, and (iii) the local extrema appear at different frequencies when measured at the same  $H$ . In the following we quantify the discrepancies in that we introduce both the relative signal strength  $\eta(H) = \frac{\Delta_{p-p}(\text{ML})}{\Delta_{p-p}(\text{SAT})}$  [Fig. 4.2 (e)], and frequency shift  $\Delta f = f_{P1}(\text{ML}) - f_{P1}(\text{SAT})$  [Fig. 4.2 (f)] evaluated at different  $H$  between peaks  $P1$  of the ML and SAT datasets. In Fig. 4.2 (e),  $\eta(H)$

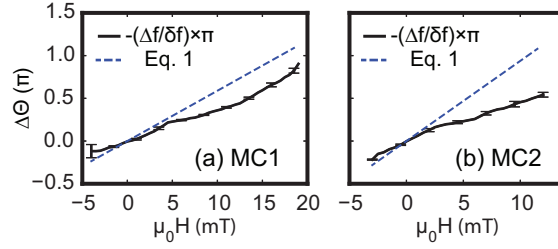


Figure 4.3 – Estimated SW phase shifts  $\Delta\Theta$  (full lines) when the long stripe is magnetized oppositely to the short stripes in (a) MC1 and (b) MC2. Phase shifts are given relative to the fully saturated MC. The dashed lines reflect model calculations based on Eq. (4.1).

is slightly above one at  $H = 0$  and then decreases with increasing  $|H|$  to a minimum value of 0.3 at  $H^*$ . This means that at 19 mT the programmed defect reduces the transmitted SW amplitude by 70 %. In Fig. 4.2 (f), the frequency shift  $\Delta f(H)$  is zero at  $H = 0$ . At 19 mT, we find  $\Delta f = -0.2$  GHz.

Corresponding measurements were also conducted for MC2. In Fig. 4.2 (g) we show  $a_{21,\text{SAT}}$  of MC2 for decreasing  $H$  after it was saturated at +90 mT and while the MC remained fully aligned. Again, we observed a clear branch with several oscillations. At  $H = 0$  [Fig. 4.2 (h)]  $\delta f$  amounted to 0.279 GHz corresponding to  $v_g = 4.2$  km/s. Compared to MC1 [Fig. 4.2 (b)] a larger number of oscillations is observed. We attribute this to the excitation spectrum of the CPW in that the  $k_I$  peak now covers a broader range of the first BZ of MC2 [Fig. 4.2 (i)]. In Fig. 4.2 (j) we show  $a_{21}$  obtained in a ML. After saturation at  $-90$  mT a field of  $\mu_0 H'^* = +12$  mT located between  $H'_{\text{SW3}}$  and  $H'_{\text{SW2}}$  was applied. In this regime the long stripe was assumed to be magnetized in opposite direction to both  $H$  and the short stripes. At  $H'^*$  the signal was small. When decreasing the field from  $H'^*$ , the signal increased until  $H = 0$ . This behaviour is analyzed by  $\eta(H)$  shown for MC2 in Fig. 4.2 (k).  $\eta$  amounts to 0.4 (1.2) at  $H'^*$  ( $H = 0$ ).  $\Delta f$  of MC2 is shown in Fig. 4.2 (l). We find  $\Delta f = -0.2$  GHz (0 GHz) at  $H'^*$  ( $H = 0$ ).

We assume that  $\Delta f$  is a measure of a magnetic-defect-induced phase shift accumulated by SWs going across a reversely magnetized nanostripe. In the following, we estimate the phase shift  $\Delta\Theta$  that appears relative to the fully saturated MC. In a fully saturated MC, SWs leading to neighboring extrema P1 and P2 of spectra  $a_{21}$  in Fig. 4.2 (a) and (g) are separated by  $\delta f(H)$  corresponding to a known phase shift of  $\pi$ . Using the relation  $\Delta\Theta(H) = -\frac{\Delta f(H)}{\delta f(H)} \cdot \pi$  we estimate the field-dependent phase shifts  $\Delta\Theta(H)$  in MC1 [solid line in Fig. 4.3 (a)] and MC2 [solid line in Fig. 4.3 (b)] considering  $\delta f(H)$  of Fig. 4.2 (a) and (g), respectively. For both samples  $\Delta\Theta$  is found to vary monotonously with  $H$ . For MC1 (MC2)  $\Delta\Theta = 0.9\pi$  ( $\Delta\Theta = 0.5\pi$ ) is reached at  $H^*$  ( $H'^*$ ).

In the following we explain these findings with different static effective fields  $H_{\text{eff}}$  for the defect and the MC when  $H \neq 0$  [Fig. 4.4 (a)].  $H_{\text{eff}}$  enters the equation of motion for spin precession [64]. To facilitate the discussion we assume infinitely long nanostripes with a demagnetization factor  $N_y = 0$  such that  $|H_{\text{eff}}| \approx H$ . For a positive magnetic field,  $H$  points parallel (antiparallel) to the static magnetization  $\mathbf{M}$  of the short stripes (the reversed long stripe) and enters  $H_{\text{eff}}$  with positive (negative) sign. This scenario leads to a variation in  $H_{\text{eff}}(x)$  as sketched in Fig. 4.4

#### 4.1. Phase control of spin waves based on a magnetic defect in a one-dimensional magnonic crystal

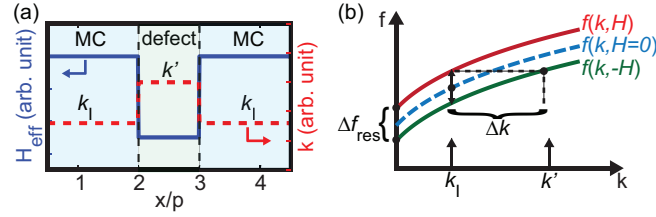


Figure 4.4 – (a) Sketch of  $H_{\text{eff}}$  for  $H > 0$ . At the defect  $H$  enters  $H_{\text{eff}}$  with opposite sign. Thereby a well is formed. Considering a small  $H_{\text{eff}}$  in the well, the wave vector  $k'$  at the defect is larger than  $k$  to match the excitation frequency. (b) Dispersion relations sketched for different  $H_{\text{eff}}$ . The resonance frequency of regular stripe arrays is shifted upwards following  $f(k, H_{\text{eff}} = +H)$ , in the oppositely magnetized long stripe it shifts downwards following  $f(k, H_{\text{eff}} = -H)$ . Such a shift results in different wavevectors  $k_1$  and  $k'$  for a fixed frequency  $f$  with  $\Delta k = k' - k_1$ .

(a). The defect represents a SW well. The corresponding dispersion relations  $f(k)$  inside and outside the SW well are sketched in Fig. 4.4 (b). When SWs are transmitted between CPW1 and CPW2 at a fixed frequency  $f$ , the relevant wavevector  $k'$  in the well is different from  $k$  of the MC. Stimulated by Ref. [148] we estimate the difference between  $k$  and  $k'$  in that we consider local dispersion relations  $f(k)$  of Fig. 4.4 (b). First we assume that for  $H = 0$  the branch shown as the broken line is valid. For  $H \neq 0$  this branch shifts to larger and smaller frequencies depending on the orientation of the magnetization vectors  $\mathbf{M}$  in nanostripes. At  $k = 0$  the two branches for opposing directions of  $\mathbf{M}$  acquire a frequency splitting of  $\Delta f_{\text{res}}$ . If, for a fixed excitation frequency  $f > f(k = 0)$ , the SW in the MC takes the wavevector  $k = k_1$  the relevant wavevector in the SW well amounts to  $k' > k_1$ .<sup>1</sup> Accordingly, the transmitted spin wave experiences an extra phase shift  $\Delta\Theta(H) = \Delta k \times p = (k' - k_1) \times p$ . To check for consistency with the evaluated values  $\Delta\Theta$ , we estimate  $\Delta k$  as follows: Based on  $a_{21, \text{SAT}}$  [Fig.4.2(a)(g)] we linearly approximate the field dependency  $df/dH$  of  $P1$  in the relevant regime below  $H^*$  ( $H'^*$ ), amounting to 80 MHz/mT (114 MHz/mT) for MC1 (MC2). Assuming  $df/dH$  as constant for negative  $H$  as well, the frequency splitting calculates as  $\Delta f_{\text{res}} \approx (df/dH) \times 2H$ . From the experimentally observed dispersion relations of the two MCs we evaluated the slope  $df/dk$ , i.e., the averaged group velocity of the lowest miniband [broken lines in Fig. 4.1 (b) and (c)], amounting to  $0.346 \frac{\text{GHz } \mu\text{m}}{\text{rad}}$  ( $0.464 \frac{\text{GHz } \mu\text{m}}{\text{rad}}$ ) for MC1 (MC2).  $\Delta k$  can be estimated via  $\Delta k \approx (df/dk)^{-1} \times \Delta f_{\text{res}}$ , thus the expected phase shift induced by a magnetic defect reads

$$\Delta\Theta \approx (df/dk)^{-1} \times (df/dH) \times 2H \times p. \quad (4.1)$$

The dashed lines shown in Fig. 4.3 (a) and (b) reflect the expected phase shifts  $\Delta\Theta$  based on Eq. (4.1). The model explains the magnitude of the experimentally extracted  $\Delta\Theta$  well and underlines that a modified wavevector in the magnetic defect causes an appreciable field-dependent phase shift. Equation (4.1) allows us to optimize the phase shift. Following Eq. 4.1 the phase shift depends on the product  $2H/\nu_g$ . To increase  $\Delta\Theta$  one needs either reduce  $\nu_g$  or, more favourably, increase the field  $H$  which one can apply before reversing the magnetic

<sup>1</sup>For the sketch in Fig. 4.4 (b) we assumed that branches differed by a constant  $\Delta f = \Delta f_{\text{res}}$  for all  $k$  as  $H$  was small compared to  $M$ .

defect. An additional uniaxial anisotropy along the long axis of the nanostripe might allow for large  $H$ .

The increase of  $k'$  in the defect might also explain the observed field-dependence of relative signal strength  $\eta(H)$ . We think of two relevant mechanisms. First, SW reflection at the defect can occur due to the inhomogeneous  $H_{\text{eff}}$  [142], inducing a mismatch of the wave impedance [49]; second, a large wavevector was found to reduce the dipolar strength across a gap [149]. Therefore we expect a reduced dipolar coupling for an increased  $k'$  at the defect. We note that in our experiment we intentionally used long stripes with a small demagnetization field. In the contrary, Halder et al. [143] explored a chain of short nanomagnets. In this case a significant change of the demagnetization field took place when the magnetization direction of an individual nanomagnet was switched. Consistently, the authors reported a pronounced SW attenuation at a reversed nanomagnet for already  $H = 0$ .

To avoid the bias magnetic field that we introduced to adjust effective fields for SW phase control, one could expose the relevant CoFeB nanostripe to a magnetic anisotropy that is induced by e.g. inverse magnetostriction [150]. If provided by a ferroelectric substrate, this anisotropy and the related  $H_{\text{eff}}$  can be controlled by an electric field [151, 152]. The concept outlined here could allow for all-magnon data processing if -in a three terminal device- spin waves induce domain-wall motion in the magnetic defect [1] and thereby control the magnetization direction of the corresponding SW well through which spin waves are transmitted.

In conclusion, we demonstrated that SW amplitudes and phases are controlled via a magnetic defect in a 1D magnonic crystal. A phase shift of almost  $\pi$  was observed and explained by a modified wavevector at the defect forming a spin-wave well.

### Supplementary Material

See supplementary information SI A.1 for  $a_{11}$  and  $a_{21}$  of MC2 for increasing  $H$ .

### Acknowledgment

We thank for funding by SNSF via grant 163016. We thank F. Stellacci and E. Athanasopoulou for support concerning MFM.

## 4.2 Microscopic observation of phase shifts at a magnetic defect

In the previous section, phase shifts introduced by a magnetic defect in a 1D MC were evidenced electrically by AESWS measurements between two CPWs. The magnetic defect was incorporated in the center of the CPWs and selectively switched on and off by tuning the magnetic history. The reported phase shifts were calculated by the difference in phase of SWs transmitted with and without the defect activated. We proposed a microscopic model (cf. Fig. 4.4), but supporting microscopic measurement data was not yet available at the moment of publication [50]. In this section we present space- and phase-resolved  $\mu$ BLS measurements on sample MC1 with periodicity  $p = 400$  nm. The  $\mu$ BLS data provides microscopic insight on how SWs are transmitted across a nanoscale magnetic defect, not accessible by AESWS due to lack of spatial resolution.

Figure 4.5a shows an optical image of MC1 taken with the  $\mu$ BLS camera. We focused a laser with wavelength of 473 nm and 1 mW power to a spot with a diameter of about 350 nm onto the sample surface. The laser spot was scanned in  $x$ -direction in 100 nm steps, while SW intensity and phase were measured. The line scan was 15  $\mu$ m long and included CPW1, the prolonged stripe and part of CPW2 (see yellow scan path indicated in Fig. 4.5a). A magnetic bias field was applied in  $+y$ -direction, corresponding to the magnetization direction of the short stripes. In the beginning of the BLS measurements, the prolonged stripe was magnetized in  $-y$ -direction, which was confirmed by MFM. I.e., the prolonged strip was magnetized in opposite direction compared the rest of the MC and represented a magnetic defect.

The MC with defect was investigated for several bias fields, then it was completely saturated in  $+y$ -direction, and measurements repeated on the defect-free MC1 using identical instrument settings. For all measurements microwave excitation was applied at CPW1. The microwave frequency  $f_{\text{ex}}$  was adapted depending on the bias field. For each bias field, we measured the BLS counts as a function of  $f_{\text{ex}}$  applied in 0.1 GHz steps for a fixed spot position and chose the peak frequency for the subsequent line scan measurements. Figure 4.5b shows exemplarily the frequency scan for  $\mu_0 H = 0$  mT. The measurement position is indicated in the inset of Fig. 4.5b. A peak is apparent at  $f_{\text{ex}} = 9.1$  GHz, which is attributed to the  $k_1$  excitation of the CPW. Figure 4.5c shows a comparison of the SW intensity (left column) and the phase signal (right column) measured with the defect (green lines) and without the defect (blue lines) at exemplary bias fields. The SW characteristics on the left side of CPW1 were similar with and without the defect. By fitting the SW intensity between  $x = 0$  and  $x = 5.5$   $\mu$ m with Eq. 3.10, we extract a decay length of  $\delta = 2.9 \pm 0.2$   $\mu$ m for  $\mu_0 H = 0$  mT. Phase-resolved BLS allowed us to measure  $\cos(\Theta(x) - \Theta')$ , where  $\Theta(x)$  is the SW phase at a position  $x$  and  $\Theta'$  is a reference phase, which is constant for a given measurement frequency. For all bias fields, the phase signal agreed with sinusoidal waves with wave lengths around  $\lambda = 3.1$   $\mu$ m. The measured wave lengths matched well to the calculated wave vector  $k_1 = 2.0$  rad  $\mu\text{m}^{-1}$  of the CPW (cf. dashed line in Fig. 3.2).

In the vicinity of the defect (highlighted in yellow) phase signals and intensities were clearly modified. We first focus on the influence of the defect on the phase signals (right column in Fig. 4.5c). For  $\mu_0 H = 0$  mT (top row) a localized phase-jump was observed at the position of the magnetic defect itself ( $x_D = 11.2$   $\mu$ m). For  $x > x_D$  however, the phase profiles with and without



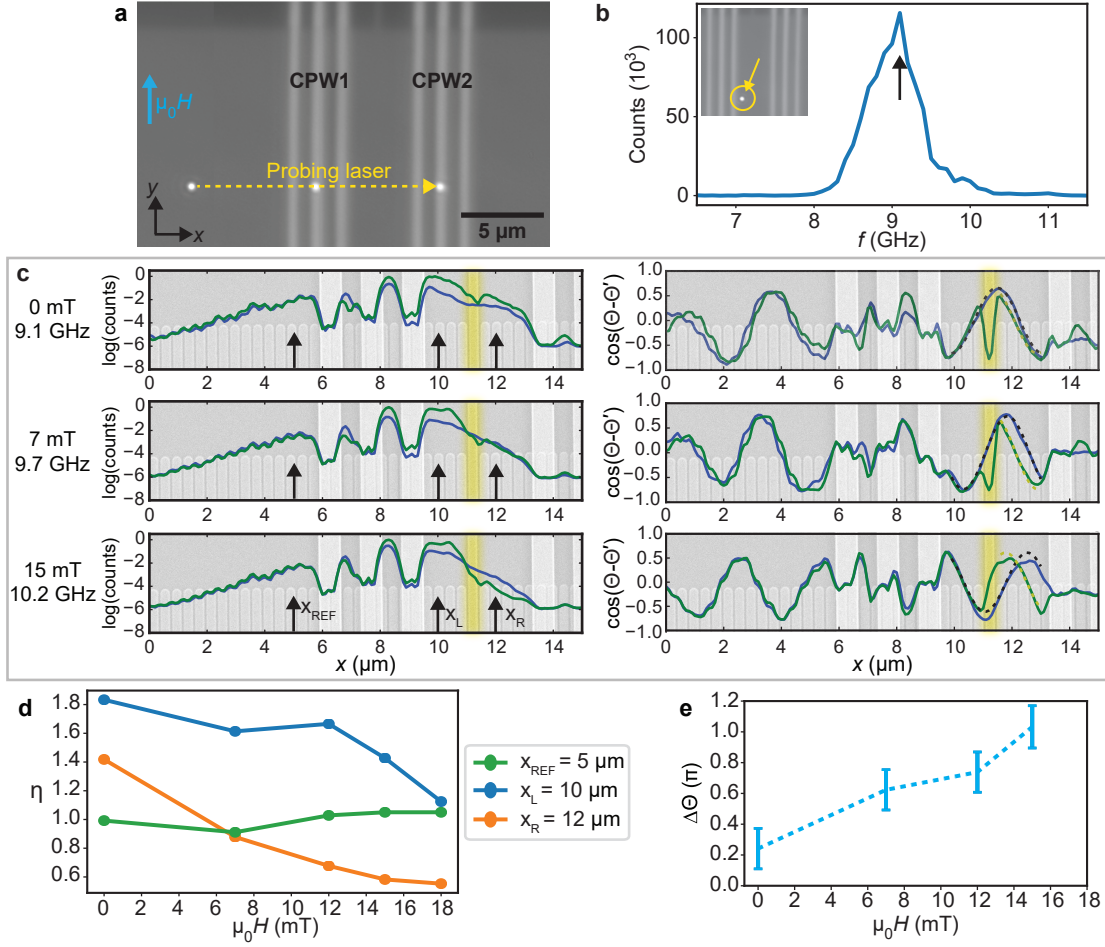


Figure 4.5 – **a** Optical image of MC1 as seen in the BLS microscope. The probing laser spot was scanned along the yellow dashed line, while SW intensity and phase signal was recorded. Microwave excitation was applied to CPW1. **b** BLS counts as function of microwave frequency measured at  $\mu_0 H = 0$  mT for a fixed spot position, indicated by the yellow circle in the inset. **c** Intensity (left column) and phase signal (right column) measured with (green lines) and without (blue lines) magnetic defect for different bias fields (rows). An aligned SEM image of MC1 is shown in the background of every plot as orientation. The position  $x_D = 11.2$  μm of the magnetic defect is highlighted in yellow. **d** Ratio  $\eta$  of SW amplitudes with and without defect extracted at different positions indicated by arrows in the left column of **c**. **e** Phase shift  $\Delta\Theta$  of SWs for  $x > x_D$ . The error bar was calculated based on the standard deviation of the fitted wave functions (dashed lines in the right column of **c**) and by assuming a possible error in positioning of  $\pm 100$  nm.

defect were again in good agreement. We attribute the localized phase-shift at  $x_s$  to an in-plane dynamic coupling of the defect to its neighboring stripes, as suggested in Huber *et al.* [49]. Due to magnetic gyrotropy, the sense of spin-precessional motion in the defect is opposite to the rest of the MC. Consequently, the in-phase coupling with the surrounding stripes results in a  $\pi$  phase-shift of the out-of-plane component of the magnetic defect. The out-of-phase



## 4.2. Microscopic observation of phase shifts at a magnetic defect

out-of-plane  $\tilde{m}_z$  component explains the local jump in the measured  $\cos(\Theta(x_D) - \Theta')$ . For increasing bias fields (second and third row), the phase profiles with and without defect are appreciably displaced relative to one another for  $x > x_D$ . This indicates a phase-shift of SWs which passed the defect, as extracted from the macroscopic AESWS measurements. Strikingly, the relative displacement is pronounced directly at the defect. This observation confirms that the phase is shifted on the length-scale of one individual stripe (325 nm), as suspected by our model in Fig. 4.4. We quantify the phase-shift  $\Delta\Theta$  by sinusoidal fitting of  $\cos(\Theta(x) - \Theta')$  on the right side of the defect (yellow dashed line in Fig. 4.5c) and for the phase trace without defect (black dashed line). In Fig. 4.5e the extracted phase differences are plotted. We find phase-shifts  $\Delta\Theta$  in Fig. 4.5e that are in qualitative agreement with the AESWS measurements (cf. Fig. 4.3a).

In the following we discuss the measured SW intensities (left column in Fig. 4.5c). In the direct vicinity of the magnetic defect ( $x_D = 11.2 \mu\text{m}$ ), we find two small dips in the measured counts visible for all bias fields. We assume a partial cancellation of the BLS signal, when the probing spot covers partly the defect and partly a neighboring stripe precessing with a  $\pi$  phase shift in  $m_z$ . To avoid such cancellation, we analyze the BLS intensity at  $x_L = 8 \mu\text{m}$  and  $x_R = 10 \mu\text{m}$  approximately  $1 \mu\text{m}$  left and right of the defect. As reference we also extracted intensities at  $x_{\text{REF}} = 5 \mu\text{m}$ . Here the distance to the defect was  $> 2\delta$  such that a significant intensity change was not expected.

In the following we discuss relative signal amplitudes  $\eta$ . For this, we calculate  $\eta$  as square root of the ratio of BLS counts with defect to counts without defect. The square root is taken as BLS counts are proportional to  $m_z^2$ , while the AESWS amplitudes used for the definition of  $\eta$  in the previous section scale with  $m_z$ . Hence  $\eta$  reflects the ratio of SW amplitudes. Figure 4.5d shows  $\eta(H, x)$  as function of the applied bias field for different positions. At the reference position  $x_{\text{REF}}$  the calculated  $\eta$  stayed close to one for all fields. This suggests that the instrument itself was stable and intensities with and without defect can be compared. On the right side of the defect we find that  $\eta(x_R)$  was gradually reduced with increasing bias field. This is in agreement with our AESWS measurements, where the transmitted SW amplitudes decreased with  $H$  (cf. Fig. 4.2e). At 0 mT  $\eta(x_R)$  was even above 1, suggesting that the defect might improve the decay length.

For  $x_L$  we find  $\eta > 1$  for all bias field values. This observation suggests SW reflection at the defect, as speculated in Ref. [49]. Counterintuitively,  $\eta(x_L)$  was largest at 0 mT and decreased gradually with  $H$ . This is surprising, as the transmission ( $\eta(x_R)$ ) decreased with  $H$  as well. I.e. the observation can not be explained solely by reflection and transmission coefficients at the defect. We note that the defect was only about half a wavelength away from the outer edge of the CPW and near-field effects can not be excluded. For clarification similar experiments should be performed on a low-damping MC for which the defect can be placed several wavelengths apart from the exciting CPW.

To conclude, the phase-resolved  $\mu\text{BLS}$  data confirmed an out-of-plane phase shift at the defect, suggesting in-plane coupling of the magnetic defect with its neighboring stripes. Depending on the bias field, a phase shift was apparent for SWs which passed the defect. The phase shift occurred at the defect itself, i.e. on the length scale of few hundred nanometers. Space re-

solved intensities suggested back-scattering of SWs at the defect. So far the experiments were performed in the near-field of a CPW. The full functionality of magnetic defects concerning reflected and transmitted SW amplitudes might be tested by using low-damping ferrimagnets and a large separation between CPW and defect.

### 4.3 Low-loss nanoscale $\pi$ -phase shifting observed in micromagnetic simulations

The results of AESWS and BLS measurements of 1D MCs with magnetic defects were promising for nanomagnonics, in that phase and amplitude manipulation on the nanoscale was demonstrated. However, observed phase shifts were concomitant with a reduction in amplitude. Especially for phase shifts approaching  $\pi$  the amplitude reduction was severe (cf. Fig. 4.2e and Fig. 4.5d). For SW logic gates based on interference of two or more SW inputs [138, 140, 141, 153] low-loss  $\pi$ -phase shifting is of uttermost relevance to reach complete destructive interference, i.e. logic "0" outputs. In this section we present micromagnetic simulations with MuMax3 [91] on a MC with defect of similar dimensions as MC1. By studying a large parameter space beyond our experiments we find conditions for which  $\pi$  phase shifts are obtained without significant changes in the amplitude level of transmitted SWs.

We simulated a 1D MC out of long CoFeB stripes arranged in  $x$ -direction with periodicity of  $p = 400$  nm and separated by  $g = 75$  nm wide air gaps, identical to MC1. Due to limitations in computational power, it was not possible to simulate a sample with the outer dimension of MC1 ( $160 \mu\text{m} \times 80 \mu\text{m} \times 19$  nm) in a fully 3-dimensional manner. Instead we computed the magnetization dynamics for a slice of the MC in  $x$ - $z$ -plane. In  $y$ -direction the periodic boundary condition (PBC) approach was used, assuming a constant magnetization along the stripe lengths. Still, MuMax3 considered a finite number of repeating cells in  $y$ -direction (summing up to  $l_y = 41 \mu\text{m}$ ) to compute a 3D-demagnetization tensor [154]. For the simulations, we used a saturation magnetization of  $\mu_0 M_s = 1.8$  T, Gilbert damping of  $\alpha = 0.006$  [155], an exchange constant  $A_{\text{ex}} = 20 \text{ pJ m}^{-1}$  [156] and a grid size of  $2 \text{ nm} \times 20 \text{ nm} \times 2 \text{ nm}$  ( $\Delta x, \Delta y, \Delta z$ ). For band structure simulations a chain of 40 stripes and for SW propagation a chain of 164 stripes was considered.

First, we extract the band structure of the MC by applying a spatial and temporal sinc-excitation (see Sec. 2.3.5) and computing the Fourier amplitudes of  $m_x(x, t)$  and  $m_y(x, t)$  [157]. To reproduce the experimentally measured band structure of MC1 (cf. Fig. 4.1b), we computed the dispersion for several film thicknesses  $d$ . A good agreement was found for  $d = 10$  nm, shown in Figure 4.6a. For comparison, the measured dispersion of MC1 is displayed by yellow circles. In the plot, we shifted the measurement data by -1 GHz to compensate for a discrepancy of the FMR frequency between simulation and experiment. The frequency shift might be due to the approximation of the demagnetization tensor using PBC in  $y$ -direction. After this adaption, band slopes and band gap width for the first and second mini-band are well matched. The discrepancy in film thickness between simulated  $d$  and nominal thickness  $d = 19$  nm of MC1 might be due to film roughness in the experiment, which reduces the

### 4.3. Low-loss nanoscale $\pi$ -phase shifting observed in micromagnetic simulations

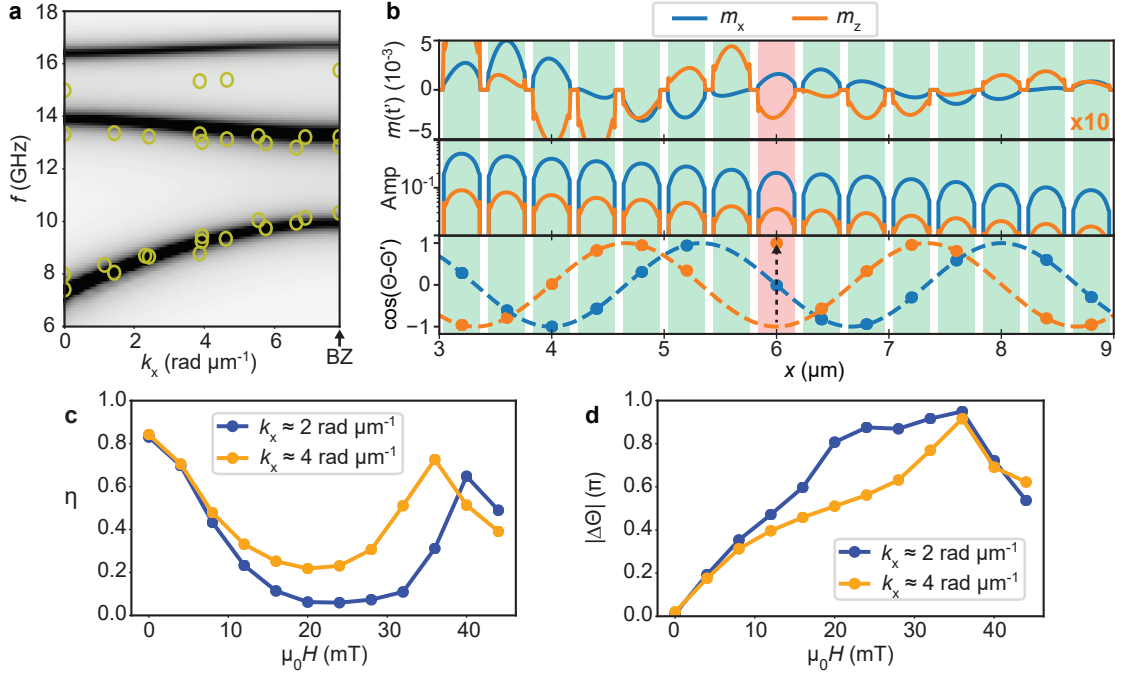


Figure 4.6 – **a** Band structure of the simulated 1D MC (black branches) in comparison with the experimental band structure of MC1 (yellow dots) shifted by  $-1$  GHz. Simulation and experiment agree well for the first and second miniband. **b** Simulated  $m_x$  and  $m_z$  for a propagating SW excited at  $x = 0 \mu\text{m}$  with  $k_x \approx 2 \text{ rad } \mu\text{m}^{-1}$  shown for  $\mu_0 H = 0$  mT. The stripe at  $x_D = 6 \mu\text{m}$  (marked in red) was oppositely magnetized. The first row shows a snapshot of  $m_x$  and  $m_z$  at  $t' = 10$  ns. The second and third row depicts the precessional amplitudes and cosine of the phase. At the defect a  $\pi$  phase-jump of the phase of  $m_z$  is observed (marked by dashed arrow). **c** Amplitude ratio  $\eta$  and **d** magnitude of the phase shift  $|\Delta\Theta|$  of SWs which trespassed the defect.

surface pinning [158] and is not considered by the simulation.

In the following, SW propagation across a magnetic defect is addressed. SWs were excited at  $x = 0 \mu\text{m}$  by a sinusoidal  $h_{x,\text{rf}}$  with a Gaussian spatial profile with a FWHM of 150 nm and a peak amplitude of 0.25 mT. The frequency  $f_{\text{ex}}$  of  $h_{x,\text{rf}}$  was selected based on the computed dispersion relation in order to excite SWs with specific wave vectors  $k_x$ . Stripe magnetization and bias field pointed in  $+y$ -direction. At  $x_D = 6 \mu\text{m}$  a stripe was magnetized in  $-y$ -direction to form a magnetic defect. We analyzed amplitude and phase of  $m_x(x, t)$  and  $m_z(x, t)$  after the simulations run for  $t' = 10$  ns, i.e. after propagating SWs reached a steady state. To avoid back-reflection, the absorbing boundary condition [159] was applied at the outer edges of the MC.

Figure 4.6b depicts exemplarily simulation results in the vicinity of the defect for  $\mu_0 H = 0$  mT and  $k_x \approx 2 \text{ rad } \mu\text{m}^{-1}$ . The first row in Fig. 4.6b displays a snapshot of  $m_x(x, t')$  and  $m_z(x, t')$  at  $t'$ . Due to ellipticity of the precession the amplitude of  $m_y$  was small compared to  $m_x$  and multiplied by a factor of 10 for better visibility. We recorded  $m_x$  and  $m_z$  for  $t \geq t'$  in 10 ps steps during a time of 2 ns and computed the FFT amplitude (Amp) and phase ( $\Theta$ ) at the

driving frequency  $f_{\text{ex}}$ .  $\text{Amp}(m_x)$  and  $\text{Amp}(m_z)$  are displayed in the second row of Fig. 4.6b. The SWs decayed exponentially with  $\delta = 3.15 \mu\text{m}$ , which is in good agreement with  $\delta$  extracted by  $\mu\text{BLS}$  measurement on MC1. At the defect, no significant change in amplitude was visible for  $\mu_0 H = 0 \text{ mT}$ . In the third row, we show  $\cos(\Theta - \Theta')$  for  $m_x$  and  $m_z$  extracted at the center of each stripe, where  $\Theta'$  is the starting phase. The phase evolution of  $m_x$  agrees with SWs exhibiting a wavelength of  $\lambda \sim 3 \mu\text{m}$ . No deviation of a fitted sinusoidal wave profile (orange dashed line) is observed at  $x = x_D$ . For  $\Theta(m_z)$  a local phase jump of  $\pi$  from the sinusoidal wave profile (blue dashed line) is apparent at the defect. We intentionally adjusted  $\Theta'$  such that the  $\pi$ -shift at  $x_D$  resulted in a change of  $\cos(\Theta - \Theta')$  from -1 to +1, i.e. is well visible in the plot. For a quantitative analysis of amplitude and phase changes introduced by the defect, we repeated simulations for the defect-free state as reference. We computed  $\eta$  as ratio of  $\text{Amp}(m_x)$  with and without defect. Further we computed the magnitude of the phase shift  $|\Delta\Theta|$  based on the difference of  $\Theta(m_x)$  with and without defect. Both  $\eta$  and  $|\Delta\Theta|$  were evaluated in the region  $x = 8$  to  $12 \mu\text{m}$  and then averaged. Bias fields from 0 to 44 mT were simulated in 4 mT steps. Here the defect was not switched by the bias fields. In experimental studies of MC1 its defect was stable only up to  $\sim 23 \text{ mT}$ . Switching fields in real stripes have already been reported to be smaller compared to ideal stripes in simulations [46]. We assume that the switching process in the real sample was initiated by domain wall movement [160]. Switching mechanisms via domain wall formation were not considered in our simulation, as constant magnetization in  $y$ -direction was implied by the PBC.

For each bias field, we computed the dispersion relation and extracted frequencies of the first miniband at  $k_x = 2 \text{ rad } \mu\text{m}^{-1}$  (as used in the experiment) and  $k_x = 4 \text{ rad } \mu\text{m}^{-1}$  (in the middle of the BZ). Then SW propagation was simulated for the extracted frequencies. In this manner, we were able to evaluate  $\eta$  and  $|\Delta\Theta|$  as function of  $H$  without significantly varying the wave vector. The extracted  $\eta$  and  $|\Delta\Theta|$  are plotted in Fig. 4.6c and d. For  $k_x \approx 2 \text{ rad } \mu\text{m}^{-1}$  we observe a decrease in transmission with the bias field until  $\mu_0 H = 24 \text{ mT}$ , where  $\eta$  reaches a minimum of 0.06. In the same field range we observe a approximately linear increase of  $|\Delta\Theta|$  from 0 to  $0.88\pi$ . The simulated  $|\Delta\Theta|$  agrees well with the experimental values of MC1 (cf. Fig. 4.3a). Strikingly, above 24 mT the simulated  $\eta$  started to increase with  $H$ . Concomitantly also  $|\Delta\Theta|$  further increased, allowing for low-loss phase-shifting. We found  $\eta = 0.65$  at 40 mT, while  $|\Delta\Theta|$  peaked at 36 mT, amounting to  $0.95\pi$ . For  $k_x \approx 4 \text{ rad } \mu\text{m}^{-1}$ , the maximum in  $|\Delta\Theta|$  at 36 mT coincided with a maximum in  $\eta$ . We observed  $|\Delta\Theta| = 0.92\pi$  and an appreciable transmission with  $\eta = 0.73$ . We note that even larger values of  $\eta$  might be reachable, when the field is tuned in finer steps.

In the following we discuss the origin of the increased transmission for large enough bias fields. Figure 4.7a shows  $\text{Amp}$  and  $\Theta$  for SWs with  $k_x \approx 4 \text{ rad } \mu\text{m}^{-1}$  excited at  $f_{\text{ex}} = 11.73 \text{ GHz}$  and  $\mu_0 H = 36 \text{ mT}$ . The plotted  $\Theta$  has been unwrapped and the slope (black dashed line) represents  $\Theta = k_x x$  with an arbitrary starting phase. The phase evolution of stripes neighboring the defect behaves regularly and their precession amplitudes agree well with a regular exponential decay. The phase shift occurs mainly at the center of the defect, where  $\Theta$  abruptly shifts by about  $\pi$ . At the same position, a node in the oscillation amplitude is observed. The dynamic magnetization profile along the width of the defect agrees well with a standing wave with

### 4.3. Low-loss nanoscale $\pi$ -phase shifting observed in micromagnetic simulations

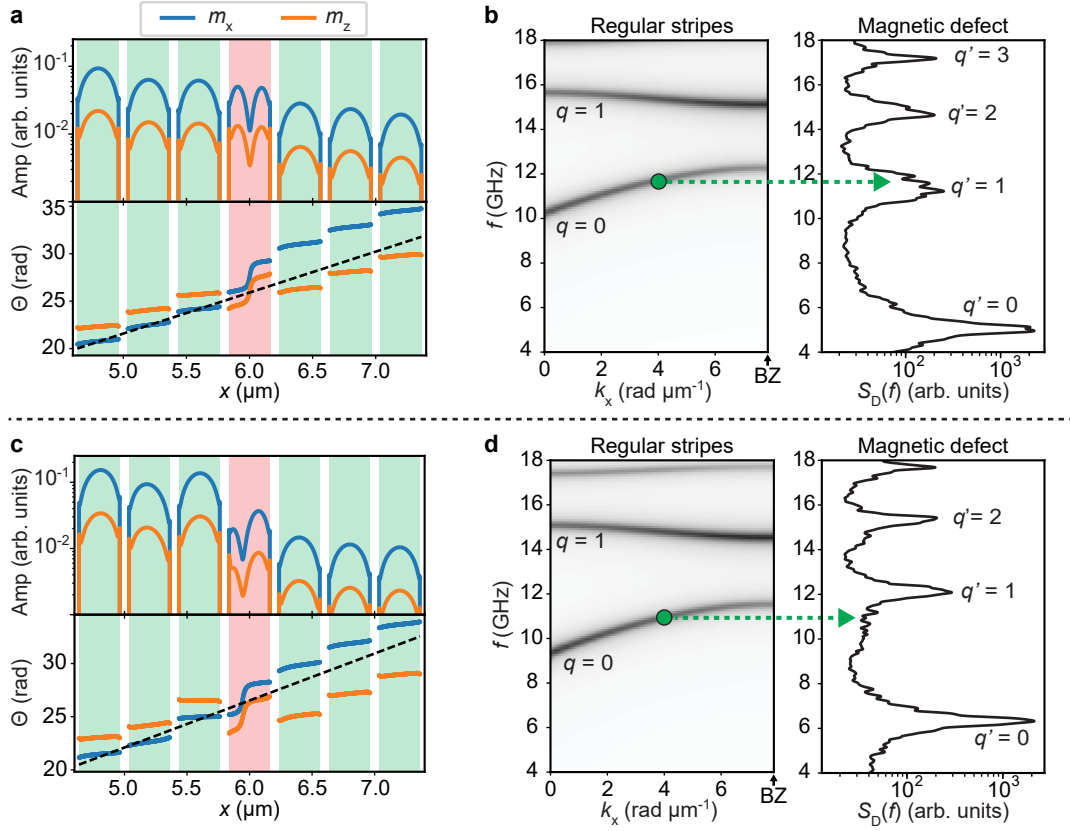


Figure 4.7 – **a** Amplitude and phase evolution for SWs with  $k_x \approx 4 \text{ rad } \mu\text{m}^{-1}$  at 36 mT. The dynamic magnetization profile at the defect shows a node at its center as expected for SWs in the second miniband of a 1D MC. **b** Dispersion relation of the 1D MC and the power spectral density  $S_D(f)$  of thermally excited magnons at the defect simulated for  $\mu_0 H = 36 \text{ mT}$ , respectively. Resonant features in  $S_D(f)$  indicate confined SW modes in the individual defect. The frequency of SWs with  $4 \text{ rad } \mu\text{m}^{-1}$  in the first miniband ( $q = 0$ ) of the MC matches with the frequency of the second spin wave resonance  $q' = 1$  of the defect. **c** Amplitude and phase of SWs at 24 mT. A significant reduction in amplitude is visible after the defect. At the frequency of excitation (green dashed line in **d**),  $S_D(f)$  is low, suggesting a band gap of the dispersion relation of the defect.

quantization number  $n = 1$  [44], i.e. with the magnetization profile expected for SWs in the second miniband ( $q = 1$ ) of a 1D MC [32]. We will denote the allowed SW state in the defect as  $q'$ . For uniformly magnetized stripes the  $q = 1$  band is located several GHz above the used driving frequency. However, we suspect that the bias field decreased the eigenfrequencies at the defect such that  $f_{\text{ex}}$  is within the  $q' = 1$  state. To identify the eigenfrequencies of the defect, we simulated with MuMax3 thermally excited magnons in the 1D MC with a defect at a finite temperature  $T = 300 \text{ K}$  [161]. The simulation was run over an extended time period of 100 ns and then the power spectral density  $S_D(f)$  of  $m_x(t)$  was computed at the position of the defect. By considering the power spectrum of thermally excited magnons we ensured that all possible SW modes of the defect are identified, instead of being limited to SW modes compatible with

the symmetry of an exciting  $h_{\text{rf}}$ .

Figure 4.7b compares the band structure of the 1D MC and  $S_D(f)$  of the magnetic defect for  $\mu_0 H = 36$  mT. The allowed SW eigenfrequencies of the defect are apparent as peaks in  $S_D(f)$  [162, 163]. We find that for a bias field of 36 mT the frequency of SWs with  $k_x = 4 \text{ rad } \mu\text{m}^{-1}$  in the first miniband ( $q = 0$ ) matches well with the frequency of the second allowed state ( $q' = 1$ ) observed in  $S_D(f)$ .

In Fig. 4.7c we show Amp and  $\Theta$  at a bias field of 24 mT. A significant reduction of the transmitted SWs is apparent. The stripe before the defect ( $x = 5.6 \text{ } \mu\text{m}$ ) shows a larger amplitude and a flattened phase evolution, corresponding locally to a wave vector close to zero. At the defect, the amplitude profile features a node and is highly asymmetric. In Fig. 4.7c the dispersion relation and  $S_D(f)$  of the defect are plotted for 24 mT. At  $f_{\text{ex}}$  the simulated  $S_D(f)$  is low, indicating a forbidden frequency gap in the defect.

In Sec. 4.1 we speculated that the wave vector  $k'$  inside a defect was adapted to a new dispersion relation shifted by two times of the external field. This earlier speculation is substantiated by the presented simulations. However, in Eq. 4.1 the dispersion was approximated by a linear slope. The simulations suggest that for larger bias fields this approximation is not suitable. Instead it is relevant to consider the specific allowed eigenfrequencies of the defect embedded in the 1D MC, including forbidden frequency gaps between the discrete SW frequencies. When the bias field shifts the dispersion at the defect such that a frequency gap resides at  $f_{\text{ex}}$ , the simulated SW transmission is low. When the bias field is large enough to create an overlap of the  $q = 0$  miniband of the regular magnetized stripes with the  $q' = 1$  state at the defect, the transmission increases again (Fig. 4.6c). Due to computational time restriction the bias field has been stepped only coarsely. We speculate that  $\eta$  close to one and a phase shift of  $\pi$  might be achievable, if  $H$  is fine-tuned such that for a constant  $k_x$  the band number  $q$  is shifted to exactly  $q' = q + 1$  at the defect. For even larger fields, not considered in the simulation, an overlap of miniband  $q$  of the regular magnetized stripes with a higher state  $q' = q + i$  (with  $i \in \mathbb{N}$  and  $i \geq 2$ ) at the defect might result in further peaks of  $\eta$ . The transmission characteristics are expected to be similar to e.g. a resonant-tunneling diode [164], where the wave function of an electron confined in an intermediate quantum well has multiple discrete energy levels and large transmission is achieved when one of the energy levels is tuned to the Fermi energy of the reservoirs. Based on the dynamic magnetization profiles, we anticipate a phase shift of  $\sim \pi$  in case  $q' - q$  is odd and  $\sim 0\pi$  in case  $q' - q$  is even. For future experimental studies, it will be relevant to either increase the switching field (e.g. by using materials with magnetocrystalline anisotropy) or to reduce the frequency spacing of the minibands. The latter could be realized by increasing the lattice period, i.e. shifting the BZ boundary to lower wave vectors. We note that electron quantization effects are visible in the 10 nanometer length scale. SWs in low damping YIG offer phase-coherence up to the millimeter scale [165]. This might allow to study SW gating with multiple transmission levels tailored at the mesoscopic scale.

#### 4.4. Reprogramming the band structure: Propagating spin waves in the antiferromagnetically ordered state

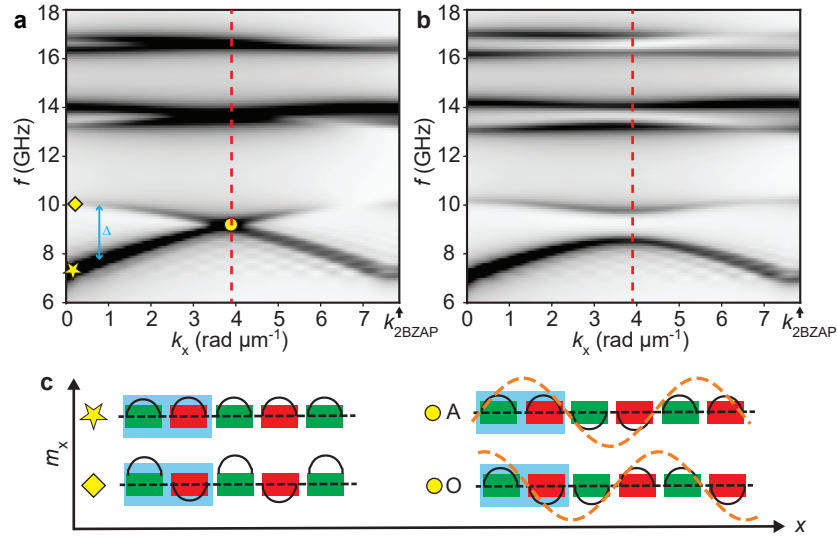


Figure 4.8 – Simulated band structure of a 1D MC with  $p = 400$  nm at **a** remanence and **b** at  $\mu_0 H = 8$  mT applied parallel to the stripe direction. **c** Sketch of the  $m_x$  component of the acoustic (yellow star) and optical (yellow diamond) mode at  $k = 0$ . Green and red rectangles symbolize the cross-section of stripes magnetized in  $+y$  and  $-y$  direction. The magnetic unit cell is marked blue. At  $B_{ZAP}$  (yellow circles) the wave length is  $4p$  (orange dashed line) and the acoustic (A) and optical (O) mode are indistinguishable if mode profiles of green and red stripes are degenerate.

#### 4.4 Reprogramming the band structure: Propagating spin waves in the antiferromagnetically ordered state

In the previous sections the influence of a single magnetic defect was addressed. In contrast, when the magnetization direction of stripes is periodically varied, the Bloch wave function is modified and a new band structure formed. J. Topp *et al.* [34] demonstrated in 2010 by AESWS measurements on a 1D MC consisting of Py nanostripes, that novel SW modes appeared, when neighboring stripes were switched from a parallel (P) to an antiparallel (AP) alignment. In the same year, S. Tacci *et al.* [166] evidenced by wave vector resolved BLS two different band structures for the P and AP state of a 1D MC with stripes of alternating width. Further experimental demonstrations with various types of MCs were published in the following years [46–48, 167, 168]. Programmable band structures are one of the main advantages of magnonic devices and are of great promise for variable microwave filters, which allow for adjustment of stop and transmission bands during operation. Other technologies, including surface acoustic wave filters, which represent today's industrial standard for analog RF filtering, lack this capability.

In most previous studies of reconfigurable 1D MCs based on AESWS [34, 45–47] a large CPW signal line width was used, exciting SWs with  $k \approx 0$ . SW absorption was detected directly at the exciting CPW. In R. Huber *et al.* [48] spin wave propagation between two CPWs was measured for a small wave vector well below the BZ boundary of the MC. In this section we address the

propagation of SWs in a reprogrammable 1D MC with either P or AP state. We measure SW propagation in a broad wave vector range covering the full BZ of the 1D MC for both P and AP state. We report on a band gap closing for short-waved SWs in the AP state, when zero magnetic bias field is applied.

Figure 4.8a and b show the simulated band structure of a 1D MC with  $p = 400$  nm in the AP state for 0 mT and 8 mT, respectively. The simulation parameters were kept identical to the previous section, where the P state was addressed (cf. Fig. 4.6a). In the AP state a magnetic unit cell is represented by a pair of oppositely magnetized stripes. Consequently the relevant lattice vector for Bloch waves is two times the physical lattice vector  $p$  and the Brillouin zone boundary in the AP state (BZAP) is half of the BZ boundary in the P state. Indeed, we observe in the simulated band structures that the modes are backfolded (mirrored) at  $k_{\text{BZAP}} = \frac{\pi}{2p}$  (marked by a red dashed line in Fig. 4.8a, b). Compared to the band structure in the P state a doubling of the modes is observed. This doubling is due to the occurrence of acoustic and optical modes [46]. In the acoustic mode  $m_x$  of neighboring stripes is in phase for  $k = 0$ , as sketched in Fig. 4.8c for the band  $q = 0$ . The acoustic modes have a similar dispersion as modes in the P state (Fig. 4.6a). For the optical mode the  $m_z$  component is in phase at  $k = 0$ , and consequently there is a phase shift of  $\pi$  between neighboring stripes in the  $m_x$  component. As  $m_x$  of neighboring stripes points against each other, the dipolar energy is increased and the optical branch starts at a higher frequency. We note that  $m_x$  at  $k = 0$  of the optical mode has the same phase profile as  $m_x$  at  $k = k_{\text{1BZ}}$  in the P state. Hence the optical mode at  $H = 0$  is similar in frequency to the P state branch at  $k = k_{\text{1BZ}}$ .

A special situation is given for  $H = 0$  at  $k = k_{\text{1BZAP}}$ , where the wavelength amounts to  $4p$  (orange dashed line in Fig. 4.8c). For identical stripes at  $H = 0$ , the effective field is degenerate for both magnetization directions. As illustrated in Fig. 4.8c (yellow circle) acoustic and optical mode are indistinguishable. Consequently, we find a crossing of acoustic and optical branches in the band structure (Fig. 4.8a). When a bias field is applied, this degeneracy is lifted, and a band gap opens at BZAP. We note that to best of our knowledge, the band crossing has not yet been experimentally reported. While in Refs. [34, 45–47] only SWs with  $k \approx 0$  were probed, wave vector resolved BLS studies [166–168] addressed MCs with two non-identical sub-lattices, which generated non-degenerate magnon states at  $k_{\text{BZAP}}$  already at  $H = 0$ .

We measured SW propagation in the P and AP state for two MCs, which were nominally identical to MC1, but equipped with differently sized CPWs. Sample MC1b (Fig. 4.9a) was fabricated with two CPWs of dimensions  $w_{\text{SL}} = w_{\text{GL}} = 2.0$   $\mu\text{m}$  and  $w_{\text{G}} = 1.7$   $\mu\text{m}$ . The center-to-center distance of CPW1 and CPW2 was 12  $\mu\text{m}$ . Sample MC1c (Fig. 4.9b) used CPWs with  $w_{\text{SL}} = w_{\text{GL}} = 0.24$   $\mu\text{m}$ ,  $w_{\text{G}} = 0.21$   $\mu\text{m}$  and center-to-center distance of 5  $\mu\text{m}$ . The two CPW widths allowed us to address different wave vector regimes. Using the script in SI C.1, we calculate  $k_1 = 0.8$   $\text{rad}\mu\text{m}^{-1}$  and  $k_{\text{max}} = 1.7$   $\text{rad}\mu\text{m}^{-1}$  for MC1b and  $k_1 = 6.1$   $\text{rad}\mu\text{m}^{-1}$  and  $k_{\text{max}} = 13.9$   $\text{rad}\mu\text{m}^{-1}$  for MC1c. I.e.  $k_{\text{max}}$  of MC1b was below  $k_{\text{BZAP}}$ , while for MC1c it extended beyond  $k_{\text{BZ}}$  and the whole 1.BZ was excited.

To magnetize the samples in the AP state, a demagnetization loop was used, in which the external field was oscillated between positive and negative values in  $y$ -direction. The amplitude of the magnetic field was reduced from  $|\mu_0 H = 30$  mT| to 0 mT in steps of 0.2 mT per full



#### 4.4. Reprogramming the band structure: Propagating spin waves in the antiferromagnetically ordered state

oscillation cycle. Figure 4.9c shows an MFM image of sample MC1c after the demagnetization protocol. Most of the neighboring stripes were found in the AP state, deviation from the AP order (yellow circle in Fig. 4.9c) was found only selectively.

Figure 4.9d, e shows  $\text{Mag}(\text{S21})$  of MC1b and MC1c measured after the sample was saturated at -90 mT and the field was stepwisely increased. In both cases a monotonous decrease of the  $q = 0$  mode (dark branch) is observed with increasing  $H$  until  $\mu_0 H_{\text{SW1}} = 6 \pm 1$  mT. In the field range up to  $H_{\text{SW1}}$  the samples are assumed in the P state. As discussed in Sec. 4.1, measured branches in  $\text{Mag}(\text{S21})$  showed an oscillatory signature due to interference of  $V_{\text{ind}}$  by SWs and

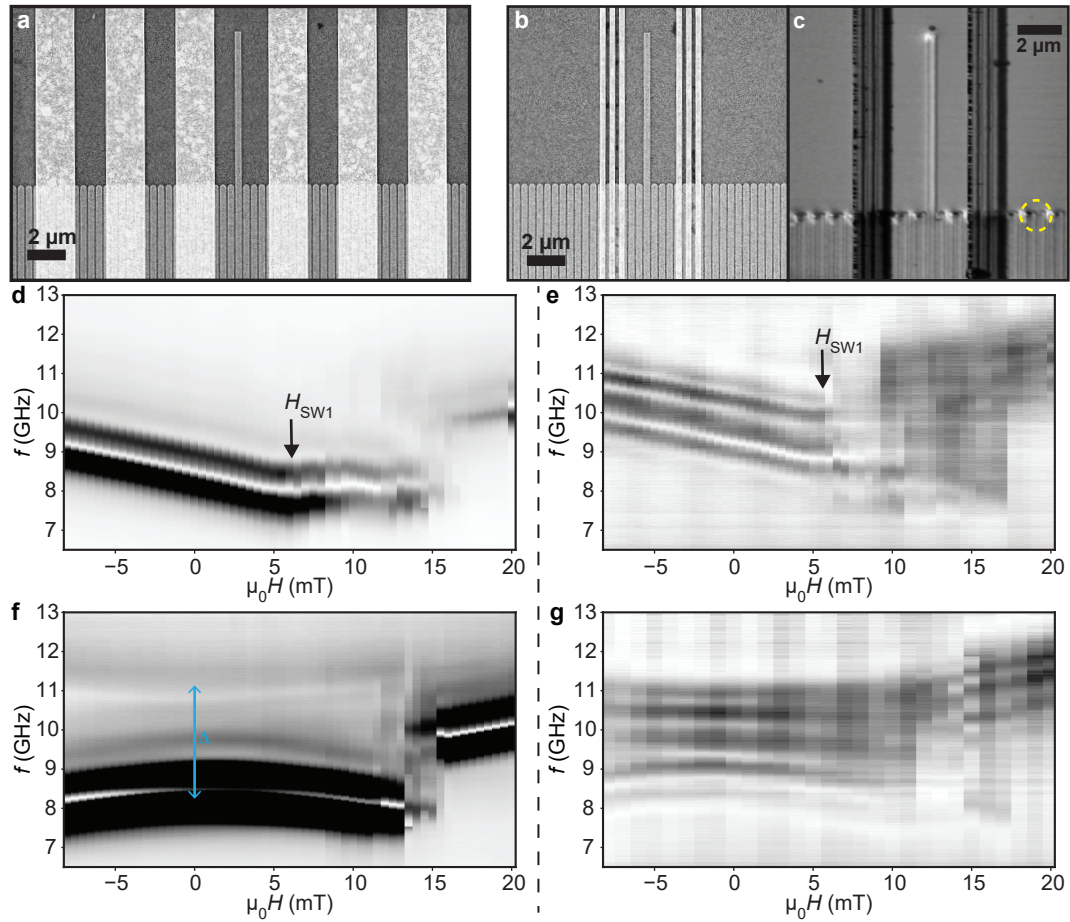


Figure 4.9 – SEM images of **a** MC1b and **b** MC1c with signal line widths of  $w_{\text{SL}} = 2.1 \mu\text{m}$  and  $w_{\text{SL}} = 0.24 \mu\text{m}$ , respectively. **c** MFM image of MC1c after a demagnetization protocol. The vast majority of stripes were found in the AP state. Local disorder was infrequent (yellow dashed circle). **d, e**  $\text{Mag}(\text{S21})$  of MC1b and MC1c measured for increasing  $H$  after saturation at -90 mT. Up to  $H_{\text{SW1}} \approx 6$  mT the branches monotonously decrease in frequency with increasing  $H$ . We attribute this behavior to an ordered magnetization in the P state. **f, g**  $\text{Mag}(\text{S21})$  for MC1b and MC1c after the demagnetization protocol. The measurement was started at -8 mT and  $H$  stepwisely increased. Between  $-8 \text{ mT} \leq \mu_0 H \leq 12 \text{ mT}$  acoustic and optical branches were observed. For MC1b (**f**) a band gap of  $\sim 3.1$  GHz was observed at  $H = 0$  (marked by blue arrow). For MC1c (**g**) only one branch is visible at 0 mT.

direct EM cross-talk between CPW1 and CPW2.

Figure 4.9f, g depicts  $\text{Mag}(\text{S21})$  of MC1b and MC1c after a demagnetization protocol was applied. The measurement was started at -8 mT and the field stepwisely increased. For MC1c we observe two branches attributed to the acoustic and optical mode. The branches are symmetric with respect to  $H = 0$  and the band gap  $\Delta$  increases with  $|H|$ . At zero field we find  $\Delta = 3.1$  GHz (marked by a blue arrow in Fig. 4.9f), evaluated at the peak frequencies of the acoustic and optical mode in  $\text{Mag}(\text{S11})$  (not shown), which we attribute to the  $k_1$  wave vector. We note that the peak frequencies were evaluated based on  $\text{Mag}(\text{S11})$ , as the oscillations in  $\text{Mag}(\text{S21})$  impeded a precise allocation. In the simulated band structure, we find  $\Delta = 2.3$  GHz for  $k_1 = 0.8 \text{ rad } \mu\text{m}^{-1}$  at  $H = 0$  (blue arrow in Fig. 4.8). We point out that the measured amplitude of the optical mode in  $\text{Mag}(\text{S21})$  was much weaker than for the acoustic one. This can be explained by a low group velocity of the optical mode for small wave vectors.

For MC1c (Fig.4.9g), we find a broad branch at  $H = 0$  without apparent band gap. For increasing  $|H|$  the mode divides slowly into two branches. The amplitudes in both branches are similar. We attribute the lack of a band gap at  $H = 0$  to a crossing of the acoustic and optical mode at  $k = k_{1\text{BZAP}}$ , as observed in the simulated band structure (Fig. 4.9f) and band structure calculations in Ref. [34].

In conclusion, we measured SW propagation in 1D MCs magnetized in the AP state. In agreement with earlier works we observed a new band structure with an acoustic and an optical mode for  $q = 0$ . For  $k_1 < k_{1\text{BZAP}}$  two separated modes were resolved at  $H = 0$  consistent with the previous works. The signal of the optical mode was weak, which we attribute to a small  $v_g$ . When SWs were excited in a broad wave vector regime with  $k$  going beyond  $k_{1\text{BZAP}}$ , we observed a broad continuous branch without band gap at  $H = 0$ , which agrees with the band structure calculations in Ref. [34]. Acoustic and optical branches were of similar intensity, which we attribute to a similar  $v_g$  of the states close to BZAP boundary.

## 5 Coupling microwaves to short-waved spin waves

Coupling of microwaves to short-waved spin waves is challenging due to the severe mismatch of wave vectors. Nevertheless, efficient coupling is required to utilize short-waved SWs for microwave technology. This Chapter presents two different approaches how such coupling can be realized. Section 5.1 reports on real-space measurements of nanoscale SWs excited by a magnonic grating coupler. The results were published in ACS Nano Letters [57] and are reproduced with the permission of the publisher. In Sec. 5.2 a magnetic coplanar waveguide (mCPW) is introduced. Short-waved SWs were achieved by means of wavelength conversion in the inhomogeneous magnetic field of the mCPW. Our finding was published in Nature Communications [59] and reproduced with the permission of the publisher.

### 5.1 Nanoimaging of Ultrashort Magnon Emission by Ferromagnetic Grating Couplers at GHz Frequencies

K. Baumgaertl, J. Gräfe, P. Che, A. Mucchietto, J. Förster, N. Träger, M. Bechtel, M. Weigand, G. Schütz and D. Grundler  
Nano Letters **20**, 7281–7286 (2020)  
doi: 10.1021/acs.nanolett.0c02645

*Reprinted with permission from Nano Letters. Copyright 2020 American Chemical Society. For uniformity the layout was reformatted and the references were integrated into the thesis' bibliography.*

#### Contribution

I contributed to the design and planning of the experiments, fabricated the samples and conducted AESWS characterization. STXM measurements were conducted in collaborative effort. I analyzed the data and wrote the draft of the manuscript.

### Abstract

On-chip signal processing at microwave frequencies is key for modern mobile communication. When one aims at small footprints, low power consumption, reprogrammable filters, and delay lines, magnons in low-damping ferrimagnets offer great promise. Ferromagnetic grating couplers have been reported to be specifically useful as microwave-to-magnon transducers. However, their interconversion efficiency is unknown and real-space measurements of the emitted magnon wavelengths have not yet been accomplished. Here, we image with subwavelength spatial resolution the magnon emission process into ferrimagnetic yttrium iron garnet (YIG) at frequencies up to 8 GHz. We evidence propagating magnons of a wavelength of 98.7 nm underneath the gratings, which enter the YIG without a phase jump. Counterintuitively, the magnons exhibit an even increased amplitude in YIG, which is unexpected and due to a further wavelength conversion process. Our results are of key importance for magnonic components, which efficiently control microwave signals on the nanoscale.

### Main Part

Magnons allow for information transfer via angular momentum propagation instead of moving electric charges. Hence, magnons attract attention for future low-power computing applications [7, 17, 18, 169], circumventing the Joule heating which limits the clock-frequency of conventional electronics. In ferro- and ferrimagnetic materials magnons occur in the frequency regime from GHz to THz, which becomes more and more important for high-speed wireless data transfer. The wavelength of magnons is several orders of magnitude smaller than that of electromagnetic waves of the same frequency. Going beyond surface acoustic waves (SAWs), magnons allow one to significantly shrink microwave components and perform analog signal processing like bandpass-filtering [30, 170, 171], multiplexing [172, 173], phase-shifting [50, 139, 174, 175], directional coupling [176], and buffering [177] on the nanoscale instead of micrometer scale. Unlike SAWs, the resonance frequency of magnons is easily tunable by the application of magnetic field or by a reprogrammed magnetic configuration [1]. Consequently, to harness the full potential of magnons, one needs an efficient microwave-to-magnon transducer that supports many frequency bands as well as a significant wavelength down-conversion. Coplanar waveguides (CPWs) on top of magnetic thin films excite magnons over a broad frequency range [178]. However, their wavelengths are about twice the width of the CPW signal line [52], restricting the accessible wave vector regime in both thin yttrium iron garnet (YIG) films [55] and along nanosized YIG magnon conduits [179]. To overcome this restriction and excite spin waves (SWs) with a wavelength  $\lambda$  much smaller than the size of the CPW is the subject of intense research [59]. Recently ultrashort SWs (magnons) were emitted by nanoscale spin textures which were irradiated by microwave fields [180–183]. Such spin textures required metallic multilayer stacks which are generally prone to large magnon damping however. Magnonic grating couplers (GCs) are particularly promising as they can both be integrated on low-damping magnetic media like yttrium iron garnet (YIG) [14] and cover large surface areas to obtain sufficient microwave coupling. For a GC, periodic lattices of nanomagnets with a lattice constant  $a$  are introduced between CPW and magnonic circuit (Fig. 5.1a, b, c). All-electrical spin wave spectroscopy (AESWS) showed additional high frequency magnon modes when a GC was present [5, 54–56], but their wavelengths and amplitudes were not quantified due to technical restrictions.

In this work we report real-space measurements of short-wave magnons in thin YIG emitted by GCs consisting of arrays of nanostripes (Fig. 5.1). Using time-resolved scanning transmission X-ray microscopy (TR-STXM) [184–186] we measure their wavelengths, amplitudes and phases at different GHz frequencies. Our data evidence that magnons are of ultrashort wavelength and propagate underneath the gratings. This observation is in contrast to ref. [56] where it was argued that GC modes were

## 5.1. Nanoimaging of Ultrashort Magnon Emission by Ferromagnetic Grating Couplers at GHz Frequencies

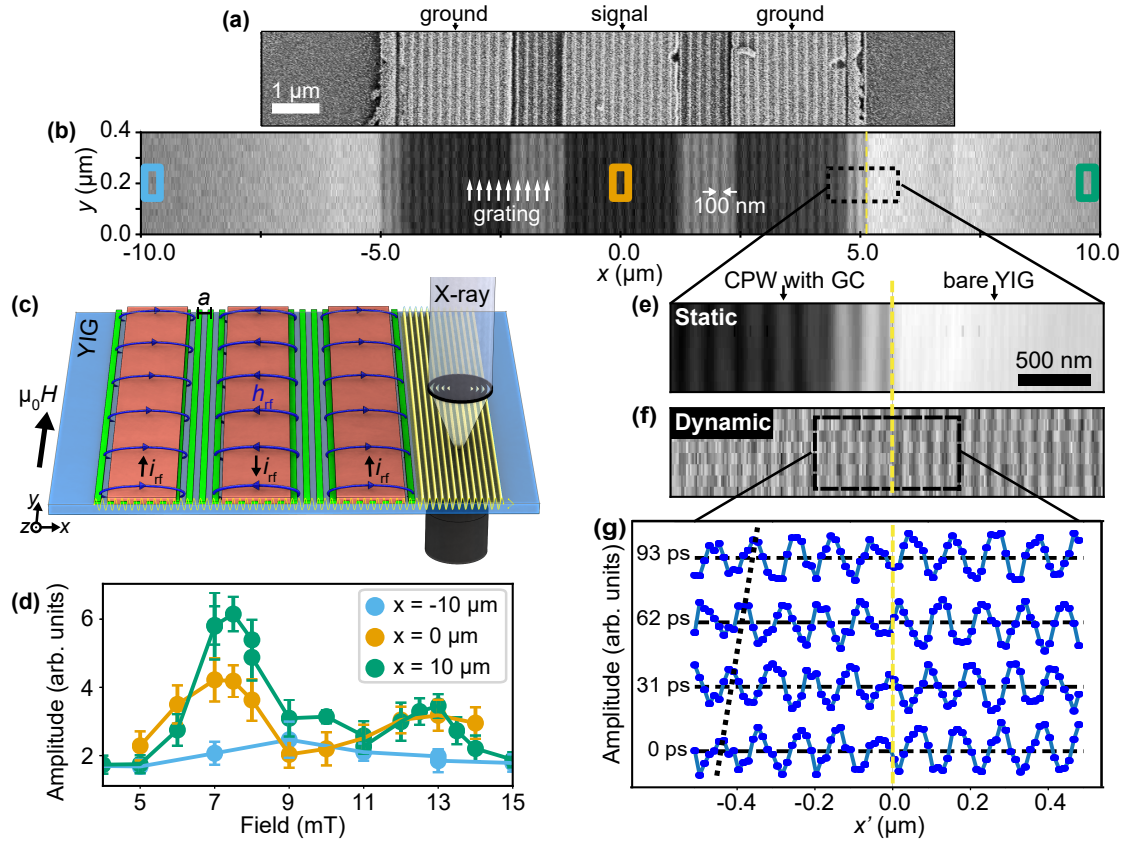


**Figure 5.1 – Real space imaging of a grating coupler mode.** (a) SEM and (b) static X-ray transmission image of sample 1a. Bright stripes in (a) represent the Py grating. Light gray regions in (b) on the left and right (high transmission) correspond to the bare YIG. The Py grating underneath the CPW creates locally dark stripes. (c) Sketch of the experimental configuration. (d) Field-dependent magnon amplitudes for 8.07 GHz measured at three different  $x$  coordinates as indicated in (b). For  $x = 0 \mu\text{m}$  (orange) and  $10 \mu\text{m}$  (green) two maxima at 7.5 mT and at 13 mT are observed matching magnons with wave vectors  $2G + k_1$  and  $2G - k_1$ . The reduced signal strength detected at  $x = -10 \mu\text{m}$  (blue) is attributed to nonreciprocity. At 7.5 mT (13 mT) the wavelength underneath the GC amounted to 98.7 nm (101.2 nm) and in the bare YIG to  $\lambda = 104.0$  nm (104.5 nm). (e) Static and (f) dynamic contrast as well as (g) time evolution of the dynamic magnetization plotted as line profiles at the interface between GC and bare YIG at 7.5 mT. We observe plane-wave magnon emission with propagating wave fronts (indicated by black dashed line) both underneath the GC and in the bare YIG.

standing waves. At the boundary between the GC and bare YIG we discover a frequency-dependent wavelength conversion, which was not yet anticipated. This discovery is highly relevant for applications where a specific wavelength in a magnonic waveguide is required. Although wavelength conversion implied a change of wave impedance at the interface, strikingly magnons were emitted from the GC into the bare YIG without a noticeable phase shift or backscattering (amplitude reduction). For some modes their amplitudes clearly increased in the bare YIG, consistent with energy conservation following the additional wavelength conversion effect. Our experimental findings are of utmost relevance for

the optimization of microwave-to-magnon transducers, which enable drastic miniaturization and enhanced functionality of microwave components.

We prepared nominally identical GC samples for STXM (sample1a, sample1b) and AESWS (sample2) measurements (Supporting Information (SI) Methods A.2.1). Figure 5.1a shows a scanning electron microscope (SEM) image of sample1a. Figure 5.1b displays its corresponding X-ray transmission image. The bare YIG film, the CPW and the GC can be distinguished due to different X-ray transmission signals. Figure 5.1c shows a sketch of the STXM experiment. The GC consisted of 20 nm thick Py ( $\text{Ni}_{81}\text{Fe}_{19}$ ) stripes fabricated directly on a 100 nm thick YIG film. The Py stripes had a width of  $w_{\text{Py}} = 100$  nm and a length of 25  $\mu\text{m}$  and were arranged with a lattice constant of  $a = 200$  nm in periodic arrays with a total width of  $w_{\text{GC}} = 10$   $\mu\text{m}$ . CPWs out of 5 nm thick Ti and 110 nm thick Cu were patterned collinearly aligned on top of the Py grating. The width of the signal and ground lines of the CPW amounted to 2.1  $\mu\text{m}$  and the gap width to 1.4  $\mu\text{m}$ , resulting in a total width of 9.1  $\mu\text{m}$ , which was slightly smaller than  $w_{\text{GC}}$ . Fourier analysis of the simulated magnetic field profile  $\tilde{h}_{\text{rf}}$  generated around the CPW by an applied microwave current  $i_{\text{rf}}$  (Figure 5.1c) showed a major peak for the transferred wave vector at  $k_1 = 0.85 \text{ rad } \mu\text{m}^{-1}$  (SI Figure A.2). We applied a continuous microwave signal at 8.07 GHz and varied the magnetic field pointing parallel to the CPW in a stepwise manner. Using TR-STXM with circular dichroism contrast, we measured phase-coherently the dynamic out-of-plane magnetic component of the YIG film  $\tilde{m}_z(x, y, t)$  (SI Methods A.2.2). We probed three different measurement windows (300 nm  $\times$  100 nm) placed at  $x = -10$   $\mu\text{m}$  (left of the CPW),  $x = 10$   $\mu\text{m}$  (right of the CPW), and  $x = 0$   $\mu\text{m}$  below the signal line as indicated in Figure 5.1b. In Figure 5.1d extracted amplitudes of  $\tilde{m}$  are shown (SI Methods A.2.3). For the windows at  $x = 0$  and 10  $\mu\text{m}$  a clear SW signal with two maxima at 7.5 mT and at 13 mT is apparent. We attribute the two peaks to magnons excited with a wave vector of  $2G + k_1$  and  $2G - k_1$ , respectively, as further substantiated below.  $G = 2\pi/a$  denotes the reciprocal lattice vector of the grating. At the window left of the CPW ( $x = -10$   $\mu\text{m}$ ) the recorded amplitudes are close to the noise floor. Consequently, there is a strong nonreciprocity of SW emission, favoring the  $+x$  direction. Large nonreciprocity of GC modes was recently modeled by Chen et al. [187] and was attributed to the dipolar coupling between a ferromagnetic grating and the YIG film. To study the SW emission process in detail, we focus on the interface region between the GC and bare YIG in the direction of large emission as depicted in Figure 5.1e. For clarity we introduce the coordinate  $x'$  for which  $x' = 0$   $\mu\text{m}$  resides at the right outer edge of the GC indicated by a yellow dashed line in Fig. 5.1b, e. At  $\mu_0 H = 7.5$  mT we find plane-wave SWs propagating in the  $+x$ -direction (Fig. 5.1f). Sinusoidal fitting of  $\tilde{m}_z$  over 10 periods provides a wavelength of  $\lambda = (98.7 \pm 0.4)$  nm in the region covered by the grating and of  $(104.0 \pm 0.2)$  nm in the bare YIG. Analogously for  $\mu_0 H = 13$  mT, we find  $\lambda = (101.2 \pm 0.1)$  nm and  $\lambda = (104.5 \pm 0.1)$  nm, respectively (not shown). We note that the wavelength found underneath the grating for  $\mu_0 H = 7.5$  mT and 13 mT, which are the two field values where maximum SW emission was found in Figure 5.1d, agree very well with the values  $2\pi/(2G + k_1) = 98.7$  nm and  $2\pi/(2G - k_1) = 101.4$  nm expected by theory [54]. Thus our measurements agree with the Bloch theorem for coherent waves applied to the periodic lattice of the GC. Propagating into the bare YIG, the SWs undergo a slight wavelength conversion process. In Figure 5.1g the time evolution of the dynamic magnetization plotted as line profiles at the boundary between GC and bare YIG is depicted. The absence of a phase jump at  $x' = 0$   $\mu\text{m}$  and the almost constant amplitude indicate a transmission coefficient of close to one from the grating into bare YIG. We observe a propagating wavefront (indicated by black dashed line) both underneath the GC and in the bare YIG. In the literature standing waves were assumed underneath the grating [56]. We do not confirm the assumption. We explain the propagating character underneath the GC by the nonreciprocal excitation and apparently vanishingly small back-reflection at the boundary. We note, that we still detected plane wave fronts at a measurement area located at  $x = 15$   $\mu\text{m}$ , i.e. 10  $\mu\text{m}$  away from the GC (SI Figure A.3). The magnons with  $\lambda \approx 99$  nm possess a wavelength which is 375000

## 5.1. Nanoimaging of Ultrashort Magnon Emission by Ferromagnetic Grating Couplers at GHz Frequencies

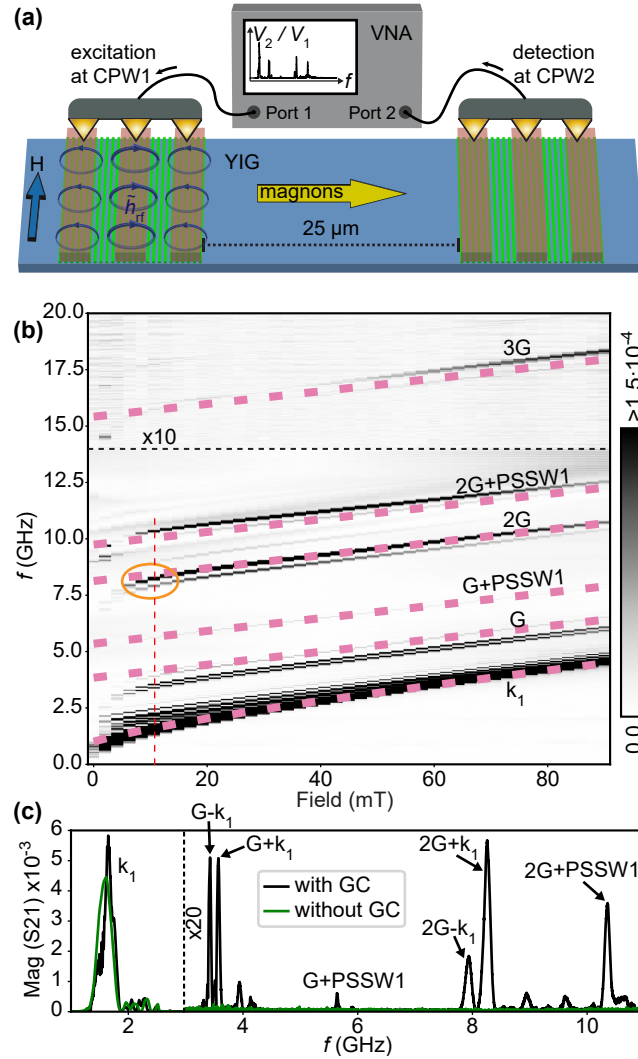


Figure 5.2 – **Magnetic grating-induced high-frequency magnon modes.** (a) Sketch of AESWS on sample2 where a VNA induced a local  $\tilde{h}_{\text{rf}}$  (dark blue arrows) generating ultrashort magnons via the GC effect. (b) Field-dependent transmission spectra  $\text{Mag}(S_{21})$  measured between CPW1 and CPW2. Several high-frequency magnon modes (dark color) are present which are not seen for bare CPWs without gratings. The field reduced in a stepwise manner from 90 mT. Signals above 14 GHz were multiplied by a factor 10 for better visibility. The circle indicates branches at 8.07 GHz which are consistent with the magnons displayed in Figure 5.1. (c) Individual spectra of sample2 (black line) and of a reference YIG sample without GCs (green line) taken at 11 mT [indicated by the dashed red line in (b)]. The signal above 3 GHz was multiplied by a factor of 20 for better visibility. The GC of sample2 induces a much richer spectrum (black) compared to the bare CPW (green) on YIG.

times smaller than the one of the free-space electromagnetic wave at 8.07 GHz and almost 3 orders of magnitude smaller than  $2\pi/k_1$  given by the geometrical size of the CPW.

To allow for comparison of our GCs with existing literature data and to show the correspondence

between microscopic STXM data and conventional AESWS, we studied SW propagation all-electrically using a nominally identical sample featuring two CPWs as sketched in Fig. 5.2a. The center-to-center distance between CPW1 and CPW2 in sample2 amounted to  $35\text{ }\mu\text{m}$ , i.e., there was a  $25\text{ }\mu\text{m}$  wide region of bare YIG between CPW1 and CPW2. The two CPWs were connected to the ports of a vector network analyzer (VNA) and scattering parameters were measured (SI Methods A.2.4). Figure 5.2 shows the magnitude of the forward transmission coefficient  $S_{21}$  that was measured between CPW1 and CPW2 as a function of magnetic field applied in parallel to the CPW. For this configuration the observed signal originated from magnons which were excited at CPW1, propagated in the bare YIG, and were detected at CPW2. In the spectra several high-frequency modes were present, which were not observable with bare CPWs [188] (cf. SI Figure A.4). We highlight two closely spaced branches in Figure 5.2b which cross  $8.07\text{ GHz}$  near  $10\text{ mT}$  (orange encircled). These branches reflect  $2G \pm k_1$  modes discussed in the previous section. To substantiate the allocation we show the calculated (SI Methods A.2.5) field dependence of a mode with  $k = 2G$  (broken line) in Fig. 5.2b. Using the formalism of [86] modes  $G$  and  $3G$  can be identified in the spectrum as well (further purple dashed lines in Fig. 5.2b). The  $3G$  mode corresponds to SWs with a wavelength of  $\lambda = 67\text{ nm}$  underneath the GC. Further observed GC mode branches agree well with the formalism [86] when we assume an additional quantization along the film thickness. The modes of  $G+\text{PSSW1}$  and  $2G+\text{PSSW1}$  are especially apparent, where PSSW1 denotes to the first perpendicular standing spin wave (PSSW) of the YIG film. We attribute the excitation of PSSW1 modes to direct exchange coupling of the Py grating to the YIG film. Pronounced excitations of PSSWs were recently reported for heterostructures consisting of a ferromagnetic layer and a YIG film [189–191]. To compare transmission amplitudes, we show in Figure 5.2c  $\text{Mag}(S_{21})$  obtained on sample2 (black line) at  $11\text{ mT}$  and  $\text{Mag}(S_{21})$  of a reference sample (green line) with CPWs without GCs (details and field-dependent spectra are displayed in SI Figure A.4). For sample2,  $1G$  and  $2G$  peaks are clearly visible. For the reference sample without GCs we did not resolve a high-frequency mode above  $3\text{ GHz}$  at  $11\text{ mT}$ .

In the following we discuss the observed wavelength conversion for different excitation frequencies at the GC/YIG interface. Figure 5.3 shows a static X-ray transmission image and corresponding snapshots of the dynamic magnetization when a microwave frequency of  $3.43\text{ GHz}$  was applied to the CPW. Peaks in emission were observed at  $8\text{ mT}$  and  $10\text{ mT}$ . By analyzing the wavelength in the region underneath the GC, the two excitation peaks can be attributed to the wave vectors  $G + k_1$  and  $G - k_1$  with a wavelength of about  $200\text{ nm}$ . Surprisingly, the wavelength of the magnons transmitted with high efficiency into the bare YIG amounts to about  $250\text{ nm}$ , i.e., it is increased by  $25\%$ . A similar increase was observed with a second sample (SI Figure A.5) as well as for the opposite field direction measured at a larger field magnitude and frequency (SI Figure A.6). We find that the conversion is more pronounced at  $G1$  than at  $G2$ . We conclude that the effect is dipolar in nature. We speculate that the Py grating decreases the dynamic demagnetization field in the underlying YIG in the out-of-plane direction, shifting the dispersion of Damon–Eshbach (DE) modes to lower frequencies.

We further analyze the amplitude change of  $1G$  magnons crossing the interface between the GC and bare YIG. Figure 5.3d shows line profiles of the signal amplitudes for seven time slices during one period at  $3.43\text{ GHz}$  and  $10\text{ mT}$  averaged along  $y$ -direction in the  $1\text{ }\mu\text{m}$  wide region indicated by a blue-dashed line in Fig. 5.3b. Sinusoidal fitting of  $\tilde{m}_z$  in the region of the GC and the bare YIG (solid orange and green lines, respectively, in Fig. 5.3d) shows that the wavelength expands from  $(209 \pm 5)\text{ nm}$  to  $(276 \pm 3)\text{ nm}$  as discussed above. We extrapolate both fits into the direct transition region (dashed lines in Fig. 5.3d). It is apparent that the change in wavelength occurs on a small length scale of about  $100\text{ nm}$ . In Fig. 5.3e we depict the time-dependent amplitudes of  $\tilde{m}_z$  in both regions extracted from the fits for each time slice. Intriguingly, the amplitude in the bare YIG (green symbols) is larger than underneath the GC (yellow symbols) for all times sampled. The ratio of the average amplitudes in the respective regions



## 5.1. Nanoimaging of Ultrashort Magnon Emission by Ferromagnetic Grating Couplers at GHz Frequencies

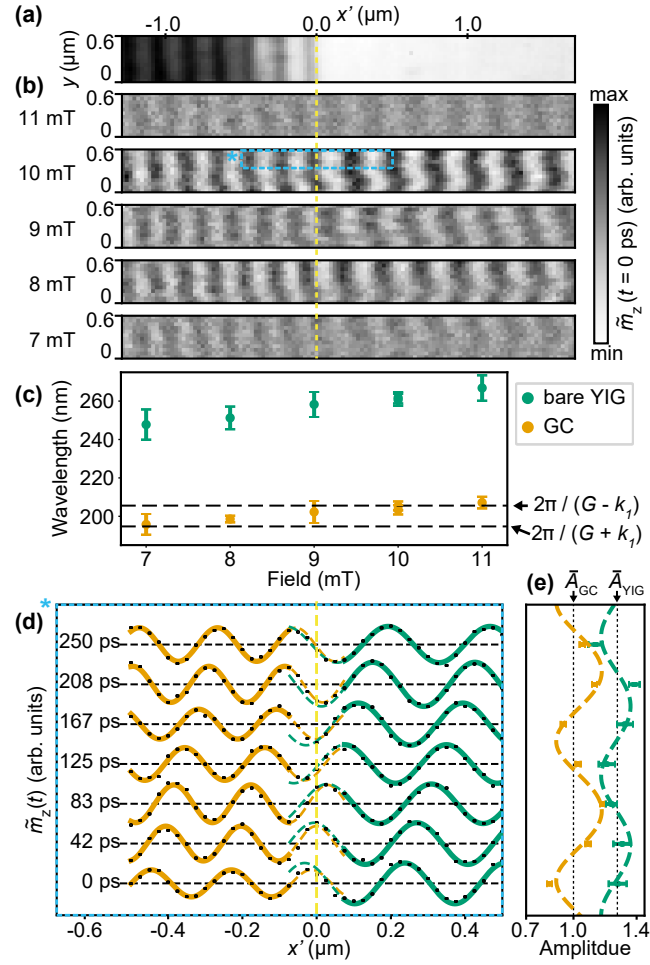


Figure 5.3 – **Wavelengths and amplitudes conversion observed for the 1G mode.** (a) Static and (b) dynamic X-ray transmission images at 3.43 GHz taken at the interface (yellow dashed line) between the GC region (left) and bare YIG (right) for decreasing magnetic field. (c) Wavelengths extracted underneath the grating (orange) and in the bare YIG regions (green). (d) Local amplitudes  $\tilde{m}_z$  (black dots) evaluated at 3.43 GHz and 10 mT in the region marked by the blue-dashed line in (b). We display different time slices. The signal is fitted with a sinusoidal time dependence for the region of the GC (solid orange line) and bare YIG (solid green line) separately. The dashed lines extrapolate the respective fits. (e) Amplitudes of the fitting functions indicate larger signals in the bare YIG (green dots) than in the GC (orange dots). The orange (green) dashed line shows a fit of the time-dependent amplitudes considering a partially standing wave in the GC (bare YIG).

amounts to  $\bar{A}_{YIG}/\bar{A}_{GC} = 1.28 \pm 0.04$ . As the signal is normalized to the absolute photon flux at any given position, the larger magnon amplitude in YIG is not due to a reduced X-ray absorption outside the gratings. At first sight, the increased amplitude of the wave emitted into YIG is counterintuitive and might indicate a transmission coefficient across the boundary of more than one. A more detailed analysis shows however, that the change in amplitude can be attributed to energy flux conservation in a dispersive medium. The energy transported by a wave is proportional to the product of the square of the oscillation amplitude  $A^2$  and the group velocity  $v_g$ . Using the formalism of ref. [86] and considering

the different wavelengths in the GC and YIG, we find  $v_{g,GC}/v_{g,YIG} = 1.38$ , i.e., the group velocity is larger underneath the GC compared to bare YIG. Assuming energy conservation, the ratio of the average amplitudes should read  $A_{YIG}/A_{GC} = \sqrt{v_{g,GC}/v_{g,YIG}} = 1.18$ . Consequently an increased amplitude is indeed expected for the bare YIG. The measured ratio is even larger. We note that  $v_{g,GC}$  was calculated from the dispersion relation of bare YIG [86] and might be underestimated. Increased group velocities were recently reported by An *et al.* for Py/YIG bilayer systems [191].

In Fig. 5.3d the propagating character of wave fronts is prominent in the region of the GC similar to the 2G mode shown in Fig. 5.1g. Still, a small oscillation of  $\tilde{m}_z$  amplitudes for different time slices is visible in Fig. 5.3e (orange symbols). This oscillation in the GC region can be consistently modeled by assuming partially standing waves following the formula  $\tilde{A}(t) = A\sqrt{1 + \Gamma^2} + 2\Gamma \cos(2\omega t)$ , where  $\Gamma$  takes into account the relative amplitude of a counter-propagating wave in the  $-x$  direction [192]. By fitting (dashed line Fig. 5.3e) we obtain a small value  $\Gamma = 0.14 \pm 0.03$ . The origin of a wave propagating in the  $-x$  direction can either be due to the excitation of  $-2G$  in the GC or some weak back-reflection at the interface. The amplitudes detected in bare YIG (green symbols in Fig. 5.3) also vary slightly with time ( $\Gamma = 0.07 \pm 0.02$ ). The tiny variation could indicate that the magnons in YIG experience some reflection at a position remote from the CPW. We speculate that the focused ion beam etching process for the  $50 \mu\text{m} \times 50 \mu\text{m}$  large X-ray transmission window has caused a small step in the YIG thickness from the backside. Assuming a concomitant change in the spin-wave dispersion relation, one could explain weak backscattering.

To conclude, enhanced magnon emission was found when the wave vector underneath the grating coupler matched the reciprocal lattice vector  $G$  or a multiple of it. This was clear evidence of the magnonic grating coupler effect, which had not yet been measured directly. Further, we reported a wavelength conversion when magnons were emitted from the GC. At 2G the wavelength  $\lambda$  expanded by about 5%. This was not anticipated by previous AESWS measurements. Our finding needs to be considered if a specific  $\lambda$  is required. For 1G we evidenced a clearly increased amplitude when a magnon entered bare YIG. Here, the SW group velocity decreased in the bare YIG and its amplitude increased to keep the energy flux constant. This effect might be purposefully employed to induce large amplitudes for read-out by slowing down SWs at specific locations of a magnonic circuit. Encouragingly, our data suggest that magnons efficiently couple out from the GC without significant back-reflection at the boundary to 100 nm thick YIG. Such YIG is commercially available on the wafer scale. At the same time, the GC modes show a huge nonreciprocity, i.e. the energy flows only in one direction (depending on field direction). The nonreciprocity is preferred for transferring a signal between an emitter and a specific receiver. In contrast, a regular SAW device is reciprocal, which leads to a reduction of transmitted power by half, if no special reflectors are used. Combined with the small damping loss of high-quality YIG, we speculate that GCs can be used as multipass high-frequency filters. While SAW filters work with interdigital transducers, where the impedance is optimized for a specific frequency only, magnonic GCs with CPWs can be applied at multiple frequency bands relevant for future telecommunication.

### Acknowledgments

The authors thank U. Eigenthaler and T. Meisner for their help with sample fabrication. We acknowledge the financial support by the Swiss National Science Foundation (SNSF), via grant numbers 163016 and 171003 (sinergia project Nanoskymionics), and by the Federal Ministry of Education and Research of Germany in the framework of DynaMAX (project number 05K18EYA). Measurements were conducted at the Maxymus endstation at BESSY2, HZB, Berlin, Germany. The authors thank HZB for the allocation of synchrotron radiation beamtime.

## 5.2. Efficient wavelength conversion of exchange magnons below 100 nm by magnetic coplanar waveguides

---

### Supporting Information

The Supporting Information is available free of charge at

<https://pubs.acs.org/doi/10.1021/acs.nanolett.0c02645>.

Methods; Fourier transform of the spatial profile of the  $x$ -component of the exciting Oersted fields of the CPW; Snapshot of propagating magnons at  $x = 15 \mu\text{m}$  and 8.07 GHz; Spin-wave spectrum of a reference sample without grating couplers; Wavelength conversion at 3.43 GHz for sample1b; Wavelength conversion of G1 mode for -25 mT.

### Author contributions

D.G., K.B., J.G., and G.S. designed and planned the experiments. K.B. fabricated the samples and conducted AESWS characterization. J.G. prepared the samples for STXM measurements. K.B., J.G., P.C., A.M., J.E., N.T., M.B., and M.W. conducted the STXM measurements. K.B. and D.G. analyzed the data and wrote the manuscript. All authors commented on the manuscript.

## 5.2 Efficient wavelength conversion of exchange magnons below 100 nm by magnetic coplanar waveguides

P. Che\*, K. Baumgaertl\*, A. Kúkol'ová, C. Dubs and D. Grundler

\*equal contributions

Nature Communications **11**, 1445 (2020)

doi: 10.1038/s41467-020-15265-1

*Material from: Che, P., Baumgaertl, K., Kúkol'ová, A. et al. Efficient wavelength conversion of exchange magnons below 100 nm by magnetic coplanar waveguides. Nat. Commun. 11, 1445 (2020). This article is licensed under Creative Commons Attribution 4.0. For uniformity the layout was reformatted and the references were integrated into the thesis' bibliography.*

### Contribution

I contributed to the design of the mCPWs and planning of the experiments, conducted the BLS measurements and micromagnetic simulations. I contributed to the analyzing of the data and wrote the parts of the manuscript draft concerning BLS and simulation results.

### Abstract

Exchange magnons are essential for unprecedented miniaturization of GHz electronics and magnon-based logic. However, their efficient excitation via microwave fields is still a challenge. Current methods including nanocontacts and grating couplers require advanced nanofabrication tools which limit the broad usage. Here we report efficient emission and detection of exchange magnons using micron-sized coplanar waveguides (CPWs) into which we integrated ferromagnetic (m) layers. We excited magnons in a broad frequency band with wavelengths  $\lambda$  down to 100 nm propagating over macroscopic distances in thin yttrium iron garnet. Applying time- and spatially resolved Brillouin light scattering as well as micromagnetic simulations we evidence a significant wavelength conversion process near mCPWs via tunable inhomogeneous fields. We show how optimized mCPWs can form microwave-to-magnon

transducers providing phase-coherent exchange magnons with  $\lambda$  of 37 nm. Without any nanofabrication they allow one to harvest the advantages of nanomagnonics by antenna designs exploited in conventional microwave circuits.

### Introduction

Collective spin excitations have attracted growing attention in view of low-power consuming information technologies that process data without moving charges [6, 14]. Here, exchange magnons with short wavelengths  $\lambda$  and correspondingly large wavevectors  $k = 2\pi/\lambda$  are of special interest in the applied sciences when aiming at miniaturization of magnon-based logic and memory devices [7, 60]. However, most of the experimental work on magnon-based computing and signal transmission has been conducted in the long-wavelength regime where the spin waves are dominated by dipolar interaction [2, 17, 140, 193–195]. In the technologically relevant frequency regime from a few to tens of GHz the on-chip excitation and detection of short-wave magnons are still challenging. The lack of efficient transducers is also detrimental in the fundamental sciences when experimentally exploring magnon scattering and band structures in non-collinear spin textures such as skyrmion lattices [196, 197]. Coplanar waveguides (CPWs) with lateral feature sizes down to 125 nm have not yet been sufficient for efficient emission of short-wave magnons [53, 185, 188]. Instead parametric pumping in the non-linear regime has been utilized to obtain exchange magnons with  $k > 20 \text{ rad } \mu\text{m}^{-1}$  [198–200]. Concerning emission of such magnons in the linear regime, non-uniform spin textures [180–182, 201], magnetic interfaces [150, 202], and the magnonic grating coupler effect [5, 54, 55] have been explored. Magnons with  $\lambda \approx 50 \text{ nm}$  ( $k \approx 120 \text{ rad } \mu\text{m}^{-1}$ ) were induced in thin yttrium iron garnet (YIG) by means of a grating coupler consisting of a periodic lattice of parallel nanostripes [56]. Here, the nanostripes were prepared by nanolithography and the gap width  $g$  between them amounted to 100 nm. Such challenging nanofabrication impedes broad application and is an obstacle to progress in this field. The conversion factor  $\eta = g/\lambda$  between critical lateral dimension  $g$  and wavelength amounted to 2. Larger factors  $\eta$  and the excitation of exchange magnons without nanofabrication are of high relevance for advancing magnonics both as a research field and possible information technology. A non-uniform effective field in a ferromagnetic film was suggested to reduce magnon wavelengths via a conversion process [58, 203–205]. However, the experimental observation of exchange magnons with  $k > 20 \text{ rad } \mu\text{m}^{-1}$  has not yet been reported.

In this work, we introduce magnetic coplanar waveguides (mCPWs) consisting of Fe|Ti|Au with micrometer-scale lateral dimensions and report excitation and detection of exchange magnons (Fig. 5.4a and b). Using not yet optimized mCPWs we extracted  $k = 62.4 \text{ rad } \mu\text{m}^{-1}$  ( $\lambda = 100 \pm 2 \text{ nm}$ ) for emitted magnons at 7.02 GHz. The effective field in YIG underneath the mCPWs was modified by the stray field of the polycrystalline Fe layer (Fig. 5.4c) and induced wavelength conversion giving rise to on-chip excitation and detection of exchange-dominated magnons (Fig. 5.4d). Avoiding challenging electron beam lithography on insulating YIG and utilizing photolithography for CPWs with a gap width  $g$  of  $1.4 \mu\text{m}$  we realized a large conversion factor of  $\eta = 14$ . This value goes beyond previously reported methods based on, e.g., the magnonic grating coupler [54] or a nanocontact [206]. Preparing the mCPWs on YIG, we evidence emission, detection, and the transport of phase-coherent exchange magnons over macroscopic distances via both electrical and optical methods. We outline how to optimize mCPWs and obtain  $k \approx 170 \text{ rad } \mu\text{m}^{-1}$ .

## 5.2. Efficient wavelength conversion of exchange magnons below 100 nm by magnetic coplanar waveguides

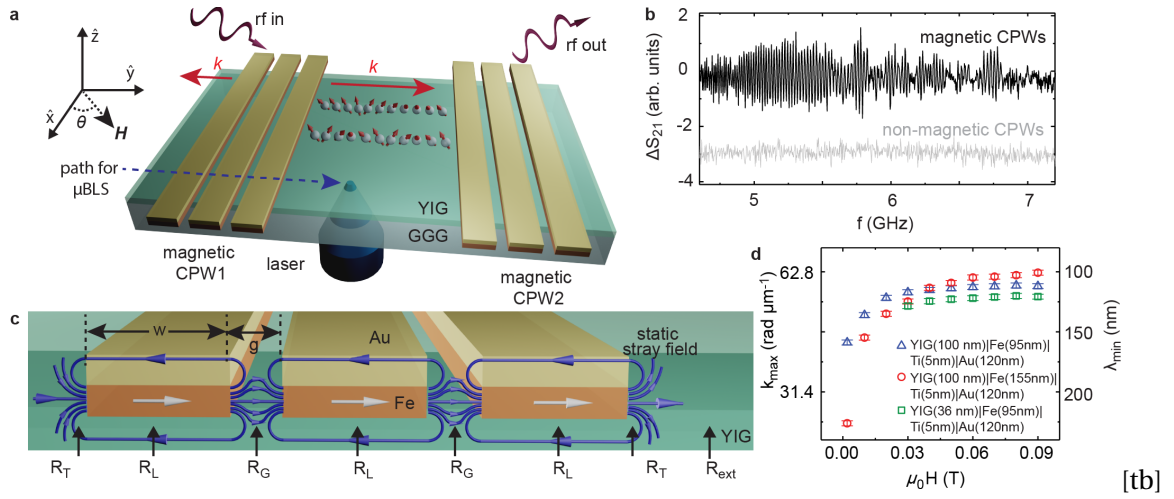


Figure 5.4 – **Schematic diagram and high frequency modes emitted by mCPWs.** **a** Sketch of the experiment showing mCPWs on YIG and micro-focus BLS performed through the GGG substrate. The red arrows indicate propagation directions of magnons. The blue arrow indicates the path along which local BLS spectra were obtained. **b**  $\Delta S_{21}$  reflecting propagating magnons (oscillatory signal) detected electrically at 0.09 T ( $\theta = 88$  deg) with mCPWs (black) and non-magnetic conventional CPWs (grey). **c** Schematic diagram of the stray field generated by Fe layers around an mCPW. White arrows display the magnetization component along the field applied at  $\theta = 90$  deg. Blue lines with arrows illustrate the stray field of Fe. We define regions (R) underneath ground and signal lines (L), in gaps (G) and a transition (T) region between the mCPW and the bare YIG which is denoted by region  $R_{ext}$  further away from the mCPW. **d** Maximum wavevectors  $k_{max}$  (and corresponding minimum wavelengths  $\lambda_{min}$ ) extracted from  $\Delta S_{21}$  data taken on three samples (symbols are labelled in the inset) by considering the relevant dispersion relations in bare YIG given by Kalinikos and Slavin [86]. The error bar refers to the frequency resolution of the VNA. For each sample the field was reduced from  $\mu_0 H = 0.09$  T to 0.002 T.

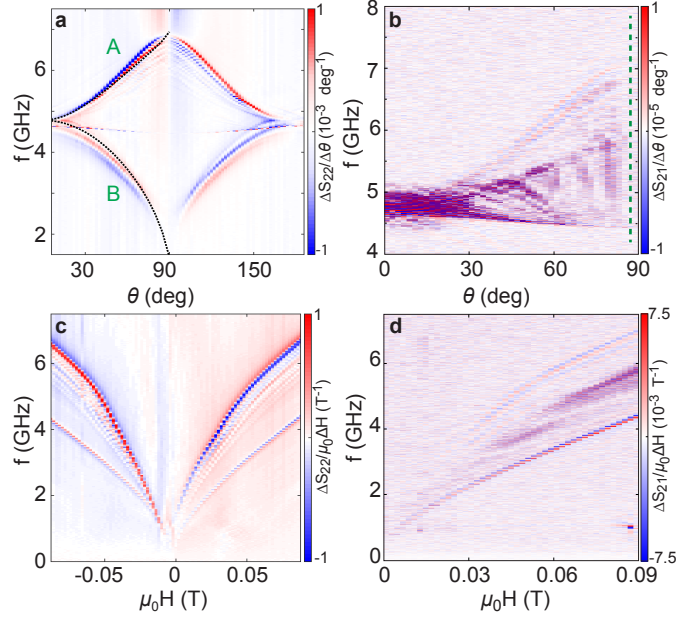


Figure 5.5 – **Spectra of magnons emitted by mCPWs for fields applied under different angles  $\theta$ .** **a** Reflection and **b** transmission spectra taken for a field of 0.09 T where  $\theta$  was varied in a step-wise manner. The data were obtained on thin YIG with mCPWs consisting of Fe(155 nm)|Ti(5nm)|Au(120nm) (sample1). Black dotted lines in **a** are resonance frequencies calculated by considering simulated effective fields  $B_{\text{eff}}$  in Kittel's formula [64]. They reflect  $B_{\text{eff}}$  taken at the central positions in regions  $R_G$  (top curve A) and  $R_L$  (bottom curve B). The dashed vertical line in **b** indicates the angle at which the top line spectrum of Fig. 5.4b is extracted. **c** Reflection and **d** transmission spectra of sample1 as a function of field applied at  $\theta = 90$  deg. The color scales are defined in the legends. The contrast was optimized to highlight the broadband magnon excitation. For datasets in **c** and **d** the field was reduced from 0.09 T to  $-0.09$  T.

## Results

**Broadband magnon excitation by mCPWs.** Two parallel mCPWs consisting of a layer sequence Fe|Ti|Au were integrated on a YIG thin film as illustrated in Fig. 5.4a. Their center-to-center separation  $s_{cc}$  was  $35 \mu\text{m}$ . The width of signal and ground lines was  $w = 2.1 \mu\text{m}$  with a gap of width  $g = 1.4 \mu\text{m}$  in between. Their lengths amounted to  $125 \mu\text{m}$ . Seven devices with different thicknesses of the Fe layer of the mCPWs were prepared on either 100 nm or 36 nm thick YIG [207] (Supplementary Tab. A.1 and Supplementary Fig. A.7). Radio-frequency currents were injected into the coplanar waveguides and induced an inhomogeneous microwave magnetic field  $\mathbf{h}_{\text{rf}}$ . The Fourier analysis of  $\mathbf{h}_{\text{rf}}$  provided a set of wavevectors  $\mathbf{k}_i$  with  $i = 1, 2, 3, \dots$  (Supplementary Fig. A.8). Scattering parameters  $S_{xy}$  with  $x, y = 1, 2$  were measured by a vector network analyzer (VNA) (experimental data can be found in Ref. [208]). Both, magnitude and phase information were collected. The reflection coefficients  $S_{11}$  and  $S_{22}$  corresponded to spectra displaying magnons excited near mCPW1 and mCPW2, respectively. The transmission coefficients  $S_{21}$  and  $S_{12}$  detected magnons propagating through the bare YIG film between mCPW1 and mCPW2. An in-plane field  $H$  was applied under different angles  $\theta$  (Fig. 5.4a). Magnitude data  $\Delta S_{21}$  of sample1 with mCPWs consisting of Fe(155 nm)|Ti(5 nm)|Au(120 nm) and sample4 with non-magnetic CPWs consisting of Fe(0 nm)|Ti(5 nm)|Au(120 nm) (Supplementary Tab.

## 5.2. Efficient wavelength conversion of exchange magnons below 100 nm by magnetic coplanar waveguides

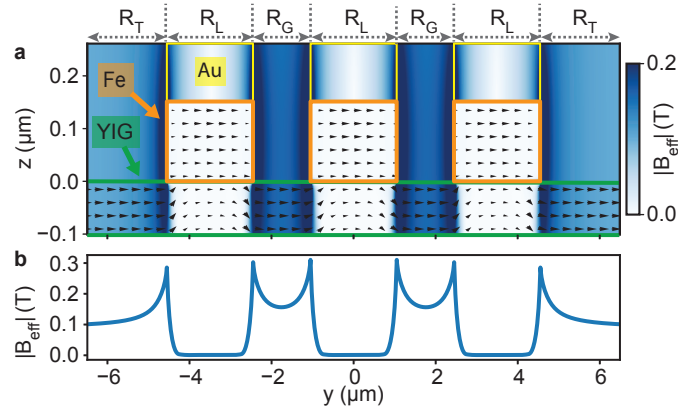


Figure 5.6 – **Micromagnetic simulation and line plot of effective magnetic field generated by mCPW.** **a** Cross-sectional view of an mCPW on YIG where the different layers of Au, Fe and YIG are indicated in yellow, orange, and green color, respectively. Arrows are extracted from micromagnetic simulations and display the local magnetization vectors in the  $y, z$ -plane for a field of 0.09 T applied in positive  $y$ -direction ( $\theta = 90$  deg). The color-coding of the background (legend on the right) indicates the magnetic field  $B_{\text{eff}}$  taken from simulations which varies locally and enters the equation of motion. **b** Line plot of the absolute  $B_{\text{eff}}$  inside YIG along the path of BLS spectroscopy as indicated in Fig. 5.4a.

A.1) are compared in Fig. 5.4b for  $\mu_0 H = 0.09$  T applied at  $\theta = 88$  deg. The spectrum of sample1 contains prominent oscillations indicating propagating magnons in YIG between mCPWs. The propagating magnons cover a frequency band of about 2.5 GHz. The spectrum of sample4 taking under the same applied field condition shows the noisy background signal but no propagating magnon signal. Figure 5.5a (b) displays the angular dependence of reflection (transmission) signals when a field of 0.09 T is rotated by  $\theta$  with respect to CPWs. It is found that the main magnon mode observed in sample1 at  $\theta = 0$  deg splits into two prominent branches A and B when the angle  $\theta$  is increased from  $0^\circ$  to  $90^\circ$ . The modes merge again when  $\theta$  is further increased and reaches  $180^\circ$ . The large splitting into two prominent branches with increasing  $\theta$  is not found in case of non-magnetic CPWs used on sample4 (Supplementary Fig. A.8). A detailed inspection of spectra at  $\theta = 88$  deg (see green broken line in Fig. 5.5b) reveals magnon excitation over a broad frequency regime as evidenced by the oscillating signal in the upper trace of Fig. 5.4b. When the angle  $\theta$  is fixed at 90 deg and the field strength is varied from 0.09 T to -0.09 T (Fig. 5.5c and d) the multi-frequency excitation of magnons over a frequency band of more than 2.5 GHz at high  $H$  is clearly resolved. Before discussing the relevant wavevectors  $k$  for magnons detected in transmission spectra such as those displayed in Figs. 5.4b, 5.5b and d it is instructive to analyze the stray fields generated by mCPWs as sketched in Fig. 5.4c.

**Local effective fields in YIG.** To explore the origin of branches A and B found in Fig. 5.5a for  $\theta \neq 0$  deg, we studied the static magnetization of an mCPW with dimensions of sample1 using micromagnetic simulations (Methods). We display the considered layer sequence in Fig. 5.6a and the simulated effective magnetic field  $B_{\text{eff}}$  in Fig. 5.6b assuming an external magnetic field of 0.09 T applied at  $\theta = 90$  deg to the mCPW. The magnitude of  $B_{\text{eff}}$  is evaluated within the thin YIG film.  $B_{\text{eff}}$  shows a characteristic variation underneath and next to the mCPW. In the following we discuss the simulated field strength in four distinct regions (R) inside YIG. The central region underneath the signal and ground lines (L) of the mCPW is labelled by  $R_L$ . Here we find the lowest field value because the applied field and stray field of Fe are of opposing direction and cancel each other almost perfectly. In the

gaps (G), i.e., the region between signal and ground lines indicated by  $R_G$ , we find high field values as externally applied and stray fields exhibit the same direction and sum up. Further away from the mCPW at large coordinates  $y$  we obtain a field strength consistent with the externally (ext) applied field. Here we label the region by  $R_{\text{ext}}$  (Fig. 5.4c). For the discussion it is instructive to consider the field strength also in the transition (T) region labelled by  $R_T$  in which the effective field is found to be larger than the external field and the microwave field  $h_{\text{rf}}$  is strong producing a large torque. Even larger inhomogeneous fields can be found in the gaps (G) enclosed by two Fe strips. Also in  $R_G$  the out-of-plane microwave component is strong for resonant excitation of spin waves. When introducing such different effective fields  $B_{\text{eff}}$  into the equation of motion of spin precession [64] different eigenfrequencies are expected. They roughly scale with  $B_{\text{eff}}$ . Considering the equation of motion we tentatively attribute the branch A which we observe at high frequency in the reflection signal of Fig. 5.5a to prominent absorption in (gap) regions  $R_G$ . Branch B is then attributed to absorption in regions  $R_L$  underneath the CPW lines. To substantiate the allocation we performed micromagnetic simulations for 0.09 T applied under different angles  $\theta$  with respect to the mCPW and extracted angle dependent  $B_{\text{eff}}(y)$  quantitatively. Introducing  $B_{\text{eff}}(y)$  extracted at central positions of  $R_G$  and  $R_L$  into Kittel's formula [64] for thin YIG we obtained the two dotted black lines displayed in Fig. 5.5a. They model the angular dependencies of the two prominent branches A and B well. The agreement indicates that the inhomogeneous effective fields induced in YIG by the stray fields of the Fe stripes are key to understand the magnon modes excited and detected by mCPWs.

**Spatially resolved magnon spectra.** To spatially resolve effective field-induced frequency variations close to an mCPW we measured thermally excited magnon spectra at characteristic positions beneath and close to mCPW1 of sample1 via micro-focus Brillouin light scattering ( $\mu\text{BLS}$ ) [125, 126]. A laser with wavelength of 473 nm was focused from the backside of sample1 through the transparent gadolinium gallium garnet (GGG) substrate to a diffraction-limited spot on the YIG surface (Fig. 5.4a). This allowed for the investigation of the different regions defined in Fig. 5.6a (top axis). To better detect all the different modes we applied a field of  $\mu_0 H = 0.15$  T at  $\theta = 90$  deg and thereby shifted eigenfrequencies to frequency values for which the interferometer provided the largest signal-to-noise ratio. Spectra marked with  $R_{\text{ext}}$  in Fig. 5.7 were recorded sufficiently away from the mCPW to reflect excitations in bare YIG. Here, considering the measured frequency range from 2 GHz to 13.5 GHz three distinct peaks were observed. By comparison with an analytical dispersion relation for 100 nm thick YIG [86] we attributed the broad main peak between about 6 and 7 GHz to the continuum of magnons exhibiting in-plane wavevectors  $|k|$  from zero up to  $\sim 20$  rad  $\mu\text{m}^{-1}$  which are allowed by the focussing optics (Methods) [198]. The mode at 8.1 GHz (12.8 GHz) is identified as first (second) perpendicular standing spin wave PSSW1 (PSSW2). The PSSW1 peak exhibits a small linewidth. When the laser spot approaches mCPW1 the magnon peaks shift to higher and higher frequencies. In Fig. 5.7c we track the position-dependent frequency of PSSW1. From 8.1 GHz at  $R_{\text{ext}}$  the PSSW1 frequency increases to around 10.6 GHz at  $R_G$  in the gap between the magnetic stripes (spectra are found to be symmetric to the mirror plane of the CPW). In regions  $R_L$  underneath the CPW lines incorporating Fe stripes the PSSW1 frequency is significantly reduced and exhibits 5.8 GHz. Qualitatively, the frequency variation reflects the spatial variation of the effective field displayed in Fig. 5.6b. We attribute the observed shifts of PSSW1 hence to a varying effective field in YIG caused by the stray field of Fe. The frequency variation from 8.1 to 10.6 GHz is consistent with a variation of  $B_{\text{eff}}$  by 88 mT following the formalism of Ref. [86]. This value agrees quantitatively well with the simulated field difference between the central position in  $R_G$  and  $R_{\text{ext}}$ .

We note that also peak shapes are modified in the vicinity of the mCPW. In  $R_L$  the observed fundamental mode is broader than in  $R_{\text{ext}}$ . We speculate that the broadening originates from the finite diameter of



## 5.2. Efficient wavelength conversion of exchange magnons below 100 nm by magnetic coplanar waveguides

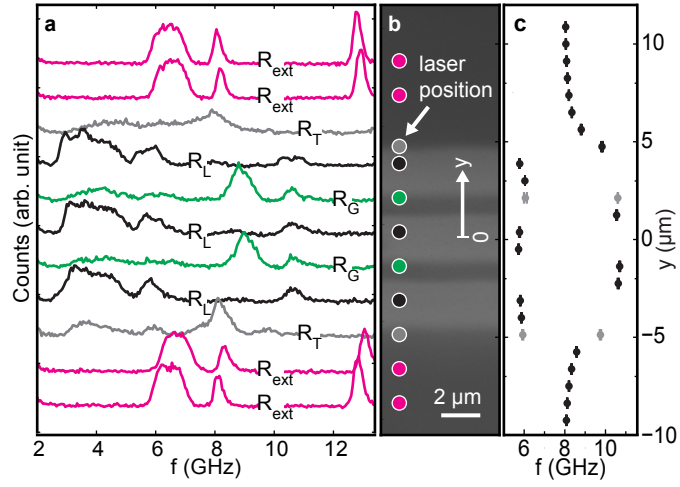


Figure 5.7 – **Spatially resolved magnon spectra at the mCPWs.** **a** Spectra of thermally excited magnons in sample1 measured by  $\mu$ BLS for  $\mu_0 H = 0.15$  T and  $\theta = 90$  deg at different laser spot positions indicated by circles in the **b** optical image taken by the BLS microscope. The systematic variation of spectra depending on laser-spot positions is color-coded consistently in **a** and **b**. **c** Variation of the frequency attributed to the PSSW1 mode along the path of BLS spectroscopy (black and gray symbols). The gray symbols indicate spectra taken at the boundary between regions  $R_G$  and  $R_L$ . In this case the spectra contained two PSSW1 peaks which were consistent with YIG subjected to either high or low effective field. We attribute this observation to the finite diameter of the BLS laser beam probing two regions at the same time. Peak positions were extracted by locally fitting the magnon spectra with a Gaussian function, error bars indicate the standard deviation of the fit.

the probing laser spot which detects magnons subjected to different effective fields. At  $R_G$  the width of the main peak is slightly narrower than at  $R_{ext}$ . We attribute this observation to a reduced range of allowed wavevectors and speculate that magnons are partially confined in the inhomogeneous field between signal and ground lines. As a consequence, long magnon wavelengths in  $y$ -direction are not allowed. Measurements conducted at  $\mu_0 H = 0.087$  T (Supplementary Fig. A.9) showed similar characteristics. Only low-frequency modes were not fully resolved due to the restricted frequency range of the interferometer stated above.

**Wavevectors of transmitted magnons.** The oscillating signal  $\Delta S_{21}$  shown in Fig. 5.4b originated from magnons that were phase-coherently detected in transmission configuration and propagated through the bare YIG film between mCPW1 and mCPW2 at specific frequencies  $f$ . The edge-to-edge separation  $\Delta y_{e-e}$  of CPWs was  $25.9 \mu\text{m}$ . We calculated the dispersion relations  $f(k)$  for YIG films of three different thicknesses according to the formalism provided by Kalinikos and Slavin [86] (Methods). For these calculations we considered the field  $H$  applied in the VNA spectroscopy setup. Our simulations showed that already about  $2 \mu\text{m}$  away from mCPWs the effective field in YIG reduced to almost the applied field. From the calculated  $f(k)$  we extracted the wavevectors  $k$  which were relevant for the magnons propagating through YIG at different frequencies  $f$ . In Fig. 5.4d we display the maximum wavevectors  $k_{max}$  (minimum wavelengths  $\lambda_{min}$ ) found in three differently thick YIG films with mCPWs. In all cases the field  $H$  was applied at  $\theta = 90$  deg, i.e., the magnetization  $\mathbf{M}$  was parallel to  $\mathbf{k}$  and magnons propagated in backward volume magnetostatic wave configuration through YIG. For all samples the maximum wavevector of propagating magnons increased with increasing  $H$ . Such an increase was not observed for non-magnetic CPWs. Remarkably for a given field mCPWs excite wavevectors smaller than  $k_{max}$  as well. The oscillating signal of propagating magnons observed in Fig. 5.4b (upper trace) reflects wavevectors varying quasi-continuously by about one order of magnitude. This large tunability of  $k$  is not known from the grating coupler effect.

**Propagation of exchange magnons.** We measured the velocity of propagating magnons emitted by an mCPW via time-resolved  $\mu\text{BLS}$ . A microwave signal generator equipped with a microwave switch was connected to mCPW1 of sample1 and applied a microwave signal at  $f = 6.64$  GHz. A field of  $\mu_0 H = (0.087 \pm 0.002)$  T was applied at  $\theta = 90^\circ$  to the sample. Once the microwave switch was opened (rise time of  $\leq 4$  ns), an increase of the BLS counts was detected at CPW1 in region  $R_T$  as shown in Fig. 5.8a. At  $R_G$  of CPW2 the signal was detected with a time delay  $\Delta t = 43 \pm 3$  ns (defined at 10% increase of the rising edge). The distance between the two measured spots amounted to  $\Delta y_{tr} = 28 \mu\text{m}$ . Considering  $\overline{v_g} = \Delta y_{tr} / \Delta t$  we calculated an average velocity  $\overline{v_g}$  of  $(0.65 \pm 0.05) \text{ km s}^{-1}$ . This value compared well with the group velocity  $v_g$  of a short-wave magnon calculated for 6.64 GHz (compare solid line in Fig. 5.8b). In bare YIG the frequency of 6.64 GHz corresponded to a magnon with a wavelength of  $105(\pm 1) \text{ nm}$  according to the Kalinkos and Slavin formalism [86]. The symbols displayed in Fig. 5.8b refer to velocities extracted from oscillation periods  $\Delta f$  occurring in VNA data  $S_{21}$  as the one shown in the inset. Here, sample1 with 155 nm thick Fe at 0.09 T was evaluated. We calculated  $\overline{v_g}$  from  $\overline{v_g} = \Delta f \times s_{eff}$  [114] where the parameter  $s_{eff}$  estimated the length of YIG over which the propagating magnon accumulated the relevant phase shift  $\Delta\phi$  between mCPW1 and mCPW2. For the symbols shown in Fig. 5.8b we assumed  $s_{eff} = \Delta y_{e-e} = 25.9 \mu\text{m}$ . The good agreement between extracted data (symbols) and the predicted group velocities indicates that the phase shift  $\Delta\phi$  along  $s_{cc}$  is accumulated mainly across region  $R_{ext}$  where we assume the propagating magnons to exhibit the maximum wavevector  $k$  for the given applied field and excitation frequency  $f$ . In Fig. 5.8b velocities increase with frequency. This behavior is consistent with exchange-dominated magnons.

At  $f = 6.64$  GHz the magnon wavelength amounted to 105 nm. Such a short wavelength did not allow

## 5.2. Efficient wavelength conversion of exchange magnons below 100 nm by magnetic coplanar waveguides

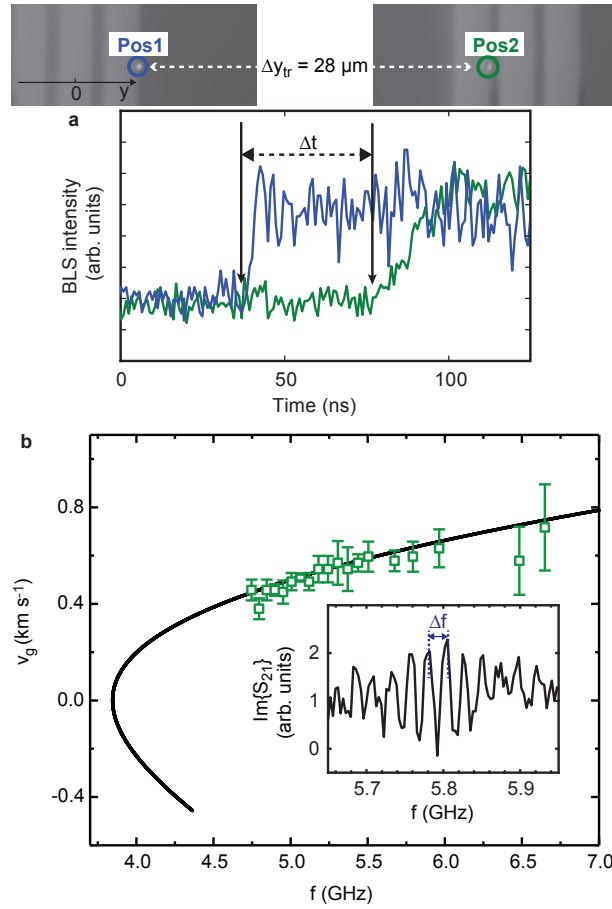


**Figure 5.8 – Group velocities of exchange magnons.** **a** Emission of exchange magnons evidenced by BLS. Time-resolved magnon intensities measured at indicated positions Pos1 of mCPW1 and Pos2 of mCPW2 are depicted as blue and green line, respectively. The measurement was conducted at  $\mu_0 H = 0.087$  T. A microwave pulse with 6.64 GHz was applied to mCPW1. A rise in BLS intensity was first observed at Pos1 and with a delay of  $\Delta t = 43 \pm 3$  ns at Pos2 which was separated from Pos1 by  $\Delta y_{tr} = 28 \mu\text{m}$ . **b** Average group velocities (open squares) extracted for sample1 from VNA transmission signals using  $v_g = \Delta f \times \Delta y_{e-e}$ . The solid curve represents calculated velocities  $v_g$  assuming a backward volume spin-wave dispersion relation at 0.09 T (see Methods). Inset:  $\Delta f$  was extracted from oscillations in the imaginary (Im) part of the transmitted magnon spectra  $S_{21}$  when at least three periods of oscillations appeared. Error bars are the standard deviation of  $v_g$  indicated by those three oscillations.

us to detect the magnon directly in the microfocus-BLS experiment on bare YIG as its diffraction limit amounted to about 300 nm. Indeed, in the YIG film between the mCPWs we did not detect an increase in BLS counts when the microwave pulse was applied. Only in regions  $R_G$  and  $R_T$  representing large effective fields in YIG we recorded increased BLS counts at the excitation frequency. Strikingly the pulsed magnon signals were detected at both  $R_G$  and  $R_T$  regions of mCPW2. We attribute this to a significant conversion of wavelength for a magnon propagating from the low-field region of bare YIG into a region of large effective field created by the stray field of Fe. In our case the wavelength was increased by a factor of at least three to become optically detectable. The conversion process

is sketched in Fig. 5.9a: At fixed excitation frequency a magnon adjusts its wavevector  $k$  as given by the dispersion relation that is valid in the specific region of the sample. The conversion process was reported for dipolarly dominated spin waves [58, 209, 210] but not yet for exchange magnons.

### Discussion

Our experiments based on broadband VNA spectroscopy, spatially and time-resolved Brillouin light scattering as well as micromagnetic simulations indicate that CPWs incorporating a ferromagnetic layer of Fe allow one to generate short-wave exchange magnons in thin YIG films. Close to the edge of the CPW the stray field of Fe generates locally a large effective field. This field enters the equation of motion and leads locally to a large eigenfrequency of spin precession at relatively small  $k$  (large wavelength determined by either the geometry of the CPW or the localization length in the inhomogeneous  $B_{\text{eff}}$ ) (Fig. 5.9a). When propagating away from the mCPW the magnon enters a region of small magnetic field in which the dispersion relation imposes a large  $k$  on the magnon. To obey energy conservation, the wavevector hence transforms along the propagation path and undergoes an up-conversion in  $k$  (Fig. 5.9a). In sample1 for  $f = 7.02$  GHz and  $\mu_0 H = 0.09$  T applied along  $y$ -direction, the wavevector is converted to  $k_{\text{max}} = 62.4 \text{ rad } \mu\text{m}^{-1}$  when the magnon propagates from region  $R_G$  at the mCPW to position  $R_{\text{ext}}$  in bare YIG.

In Fig. 5.4d we summarize the maximum wavevectors  $k_{\text{max}}$  attributed to the high-frequency magnons propagating through the bare YIG of three different thicknesses. These maximum wavevectors vary with the strength of  $H$  applied at  $\theta = 90$  deg. A reduction of the applied field leads to a decrease of  $k_{\text{max}}$  from 62.4 at 0.09 T to about  $28 \text{ rad } \mu\text{m}^{-1}$  at 0.002 T. We attribute the decrease to the variation of magnetization  $M$  in the Fe stripes. With decreasing  $H$  magnetic moments in Fe turn into a direction collinear with the long axis. Thereby the peak-to-peak variation of effective fields in YIG next to the mCPWs is less pronounced. We note that at  $\mu_0 H = 0.002$  T the evaluated wavevector is still larger than expected from a non-magnetic CPW. We attribute this observation to either the hysteresis of the Fe stripe (i.e., a finite remanent magnetization component of Fe along  $\theta = 90$  deg) or the differences in magnetic susceptibilities of Fe and YIG [202]. The observation of a significant wavelength-conversion process in very small applied field is promising in view of low power consuming and compact magnonic applications where an additional biasing magnetic field is avoided and instead electric fields control the magnonic functionality [211, 212].

The transmission signals  $S_{21}$  showed that both up- and down-conversion of  $k$  took place. Via down-conversion the spin-precessional motion of an incoming magnon induced a voltage in the metallic receiver CPW which was phase-coherently detected by the VNA. In Fig. 5.9b we display relative signal strengths  $I/I_0$  depending on the wavevector  $k$  which we attributed to the magnons in bare YIG at 0.09 T.  $I$  is the signal strength in  $\Delta S_{21}$  of the corresponding magnon, and  $I_0$  is the signal strength of the most prominent low-frequency branch  $k_1$ . Strikingly  $I/I_0$  of magnons with  $k \approx 52 \text{ rad } \mu\text{m}^{-1}$  is about 86 % of the signal of magnons at  $k_1$ . For a non-magnetic CPW one would expect  $I/I_0$  of only about 0.04 % (gray curve), i.e., more than three orders of magnitude smaller. The wavelength conversion process hence offers a powerful methodology which does not require the nanolithography established for grating couplers or nanopillars. At the same time mCPWs offer a broad frequency regime for magnon emission (Fig. 5.4b) not provided by grating couplers. Considering spatially resolved BLS data performed at 0.087 T (Supplementary Fig. A.9) we suppose that the large signals  $I/I_0$  for  $k$  near  $52 \text{ rad } \mu\text{m}^{-1}$  are attributed to spin waves excited (and detected) in  $R_T$  right at the outer edges of the mCPW. Here, both  $B_{\text{eff}}(y)$  and the exciting microwave field  $h_{\text{rf}}$  exhibit large strengths. For propagation at wavevectors

## 5.2. Efficient wavelength conversion of exchange magnons below 100 nm by magnetic coplanar waveguides

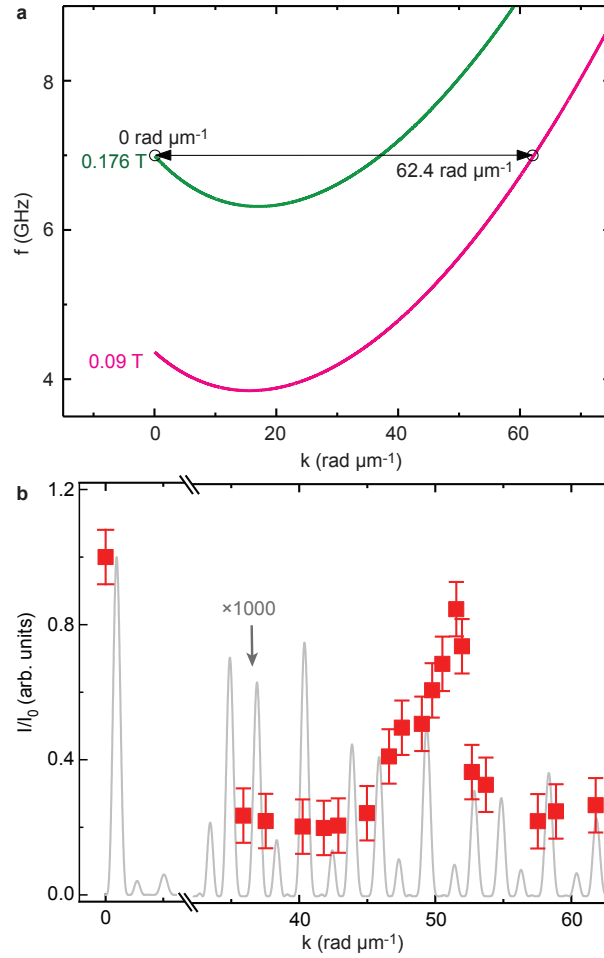


Figure 5.9 – **Wavelength conversion and magnon signal strengths.** **a** Dispersion relations of magnons which are calculated using the formalism of Kalinikos and Slavin [86] in the gap region  $R_G$  of an mCPW (green) and in the region  $R_{\text{ext}}$  of bare YIG (pink) considering sample1. **b** Normalized signal strength  $I/I_0$  of magnon resonances extracted from data such as those shown in Fig. 5.5d (squares) at 0.09 T.  $I$  ( $I_0$ ) is the peak-to-peak signal strength in  $\Delta S_{21}$  at  $k$  ( $k_1$  of a CPW). Error bars represent the noise level observed in the spectra. The solid gray line reflects the Fourier transformation (power spectrum) of the in-plane radiofrequency field component of  $h_{\text{rf}}$  of a non-magnetic CPW. Source data are provided as a Source Data file.

$k > 52$  rad  $\mu\text{m}^{-1}$  the gap regions  $R_G$  of mCPWs (Fig. 5.4b) provide the high effective fields that are required for resonant excitation in YIG. The corresponding spin waves undergo additional conversion processes when passing through the inhomogeneous  $B_{\text{eff}}(y)$  induced by the ground lines. The reduction of  $I/I_0$  observed for propagating magnons at large  $k$  is most likely caused by these processes inducing e.g. partial reflection. Still, the relative efficiencies for magnon emission and detection at large  $k$  are overall similar to the grating couplers [5, 56]. In Fig. 5.4d we observe a reduction of  $k_{\text{max}}$  by about 10 % when using an Fe thickness  $\delta$  of 95 nm (sample2) instead of 155 nm (sample1). The observation is consistent with micromagnetic simulations predicting less peak-to-peak variation of  $B_{\text{eff}}(y)$  inside YIG for decreasing  $\delta$ . Correspondingly, the frequency splitting between branches A and B (Fig. 5.5a) depends on  $\delta$  (Supplementary Fig. A.7). The thickness  $\delta$  hence offers control over the frequency band

of magnon emission and detection. For a fixed Fe thickness of  $\delta = 95$  nm we find  $k_{\max}$  to decrease with decreasing thickness of YIG (compare sample2 and sample5 in Fig. 5.4d). The observed reduction in  $k_{\max}$  reflects the change in magnon dispersion relation  $f(k)$  depending on the YIG thickness. Still the wavelength conversion is found to be significant for the small YIG thickness of 36 nm and hence advantageous for coherent nanomagnonics [188]. To optimize mCPWs and further reduce  $\lambda$  it is suggested to embed the ferromagnetic layers into YIG and thereby reduce the demagnetization effect in the Fe (Supplementary Fig. A.10a and b). In this Schloemann-type configuration [203] the effective field in YIG would be locally further increased enabling correspondingly higher excitation frequencies close to the CPW. In case of embedded FeCo with a saturation magnetization  $M_S = 1,950$  kA m<sup>-1</sup> [213] our dynamic simulations suggest excited spin waves with  $\lambda = 37$  nm at 28 GHz in YIG (Supplementary Fig. A.10c to e), corresponding to  $k \approx 170$  rad  $\mu\text{m}^{-1}$ . We argue that the wavelength conversion based on mCPWs is very versatile and works in both insulating and metallic magnets, in nanoscopic ferromagnetic waveguides [174] and skyrmion-hosting materials [214]. The magnons with  $k_{\max} = 62.4$  rad  $\mu\text{m}^{-1}$  reported here possess wavelengths shorter than the minimum ones reported so far for non-magnetic microwave waveguides [53, 55, 185] and signals are about three orders of magnitude larger (Fig. 5.9b). To quantitatively understand the magnon amplitudes induced by mCPWs and model the frequency-dependent signal variation observed in Fig. 5.4b a formalism needs to be developed which, in the spin-precessional equation of motion, considers both the inhomogeneous effective field  $B_{\text{eff}}(y)$  and non-collinear spin structures (Fig. 5.6a) as well as local differences in magnetic susceptibilities [202]. In conclusion, we reported the emission and detection of short-wave magnons in YIG from CPWs incorporating ferromagnetic layers. Their stray field induced a non-uniform magnetic field. The non-uniformity was strong when the in-plane external magnetic field was applied perpendicular to the long axis of the mCPWs, i.e., perpendicular to the incorporated Fe stripes. The observed conversion efficiency was large, both concerning wavevector  $k$  and signal strength. Local wavelength conversion also allowed us to study propagating exchange magnons via optical detection. Importantly, for the fabrication only photo-lithography was needed and a conventional microwave antenna design was suitable. We find that mCPWs emit magnons over a broad frequency band and thereby allow for continuous tuning of exchange magnons at telecommunication frequencies. This is different from grating couplers which emit at specific frequencies defined by discrete reciprocal lattice vectors. A growth-induced anisotropy axis for the ferromagnetic layer could stabilize a magnetization component transverse to the CPW in zero magnetic field, thereby enabling low power consuming magnonic devices based on mCPWs. Wavelengths down to below 40 nm are achievable. We expect these features to make mCPWs a very versatile microwave-to-magnon transducer technology and promote advancements in experimental nanomagnonics both in the fundamental and applied sciences.

## Methods

**Sample fabrication.** The mCPWs were fabricated on YIG thin films with thicknesses of either 36 nm or 100 nm by means of photo-lithography and lift-off processing. The single-crystalline YIG films were grown on (111) GGG substrates by liquid phase epitaxy (LPE). The 36 nm thick YIG was grown at INNOVENT e.V. in Jena, Germany, on a 1-inch GGG wafer from a PbO-B<sub>2</sub>O<sub>3</sub> based high-temperature solution using a standard dipping technique [207]. The 100 nm thick YIG was deposited on a 3-inch wafer via LPE and purchased commercially from the company Matesy GmbH in Jena, Germany. Double layers of photo-resist were coated on the YIG and the CPW structures were written directly by a laser lithography system. Fe was first thermally evaporated in one chamber. Second, the chip was moved to another chamber for Ti and Au thermal evaporation. Seven devices were prepared. We explored three different thicknesses of Fe (155 nm, 95 nm, and 17 nm). The Au (Ti) layers were kept at a constant

## 5.2. Efficient wavelength conversion of exchange magnons below 100 nm by magnetic coplanar waveguides

thickness of 120 nm (5 nm) (Supplementary Tab. A.1). The non-magnetic reference CPW did not contain an Fe layer and consisted of Au and Ti only.

**All electric broadband spin-wave spectroscopy.** Magnons were electrically excited and detected on a broadband spectroscopy setup with a microwave probe station. Microwave currents  $i_{\text{rf}}$  from 10 MHz to 26.5 GHz were extracted from one port of a vector network analyzer (VNA) and injected into the coplanar waveguide using the high frequency coaxial cable and probe. The dynamic microwave field  $\mathbf{h}_{\text{rf}}$  generated by  $i_{\text{rf}}$  applied the dynamic torques on the magnetization and excited the magnons in the YIG thin film underneath the CPW. We report VNA experiments performed in the linear regime at -15 dBm, i.e., at a power of 0.03 mW. In the center of the 100 nm thick YIG beneath the signal line of a bare CPW without Fe, we estimated the strength of  $\mu_0 \mathbf{h}_{\text{y,rf}}$  [215] to be 0.68 mT at -15 dBm. The additional Fe layer of an mCPW increased the relevant distance in  $z$ -direction by 155 nm corresponding to  $\mu_0 \mathbf{h}_{\text{y,rf}} = 0.61$  mT in the YIG center. The reduction in excitation strength amounts to about 10 %. From -28 dBm to -5 dBm we observed that the measured scattering parameter scaled linearly with the microwave signal. At -15 dBm the main resonance in YIG was red-shifted by 46 MHz compared to -28 dBm. Considering the temperature dependent resonance frequencies reported in Ref. [216] we estimate a temperature increase of about 6 K. The wavevectors of the magnons were defined by the geometric design in conventional non-magnetic CPWs as reported earlier, but were modified when mCPWs were used. In mCPW2, the microwave currents induced by the propagated magnons were probed via a coaxial cable by a port of the VNA and corresponding scattering parameters were analyzed. The setup was calibrated using the standard kit designed for coaxial microwave probes of 50 ohm impedance matching before measurements. External magnetic fields were applied in the  $x, y$ -plane as indicated in Fig. 5.4 a. The reflection and transmission spectra of angular dependent measurements with mCPWs are plotted in Fig. 5.5 a and b. The spectra were obtained while  $\mu_0 H = 0.09$  T was applied and  $\theta$  was varied from -2 deg to 200 deg. Field-dependent reflection measurements taken at  $\theta = 90$  deg are depicted in Fig. 5.5 c. Figure 5.5 d shows the transmission spectra for  $\mu_0 H$  scanned from 0.09 T to 0 T. To enhance the signal-to-noise ratio and remove drifts in the background signal in Figs. 5.4 b and 5.5 we display  $\Delta S$  which reflects the difference in scattering parameters taken at successive field values or angles.

**Brillouin light scattering.** Micro-focus Brillouin light scattering ( $\mu$ BLS) measurements were conducted at room temperature. A monochromatic continuous-wave solid-state laser with a wavelength of 473 nm and power of  $< 1$  mW was focused through the sample backside to a diffraction-limited-spot using a specially corrected 100 $\times$  objective lens with a large numerical aperture of  $NA = 0.85$ . The diffraction limit corresponded to a maximum accessible wave vector  $k$  of  $4\pi \sin \phi / (473 \text{ nm}) = 22.6 \text{ rad } \mu\text{m}^{-1}$ , considering  $\sin \phi = NA = 0.85$  in air ( $\phi$  is the incident angle,  $NA$  is the numerical aperture). We tested the limit experimentally on propagating spin waves in YIG while focussing through the transparent GGG substrate. We detected propagating spin waves with wavelengths down to 330 nm corresponding to a wavevector of  $19 \text{ rad } \mu\text{m}^{-1}$ . Permanent magnets were used to apply external magnetic fields in the plane of the YIG either along or perpendicular to the CPWs. Backscattered light was analysed with a six-pass Fabry–Perot interferometer TFP-2 (JRS Scientific Instruments). The recorded BLS signal is proportional to the square of the amplitude of the dynamic magnetization at the position of the laser spot. The sample was mounted on a closed-loop piezo-stage and spatial maps were obtained by scanning the laser spot over the sample. mCPW1 was wire-bonded to a macroscopic CPW prepared on a rigid board connected via an end launch adapter to a microwave signal generator (Anritsu MG3692C). For propagation measurements the microwave signal was applied in 300 ns long pulses by opening and closing of a switch (SR-T400-1S, rise time  $\leq 4$  ns) and the BLS counts were registered as a function of time with 0.8 ns resolution. With the help of phase-resolved BLS measurements (Supplementary

Fig. A.11), we extracted the exchange constant and the effective magnetization of the thin YIG in sample1:  $J = (2.7 \pm 0.2) \times 10^{-7} \text{ erg cm}^{-1}$ , and  $\mu_0 M_{\text{eff}} = (0.180 \pm 0.002) \text{ T}$ . The values were consistent with the values reported in the literature [55, 207, 217]. We used the experimentally determined values for the calculation of wavevectors. For the extraction of the frequency of PSSW1 modes in thin YIG for different effective fields we measured the thermally excited magnon modes [218] using spatially resolved BLS. Due to the thermal fluctuations, a spin system possesses a large variety of magnons at a finite temperature. These are spread over a large momentum and energy space, depending on the temperature. We proceeded as follows. We first looked for broad peaks associated to the thermally excited magnon continuum. We attributed the first peak after the continuum to the PSSW1 and extracted manually the peak frequency. Then a local fit with a Gaussian function in a frequency window of 1 GHz was conducted to get a precise value of the peak frequency and its standard deviation. We note that PSSW1 is not resolved in VNA spectroscopy data due to its small spectral weight in inductive measurements.

**Micromagnetic simulations.** Micromagnetic simulations were conducted using Mumax<sup>3</sup> (version 3.9.3) [91]. The nominal cross-section ( $y-z$  plane) of sample1 (using rectangular geometries for the Fe lines) was discretized into  $(1, 16384, 512)(x, y, z)$  cells with a cell size of  $25 \times 2.5 \times 2.5 \text{ nm}^3$ . Along the  $x$ -direction periodic boundary conditions (1024 repetitions) were used, implying the magnetization did not vary along the  $x$ -direction. The periodic repetitions were added in negative and positive  $x$ -direction and considered for the calculation of the demagnetization field [154] by Mumax3. For YIG  $M_s = 143.2 \text{ kA m}^{-1}$  and  $A_{\text{ex}} = 2.7 \text{ pJ m}^{-1}$  were used. For Fe  $M_s = 1,710 \text{ kA m}^{-1}$  and exchange stiffness  $A_{\text{ex}} = 21 \text{ pJ m}^{-1}$  [219] were considered. Exchange coupling between Fe and YIG was considered in the simulations with the default scaling factor  $S = 1$  following Ref. [91]. For each field direction the magnetic ground state was found using the 'Minimize()' method of Mumax<sup>3</sup>. The cell sizes in  $y$ - and  $z$ - directions were smaller than the exchange lengths of Fe (3.4 nm) and YIG (14.5 nm). When using  $50 \times 5 \times 5 \text{ nm}^3$  the effective field and its spatial dependence were similar; the simulated values in region R<sub>G</sub> agreed within 0.3 %.

**Magnon dispersion relation and group velocity calculations.** The magnon dispersion relations of backward volume mode were taken from Ref.[86]:

$$\omega = \sqrt{(\omega_H + \beta\omega_M k^2)[\omega_H + \beta\omega_M k^2 + \omega_M(1 - \frac{kd}{2})]} \quad (5.1)$$

In our case,  $k$  is the in-plane wavevector of magnons along  $y$ -direction.  $\omega_H = \gamma B_{\text{eff}}$ ,  $\omega_M = \mu_0 M_{\text{eff}}$  and  $\beta = (2J)(\mu_0 M_s^2)^{-1}$ .  $\mu_0$  is the permeability of free space.  $B_{\text{eff}}$  is the effective magnetic field in the YIG thin film.  $M_{\text{eff}}$  is the effective magnetization.  $J$  is the exchange stiffness.  $d$  is the thickness of the YIG thin film. The group velocity  $v_g$  is calculated from Eq. (5.1) according to

$$v_g = \frac{\partial \omega}{\partial k} \approx \frac{\Delta \omega}{\Delta k}. \quad (5.2)$$

Evaluated group velocities are plotted in Fig.5.8 **b** as a solid black curve.

### Data Availability

Requests concerning data should be addressed to D.G. The datasets analysed in the current study are available in the Zenodo repository, <https://doi.org/10.5281/zenodo.3633075>.



## 5.2. Efficient wavelength conversion of exchange magnons below 100 nm by magnetic coplanar waveguides

---

### Acknowledgments

We acknowledge the financial support from the Swiss National Science Foundation (SNSF) via sinergia project NanoSkyrmionics CRSII5 171003 and Grant No. 163016 as well as Deutsche Forschungsgemeinschaft via grant DU 1427/2-1.

### Author contributions

D.G. and K.B. designed the mCPWs and planned the experiments. P.C. and A.K. fabricated the samples and conducted atomic force microscopy characterization. C.D. provided the thin YIG films. K.B. conducted the micromagnetic simulations. P.C., K.B. and D.G. planned and conducted the VNA and BLS measurements, analyzed the data and wrote the manuscript. All authors commented on the manuscript.

### Competing interests

The authors declare no competing interests.

### Materials & Correspondence

Correspondence and material requests should be addressed to D.G.



## 6 Magnonic memory

To utilize the gating functionality of magnetic defects (cf. Sec. 4.1) or the tunability of the band structure of magnonic crystals (cf. Sec. 4.4), it is of uttermost importance to achieve fast, reliable and energy-efficient programmability of the static magnetization of selected nanomagnets. In Sec. 4.1 engineering of the coercive field was used to program differently oriented nanomagnets and a magnetic defect by applying a specific bias field. While serving as a proof of concept, switching by an externally applied bias field is slow and might be unreliable, due to the stochastic nature of non-coherent switching [220–222].

In R. Huber *et al.* [49] it was proposed to program the magnetization direction of a gating nanostripe by current-driven domain wall movement [223, 224]. While fast, for in-plane magnetized Py nanostripes large current densities in the order of  $10^{11}$  to  $10^{12}$  A/m<sup>2</sup> are required [225], which limits the energy efficiency.

During the investigation of grating couplers on YIG thin films presented in Chapter 5 and published in ACS Nano Letters [57], I discovered spin wave assisted switching of the Py stripes positioned underneath a CPW at ultra-low microwave powers in the  $\mu$ W range. Strikingly the switching was also observed at a second grating 25  $\mu$ m away from the emitter CPW, which suggested that it was induced by propagating SWs. This discovery of switching by propagating SWs opens up the possibility to store information by using magnons (instead of fields and currents) in a non-volatile manner, which we will refer to as *magnonic memory*. Switching by SWs might allow to program specific magnetic states of MCs by using tailored SW interference patterns. This chapter presents the experimental results considered as propagating spin wave assisted switching measured on a periodic grating coupler. The observed phenomenon represents an important step towards a magnonic memory allowing one to store the outcome of magnonic logic operations in a nonvolatile manner.

### 6.1 Switching of Py stripes with propagating spin waves

#### 6.1.1 Introduction

The concept of microwave assisted switching (MAS) has attracted interest of researchers and industry alike. To increase the storage densities of magnetic hard disk drives, the magnetic volume for storing a binary digit (bit) has been continuously decreased. As the magnetic grain size was shrunk, its coercivity had to be increased to insure thermal stability [220, 226]. However, the achievable field by the write-head imposes a limiting factor on the grain coercivity and thus on the storage density [227].

In MAS resonant microwave excitation is used to achieve large cone angle precession of the magnetic moments, which can significantly decrease the switching field [228–230]. For high-coercivity materials the required frequency for efficient MAS reaches tens of GHz [231], which is technologically challenging. To reduce the required frequency, it was proposed by Li *et al.* [232] to use exchange-coupled composite media, where low-frequency excitation of a soft magnetic layer reduces the switching field of an adjacent hard magnetic layer. An experimental demonstration of this effect was shown by Seki *et al.* [233], in that a switching field reduction of a high-coercivity FePt layer was achieved by excitation of standing spin waves in an adjunct permalloy (Py) layer. The Py layer was located directly beneath the signal line of a coplanar wave guide (CPW) and driven by large dynamic magnetic fields of several millitesla.

In this work, we demonstrate the switching of Py nanomagnets by spin waves (SWs) excited in an underlaying low-damping YIG film excited at ultra-low powers of tens of microwatts, corresponding to driving fields in the microtesla range. Strikingly, the switching was not only found locally at the point of microwave excitation, but also for remote nanomagnets more than 25  $\mu\text{m}$  away from the emitter CPW. This discovery of propagating spin wave assisted switching (PSWAS) opens up new possibilities for storing SW amplitudes in magnetic bits, e.g. the outcome of wave-based computational operations [17, 60, 234, 235], in a non-volatile way. Gertz *et al.* [236] demonstrated parallel read-out of magnetic bits by propagating SWs, however the writing-capability was lacking. PSWAS closes this gap and allows for a holographic memory, where magnetic bits are both read and written by SWs. Further we speculate that magnonic memory might contribute to the development of in-memory computing architectures [237] based on magnons.

### 6.1.2 Switching by spin waves - magnetic force microscopy and spin-wave spectroscopy

Figure 6.1a shows a sketch of the experimental configuration. We investigate a sample with CPWs and 1D grating couplers (GCs) as described in Sec. 5.1. Each GC has a periodicity of  $a = 200$  nm and consists of 20 nm thick and  $w_{\text{Py}} = 100$  nm wide Py ( $\text{Ni}_{81}\text{Fe}_{19}$ ) nanostripes fabricated on a 100 nm thick YIG film. Nanostripes with 25.0  $\mu\text{m}$  and 27.0  $\mu\text{m}$  length are alternated to reduce the dipolar coupling of stripe ends and modulate their coercivity. Each GC comprises 51 nanostripes resulting in a total width of  $w_{\text{GC}} = 10.1$   $\mu\text{m}$ . The GCs are covered by two CPWs with a center-to-center distance of 35  $\mu\text{m}$ . The CPWs were fabricated out of 5 nm thick Ti and 110 nm thick Cu and the width of the signal and ground lines amounted to  $w_{\text{L}} = 2.1$   $\mu\text{m}$ . The gap width was 1.4  $\mu\text{m}$ . The geometrical parameters were optimized for an impedance of  $Z_0 = 50$   $\Omega$ . The length of the CPWs amounted to 122  $\mu\text{m}$ . To increase the signal-to-noise ratio in all electrical spin wave spectroscopy (AESWS) measurements, three identical GCs were arranged consecutively under CPW1 and CPW2 (not sketched). The GCs were separated by 15  $\mu\text{m}$  to reduce dipolar interaction to a minimum (layout and SEM images in Appendix Fig. A.12). CPW1 and CPW2 were connected with microwave tips to port 1 and 2 of a VNA, respectively. The VNA was used to trigger switching events by applying microwaves to CPW1 as well as for measuring scattering parameters S11 and S21. For all measurements presented in this section, the sample was first saturated at  $\mu_0 H = -90$  mT in  $y$ -direction and PSWAS of the stripes was studied for positive fields. The YIG film itself had a negligible coercivity (expected below 1 mT [76]), such that its magnetization  $\mathbf{m}_{\text{YIG}}$  is assumed to be aligned with  $+H$  for relevant switching fields (SFs) of the Py stripes. For  $\mathbf{m}_{\text{YIG}}$  pointing in  $+y$ -direction, the non-reciprocal excitation of a CPW [238] favors the emission of Damon-Eshbach (DE) SWs in  $+x$ -direction, i.e. in the direction of CPW2. The individual nanostripes composing the GCs represent bistable nanomagnets. Due to their shape anisotropy [73], their magnetization tends

## 6.1. Switching of Py stripes with propagating spin waves

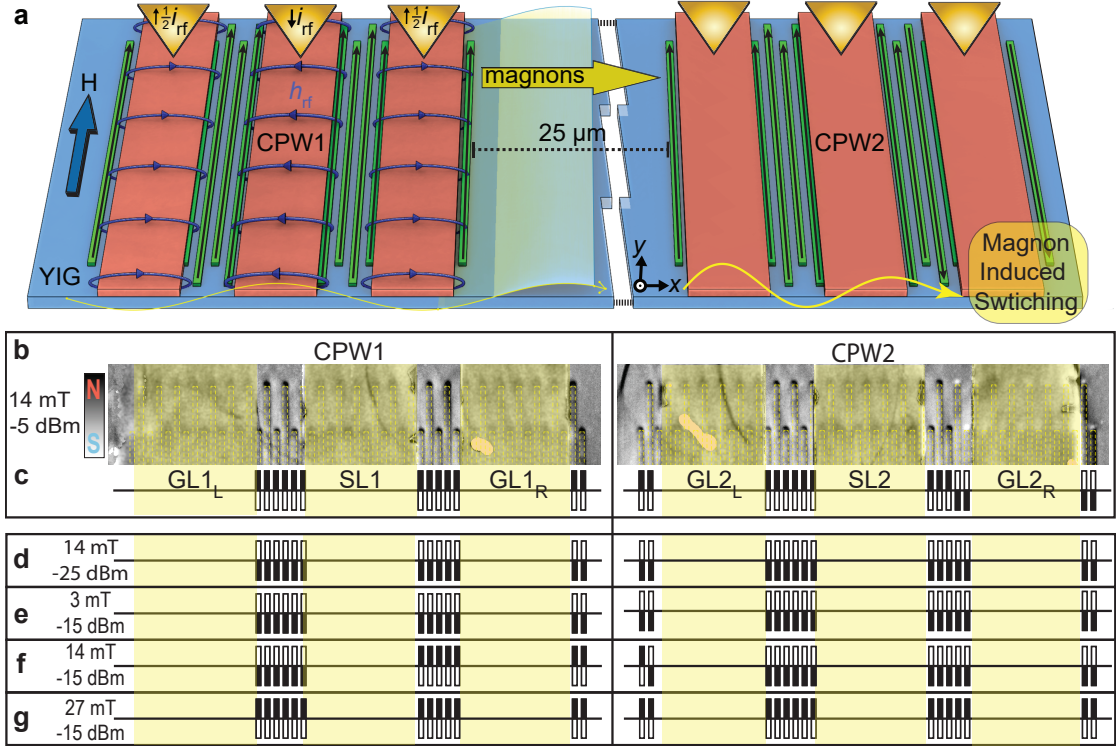


Figure 6.1 – **a** Sketch of the experiment. Two CPWs with 1D GCs out of 20 nm thick and 100 nm wide Py nanostripes are fabricated on 100 nm thick YIG. The nanostripes represent bistable nanomagnets. The nanostripes are first saturated in  $-y$ -direction (*downwards* magnetized) and subsequently their switching fields are studied under SW irradiation for positive magnetic fields. The SWs are excited at CPW1 by injection of a microwave current. Due to non-reciprocity SWs preferably propagate in  $+x$ -direction towards CPW2. Switching is detected by microwave-induced irreversible changes in the SW spectra recorded with a VNA and further evidenced by MFM imaging. **b** Exemplary MFM image after a microwave power of  $P_{irr} = -5$  dBm was applied in the range of 0.01 GHz to 12.50 GHz at a field of 14 mT. In regions where Py stripes were covered by the CPWs (shaded in yellow) the MFM signal was weak. In **c** we summarize the magnetization directions in the gap regions where the magnetic contrast was strong. Stripes at CPW1 are aligned upwards. At CPW2 Py stripes closest to CPW1 are switched upwards, on the right side further away from CPW1 Py stripes still point in the initial direction (downwards). In **d**, a low power of -25 dBm was applied at 14 mT and all stripes are still magnetized downwards. We attribute the switching of stripes in **c** to their irradiation with large SW amplitudes in the YIG film. With increasing distance to CPW1, SW amplitudes gradually decay and stripes on the right (far) side of CPW2 were not subjected to large enough amplitudes. The magnetization direction of the stripes served as a magnonic memory which stored the exposure to magnon amplitudes exceeding a critical threshold. **e**, **f**, **g** show the magnetic configuration at  $P_{irr} = -15$  dBm for different field values, related to the VNA spectra shown in Fig. 6.2e.

to point along their long- (easy-) axis either in  $+y$ - or  $-y$ -direction. For simplicity we denote stripes magnetized in  $+y$ - direction as pointing *upwards*, in  $-y$ -direction as pointing *downwards*. We detect

the magnetization direction of the stripes both directly via magnetic force microscopy (MFM) and indirectly via changes in the SW mode spectra measured with the VNA.

Figure 6.1b shows an exemplary MFM image. Before taken in zero field, we applied a microwave power of  $P_{\text{irr}} = -5$  dBm in a frequency window from  $f = 0.01$  GHz to 12.50 GHz to CPW1. During the microwave irradiation,  $\mu_0 H$  was increased in 1 mT steps up to +14 mT. The microwave power was turned off and the MFM image taken at  $H = 0$ . Due to the shape anisotropy of the nanostripes we assumed that their magnetic state was not altered when  $H$  was reduced to zero. From the MFM image we evaluate the magnetization directions in regions where the magnetic contrast was not obscured by the CPW coverage (cf. Fig. 6.1c). Stripes at CPW1 were found switched upwards. At CPW2 the stripes closest to CPW1 pointed upwards. However on the right end furthest away from CPW1 the stripes were still magnetized downwards. In contrast, for the identical magnetic history, but  $P_{\text{irr}} = -25$  dBm, none of the stripes was switched upwards (Fig. 6.1d). As substantiated in the course of this work, we attribute the occurrence of switched stripes at  $P_{\text{irr}} = -5$  dBm (Fig. 6.1b, c) to their exposure with propagating SWs in the YIG film of sufficient amplitude. A switching event thereby serves as a magnonic memory that indicates if a certain threshold SW amplitude was reached. Stripes below CPW1, where the SWs were excited and exhibited the largest amplitude, switched at a relatively small power level. As SWs propagated towards and beneath GC2, their amplitudes continuously decayed. As a result stripes with larger distance to CPW1 required larger  $P_{\text{irr}}$  for switching, consistent with Fig. 6.1b, c.

Figure 6.2 shows field-dependent magnitudes of the reflection coefficient  $\text{Mag}(S_{11})$  and the forward

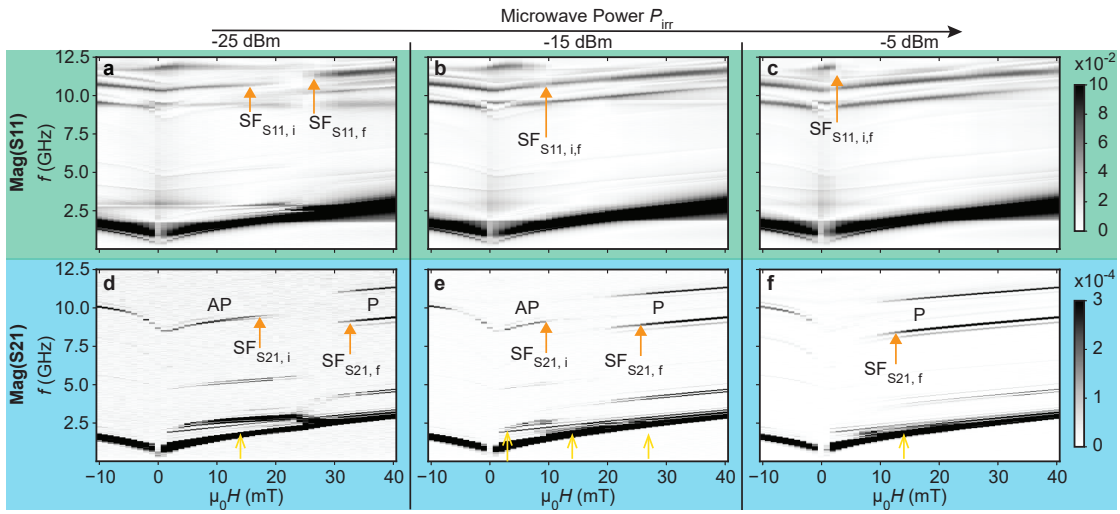


Figure 6.2 – SW reflection  $\text{Mag}(S_{11})$  (a-c) and transmission  $\text{Mag}(S_{21})$  (d-f) coefficients measured with different  $P_{\text{irr}}$  in the frequency range from 0.01 GHz to 12.5 GHz. The sample was saturated at -90 mT and the field stepped from -10 mT to 40 mT in 1 mT steps. The switching fields  $\text{SF}_{S_{11},i}$  and  $\text{SF}_{S_{11},f}$  ( $\text{SF}_{S_{21},i}$  and  $\text{SF}_{S_{21},f}$ ) at which mode transitions take place in  $\text{Mag}(S_{11})$  [ $\text{Mag}(S_{21})$ ] both decrease for increasing  $P_{\text{irr}}$ . Yellow arrows in d, e, f mark field values for which MFM images are depicted in Fig. 6.1.

transmission coefficient  $\text{Mag}(S_{21})$  measured by VNA for different powers. Dark branches in  $\text{Mag}(S_{11})$  indicate SW excitation at CPW1, branches in  $\text{Mag}(S_{21})$  indicate SWs transmitted through the bare YIG film from CPW1 to CPW2. We found for both  $\text{Mag}(S_{11})$  and  $\text{Mag}(S_{21})$  that the hysteretic mode behavior shifted to lower fields when  $P_{\text{irr}}$  was increased. It is instructive to start our analysis with Fig. 6.2e showing  $\text{Mag}(S_{21})$  measured at  $P_{\text{irr}} = -15$  dBm. The most prominent low-frequency branch is attributed to the  $k_1$ -excitation of the CPW. This mode is continuous and doesn't show appreciable

## 6.1. Switching of Py stripes with propagating spin waves

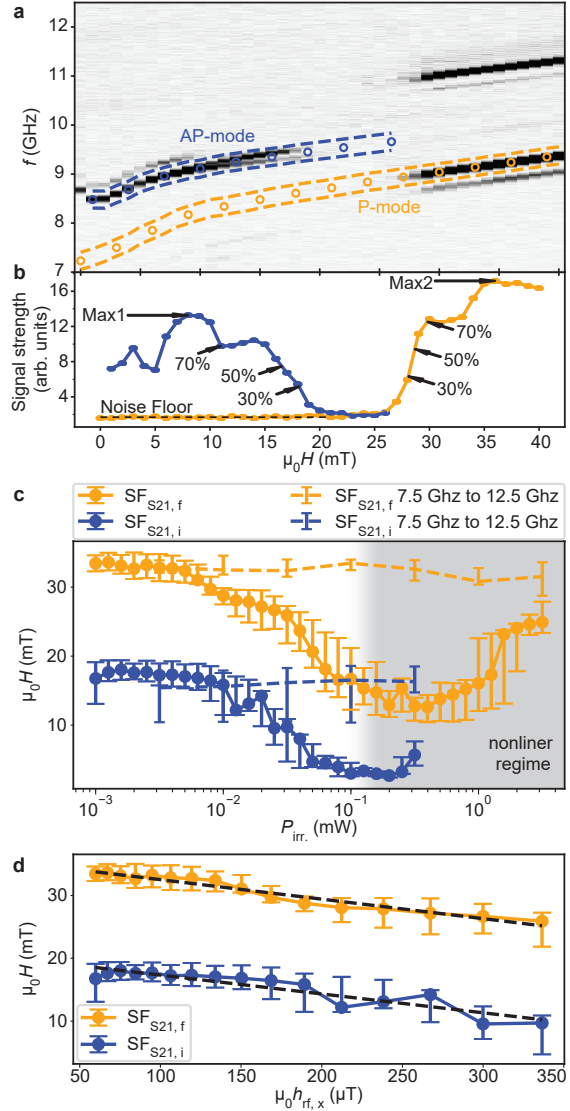
hysteretic behavior, suggesting a small coercivity of the YIG film itself. Higher frequency branches are attributed to the magnonic grating coupler effect [5, 54, 56], presented in Chapter 5.1. For the GC modes at  $+H$ , three field regions are apparent. For  $0 < \mu_0 H < \text{SF}_{\text{S21,i}} = 9.7$  mT a single high-frequency branch is visible starting at around 8.5 GHz. Between  $\text{SF}_{\text{S21,i}}$  and  $\text{SF}_{\text{S21,f}} = 25.9$  mT high-frequency modes were barely resolved vanished. Above  $\text{SF}_{\text{S21,f}}$  two pronounced GC modes become prominent with further increasing  $H$ . They start at 8.8 GHz and 10.8 GHz. To clarify the magnetic states of the GCs in these three characteristic field regions, we repeated the VNA measurements until specific field values located within each of the regions were reached, for which stopped the VNA measurement and took MFM images.

Figure 6.1e shows the extracted magnetic configuration for  $\mu_0 H = 3$  mT below  $\text{SF}_{\text{S21,i}}$ . Stripes at CPW1 and CPW2 were still magnetized downwards. We attribute the region from 0 mT to  $\text{SF}_{\text{S21,i}}$  to an antiparallel (AP) alignment of the magnetization of all stripes (below CPW1 and CPW2) with respect to the magnetization of YIG  $\mathbf{m}_{\text{YIG}}$ . In contrast, at  $\mu_0 H = 27$  mT (Fig. 6.1g) just above  $\text{SF}_{\text{S21,f}}$  all stripes are magnetized upwards, i.e. their magnetization is parallel (P-configuration) with  $\mathbf{m}_{\text{YIG}}$ . For  $\mu_0 H = 14$  mT (Fig. 6.1f) located between  $\text{SF}_{\text{S21,i}}$  and  $\text{SF}_{\text{S21,f}}$ , nanostripes on the left side of the signal line (SL1) of CPW1 were still magnetized downwards, whereas on its right side stripes were switched to the upwards orientation. This observation indicates that the VNA-induced heating of the CPW1 and GC is not the reason for partial switching. Heating is not expected to discriminate between the left and right part of the CPW. As will be later shown, we assume the SW excitation  $k_1$  in YIG to trigger the reversal in Py stripes. For the  $k_1$  mode non-uniform distribution of SW amplitudes is expected. Fallarino *et al.* [238] reported larger SWs amplitudes of the  $k_1$  mode on the right side of a SL, supporting our interpretation. Stripes at CPW2 were still all magnetized downwards. Hence the the two GCs incorporate different magnetic orientations leading to a different coupling between the corresponding CPWs and spin waves in the underlaying YIG. Consequently, we attribute the vanished signal in  $\text{Mag}(\text{S21})$  to a detuning of the emitter (CPW1 exciting the right-going spin waves in the P configuration) and receiver (CPW2 in the AP-configuration). We note that suppressed transmission might origin further from an intrinsic switching field distribution of the GC stripes, possibly resulting in disordered magnetic states.

To distinguish both effects it is useful to study  $\text{Mag}(\text{S11})$ . The fields  $\text{SF}_{\text{S11,i}}$  where modes vanish in  $\text{Mag}(\text{S11})$  (cf. 6.1a, b, c) agree well with  $\text{SF}_{\text{S21,i}}$  (cf. 6.1d, e, f). For  $P_{\text{irr}} = -25$  dBm (Fig. 6.2a), between  $\text{SF}_{\text{S11,i}} = 15.4$  mT and  $\text{SF}_{\text{S11,f}} = 26.8$  mT the high-frequency branches are suppressed. We attribute the mode suppression in  $\text{Mag}(\text{S11})$  to a random stripe magnetization of the GCs below CPW1. For increasing microwave powers  $\text{SF}_{\text{S11,i}}$  and  $\text{SF}_{\text{S11,f}}$  gradually converge, at  $P_{\text{irr}} = -15$  dBm and  $P_{\text{irr}} = -5$  dBm the high-frequency mode transitions appear almost instantly in  $\text{Mag}(\text{S11})$ , indicating a small switching field distribution equal or below the measurement field resolution (1 mT). This is in agreement with J. Topp *et al.* [239], who found a significant reduction in the switching field distribution of a Py grating when microwave were irradiated. A detailed analysis of  $\text{SF}_{\text{S11,i}}$  and  $\text{SF}_{\text{S11,f}}$  is shown in Appendix Fig. A.13. We note that for all powers  $\text{SF}_{\text{S11,f}}$  was lower than  $\text{SF}_{\text{S21,f}}$ , i.e. stripes at CPW1 switched before the ones at CPW2. Hence  $\text{SF}_{\text{S21,f}}$  is a good measure of the switching field of stripes below CPW2, while  $\text{SF}_{\text{S21,i}} \simeq \text{SF}_{\text{S11,i}}$  is a measure of the switching field of stripes below CPW1.

In the following we discuss the dependence of  $\text{SF}_{\text{S21,i}}$  and  $\text{SF}_{\text{S21,f}}$  on  $P_{\text{irr}}$ . For quantitative analysis we extract from  $\text{Mag}(\text{S21})$  the signal strength of the AP-configuration GC mode (AP-mode) and of the strongest P-configuration GC mode (P-mode) as indicated in Fig.6.3a for  $P_{\text{irr}} = -25$  dBm. We define  $\text{SF}_{\text{S21,i}}$  as the field value at which the signal strength of the AP-mode falls to 50 % of its maximum value (Max1), and  $\text{SF}_{\text{S21,f}}$  to the field value at which the P-mode reaches 50 % of its maximum value (Max2) (cf. Fig.6.3b). Further we extract the field values for which 30 % and 70 % of the signal strength is reached, in order to characterize the switching field distribution. Figure 6.3c summarizes the power-dependence of  $\text{SF}_{\text{S21,i}}$  (blue line with dots) and  $\text{SF}_{\text{S21,f}}$  (orange line with dots). The error bars in Fig.6.3c represent

Figure 6.3 – **a**  $\text{Mag}(S_{21})$  measured with  $P_{\text{irr}} = -25$  dBm applied from 0.01 GHz to 12.5 GHz. We mark the frequency response of the strongest GC mode in the AP-state (blue circles) and the P-state (orange circles). **b** The signal strength of the AP-mode (P-mode) is extracted by adding  $\text{Mag}(S_{21})$  in the frequency region enclosed by blue (orange) dashed lines in **a**. We determine the maximum value Max1 (Max2) of the AP (P) signal strength and the noise floor.  $\text{SF}_{S_{21,i}}$  ( $\text{SF}_{S_{21,f}}$ ) is defined as the field value for which the signal strength of the AP-mode (P-mode) is decreased (increased) to 50 % of Max1 (Max2) in respect to the noise floor. **c** Power-dependence of  $\text{SF}_{S_{21,i}}$  (solid blue line) and  $\text{SF}_{S_{21,f}}$  (solid orange line). The region where we expect nonlinear SW scattering is shaded in light gray. Dashed blue (orange) lines indicate  $\text{SF}_{S_{21,i}}$  ( $\text{SF}_{S_{21,f}}$ ) for  $P_{\text{irr}}$  applied from 7.5 GHz to 12.5 GHz, thereby avoiding particularly the excitation of the  $k_1$  mode in YIG. For this case no significant power-dependence was observed. **d**  $\text{SF}_{S_{21,i}}$  and  $\text{SF}_{S_{21,f}}$  plotted as a function of the estimated in-plane dynamic field  $\mu_0 h_{\text{rf},x}$  of the CPW in the linear SW regime. For both SFs we find a linear decrease with increasing  $\mu_0 h_{\text{rf},x}$  (black dashed lines).



the 30 % and 70 % switching field values. We find that  $\text{SF}_{S_{21,i}}$  ( $\text{SF}_{S_{21,f}}$ ) decreases from 16.8 mT (33.4 mT) at  $P_{\text{irr}} = 0.001$  mW to 2.7 mT (12.9 mT) at 0.2 mW. This corresponds to a reduction of  $\text{SF}_{S_{21,i}}$  by 84 % and of  $\text{SF}_{S_{21,f}}$  by 61 %. We point out that the measured direct electrical cross-talk between CPW1 and CPW2 was below -55 dB, i.e. not sufficient for MAS at CPW2. Hence the reduction of  $\text{SF}_{S_{21,f}}$  is attributed to SWs which reach GC2.

Surprisingly, for large  $P_{\text{irr}}$  we find again an increase of  $\text{SF}_{S_{21,i}}$  and  $\text{SF}_{S_{21,f}}$ . We attribute this effect to the onset of nonlinear SW scattering [240], which first limits and then even deteriorates the peak amplitude of SWs emitted from CPW1. For  $P_{\text{irr}}$  above -9 dBm (shaded with gray in Fig.6.3c) we found a decrease of the  $k_1$  mode resonance frequency (Appendix Fig. A.14), which is a typical indication for the nonlinear regime [241].

The blue (orange) dashed line in Fig.6.3c shows  $\text{SF}_{S_{21,i}}$  ( $\text{SF}_{S_{21,f}}$ ) for  $P_{\text{irr}}$  applied only from 7.5 GHz to 12.5 GHz. This frequency regime covers the resonant frequency of the Py stripes and in former studies were used to initiate MAS [239, 242]. In our experiments no apparent reduction of  $\text{SF}_{S_{21,i}}$  or  $\text{SF}_{S_{21,f}}$  was found. Hence, the power levels were not yet high enough to induce conventional MAS in the GCs.



## 6.1. Switching of Py stripes with propagating spin waves

We conclude that the previously observed switching field reduction originates from a low-frequency excitation in the YIG film and not from conventional MAS.

Figure 6.3d shows  $SF_{S21,i}$  and  $SF_{S21,f}$  as a function of  $\mu_0 h_{rf,x}$ , which is approximated by  $\mu_0 h_{rf,x} = \mu_0 \sqrt{P_{irr}/(2Z_0 w_L^2)}$  [243]. Here we limit the power levels to the linear regime, i.e.  $P_{irr} \leq -15$  dBm. We find for both  $SF_{S21,i}$  and  $SF_{S21,f}$  a linear dependence on  $\mu_0 h_{rf,x}$ . This suggests that the PSWAS is proportional to the SW amplitude ( $\propto m \propto h_{rf,x}$ ), not to the SW power ( $\propto m^2 \propto h_{rf,x}^2$ ). By linear fitting (black dashed line in Fig. 6.3d) we extracted similar slopes amounting to  $-30 \pm 3$  and  $-31 \pm 2$  T/T for  $SF_{S21,i}$  and  $SF_{S21,f}$ , respectively. We point out that for an additional static magnetic field applied in  $y$ -direction obviously the slope would be -1. Thus PSWAS requires a 30 times smaller field amplitude than switching with a static field. In [239] for a similar Py grating without YIG film a reduction of the switching field (SF) from 14 mT to 7 mT was found for  $\mu_0 h_{rf,x} \simeq 3.5$  mT, corresponding to a slope  $\Delta SF/\Delta(\mu_0 h_{rf,x}) = -2$ . Hence the observed PSWAS is about an order of magnitude more efficient than conventional MAS of a similar grating.

To determine the frequency dependence of the PSWAS, the following measurement routine was conducted: The stripes were first magnetized downwards with  $\mu_0 H = -90$  mT and then the field increased slowly to a positive bias field of  $\mu_0 H_B = 14$  mT. We monitored  $\text{Mag}(S21)$  with a low  $P_{irr} = -25$  dBm to which we refer from now on as sensing power  $P_{sens}$ . This power level was chosen such that  $\mu_0 H_B < SF_{S21,i}$  for  $P_{sens}$  (cf. Fig. 6.4a and Fig. 6.1d), i.e.  $P_{sens}$  itself was insufficient to induce switching. While staying at a fixed  $\mu_0 H_B$ , we applied a  $P_{irr}$  in a small frequency window  $f_{irr}$  with a range of 0.25 GHz.  $P_{irr}$  was increased from -30 dBm to 6 dBm in 1 dBm steps. After each power step,  $\text{Mag}(S21)$  was measured with  $P_{sens}$  in a frequency window from 7.5 GHz to 12.5 GHz. Figure 6.4b shows  $\text{Mag}(S21)$  measured as function of  $P_{irr}$  applied from  $f_{irr} = 1.5$  GHz to 1.75 GHz. Similar to the mode transitions found for increasing  $\mu_0 H$ , we observe a transition from the AP-mode to the P-mode for increasing  $P_{irr}$ . We denote the characteristic switching power levels  $SP_{S21,i}$  and  $SP_{S21,f}$ . Again we add  $\text{Mag}(S21)$  amplitudes in the vicinity of the AP-mode (enclosed by blue dashed lines) and P-mode (enclosed by orange dashed lines). We use the 50 % signal strength criterium to quantify  $SP_{S21,i}$  and  $SP_{S21,f}$ , 70 % and 30 % transitions are extracted to quantify the switching power distribution (Fig. 6.4c). The measurements were repeated for different  $f_{irr}$  altered from 1 GHz to 13.25 GHz in 0.25 GHz wide windows. Figure 6.4d shows the signal strength of the AP-mode color plotted as a function of  $f_{irr}$  and  $P_{irr}$ . It can be interpreted as diagram of the stripe magnetization below CPW1. For strong signal of the AP-mode (yellow colored area), stripes at CPW1 are pointing downwards. For low signal (blue area) stripes at CPW1 are switched upwards. The 50 % transitions are marked as black dots in Fig. 6.4d, 70 % and 30 % transitions as error bars. We note that there are several dips in the diagram, where a low  $P_{irr}$  is required for switching.

In Fig. 6.4f we plot  $\text{Mag}(S11)$  at 14 mT and -30 dBm for comparison. It is apparent that the dip frequencies in Fig. 6.4d match peak positions in the SW absorption spectrum (indicated by red arrows). The lowest  $SP_{S21,i}$  amounts to only 12.6  $\mu$ W and is located at  $f_{irr} = 1.5$  GHz to 1.75 GHz closely followed by 13.6  $\mu$ W at  $f_{irr} = 1.75$  GHz to 2.0 GHz. Both regions are in the vicinity of the  $k_1$  mode in the YIG film which peaks at 1.7 GHz. There are three dips at the frequency range where the eigenresonance of the Py stripes is expected. The corresponding  $SP_{S21,i}$  amounts to 0.69 mW, 1.91 mW, 1.13 mW at  $f_{irr}$  starting at 9.25 GHz, 10.75 GHz, 11.75 GHz. We conclude that indirect switching by excitation of the  $k_1$  mode in YIG is more than 50 times more efficient than MAS of the stripes itself. Figure 6.4e shows a color plot of the P-mode. It can be interpreted as switching diagram of stripes at CPW2. Strikingly, we found switching of the remote stripes at CPW2 for powers as low as  $SP_{S21,f} = 58.4$   $\mu$ W. The minimum  $SP_{S21,f}$  was required for  $f_{irr} = 1.75$  GHz to 2.0 GHz, which is again close to the  $k_1$ -peak. We note that the minimum  $SP_{S21,f}$  is about 4 to 5 times larger than the minimum  $SP_{S21,i}$ . We attribute the larger  $SP_{S21,f}$  to the spatial decay of propagating SW amplitudes. Based on the intrinsic Gilbert damping  $\alpha_i = 9 \times 10^{-4}$

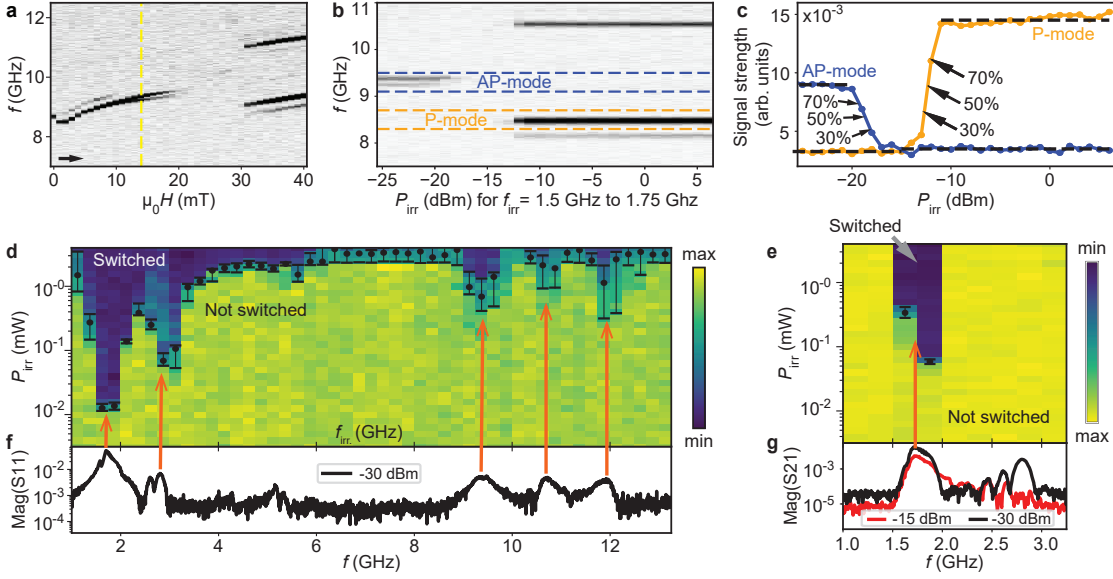


Figure 6.4 – **a** Stripes are magnetized downwards and a small power of  $P_{\text{sens}} = -25$  dBm was used to measure  $\text{Mag}(\text{S}_{21})$ . We selected a positive bias field  $\mu_0 H_B = 14$  mT (indicated by yellow dashed line), at which stripes are not yet switched upwards at  $P_{\text{sens}}$ . **b** Staying at  $\mu_0 H_B = 14$  mT a  $P_{\text{irr}}$  was applied in 0.25 GHz windows (exemplary plotted for  $f_{\text{irr}} = 1.5$  GHz to 1.75 GHz) and step wise increased. After each step,  $\text{Mag}(\text{S}_{21})$  was measured with  $P_{\text{sens}}$  from 7.5 GHz to 12.5 GHz. A transition from the AP-mode (blue dashed lines) to the P-mode (orange dashed lines) as function of  $P_{\text{irr}}$  is observed. **c** We quantify switching powers  $\text{SP}_{\text{S}_{21},i}$  and  $\text{SP}_{\text{S}_{21},f}$  by evaluating the 50 % transitions of the respective mode signal strengths. Measurements were repeated for different  $f_{\text{irr}}$  windows covering 1 GHz to 13.25 GHz. **d** shows the amplitude of the AP-mode color-plotted as function of  $P_{\text{irr}}$  and  $f_{\text{irr}}$ . Yellow (blue) indicates the parameter regime for which stripes at CPW1 were magnetized downwards (upwards). Black dots indicated  $\text{SP}_{\text{S}_{21},i}$ , the error bar 70 % and 30 % transitions. Minima in  $\text{SP}_{\text{S}_{21},i}$  agree well with peaks in  $\text{Mag}(\text{S}_{11})$  shown in **f** for -30 dBm. **e** shows the switching diagram of CPW2 (signal strength of the P-mode). The dip corresponds to the  $k_1$  SW mode, propagating from CPW1 to CPW2. **e** indicates  $\text{Mag}(\text{S}_{21})$  depicted for -30 dBm (below  $\text{SP}_{\text{S}_{21},i}$ ) and -15 dBm (above  $\text{SP}_{\text{S}_{21},i}$ ). The switching of CPW1 has little influence on the  $k_1$  mode. However the peak at 2.8 GHz is not present anymore at -15 dBm, which might explain the lack of a dip in **e** at this frequency range.

of the YIG film, we calculate a required factor of 1.4 to match SW amplitudes of the  $k_1$  mode at CPW1 and CPW2 (details in Appendix A.4.1). However it is expected that the effective damping is larger due to magnon-magnon scattering in the in-plane field configuration, energy transfer to the grating and radiative loss [244] due to the inductive coupling with the CPWs.

We further point out that as stripes at CPW2 switch at a higher  $P_{\text{irr}}$  than at CPW1, the SW emission of CPW1 with stripes switched upwards (black line in Fig. 6.4g for -15 dBm) is relevant. We found that the  $k_1$ -mode depends little on the magnetic configuration of CPW1. However the peak at 2.8 GHz observed in  $\text{Mag}(\text{S}_{11})$  and  $\text{Mag}(\text{S}_{21})$  at -30 dBm is vanished after CPW1 is switched. This might explain why there is a deep dip of  $\text{SP}_{\text{S}_{21},i} = 69.0$   $\mu\text{W}$  for  $f_{\text{irr}} = 2.75$  GHz to 3.0 GHz in Fig. 6.4d, which is completely missing in  $\text{SP}_{\text{S}_{21},f}$  (Fig. 6.4e).

## 6.1. Switching of Py stripes with propagating spin waves

To conclude, using AESWS and MFM we evidenced assisted switching of Py nanomagnets by SWs propagating in the YIG film. PSWAS was most efficient via the excitation of the  $k_1$  mode of the CPW in the YIG film. In the vicinity of the  $k_1$  frequency, a power of  $12.6 \mu\text{W}$  was sufficient to switch stripes at CPW1 at a bias field of 14 mT. When the microwave power was applied for frequencies in the regime of direct MAS of the Py grating, the required power was more than 50 times larger. For stripes at CPW2 separated by more than  $25 \mu\text{m}$  from CPW1, the static switching field  $\geq 33.4 \text{ mT}$  (measured at -30 dBm) was reduced to 14 mT by exciting SWs with a power of only  $\text{SP}_{\text{S21},f} = 58.4 \mu\text{W}$  at CPW1. For low powers we observed a linear dependence of the switching fields on the calculated dynamic magnetic field of the CPW. This observation suggests that PSWAS is proportional to the SW amplitude. The switching field reduction found by applying a  $\mu_0 h_{\text{rf},x}$  in the linear regime was  $\sim 30$  times larger than for applying a static field oppositely to the stripe magnetization. We speculate that due to the low Gilbert damping of the YIG, the effect of a  $\mu_0 h_{\text{rf},x}$  is resonantly enhanced. The microscopic origin of the PSWAS is still unclear at this point and subject to future studies. We assume that exchange coupling and spin-pumping at the YIG-Py interface might play a significant role. In both cases energy is transferred from the low-damping YIG (larger SW amplitudes) to the Py stripes. A combination of thick YIG (energy source) and thin Py stripes (energy sink) seems favorable to optimize the energy transfer.

Our results are promising for the realization of a holographic magnonic memory, where bits are written and read out by SWs. Compared to a traditional HDD with a single read and write head, magnonic memory would allow for ultra-fast parallel read out of many bits at the same time. In this work PSWAS was demonstrated at small bias fields. This means to erase and rewrite the memory, a refreshment cycle, where all the nanomagnets are magnetized downwards would be required. At this point it is still unclear whether toggle-switching without bias-field is achievable in an optimized sample. Toggle switching was recently demonstrated by spin torque mediated through an antiferromagnetic insulator [245]. Also it is thinkable to substitute the bias field with a voltage bias by using magnetoelectric nanomagnets [246]. For wave-computation with magnons, the outcome of a logic operation is often encoded in the SW amplitude. PSWAS provides a direct pathway to store computed SWs amplitudes without the necessity to convert SW signals into the electrical domain. Magneto-electric conversion losses are seen as one of the largest obstacles to magnon computing [60]. We further point out that magnonic memory might be a suitable candidate for in-memory computing. As observed in AESWS measurements, the magnetic state of the nanomagnets changes the spectra of transmitted SWs, e.g. could be used to weight the connections between artificial neurons in a neuronal network connected by magnons.



## 7 Summary and Outlook

In this thesis we investigated the control, excitation and storage of SWs at the nanoscale. This chapter provides a short summary of the main research outcomes and an outlook on possible future studies.

### *Magnetic defects as nanoscale phase shifters*

We fabricated prototypical 1D MCs out of closely spaced CoFeB nanostripes with a periodicity of  $p = 400$  nm and  $p = 600$  nm. An individual stripe in the middle of the 1D MCs was prolonged and could be selectively magnetized oppositely to the others. AESWS measurements showed a modification of phases and amplitudes of SWs which propagated across the defect between two CPWs. Intriguingly, the measured phase shifts were tunable by the application of a magnetic bias field and ranged from zero at  $H = 0$  to almost  $\pi$ , when a bias field just below the switching field of the defect was applied.

Using space- and phase-resolved  $\mu$ BLS measurements, we found that the phase shift occurred within the tailored defect itself, which had a width of only 325 nm. We explained the phase shift by a different effective magnetic field experienced by the defect when a bias field was applied. Thereby the dispersion relation was shifted in frequency and SWs in the defect adapted their wave vectors accordingly. In the AESWS and  $\mu$ BLS measurements phase shifts close to  $\pi$  were concomitant with a significant reduction in amplitude, which was unwanted for the application as a phase shifter.

Strikingly, using micromagnetic simulations we found that for specific bias fields phase shifts of close to  $\pi$  were achieved without a significant drop in amplitude. The simulations suggested that the transmission across a magnetic defect increased again, once the bias field was large enough to shift the SW resonances of the defect at the driving frequency to the second miniband. Such a nanoscale  $\pi$  phase shifter with low transmission loss would be of high relevance for SW logic gates based on interference of phase-controlled SWs and for analog microwave applications.

The promising simulation results might be a starting point for further experimental work. In the experimentally investigated samples, the simulated bias fields for  $\pi$  phase shifts and low attenuation were above the experimentally observed switching fields of the magnetic defect and thus could not be addressed. Future studies might employ materials with magnetocrystalline anisotropy in order to increase the switching fields of nanostripes and study MCs with larger lattice periods such that the frequency spacing between minibands is smaller and higher minibands require lower bias fields.

From an application point of view, it would be advantageous to achieve phase-control without requiring the application of a bias magnetic field. Electromagnets are high in energy consumption and magnetic fields might need to be shielded between different logic cells in an integrated device. In Ref. [50] we therefore proposed to manipulate the effective field inside a magnetic defect via a magnetic anisotropy induced by inverse magnetostriction [150]. When fabricated on a ferromagnetic substrate,

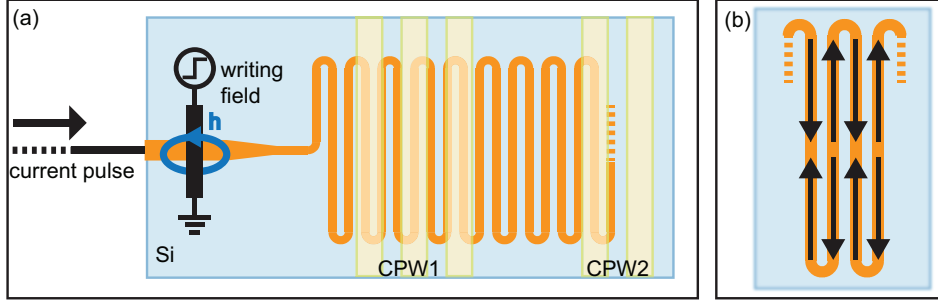


Figure 7.1 – (a) Sketch of an all-programmable 1D MC. Neighboring nanostripes are connected by magnetic half-circles to form a continuous magnetic nanowire. At one end of the MC the magnetization in the wire can be written by the magnetic field of a current-carrying wire. By applying current pulses along the nanowire, magnetic domains can be shifted and the magnetic state of the MC can be fully reprogrammed. (b) By applying a pulse of correct length the magnetic order might be changed directly from the P-state to a quasi AP-state.

the anisotropy could be controlled by an electric field [151, 152].

By tuning the magnetic history, we addressed three different magnetic states in the investigated 1D MCs: The P-state with all stripes magnetized in parallel, the AP-state where every second stripe was magnetized in opposite direction and a defect state with an individual stripe magnetized oppositely to the others. In principle many more magnetic states are possible. For further periodically ordered states, (e.g. every third stripe magnetized oppositely) we expect additional distinctive band structures. This would be promising for realization of adjustable microwave filters, where many different band structures (i.e. pass- and stopbands) can be programmed. Also it would be interesting to introduce several magnetic defects. With defects in series, the phase shifts might add up and instead of changing the effective field of the defects, the phase might be controlled by selecting the number of switched nanostripes. In Fig. 7.1 we propose an approach how an all-programmable 1D MC might be experimentally realized. Inspired by the magnetic racetrack memory [247], we propose that magnetic nanostripes are interconnected by half-circles at their ends, such that a continuous serpentine nanowire is formed as sketched in Fig. 7.1a. In the beginning of the 1D MC the width of the nanowire is increased to form a writing pad, where the magnetization direction can be written by the application of a local magnetic field generated by an electric wire (writing field). By applying a current pulse along the nanowire, the magnetic domain of the writing pad can be driven into the MC [248–250]. By this mechanism a multitude of tailored magnetic states might be programmed. By using a current pulse of correct length, it might be possible to switch directly from a P-state to a quasi AP-state as sketched in Fig. 7.1b. Further individual stripes might be magnetized into a multiple domain state. Thereby the phase and amplitude of a plane wave might be spatially modulated. Tailored wave front shaping would allow to steer and focus SW beams [251, 252].

#### *Interfacing microwaves with short-waved spin waves*

We fabricated 1D grating couplers out of Py nanostripes on a thin YIG film. By TR-STXM we recorded for the first time magnonic GC modes with spatial and temporal resolution. We observed that the excited wave vectors underneath the GC matched the reciprocal lattice vector  $G$  or a multiple of it. An additional unanticipated wavelength conversion was found at the interface of GC and bare YIG. Counterintuitively, SWs exhibited even larger amplitudes in the bare YIG, which we attributed to a change in group velocity while the energy flow stayed conserved. The measurements suggested that magnons were efficiently coupled out from the GC into the bare YIG without significant back-reflection

---

at the boundary. This is very promising for the application of GCs as efficient transducers between electromagnetic and spin waves. We note that in AESWS measurements, electrically detected reflection and transmission signals were still of small amplitude. Further studies might aim at improving the power transfer from the CPW antenna to the GC itself. For efficient coupling of electromagnetic waves to surface acoustic waves, commonly interdigital transducers are used, which are designed with a large static capacitance [253]. In analogy we suggest designing CPWs with an increased total inductance. For example meander shaped CPWs [254] with a larger total length might be employed to cover a wide GC surface.

We also demonstrated an alternative approach for short-waved SW generation, which only required photo-lithography during the fabrication. Magnetic mCPWs with micrometer-scale lateral dimension were prepared out of a magnetic Fe bottom layer and a high-conductance Au top layer, both fabricated on a YIG thin film. When a magnetic field was applied perpendicular to the mCPW, broadband SW excitation and transmission with wave lengths down to 100 nm was measured by AESWS. Thermal  $\mu$ BLS measurements and micromagnetic simulations showed that the Fe layer introduced a stray field in the YIG film and thus shifted the resonance frequency in the vicinity of the mCPW. SWs which were excited in the stray field of the mCPW at a high frequency experienced a decrease of the effective field when they propagated away from it and consequently their wave length took smaller values. Magnetic mCPWs represent an easy-to-fabricate broadband microwave-to-magnon transducer. As suggested in our publication [59], for optimized mCPWs the magnetic layer might be embedded into the SW medium in order to increase the stray field exposure of the thin film and hence generate shorter SWs. We have demonstrated in micromagnetic simulations that wave lengths below 40 nm are achieved with an optimized design. Further we proposed to employ magnetic materials with growth-induced anisotropy for the mCPW, such that a large stray field is also generated without the application of an external magnetic field.

#### *Magnonic memory*

During the investigation of the GC samples, we discovered switching of the Py nanostripes induced by propagating SWs in the YIG film. Using AESWS and MFM measurements, we studied the switching of nanostripes as function of microwave power, frequency and bias field. We found that the switching was most effective at the frequency of the  $k_1$  mode of the CPW in the YIG film. At a bias field of 14 mT, nanostripes more than 25  $\mu$ m away from the emitter CPW were switched by propagating SWs excited with a power of only 58.4  $\mu$ W. We found a linear dependence of the switching field on the SW amplitude in the YIG film. Magnetization switching of nanomagnets by propagating SWs opens up the possibility to store information by using magnons in a non-volatile manner. We termed our discovery therefore as magnonic memory.

The presented findings might mark a starting point for more intensive research on the topic. Still the microscopy mechanisms which mediated the switching process are unclear. Samples with different interface layers between YIG and Py are required to address the dependencies of the switching process on dipolar- and exchange-coupling as well as on spin-pumping effects at the interface. Measurements with short SW pulses are also required to learn about the time-scale of the switching process. We hope that an optimized magnonic memory will allow for toggle switching of nanomagnets by pulsed SW wavelets.





## Appendix Part



# A Supporting Information

This Chapter contains supporting information (SI). Supplementaries of published paper have been reformatted, the content was not modified.

## A.1 SI – Phase control of spin waves based on a magnetic defect in a one-dimensional magnonic crystal

This section provides supporting information for publication Ref. [50] reprinted in Section 4.1.

### A.1.1 Spin wave spectra for increasing $H$ of MC2

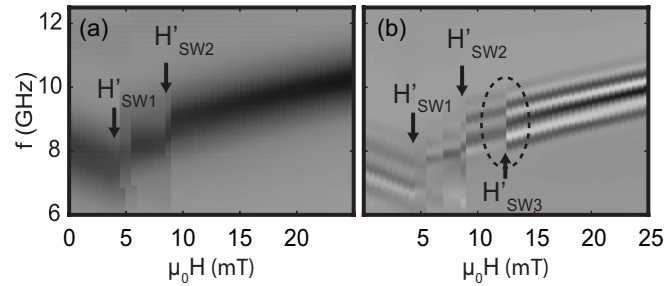


Figure A.1 – Grey scale plot of (a) reflection signal  $a_{11}(H)$  and (b) transmission signal  $a_{21}(H)$  of MC2 for increasing  $H$ , after saturation at  $\mu_0 H = -90$  mT. Relevant field values  $H'_{SW1}$ ,  $H'_{SW2}$  and  $H'_{SW3}$  are marked.

## A.2 SI – Nanoimaging of Ultrashort Magnon Emission by Ferromagnetic Grating Couplers at GHz Frequencies

This section provides supporting information for publication Ref. [50] reprinted in Section 5.1.

### A.2.1 Sample fabrication.

All samples were prepared on 100 nm thick YIG originating from the same wafer. The YIG had been deposited on a 3-inch wafer via liquid phase epitaxy and purchased from the company Matesy GmbH in Jena, Germany. The nanogratings were fabricated from 20 nm thick Py ( $\text{Ni}_{81}\text{Fe}_{19}$ ) deposited via electron beam evaporation on the YIG. The gratings were written with electron beam lithography (EBL) using negative hydrogen silsesquioxane (HSQ) resist and subsequently transferred into the Py by ion beam etching. The etching time was optimized for the Py thickness so that overetching into the YIG was minimized. Coplanar waveguides (CPWs) were fabricated on top of the nanograting using lift-off processing after EBL and evaporation of Ti/Cu (5 nm/110 nm). The substrate was thinned both mechanically and by focused ion beam etching from the back side to allow for X-ray transmission experiments [186].

### A.2.2 Time-resolved STXM.

Synchrotron-based time-resolved STXM (TR-STXM) was conducted at the Maxymus endstation at BESSY2, HZB, Berlin, Germany. We measured with monochromatic X-rays with an energy of 710.3 eV, which corresponds to the  $L_3$  absorption edge of Fe in YIG. The X-ray beam was circularly polarized and the incidence angle was normal to the sample surface. In this configuration its absorption is sensitive to  $m_z$  [255]. We estimate that the XMCD contrast at the used energy is similar for Py and YIG [256]. Due to the five-times smaller film thickness of the Py grating the main signal is coming from the YIG film. The beam was focused with a zone plate to a spot-size of about 20 nm on the sample surface and a 2D image was obtained by raster scanning. For measurements at 8.07 GHz a step-size of 12.5 nm was used, for measurements at 4.07 GHz and 3.43 GHz a step-size of 25 nm. Time resolution was obtained by stroboscopic imaging with X-ray pulses with an effective width of about  $\sim 100$  ps. The magnetic field was applied using a permanent magnet system. By comparison with the AESWS data we found a consistent shift of 1 mT, which we attribute to a systematic error of the magnet system. We readjusted the scale of STXM measurements to account for this shift. The CPW was electrically connected on both of its ends with silver paste to waveguides on a printed circuit board. The transmitted power during the experiment was measured with a signal analyzer. For the shown measurement data the transmitted power was between -6 dBm and -7 dBm.

### A.2.3 Processing of TR-STXM raw data

The TR-STXM raw data contains the measured X-ray counts at each position and time step.  $\tilde{m}_z(x, y, t)$ . We normalize the raw data by dividing each spatial point by the time-average of its photon counts, i.e. by the position dependent static transmission. By this normalization the signal becomes independent of the photon flux, which is lower underneath the CPW than for the bare YIG. By subtracting one from the normalized counts, we obtain a signal proportional to  $\tilde{m}_z$ . For some frequencies we observed time-varying signal which was not depending on the spatial position. We attribute this signal to a electrical crosstalk of the microwaves and the detector. To suppress it, we subtract for every time-frame the spatial average of the signal. This is valid as the spatial average of the magnetic signal itself is close to zero for studied magnons with wavelengths much smaller than the measurement window. To further improve signal-to-noise ratio (SNR), we applied a Fourier filter to select for the frequency component consistent with the microwave driving frequency [257]. For Figure 5.1c (Figure 5.3c) we calculated for each measurement window the fast Fourier transform amplitudes of  $\tilde{m}_z(x, y, t)$  in  $x$ -direction, average it over time  $t$  and  $y$ -direction, and read out the peak amplitude (peak wave vector) in a reasonable

## A.2. SI – Nanoimaging of Ultrashort Magnon Emission by Ferromagnetic Grating Couplers at GHz Frequencies

---

wave vector regime  $\pm 15\%$  around  $2G$  ( $\pm 50\%$  around  $1G$ ). Error bars indicate the standard deviation of peak amplitudes (peak wave vectors) evaluated separately for every row of the spatial scan.

### A.2.4 All electric broadband spin wave spectroscopy.

AESWS measurements were conducted with a vector network analyzer in a microwave probe station. Microwave probes were used to connect to the CPWs on the samples. The magnetic field was applied by an electromagnet and controlled with a Hall sensor. For the depicted measurements an input power of -10 dBm was used. In Fig. 2b the transmission magnitude  $\text{Mag}(S_{21})$  was calculate as square-root of the sum of the squared real ( $\text{Real}(S_{21})$ ) and squared imaginary ( $\text{Imag}(S_{21})$ ) part after removing background signal. This background correction was done by subtracting for each frequency the median value of all field points. The field was applied collinear with the CPWs.

### A.2.5 Magnon dispersion relation.

The purple dashed lines in Fig. 5.2b were calculated using the Kalinikos-Slavin formalism for unpinned surface spins and Damon-Eshbach configuration [86]. As parameters we used an effective magnetization of  $\mu_0 M_{\text{eff}} = 176$  mT, an exchange stiffness of  $A_{\text{ex}} = 3.75$  pJ/m and a gyromagnetic ratio of  $\gamma = 28.0$  GHz/T. The dispersion relation reads:

$$\omega = \sqrt{(\omega_H + \alpha\omega_M k_n^2)(\omega_H + \alpha\omega_M k_n^2 + \omega_M F_n)} \quad (\text{A.1})$$

with  $F_n = 1 + (\omega_M P_n (1 - P_n)) / (\omega_H + \alpha\omega_M k_n^2)$  and

$$P_n = \frac{k_\zeta^2}{k_n^2} + \frac{2k_\zeta^3}{k_n^4 L} \left[ 1 - (-1)^n e^{-k_\zeta L} \right] \frac{1}{[(1 + \delta_{0n})(1 + \delta_{0n})]}.$$

Here  $n$  denotes to the quantization number ( $n = 0, 1, 2, \dots$ ) with the out-of-plane wave vector  $\kappa_n = n\pi/L$  with  $L$  being the sample thickness.  $k_\zeta$  is the in-plane wave vector and the magnitude of the wave vector amounts to  $k_n = \sqrt{k_\zeta^2 + \kappa_n^2}$ . Further terms are  $\omega_H = \gamma\mu_0 H$ ,  $\omega_M = \gamma\mu_0 M_{\text{eff}}$  and  $\alpha = 2A_{\text{ex}}/(\mu_0 M_s^2)$ . The group velocity  $v_g = \partial\omega/\partial k$  was calculated numerically by approximating the derivative with small increments  $\Delta\omega$  and  $\Delta k$ , i.e.  $v_g = \Delta\omega/\Delta k$ .

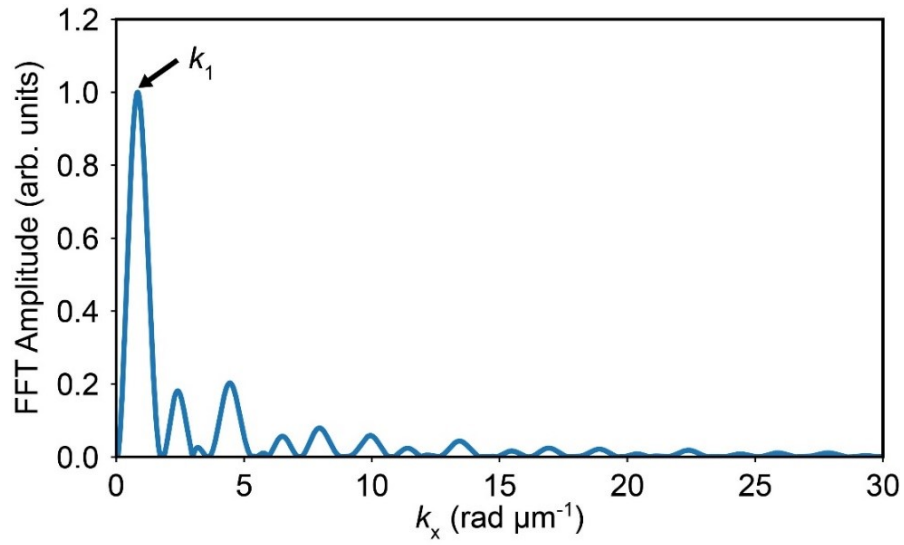


Figure A.2 – Excitation efficiency of the CPW. Fourier transform of the spatial profile of the  $x$ -component of the exciting Oersted fields of the CPW. The prominent peak is denoted  $k_1$  excitation.

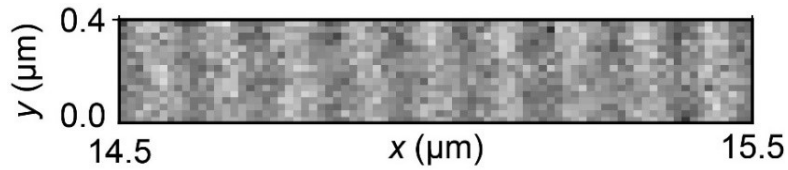


Figure A.3 – Snapshot of propagating magnons around  $x = 15 \mu\text{m}$ . At 8.07 GHz and 7.5 mT propagating magnons with  $\lambda \sim 100 \text{ nm}$  were still observed about  $10 \mu\text{m}$  away from the outer edge of the CPW.

## A.2. SI – Nanoimaging of Ultrashort Magnon Emission by Ferromagnetic Grating Couplers at GHz Frequencies

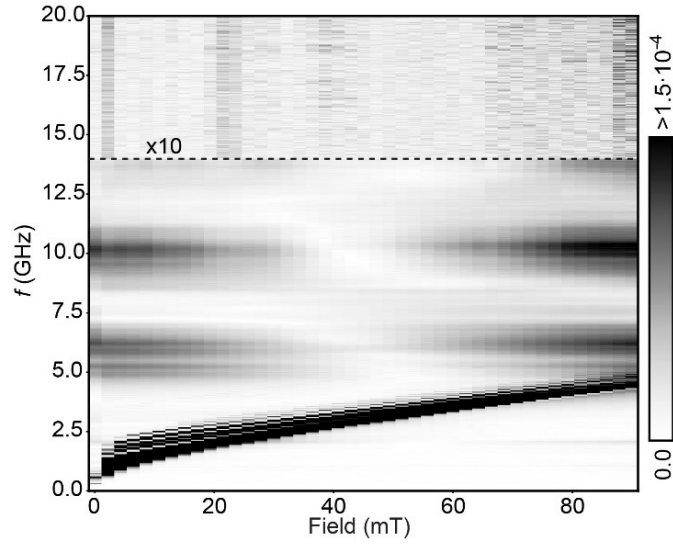


Figure A.4 – Mag(S21) of a reference sample with CPWs without GCs, fabricated on 100 nm thick YIG taken from the same wafer. The CPWs were of identical dimension and separation as in sample2. In contrast to Fig. 5.2a with GCs, only low-frequency branches (field-dependent dark contrast) are visible, corresponding to the wave-vector excitation efficiency of the bare CPW (SI Figure A.2). The field-independent (horizontal) dark stripes are an artefact from the CPWs. We note that the CPWs of the reference sample were made of Ti(5 nm)/Au(120 nm) and the YIG film was etched to a  $90\ \mu\text{m} \times 90\ \mu\text{m}$  wide mesa. These changes might have slightly altered the signal strength of the  $k_1$  mode (lowest branch) compared to sample2. For  $f > 14$  GHz we increased the contrast of the gray-scaled Mag(S21) spectra. Due to the lack of GCs the field-dependent high-frequency branches are missing here which are resolved on sample2 beyond 3 GHz at 11 mT.

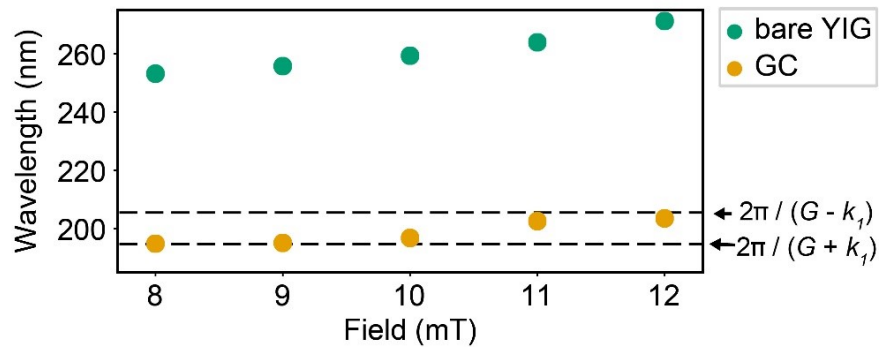


Figure A.5 – Wavelength conversion at 3.43 GHz for sample1b. A pronounced wavelength conversion of about 25 % at the boundary of GC and bare YIG was found also for a second nominally identical sample: green symbol – wavelengths measured in the bare YIG film, yellow symbols - wavelengths underneath the grating coupler (GC).

## Appendix A. Supporting Information

---

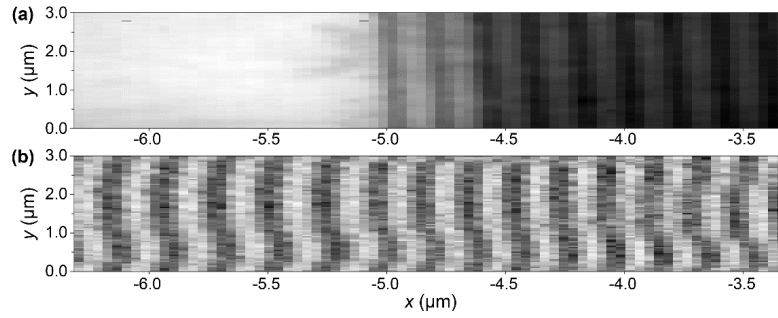


Figure A.6 – Wavelength conversion of G1 mode for -25 mT. For negative magnetic fields, we observed a reversed non-reciprocity with dominant emission on - $x$  – direction. (a) Static X-ray transmission image of sample 1a at the left interface between bare YIG and GC. (b) Snapshot of the dynamic magnetization at -25 mT and 4.21 GHz, which is chosen in the vicinity of the G1 excitation (cf. Fig. 5.2b). The wavelength below the GC amounts to 189 nm and in the bare YIG to 223 nm, corresponding to a wavelength increase of 18 %. We note that an increase of signal amplitude in the bare YIG is apparent, consistent with the discussion of Fig. 5.3e.



### A.3 SI – Efficient wavelength conversion of exchange magnons below 100 nm by magnetic coplanar waveguides

This section provides supporting information for publication Ref. [59] reprinted in Section 5.2.

Table A.1 – Parameters of samples investigated. In sample3 and sample6 with mCPWs consisting of 17 nm thick Fe, the conversion of magnon wavelengths was smallest as the dipolar fields did not vary the effective fields as much as in case of thick Fe. In their case the frequency separation between branches A and B at 90 deg amounted to only 0.4 GHz (Supplementary Fig. A.7).

Device No.	Thickness of YIG film (nm)	Thickness $\delta$ of Fe in mCPW (nm)
sample1	100	155
sample2	100	95
sample3	100	17
sample4	100	Non
sample5	36	95
sample6	36	17
sample7	36	non

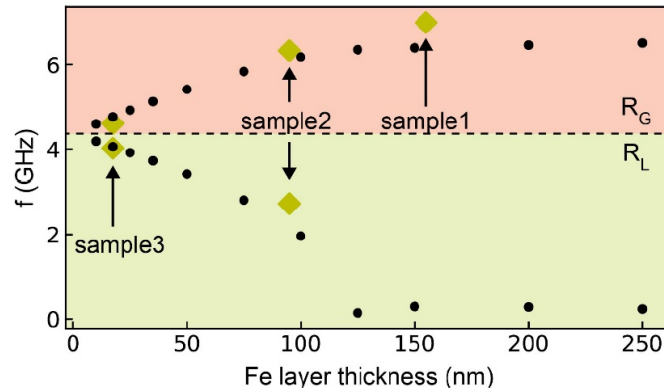


Figure A.7 – Dependence of high and low frequency branches on Fe layer thickness  $\delta$  in a 100 nm-thick YIG film. Using the parameters and geometry of Fig. 5.6a, the effective field was simulated for different thicknesses  $\delta$  of the Fe layer. The field was kept constant at 0.09 T applied under  $\theta = 90$  deg. The effective field in the YIG film was extracted in the middle of the regions  $R_G$  and  $R_L$  (cf. Fig. 5.6b), and the resonance frequency for  $k = 0 \text{ rad } \mu\text{m}^{-1}$  was calculated (black circles). Up to a Fe thickness of about 130 nm the mode splitting is found to increase with the Fe thickness. For larger thicknesses a saturation effect is observed. The yellow diamonds indicate the highest and lowest resonance signal in S11 for sample1, sample2 and sample3 at 0.09 T under  $\theta = 90$  deg. For sample1 the lowest branch was not resolved at  $\theta = 90$  deg (c.f. Fig. 5.5a). Overall there is a good agreement between resonance frequencies calculated from simulated effective fields and the experimental data (diamonds).

## Appendix A. Supporting Information

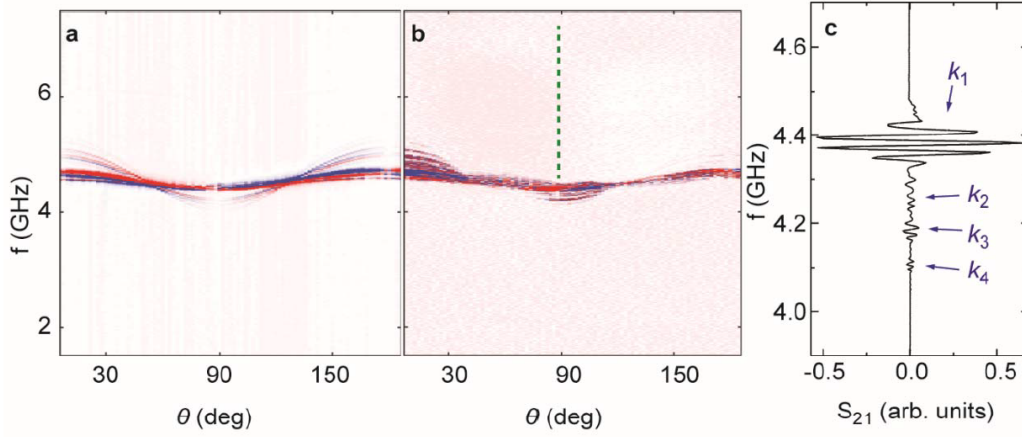


Figure A.8 – Spectra of magnons emitted and detected by conventional nonmagnetic CPWs (sample4). The CPWs consist of Ti(5nm)/Au(120nm). **a** Angular dependent reflection signals  $\Delta S_{22}$  and **b** transmission signal  $\Delta S_{21}$  at  $\mu_0 H = 0.09$  T measured on 100 nm-thick YIG with a non-magnetic CPW. Red (blue) color represents 1 (-1). The dashed vertical line indicates where the bottom line spectrum of Fig. 5.4b is extracted. **c** Detailed spectrum of  $S_{21}$  at  $\mu_0 H = 0.09$  T measured with the non-magnetic CPWs of sample4. The strongest branch belongs to the excitaton at  $k_1$ . The weaker ones to  $k_2, k_3$  and  $k_4$ , i.e., wavevectors transferred by a non-magnetic CPW.

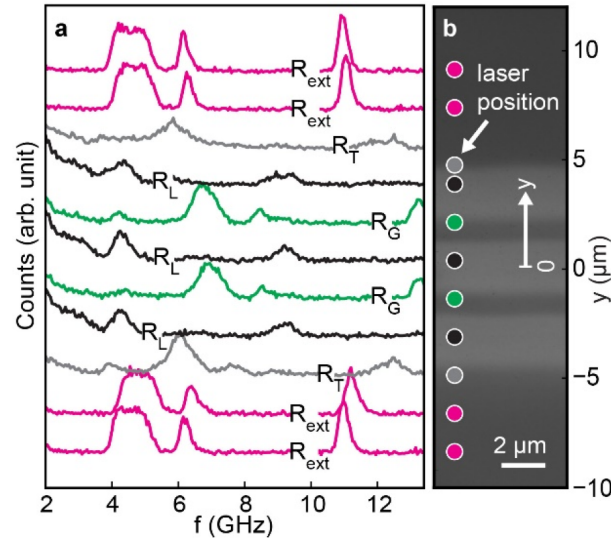


Figure A.9 – Spatially resolved magnon spectra at the mCPWs at 0.087 T. **a** Spectra of thermally excited magnons in sample1 measured by  $\mu$ BLS for  $\mu_0 H = 0.087$  T and  $\theta = 90$  deg at different laser spot positions indicated by colored circles in **b** the optical image taken by the BLS microscope. The data shows similar characteristics as discussed for  $\mu_0 H = 0.15$  T in the main text. We consider the same color-code concerning positions and spectra as in the main text. The lowest frequency mode in region RL was not fully resolved due to the frequency range of the interferometer setting, restricted to  $f > 2$  GHz.

### A.3. SI – Efficient wavelength conversion of exchange magnons below 100 nm by magnetic coplanar waveguides

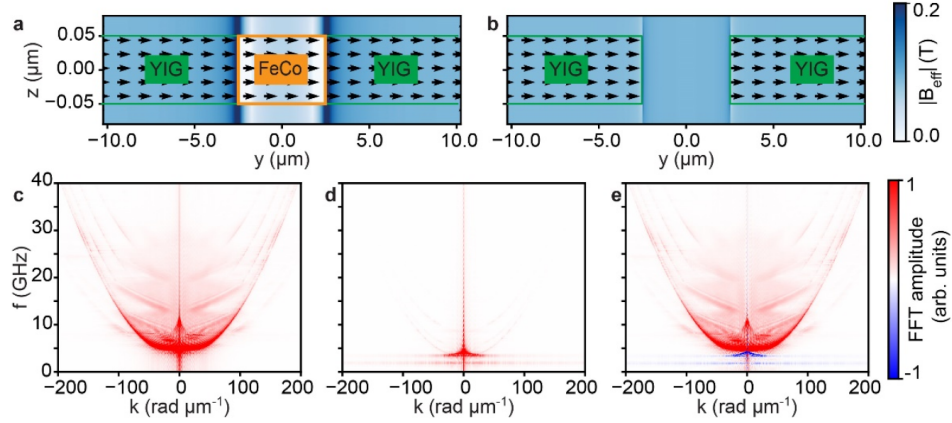


Figure A.10 – Micromagnetic simulation of spin wave emission by an embedded FeCo stripe. **a** Cross-sectional view of a 100 nm thick YIG film with a 5  $\mu\text{m}$  wide FeCo stripe with  $\mu_0 M_s = 2.45$  T fully embedded. Arrows are extracted from micromagnetic simulations and display locally averaged magnetization components in the  $y$ - $z$ -plane. A field of 0.09 T is applied in positive  $y$ -direction ( $\theta = 90$  deg). The color-coding of the background (legend on the right) indicates the magnetic field  $|B_{\text{eff}}|$ . **b** For comparison, the same YIG film is simulated with an air gap of 5  $\mu\text{m}$  instead of the FeCo. Using the static magnetization configurations of panels **a** and **b**, we conducted dynamic simulations for both cases by applying a Sincpulse [258] with a cut-off frequency of 40 GHz. The dynamic field was applied uniformly under 45 degree in the  $y$ - $z$ -plane with a peak amplitude of 1 mT. The simulations were conducted for 6 ns and the normalized magnetization vectors  $\mathbf{m}$  stored every 5 ps for each cell. We performed a Fourier transform of the magnetization component  $m_z$  in time and  $y$ -direction. The Fourier amplitudes are displayed in **c** for YIG with embedded FeCo and in **d** for YIG with an air gap. In **e** we show the difference between the data displayed in **c** and **d**, highlighting the effect of the FeCo. All spectra of **c** to **e** are plotted with the same colorscale. From **e** we extract that the FeCo stripe induces additional large wavevector spin waves in YIG compared to the air gap. Excitation at wave vectors up to  $170 \text{ rad } \mu\text{m}^{-1}$  is visible in **e**. The corresponding wavelength amounts to 37 nm in YIG.

Simulation details: For FeCo we assumed  $M_s = 1950 \text{ kA m}^{-1}$ ,  $A_{\text{ex}} = 21 \text{ pJ m}^{-1}$  and Gilbert damping parameter  $\alpha = 0.01$ , for YIG we used  $M_s = 143.2 \text{ kA m}^{-1}$ ,  $A_{\text{ex}} = 2.7 \text{ pJ m}^{-1}$  and  $\alpha = 0.0005$ . The sample was discretized into  $(1; 8192; 32)(x; y; z)$  cells with a mesh size of  $25 \times 5 \times 5 \text{ nm}^3$ . In  $x$ -direction a periodic boundary conditions was used (1024 repetitions into both side). At the outer boundaries in  $y$ -direction the Gilbert damping of the YIG was gradually increased to absorb spin waves and avoid back-reflection following [159].

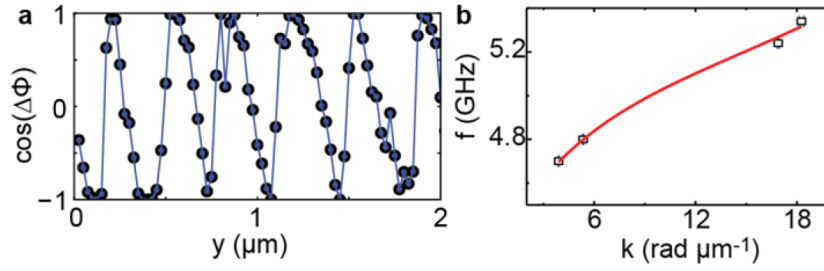


Figure A.11 – Phase evolution of magnons emitted by a non-magnetic CPW. **a** Phase-resolved BLS data measured in region  $R_{\text{ext}}$  at an excitation frequency of 5.34 GHz and  $\mu_0 H = 0.087$  T. The spatial variation of the magnon phase is consistent with a wavelength of about 340 nm, i.e., a wavevector of  $18.3(\pm 0.14)\text{rad } \mu\text{m}^{-1}$ . **b** Symbols show measured wavevectors of magnons excited at different frequencies in the phase-resolved BLS. The wave vectors were extracted by linear fitting of the unwrapped phase  $\Delta\phi(y)$ , the error bars in  $k$  indicate the standard deviation of the fitting. The solid line reflects the dispersion relation consistent with the Damon-Eshbach geometry ( $\theta = 0$  deg) following the formalism of Kalinikos and Slavin [86].

## A.4 SI – Chapter 6: Magnonic memory

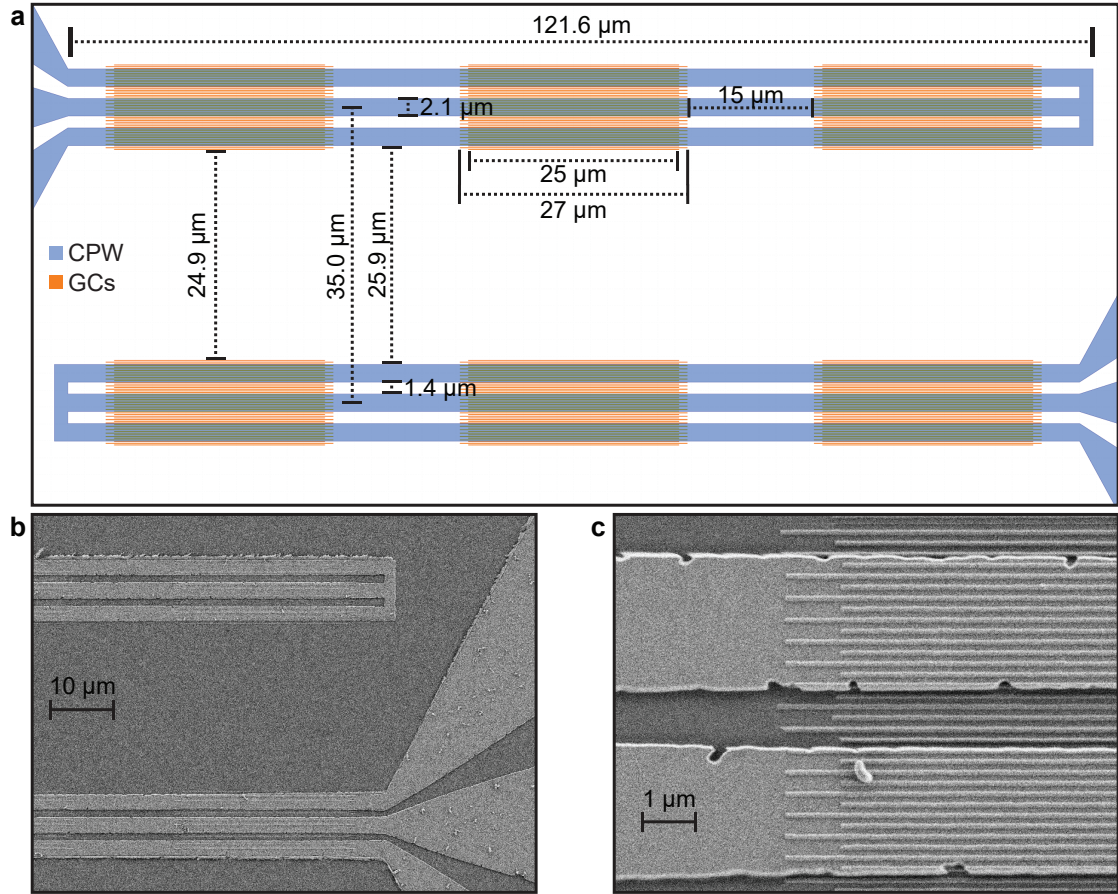


Figure A.12 – **a** Layout of the GC sample. Two CPWs (blue color) with a total length of 121.6 μm are separated by a center-to-center distance of 35 μm. Below each CPW, three 25 μm long Py GCs are arranged. The edge-to-edge distance of neighboring GCs amounts to 15 μm to avoid dipolar interactions. Every second stripe of the GCs is prolonged on both sides by 1 μm. **b** SEM picture showing both CPWs with GCs. **c** Zoom in on the end of one of the GCs.

## Appendix A. Supporting Information

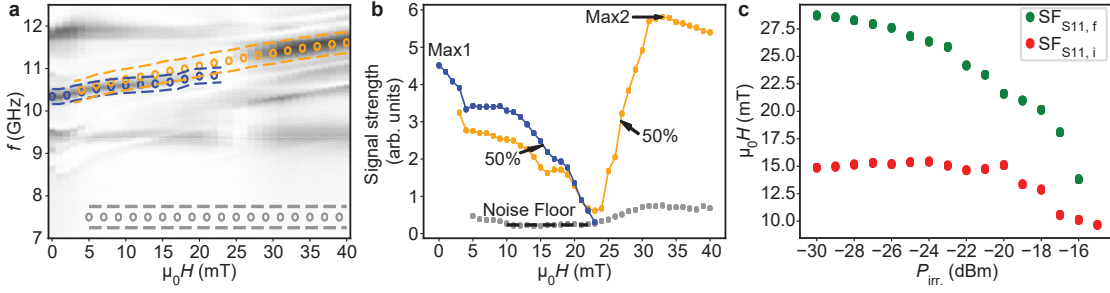


Figure A.13 – **a** Exemplary  $\text{Mag}(S_{11})$  for  $P_{\text{irr.}} = -25$  dBm. We track a characteristic mode of the AP-configuration (blue dots) and the P-configuration (orange dots). **b** We quantify  $\text{SF}_{S_{11},i}$  ( $\text{SF}_{S_{11},f}$ ) by evaluating the decay (rise) of the signal strength to 50% of its maximum in respect to the noise floor (estimated from area between the gray dashed lines in **a**). **c**  $\text{SF}_{S_{11},f}$  decays faster than  $\text{SF}_{S_{11},i}$  and the two SFs are separated by less than 1 dBm (power resolution of the measurement) for  $P_{\text{irr.}} \geq -15$  dBm.

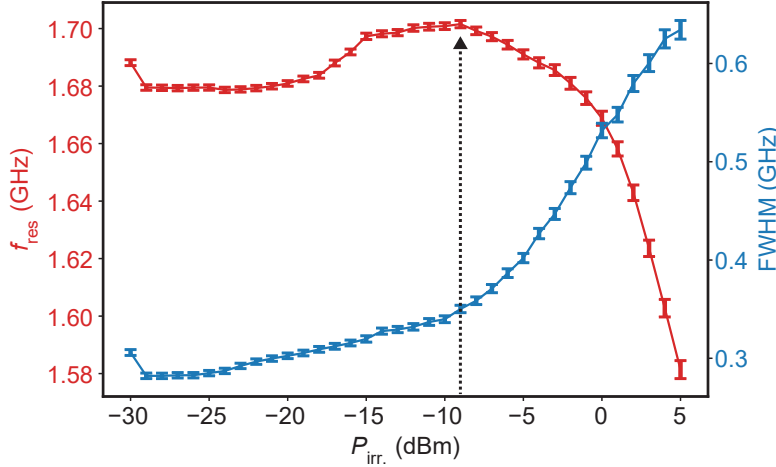


Figure A.14 – Power dependence of resonance frequency  $f_{\text{res}}$  (red color) and full width half maximum (FWHM) of the  $k_1$  peak in  $\text{Mag}(S_{11})$  extracted by fitting with an Lorentzian function at  $\mu_0 h = -10$  mT. Above  $P_{\text{irr.}} = -9$  dBm (indicated by dashed arrow)  $f_{\text{res}}$  starts to decrease with increasing power. Reduction of  $f_{\text{res}}$  is an indication for the non-linear regime of SW excitation. Around the same  $P_{\text{irr.}}$  the FWHM starts to increase significantly.

### A.4.1 Estimation of spin wave decay

To extract the intrinsic Gilbert damping  $\alpha_i$  of the YIG film we measured the linewidth broadening with perpendicular-to-plane magnetic fields up to 500 mT. A CPW with a broad signal line of 20  $\mu\text{m}$  width was used, which excites SWs at a  $k_1 \approx 0$ , i.e. at the ferromagnetic resonance (FMR). Figure A.15 shows the extracted full width half maximum (FWHM) of the FMR mode in  $\text{Mag}(S_{11})$  as function of its resonance frequency. We found a slope of  $m = 0.0031$ . The linewidth broadening depends on  $\alpha_i$  following [259]

$$\delta f = \frac{|\gamma|}{2\pi} \mu_0 \Delta H + 2\alpha_i f,$$



where  $\gamma$  is the gyromagnetic splitting factor and  $\Delta H$  the inhomogeneous line broadening.  $\delta f$  is the linewidth of the imaginary part, which can be estimated by dividing the linewidth of the magnitude with a factor of  $\sqrt{3}$  [260]. Accordingly we calculate  $\alpha_1 = m/(2\sqrt{3}) = 9 \times 10^{-4}$ . The decay of the power is proportional to  $A_{\text{CPW1}}^2 / A_{\text{CPW2}}^2 = 0.70$ . The amplitude decay length  $l_d$  is calculated by  $l_d = \tau \cdot v_g$ , where

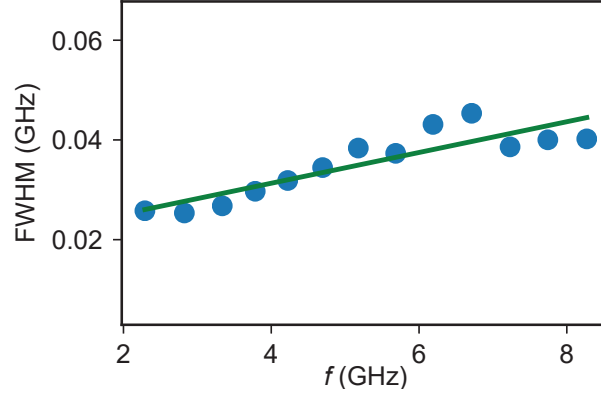


Figure A.15 – FWHM of the FMR peak in Mag(S11) determined with a flip-chip measurement with the field applied out-of-plane. The FWHM increases with the resonance frequency with a slope of 0.0031 (fitted by green line).

$\tau = \frac{1}{2\pi\alpha f}$  is the relaxation time and  $v_g$  the SW group velocity. Figure A.16 shows  $v_g$  calculated for 14 mT using Kalinikos-Slavin formalism for unpinned surface spins and Damon-Eshbach (DE) configuration with the YIG parameters  $\mu_0 M_S = 176$  mT,  $A_{\text{ex}} = 3.7$  pJ/m and  $\gamma = 28.0$  GHz/T. For a wave vector of  $k_1 = 0.85$   $\mu\text{m}/\text{rad}$  we obtain  $v_g = 1.9$   $\mu\text{m}/\text{ns}$ . The decay length at  $k_1$  and  $f = 1.70$  GHz amounts then to  $l_d = 198$   $\mu\text{m}$ . For a propagation distance of  $s = 35$   $\mu\text{m}$  the amplitude decay from CPW1 to CPW2 calculates

$$A_{\text{CPW2}} / A_{\text{CPW1}} = e^{-s/l_d} = 0.84.$$

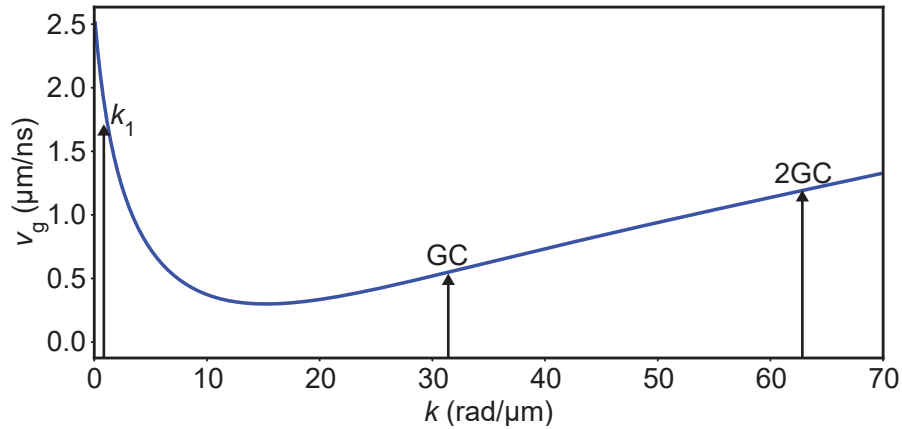


Figure A.16 – Group velocity  $v_g$  of DE SWs calculated based on Kalinikos-Slavin formalism for a 100 nm thick YIG film at 14 mT. At  $k_1 = 0.85$   $\mu\text{m}/\text{rad}$  (marked by black arrow) the group velocity amounts to 1.9  $\mu\text{m}/\text{ns}$ . We further mark the wave vector of the first and second grating coupler mode GC and 2GC of a grating with periodicity of 200 nm.





## B Sample fabrication: Detailed steps

### B.1 Fabrication of NiFe gratings on YIG

This Section provides a detailed process flow for the fabrication of nanogratings on YIG. The process flow was optimized for tools available at CMi cleanroom facilities at EPFL.

For fabrication a 10 mm x 10 mm chip of YIG on GGG substrate was used. Alignment markers for e-beam were fabricated by P. Che using standard photo-lithography and evaporation of 5 nm Ti/120 nm Au. Alternatively, e-beam lithography and subsequent lift-off processing might be applied, using the same exposure parameters as listed below for the fabrication of the CPW layer.

1. Surface cleaning: Rinse chip with Acetone, then IPA. Dry with nitrogen and dehydrate on hot-plate at 120°C for 20 min.
2. Attach chip with mounting wax (PELCO® Quickstick 135) into middle of a 4" -Si dummy wafer. For safety, the edges off the chip can be additionally secured with Kapton tap. (The mounting wax is intended to ensure good thermal transport between chip and Si wafer.)
3. Evaporate 20 nm of Py with *Leybold – Optics LAB 600 H* electron beam evaporator.
4. Remove chip from dummy wafer (by heating the mounting wax using a hotplate at 135°C). Clean back side with cotton swab dipped in Acetone.
5. Surface cleaning and activation for HSQ resist: Rinse chip with Acetone and subsequently IPA. Bath in MF CD26 Developer for 90 sec. Rinse in DI water bath for few minutes. At the CMi wet bench in Zone 7 the water tank resistivity should become above 12 MΩ. Dehydrate chip on hot-plate at 120°C for 20 min.
6. Cool down of 1 minute.
7. Spin coating of HSQ A2 with 4000 RPM (nominal thickness of 40 nm ) directly before e-beam exposure. Attach a small piece of copper tape used for grounding before spin coating.
8. Mount chip on e-beam holder and ground with the copper tape.
9. Exposure with *Raith EBPG5000* e-beam tool at 100 keV.  
Patterns were exported with the GenISys Layout BEAMER software using a resolution of 1.25 nm and proximity effect correction parameters  $\beta = 7.0 \mu\text{m}$  and  $\eta = 1.4$ . The patterns were exposed with a beam current of 3 nA and a dose of 5300  $\mu\text{C}/\text{cm}^2$ . Note: The required dose can vary

## Appendix B. Sample fabrication: Detailed steps

---

depending on the age and batch of the HSQ resist. It is recommended to write several exposures with doses from  $4000 \mu\text{C}/\text{cm}^2$  to  $6000 \mu\text{C}/\text{cm}^2$ . CPWs can then be written for the optimally exposed patterns.

10. Development directly after e-beam writing: 2 min dip in CD26/NaCl solution (custom mixture: 25 g NaCl per 1l CD26). Rinsing in DI bath until resistivity exceeds 12 M $\Omega$ .  
Note: Try to avoid bubbles when dipping the chip into the developer. Dipping slowly under an vertical angle worked well.
11. Optional: Inspection of HSQ mask by SEM.
12. Pattern transfer by ion-beam etching with *NEXUS IBE350*: Low-IBE program for 56 sec under an angle of -3 deg.
13. Check via SEM if etch time was sufficient. Select best patterns for CPW fabrication.

CPW layer fabrication:

13. Rinse sample with Acetone, then IPA. Dry with nitrogen.
14. Dehydration: Use PRAZITHERM hot plate. Adjust set point to a nominal temperature of 170°C. (The actual temperature of the hot plate is around 160°C.) Place chip in middle of the hot plate and bake for 20 min.
15. Spin coating of MMA EL9 at 4000 RPM.
16. Backing at 170°C for 10 min.
17. Spin coating of PMMA A4 at 4000 RPM.
18. Backing at 170°C for 10 min.
19. Preparing of discharging layer for e-beam: Sputtering of 10 nm Au with DP 650 sputtering system. Chip can be placed on a dummy wafer without necessity of gluing it. RTU-Au (Au-unif) program was used for 9 sec.
20. E-beam exposure: Mount chip and ground the surface to the holder with copper tape. CPWs were written with a beam current of 30 nA and a dose of  $500 \mu\text{C}/\text{cm}^2$ . The patterns were exported using BEAMER with  $\beta = 7.0 \mu\text{m}$  and  $\eta = 0.2$  and a resolution of 12.5 nm.
21. Remove Au layer: Dip into KI+J2 solution for 15 sec (at Arias Wet Bench). Rinse in DI bath (two times for 2 min).
22. Development: 70 sec in MiBK:IPA 1:3 solution directly followed by 70 sec in IPA. Blow dry with nitrogen. Inspect by optical microscope if resist is fully removed in exposed areas. If not, extend development time.
23. Evaporation of CPW layer: Alliance-Concept EVA 760 (e-beam evaporator) was used at 450 mm source-substrate working distance. Evaporation of 5 nm Ti followed by 110 nm Cu.
24. Lift-off: Thermal bath in Remover 1165 at 70°C for several hours. Metal blown away with pipette. Optional: Use ultrasonic at low powers (level 1 and 2 in CMi Zone 13 wet bench).

Note that several steps in my process flow were chosen precautionary and had not been optimized for time efficiency yet. For example, dehydration steps were conducted at rather low temperatures (and hence for longer periods of time) to avoid potential overstrain by thermal expansion of the metallic structures on the YIG surface. (I observed fractures of Au patterns on YIG after backing at 180°C for another sample, however the critical temperature was not explored.)

# C Scripts

## C.1 Numerical calculation of the CPW excitation profile

We assume a CPW with uniform current densities in signal and ground lines, respectively. The current in the signal line flows in  $-y$ -direction (compare with Fig. 3.1). Each ground line carries half the current in  $+y$  direction. We approximate the signal and ground lines by a series of infinite current carrying wires. The magnetic field of a infinite current carrying wire is analytically calculated by [261]

$$\mu_0 \mathbf{H} = \frac{\mu_0 I}{2\pi R} \hat{\Phi}, \quad (\text{C.1})$$

where  $R = \sqrt{(x - x_0)^2 + (z - z_0)^2}$  represents the radial distance from the wire center at  $(x_0, z_0)$  and  $\hat{\Phi}$  is the tangential unit vector. In the Python 3.7 script shown below, we sum over the field contributions of many wires, spaced throughout the cross-sectional area of signal and ground lines. We assume a current of  $I = 1$  A in the signal line.

Listing C.1 – Python 3 script for CPW excitation profile

```
1
2 import numpy as np
3 import matplotlib.pyplot as plt
4 from scipy import fftpack
5
6 plt.rcParams.update({'figure.figsize': [9,3]})
7
8 Off = 1e-6
9 m0 = 4*np.pi*1e-7 # vacuum permability [N/A^2]
10
11 #CPW geometrical parameters in [m]
12 width=2.1e-6
13 gap=1.4e-6
14 thickness = 0.11e-6
15
16 #Field read out below the CPW with distance d – half film thickness might be taken if
17   CPW is directly on top of film
18 d = 0.01e-6 #below CPW
```

## Appendix C. Scripts

---

```
19 # field evaluted in x-direction over a distance:
20 length=100e-6 # units in um
21
22 N=10000 # x-steps
23
24 xnew = np.linspace(-length/2, length/2, num=N, endpoint=True)
25
26
27
28 # Field of current carrying wire
29 # x-component
30 def fieldZOff(x,y,Offx):
31     x = x-Offx #Offx: x-coordinate of wire center
32     r = np.sqrt(x**2+y**2)
33     phi = np.arctan(x/y)
34     mag = 1/r
35     return mag* np.sin(phi)*m0/(2*np.pi)
36
37 # z-component
38 def fieldXOff(x,y,Offx):
39     x = x-Offx #Offx: x-coordinate of wire center
40     r = np.sqrt(x**2+y**2)
41     phi = np.arctan(x/y)
42     mag = 1/r
43     return mag* np.cos(phi)*m0/(2*np.pi)
44
45
46 GL_off=width+gap #shift of ground line compared to signal line
47
48 points1 = 500 #iterating wire center position over point1 - points in x-driection
49 points2 = 10 #iterating wire center position over point2 - points in z-driection
50
51 OffsetX= np.linspace(-width/2,width/2, points1,endpoint=True)
52 OffsetY= np.linspace(0,thickness, points2,endpoint=True)
53
54 Hx=0
55 Hz=0
56 for z in OffsetY:
57     for i in OffsetX:
58         # print(i)
59         Hx = Hx+fieldXOff(xnew,d+z,i)-0.5*fieldXOff(xnew,d+z,i-GL_off)-0.5*fieldXOff(xnew,d+z,-
60             i+GL_off)
61         Hz = Hz+fieldZOff(xnew,d+z,i)-0.5*fieldZOff(xnew,d+z,i-GL_off)-0.5*fieldZOff(xnew,d+z,-
62             i+GL_off)
63
64
65 Hx = Hx/(points1*points2) #normalize by number of points. Total current in signal line
66 is 1 Ampere
67 Hz = Hz/(points1*points2)
68
69 f, (ax1, ax2) = plt.subplots(1, 2)
70 ax1.plot(xnew*1e6,Hx, label="hz")
71 ax1.plot(xnew*1e6,Hx, label="hx")
```

### C.1. Numerical calculation of the CPW excitation profile

```
68 ax1.set_xlim(-10,10)
69 ax1.legend()
70 # plt.hlines(y=0.2999199,xmin=xnew[0]*1e6,xmax=xnew[-1]*1e6,linestyle='dashed')
71 ax1.set_xlabel('Position (micrometer)')
72 ax1.set_ylabel('Field (T) per 1 Amper input')
73 ##
74 ftX=fftpack.fft(Hx)
75 ftZ=fftpack.fft(Hz)
76
77 k=np.arange(len(ftX))*np.pi*2*1e-6/length
78 ax2.plot(k,np.abs(ftX),label="hx")
79 ax2.plot(k,np.abs(ftZ),label="hz")
80 ax2.legend()
81 ax2.set_xlabel('k_x (rad/um)')
82 ax2.set_ylabel('FFT amplitude (arb.units)')
83 ax2.set_xlim(0,10)
84 plt.tight_layout()
85 plt.show()
86 plt.savefig('CPW_Field.pdf')
```

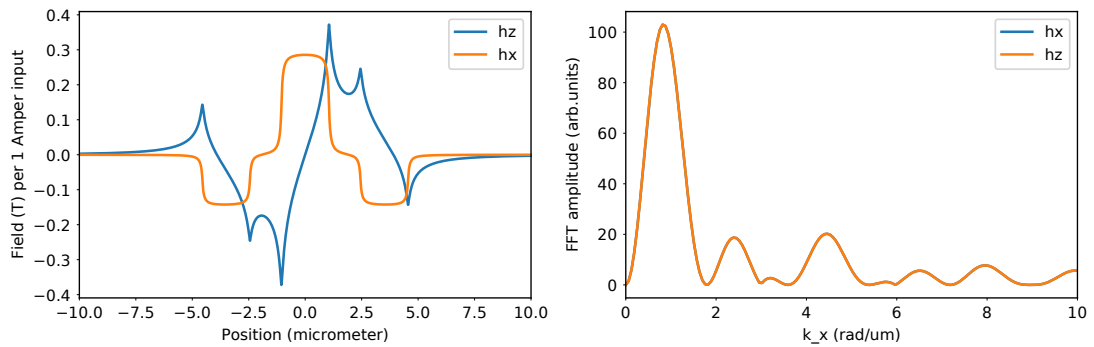


Figure C.1 – Output file of the Python 3 script. The results are in very good correspondence with more involved Comsol Multiphysics® simulations (cf. Fig. 3.2).



# Bibliography

- [1] Krawczyk, M. & Grundler, D. Review and prospects of magnonic crystals and devices with reprogrammable band structure. *J. Phys.: Condens. Matter* **26**, 123202 (2014). DOI: 10.1088/0953-8984/26/12/123202.
- [2] Lenk, B., Ulrichs, H., Garbs, F. & Münzenberg, M. The building blocks of magnonics. *Phys. Rep.* **507**, 107 – 136 (2011). DOI: 10.1016/j.physrep.2011.06.003.
- [3] Chumak, A. V., Serga, A. A. & Hillebrands, B. Magnonic crystals for data processing. *J. Phys. D: Appl. Phys.* **50**, 244001 (2017). DOI: 10.1088/1361-6463/aa6a65.
- [4] Phillips, T. G. & Rosenberg, H. M. Spin waves in ferromagnets. *Rep. Prog. Phys.* **29**, 285–332 (1966). DOI: 10.1088/0034-4885/29/1/307.
- [5] Yu, H., d'Allivy Kelly, O., Cros, V., Bernard, R., Bortolotti, P., Anane, A., Brandl, F., Heimbach, F. & Grundler, D. Approaching soft X-ray wavelengths in nanomagnet-based microwave technology. *Nat. Commun.* **7**, 11255 (2016). DOI: 10.1038/ncomms11255.
- [6] Kruglyak, V. V., Demokritov, S. O. & Grundler, D. Magnonics. *J. Phys. D: Appl. Phys.* **43**, 264001 (2010). DOI: 10.1088/0022-3727/43/26/264001.
- [7] Chumak, A. V., Vasyuchka, V. I., Serga, A. A. & Hillebrands, B. Magnon spintronics. *Nat. Phys.* **11**, 453–461 (2015). DOI: 10.1038/nphys3347.
- [8] Ashton, K. *et al.* That 'Internet of Things' Thing. *RFID Journal* **22**, 97–114 (2009).
- [9] "Global IoT market will grow to 24.1 billion devices in 2030, generating \$1.5 trillion annual revenue". <https://transformainsights.com/news/iot-market-24-billion-usd15-trillion-revenue-2030> (2020). Accessed: 2020-11-24.
- [10] Häggström, F. & Delsing, J. IoT Energy Storage - A Forecast. *Energy Harvesting and Systems* **5**, 43–51 (2018). DOI: 10.1515/ehs-2018-0010.
- [11] Bronckers, S., Roc'h, A. & Smolders, B. Wireless Receiver Architectures Towards 5G: Where Are We? *IEEE Circuits Syst. Mag.* **17**, 6–16 (2017). DOI: 10.1109/MCAS.2017.2713306.
- [12] Adam, J. D. Analog signal processing with microwave magnetics. *Proc. IEEE* **76**, 159–170 (1988). DOI: 10.1109/5.4392.
- [13] Ishak, W. S. Magnetostatic wave technology: a review. *Proc. IEEE* **76**, 171–187 (1988). DOI: 10.1109/5.4393.

## Bibliography

---

- [14] Serga, A. A., Chumak, A. V. & Hillebrands, B. YIG magnonics. *J. Phys. D: Appl. Phys.* **43**, 264002 (2010). DOI: 10.1088/0022-3727/43/26/264002.
- [15] Stamps, R. L., Breitkreutz, S., Åkerman, J. *et al.* The 2014 Magnetism Roadmap. *J. Phys. D: Appl. Phys.* **47**, 333001 (2014). DOI: 10.1088/0022-3727/47/33/333001.
- [16] Grundler, D. Nanomagnonics. *J. Phys. D: Appl. Phys.* **49**, 391002 (2016). DOI: 10.1088/0022-3727/49/39/391002.
- [17] Khitun, A., Bao, M. & Wang, K. L. Magnonic logic circuits. *J. Phys. D: Appl. Phys.* **43**, 264005 (2010). DOI: 10.1088/0022-3727/43/26/264005.
- [18] Csaba, G., Papp, Á. & Porod, W. Perspectives of using spin waves for computing and signal processing. *Phys. Lett. A* **381**, 1471 – 1476 (2017). DOI: 10.1016/j.physleta.2017.02.042.
- [19] Dieny, B., Prejbeanu, I. L., Garello, K. *et al.* Opportunities and challenges for spintronics in the microelectronics industry. *Nat. Electron.* **3**, 446–459 (2020). DOI: 10.1038/s41928-020-0461-5.
- [20] Veselago, V. G. The Electrodynamics of substances with simulatnously negative values  $\epsilon$  and  $\mu$ . *Sov. Phys. Uspekhi* **10**, 509–514 (1968). DOI: 10.1070/pu1968v010n04abeh003699.
- [21] Shelby, R. A., Smith, D. R. & Schultz, S. Experimental Verification of a Negative Index of Refraction. *Science* **292**, 77–79 (2001). DOI: 10.1126/science.1058847.
- [22] Shvets, G. & Urzhumov, Y. A. Electric and magnetic properties of sub-wavelength plasmonic crystals. *J. Opt. A: Pure Appl. Opt.* **7**, S23–S31 (2005). DOI: 10.1088/1464-4258/7/2/003.
- [23] Gorishnyy, T., Maldovan, M., Ullal, C. & Thomas, E. Sound ideas. *Phys. World* **18**, 24–29 (2005). DOI: 10.1088/2058-7058/18/12/30.
- [24] Vasseur, J. O., Dobrzynski, L., Djafari-Rouhani, B. & Puzzkarski, H. Magnon band structure of periodic composites. *Phys. Rev. B* **54**, 1043–1049 (1996). DOI: 10.1103/PhysRevB.54.1043.
- [25] Gulyaev, Y. V. & Nikitov, A. A. Magnonic crystals and spin waves in periodic structures. *Doklady Physics* **46**, 687–689 (2001). DOI: 10.1134/1.1415579.
- [26] Gubbiotti, G., Tacchi, S., Madami, M., Carlotti, G., Adeyeye, A. O. & Kostylev, M. Brillouin light scattering studies of planar metallic magnonic crystals. *J. Phys. D: Appl. Phys.* **43**, 264003 (2010). DOI: 10.1088/0022-3727/43/26/264003.
- [27] Gubbiotti, G. (ed.). *Three-Dimensional Magnonics*. Jenny Stanford Publishing, New York (2019). DOI: 10.1201/9780429299155.
- [28] Sykes, C. G., Adam, J. D. & Collins, J. H. Magnetostatic wave propagation in a periodic structure. *Appl. Phys. Lett.* **29**, 388–391 (1976). DOI: 10.1063/1.89098.
- [29] Parekh, J. P. & Tuan, H. S. Magnetostatic surface wave reflectivity of a shallow groove on a YIG film. *Appl. Phys. Lett.* **30**, 667–669 (1977). DOI: 10.1063/1.89279.
- [30] Reed, K., Owens, J. & Carter, R. Current status of magnetostatic reflective array filters. *Circuits, Syst. Signal Process.* **4**, 157–180 (1985). DOI: 10.1007/BF01600078.



- [31] Chumak, A. V., Serga, A. A., Wolff, S., Hillebrands, B. & Kostylev, M. P. Design and optimization of one-dimensional ferrite-film based magnonic crystals. *J. Appl. Phys.* **105**, 083906 (2009). DOI: 10.1063/1.3098258.
- [32] Gubbiotti, G., Tacchi, S., Carlotti, G., Vavassori, P., Singh, N., Goolaup, S., Adeyeye, A. O., Stashkevich, A. & Kostylev, M. Magnetostatic interaction in arrays of nanometric permalloy wires: A magneto-optic Kerr effect and a Brillouin light scattering study. *Phys. Rev. B* **72**, 224413 (2005). DOI: 10.1103/physrevb.72.224413.
- [33] Gubbiotti, G., Tacchi, S., Carlotti, G., Singh, N., Goolaup, S., Adeyeye, A. O. & Kostylev, M. Collective spin modes in monodimensional magnonic crystals consisting of dipolarly coupled nanowires. *Appl. Phys. Lett.* **90**, 092503 (2007). DOI: 10.1063/1.2709909.
- [34] Topp, J., Heitmann, D., Kostylev, M. P. & Grundler, D. Making a Reconfigurable Artificial Crystal by Ordering Bistable Magnetic Nanowires. *Phys. Rev. Lett.* **104**, 207205 (2010). DOI: 10.1103/PhysRevLett.104.207205.
- [35] Wang, Z. K., Zhang, V. L., Lim, H. S., Ng, S. C., Kuok, M. H., Jain, S. & Adeyeye, A. O. Observation of frequency band gaps in a one-dimensional nanostructured magnonic crystal. *Appl. Phys. Lett.* **94**, 083112 (2009). DOI: 10.1063/1.3089839.
- [36] Mruczkiewicz, M., Krawczyk, M., Sakharov, V. K., Khivintsev, Y. V., Filimonov, Y. A. & Nikitov, S. A. Standing spin waves in magnonic crystals. *J. Appl. Phys.* **113**, 093908 (2013). DOI: 10.1063/1.4793085.
- [37] Wang, Z. K., Zhang, V. L., Lim, H. S., Ng, S. C., Kuok, M. H., Jain, S. & Adeyeye, A. O. Nanostructured Magnonic Crystals with Size-Tunable Bandgaps. *ACS Nano* **4**, 643–648 (2010). DOI: 10.1021/nn901171u.
- [38] Obry, B., Pirro, P., Brächer, T., Chumak, A. V., Osten, J., Ciubotaru, F., Serga, A. A., Fassbender, J. & Hillebrands, B. A micro-structured ion-implanted magnonic crystal. *Appl. Phys. Lett.* **102**, 202403 (2013). DOI: 10.1063/1.4807721.
- [39] Vogel, M., Chumak, A. V., Waller, E. H., Langner, T., Vasyuchka, V. I., Hillebrands, B. & von Freymann, G. Optically reconfigurable magnetic materials. *Nat. Phys.* **11**, 487–491 (2015). DOI: 10.1038/nphys3325.
- [40] Popkov, A. F., Fetisov, Y. K. & Ostrovskii, N. V. Parametric interaction of volume magnetostatic waves in a ferrite film with spatiotemporal modulation of the magnetic field. *Techn. Phys.* **43**, 576–583 (1998). DOI: 10.1134/1.1259013.
- [41] Chumak, A. V., Neumann, T., Serga, A. A., Hillebrands, B. & Kostylev, M. P. A current-controlled, dynamic magnonic crystal. *J. Phys. D: Appl. Phys.* **42**, 205005 (2009). DOI: 10.1088/0022-3727/42/20/205005.
- [42] Karenowska, A. D., Gregg, J. E., Tiberkevich, V. S., Slavin, A. N., Chumak, A. V., Serga, A. A. & Hillebrands, B. Oscillatory Energy Exchange between Waves Coupled by a Dynamic Artificial Crystal. *Phys. Rev. Lett.* **108**, 015505 (2012). DOI: 10.1103/PhysRevLett.108.015505.
- [43] Mathieu, C., Jorzick, J., Frank, A. *et al.* Lateral Quantization of Spin Waves in Micron Size Magnetic Wires. *Phys. Rev. Lett.* **81**, 3968–3971 (1998). DOI: 10.1103/PhysRevLett.81.3968.

## Bibliography

---

- [44] Guslienko, K. Y., Demokritov, S. O., Hillebrands, B. & Slavin, A. N. Effective dipolar boundary conditions for dynamic magnetization in thin magnetic stripes. *Phys. Rev. B* **66**, 132402 (2002). DOI: 10.1103/PhysRevB.66.132402.
- [45] Ding, J., Kostylev, M. & Adeyeye, A. O. Magnonic Crystal as a Medium with Tunable Disorder on a Periodical Lattice. *Phys. Rev. Lett.* **107**, 047205 (2011). DOI: 10.1103/PhysRevLett.107.047205.
- [46] Topp, J., Duerr, G., Thurner, K. & Grundler, D. Reprogrammable magnonic crystals formed by interacting ferromagnetic nanowires. *Pure Appl. Chem.* **83**, 1989–2001 (2011). DOI: 10.1351/pac-con-11-03-06.
- [47] Ding, J., Kostylev, M. & Adeyeye, A. O. Realization of a mesoscopic reprogrammable magnetic logic based on a nanoscale reconfigurable magnonic crystal. *Appl. Phys. Lett.* **100**, 073114 (2012). DOI: 10.1063/1.3687177.
- [48] Huber, R., Krawczyk, M., Schwarze, T., Yu, H., Duerr, G., Albert, S. & Grundler, D. Reciprocal Damon-Eshbach-type spin wave excitation in a magnonic crystal due to tunable magnetic symmetry. *Appl. Phys. Lett.* **102**, 012403 (2013). DOI: 10.1063/1.4773522.
- [49] Huber, R., Schwarze, T. & Grundler, D. Nanostripe of subwavelength width as a switchable semitransparent mirror for spin waves in a magnonic crystal. *Phys. Rev. B* **88**, 100405 (2013). DOI: 10.1103/PhysRevB.88.100405.
- [50] Baumgaertl, K., Watanabe, S. & Grundler, D. Phase control of spin waves based on a magnetic defect in a one-dimensional magnonic crystal. *Appl. Phys. Lett.* **112**, 142405 (2018). DOI: 10.1063/1.5024541.
- [51] Dmitriev, V. F. & Kalinikos, B. A. Excitation of propagating magnetization waves by microstrip antennas. *Sov. Phys. J.* **31**, 875–898 (1988). DOI: 10.1007/bf00893541.
- [52] Kennewell, K. J., Kostylev, M. & Stamps, R. L. Calculation of spin wave mode response induced by a coplanar microwave line. *J. Appl. Phys.* **101**, 09D107 (2007). DOI: 10.1063/1.2710068.
- [53] Ciubotaru, F., Devolder, T., Manfrini, M., Adelmann, C. & Radu, I. P. All electrical propagating spin wave spectroscopy with broadband wavevector capability. *Appl. Phys. Lett.* **109**, 012403 (2016). DOI: 10.1063/1.4955030.
- [54] Yu, H., Duerr, G., Huber, R., Bahr, M., Schwarze, T., Brandl, F. & Grundler, D. Omnidirectional spin-wave nanograting coupler. *Nat. Commun.* **4**, 2702 (2013). DOI: 10.1038/ncomms3702.
- [55] Maendl, S., Stasinopoulos, I. & Grundler, D. Spin waves with large decay length and few 100 nm wavelengths in thin yttrium iron garnet grown at the wafer scale. *Appl. Phys. Lett.* **111**, 012403 (2017). DOI: 10.1063/1.4991520.
- [56] Liu, C., Chen, J., Liu, T. *et al.* Long-distance propagation of short-wavelength spin waves. *Nat. Commun.* **9**, 1–8 (2018). DOI: 10.1038/s41467-018-03199-8.
- [57] Baumgaertl, K., Gräfe, J., Che, P., Mucchietto, A., Förster, J., Träger, N., Bechtel, M., Weigand, M., Schütz, G. & Grundler, D. Nanoimaging of Ultrashort Magnon Emission by Ferromagnetic Grating Couplers at GHz Frequencies. *Nano Lett.* **20**, 7281–7286 (2020). DOI: 10.1021/acs.nanolett.0c02645.

- [58] Demidov, V. E., Kostylev, M. P., Rott, K., Münchenberger, J., Reiss, G. & Demokritov, S. O. Excitation of short-wavelength spin waves in magnonic waveguides. *Appl. Phys. Lett.* **99**, 082507 (2011). DOI: 10.1063/1.3631756.
- [59] Che, P., Baumgaertl, K., Kúkol'ová, A., Dubs, C. & Grundler, D. Efficient wavelength conversion of exchange magnons below 100 nm by magnetic coplanar waveguides. *Nat. Commun.* **11** (2020). DOI: 10.1038/s41467-020-15265-1.
- [60] Csaba, G., Papp, Á. & Porod, W. Perspectives of using spin waves for computing and signal processing. *Phys. Lett. A* **381**, 1471–1476 (2017). DOI: 10.1016/j.physleta.2017.02.042.
- [61] Han, J., Zhang, P., Hou, J. T., Siddiqui, S. A. & Liu, L. Mutual control of coherent spin waves and magnetic domain walls in a magnonic device. *Science* **366**, 1121–1125 (2019). DOI: 10.1126/science.aau2610.
- [62] Stöhr, J. & Siegmann, H. *Magnetism: From Fundamentals to Nanoscale Dynamics*. Springer Series in Solid-State Sciences Springer (2006). DOI: 10.1007/978-3-540-30283-4.
- [63] Nolting, W. & Ramakanth, A. *Quantum Theory of Magnetism*. Springer Berlin Heidelberg (2009). DOI: 10.1007/978-3-540-85416-6.
- [64] Gurevich, A. & Melkov, G. *Magnetization Oscillations and Waves*. Taylor & Francis (1996). ISBN: 9780849394607.
- [65] Gross, R. & Marx, A. *Festkörperphysik*. De Gruyter Oldenbourg (2014). DOI: 10.1524/9783110358704.
- [66] Stefanita, C.-G. *Magnetism*. Springer Berlin Heidelberg (2012). DOI: 10.1007/978-3-642-22977-0.
- [67] W, A., Ashcroft, N., Mermin, N., Mermin, N. & Company, B. P. *Solid State Physics*. Holt, Rinehart and Winston (1976). ISBN: 9780030839931.
- [68] Holtzberg, F., McGuire, T. R., Methfessel, S. & Suits, J. C. Ferromagnetism in Rare-Earth Group VA and VIA Compounds with Th<sub>3</sub>P<sub>4</sub> Structure. *J. Appl. Phys.* **35**, 1033–1038 (1964). DOI: 10.1063/1.1713367.
- [69] Brown, W. *Micromagnetics*. Interscience Publishers, J. Wiley (1963). ISBN: 0470110376.
- [70] Herring, C. & Kittel, C. On the Theory of Spin Waves in Ferromagnetic Media. *Phys. Rev.* **81**, 869–880 (1951). DOI: 10.1103/PhysRev.81.869.
- [71] Rüffer, D. *Magnetic states and spin-wave modes in single ferromagnetic nanotubes*. Ph.D. thesis, Lausanne, EPFL (2014).
- [72] Schlömann, E. A Sum Rule Concerning the Inhomogeneous Demagnetizing Field in Nonellipsoidal Samples. *J. Appl. Phys.* **33**, 2825–2826 (1962). DOI: 10.1063/1.1702557.
- [73] Aharoni, A. Demagnetizing factors for rectangular ferromagnetic prisms. *J. Appl. Phys.* **83**, 3432–3434 (1998). DOI: 10.1063/1.367113.
- [74] Hubert, A. & Schäfer, R. *Magnetic Domains: The Analysis of Magnetic Microstructures*. Springer (1998). ISBN: 9783540641087.

## Bibliography

---

- [75] Yin, L. F., Wei, D. H., Lei, N., Zhou, L. H., Tian, C. S., Dong, G. S., Jin, X. F., Guo, L. P., Jia, Q. J. & Wu, R. Q. Magnetocrystalline Anisotropy in Permalloy Revisited. *Phys. Rev. Lett.* **97**, 067203 (2006). DOI: 10.1103/PhysRevLett.97.067203.
- [76] Rao, Y., Zhang, D., Zhang, H., Jin, L., Yang, Q., Zhong, Z., Li, M., Hong, C. & Ma, B. Thickness dependence of magnetic properties in submicron yttrium iron garnet films. *J. Phys. D: Appl. Phys.* **51**, 435001 (2018). DOI: 10.1088/1361-6463/aade43.
- [77] Landau, L. D. & Lifshitz, E. On the theory of the dispersion of magnetic permeability in ferromagnetic bodies. *Phys. Z. Sowjet.* **8**, 153 (1935). DOI: 10.1016/B978-0-08-036364-6.50008-9.
- [78] Gilbert, T. L. A Lagrangian formulation of the gyromagnetic equation of the magnetization field. *Phys. Rev.* **100**, 1243 (1955).
- [79] Polder, D. VIII. On the theory of ferromagnetic resonance. *Lond. Edinb. Dubl. Phil. Mag.* **40**, 99–115 (1949). DOI: 10.1080/14786444908561215.
- [80] Kittel, C. On the Theory of Ferromagnetic Resonance Absorption. *Phys. Rev.* **73**, 155–161 (1948). DOI: 10.1103/PhysRev.73.155.
- [81] Giesen, F. *Magnetization Dynamics of Nanostructured Ferromagnetic Rings and Rectangular Elements*. Cuvillier Verlag (2005). ISBN: 9783865376305.
- [82] Huber, R. *Control of spin waves on the nanoscale in one-dimensional magnonic crystals and atomic layer deposition of metallic ferromagnets for second generation of nanomaterials*. Ph.D. thesis, Technische Universität München (2013).
- [83] Bilzer, C. *Microwave susceptibility of thin ferromagnetic films: metrology and insight into magnetization dynamics*. Theses, Université Paris Sud - Paris XI (2007). URL <https://tel.archives-ouvertes.fr/tel-00202827>.
- [84] Yu, H., Huber, R., Schwarze, T., Brandl, F., Rapp, T., Berberich, P., Duerr, G. & Grundler, D. High propagating velocity of spin waves and temperature dependent damping in a CoFeB thin film. *Appl. Phys. Lett.* **100**, 262412 (2012). DOI: 10.1063/1.4731273.
- [85] Brandl, F. *Thermal effects in laser-heated freestanding permalloy and multiferroic hybrid structures forming magnonic grating couplers and prototype spin wave multiplexers*. Ph.D. thesis, Technische Universität München (2014).
- [86] Kalinikos, B. A. & Slavin, A. N. Theory of dipole-exchange spin wave spectrum for ferromagnetic films with mixed exchange boundary conditions. *J. Phys. C: Solid State Phys.* **19**, 7013–7033 (1986). DOI: 10.1088/0022-3719/19/35/014.
- [87] Kronmüller, H. Mikromagnetische Berechnung der Magnetisierung in der Umgebung unmagnetischer Einschlüsse in Ferromagnetika. *Z. Phys.* **168**, 478–494 (1962). DOI: 10.1007/BF01378144.
- [88] Abo, G. S., Hong, Y., Park, J., Lee, J., Lee, W. & Choi, B. Definition of Magnetic Exchange Length. *IEEE Trans. Magn.* **49**, 4937–4939 (2013). DOI: 10.1109/TMAG.2013.2258028.
- [89] Krawczyk, M. & Puzskarski, H. Plane-wave theory of three-dimensional magnonic crystals. *Phys. Rev. B* **77**, 054437 (2008). DOI: 10.1103/PhysRevB.77.054437.

- 
- [90] Dvornik, M., Au, Y. & Kruglyak, V. V. Micromagnetic Simulations in Magnonics. In *Topics in Applied Physics*, 101–115 (Springer Berlin Heidelberg, 2012).
  - [91] Vansteenkiste, A., Leliaert, J., Dvornik, M., Helsen, M., Garcia-Sanchez, F. & Van Waeyenberge, B. The design and verification of MuMax3. *AIP Adv.* **4**, 107133 (2014). DOI: 10.1063/1.4899186.
  - [92] Kumar, D. & Adeyeye, A. O. Techniques in micromagnetic simulation and analysis. *J. Phys. D: Appl. Phys.* **50**, 343001 (2017). DOI: 10.1088/1361-6463/aa7c04.
  - [93] Hartmann, U. Magnetic Force Microscopy. *Annu. Rev. Mater. Sci.* **29**, 53–87 (1999). DOI: 10.1146/annurev.matsci.29.1.53.
  - [94] Thiaville, A., Miltat, J. & García, J. Magnetic Force Microscopy: Images of Nanostructures and Contrast Modeling. In *Magnetic Microscopy of Nanostructures*, 225–251 (Springer, 2005).
  - [95] Weigand, M. *Realization of a new magnetic scanning X-ray microscope and investigation of Landau structures under pulsed field excitation*. Cuvillier Verlag (2015). ISBN: 9783736949911.
  - [96] Stoll, H., Noske, M., Weigand, M. *et al.* Imaging spin dynamics on the nanoscale using X-Ray microscopy. *Front. Phys.* **3**, 26 (2015). DOI: 10.3389/fphy.2015.00026.
  - [97] Follath, R., Schmidt, J. S., Weigand, M. & Fauth, K. The X-ray microscopy beamline UE46-PGM2 at BESSY. *AIP Conf. Proc.* **1234** (2010). DOI: 10.1063/1.3463201.
  - [98] Griffiths, J. H. Anomalous high-frequency resistance of ferromagnetic metals. *Nature* **158**, 670–671 (1946). DOI: 10.1038/158670a0.
  - [99] Yager, W. A., Galt, J. K., Merritt, F. R. & Wood, E. A. Ferromagnetic Resonance in Nickel Ferrite. *Phys. Rev.* **80**, 744–748 (1950). DOI: 10.1103/PhysRev.80.744.
  - [100] Bailleul, M., Olligs, D., Fermon, C. & Demokritov, S. O. Spin waves propagation and confinement in conducting films at the micrometer scale. *EPL* **56**, 741–747 (2001). DOI: 10.1209/epl/i2001-00583-2.
  - [101] Bailleul, M., Olligs, D. & Fermon, C. Propagating spin wave spectroscopy in a permalloy film: A quantitative analysis. *Appl. Phys. Lett.* **83**, 972–974 (2003). DOI: 10.1063/1.1597745.
  - [102] Egan, W. F. E. *Practical RF Design*. John Wiley and Sons (2003). DOI: 10.1002/0471654094.
  - [103] Wadell, B. *Transmission Line Design Handbook*. Artech House (1991). ISBN: 9780890064368.
  - [104] Stasinopoulos, I. *Low damping and linearly polarized GHz magnetization dynamics in the chiral magnet Cu<sub>2</sub>OSeO<sub>3</sub> hosting spin helices and skyrmions*. Dissertation, Technische Universität München, München (2017). URL <http://nbn-resolving.de/urn/resolver.pl?urn:nbn:de:bvb:91-diss-20170323-1341337-1-8>.
  - [105] Mändl, S. H. M. *Spin waves in periodically patterned thin yttrium iron garnet films with lattice constants down to 100 nm produced by helium ion microscopy*. Dissertation, Technische Universität München, München (2017). URL <http://nbn-resolving.de/urn/resolver.pl?urn:nbn:de:bvb:91-diss-20171130-1380641-1-5>.
  - [106] Schwarze, T. *Spin Waves in 2D and 3D Magnonic Crystals: From Nanostructured Ferromagnetic Materials to Chiral Helimagnets*. Ph.D. thesis, Technische Universität München (2013).

## Bibliography

---

- [107] Neusser, S. *Spin waves in antidot lattices: From quantization to magnonic crystals*. Ph.D. thesis, Technische Universität München (2011). URL <http://nbn-resolving.de/urn/resolver.pl?urn:nbn:de:bvb:91-diss-20110420-1063590-1-5>.
- [108] Silva, T. J., Lee, C. S., Crawford, T. M. & Rogers, C. T. Inductive measurement of ultrafast magnetization dynamics in thin-film Permalloy. *J. Appl. Phys.* **85**, 7849–7862 (1999). DOI: 10.1063/1.370596.
- [109] Edwards, T. C. & Steer, M. B. *Foundations for microstrip circuit design*. John Wiley & Sons (2016). DOI: 10.1002/9781118936160.
- [110] Van Rossum, G. & Drake, F. L. *Python 3 Reference Manual*. CreateSpace, Scotts Valley, CA (2009). ISBN: 1441412697.
- [111] Fallarino, L., Madami, M., Duerr, G., Grundler, D., Gubbiotti, G., Tacchi, S. & Carlotti, G. Propagation of Spin Waves Excited in a Permalloy Film by a Finite-Ground Coplanar Waveguide: A Combined Phase-Sensitive Micro-Focused Brillouin Light Scattering and Micromagnetic Study. *IEEE Trans. Magn.* **49**, 1033–1036 (2013). DOI: 10.1109/TMAG.2012.2229385.
- [112] Mucchietto, A. *Application and exploration of magnetic nanoparticles as magnetic scatterers in magnonic devices*. Ph.D. thesis, Politecnico di Torino (2018). URL <http://webthesis.biblio.polito.it/id/eprint/8479>.
- [113] Chang, C. S., Kostylev, M., Ivanov, E., Ding, J. & Adeyeye, A. O. The phase accumulation and antenna near field of microscopic propagating spin wave devices. *Appl. Phys. Lett.* **104**, 032408 (2014). DOI: 10.1063/1.4863078.
- [114] Neusser, S., Duerr, G., Bauer, H. G., Tacchi, S., Madami, M., Woltersdorf, G., Gubbiotti, G., Back, C. H. & Grundler, D. Anisotropic Propagation and Damping of Spin Waves in a Nanopatterned Antidot Lattice. *Phys. Rev. Lett.* **105**, 067208 (2010). DOI: 10.1103/PhysRevLett.105.067208.
- [115] On wafer vector network analyzer calibration and measurements. Tech. Rep., Cascade Microtech (1997). URL <https://www.cascademicrotech.com/files/ONWAFER.pdf>. Accessed: 2020–11.
- [116] Olson, T. *Applied Fourier Analysis*. Birkhäuser Basel (2017). DOI: 10.1007/978-1-4939-7393-4.
- [117] Brillouin, L. Diffusion de la lumière et des rayons X par un corps transparent homogène. *Annales de Physique* **9**, 88–122 (1922). DOI: 10.1051/anphys/192209170088.
- [118] Mandelstam, L. *Zh. Radio-Fiziko-Khimicheskogo Obshchestva* **58**, 381 (1926).
- [119] Cottam, M. *Light scattering in magnetic solids*. Wiley, New York (1986). ISBN: 9780471817017.
- [120] Sandercock, J. *Light Scattering in Solids*, Edited by M. Balkanski (1971). Paris: Flammarion Press.
- [121] Lindsay, S. M., Anderson, M. W. & Sandercock, J. R. Construction and alignment of a high performance multipass vernier tandem Fabry–Perot interferometer. *Rev. Sci. Instrum.* **52**, 1478–1486 (1981). DOI: 10.1063/1.1136479.
- [122] Hillebrands, B. Progress in multipass tandem Fabry–Perot interferometry: I. A fully automated, easy to use, self-aligning spectrometer with increased stability and flexibility. *Rev. Sci. Instrum.* **70**, 1589–1598 (1999). DOI: 10.1063/1.1149637.
- [123] Sandercock, J. & Wettling, W. Light scattering from thermal acoustic magnons in yttrium iron garnet. *Solid State Commun.* **13**, 1729–1732 (1973). DOI: 10.1016/0038-1098(73)90276-7.

- [124] Sebastian, T., Schultheiss, K., Obry, B., Hillebrands, B. & Schultheiss, H. Micro-focused Brillouin light scattering: imaging spin waves at the nanoscale. *Front. Phys.* **3**, 35 (2015). DOI: 10.3389/fphy.2015.00035.
- [125] Demokritov, S. & Demidov, V. Micro-Brillouin Light Scattering Spectroscopy of Magnetic Nanostructures. *IEEE Trans. Magn.* **44**, 6–12 (2008). DOI: 10.1109/tmag.2007.910227.
- [126] Demidov, V. E. & Demokritov, S. O. Magnonic Waveguides Studied by Microfocus Brillouin Light Scattering. *IEEE Trans. Magn.* **51**, 1–15 (2015). DOI: 10.1109/tmag.2014.2388196.
- [127] Demidov, V. E., Dzyapko, O., Demokritov, S. O., Melkov, G. A. & Slavin, A. N. Observation of Spontaneous Coherence in Bose-Einstein Condensate of Magnons. *Phys. Rev. Lett.* **100**, 047205 (2008). DOI: 10.1103/PhysRevLett.100.047205.
- [128] Sebastian, T., Ohdaira, Y., Kubota, T. *et al.* Low-damping spin-wave propagation in a microstructured Co<sub>2</sub>Mn<sub>0.6</sub>Fe<sub>0.4</sub>Si Heusler waveguide. *Appl. Phys. Lett.* **100**, 112402 (2012). DOI: 10.1063/1.3693391.
- [129] Serga, A. A., Schneider, T., Hillebrands, B., Demokritov, S. O. & Kostylev, M. P. Phase-sensitive Brillouin light scattering spectroscopy from spin-wave packets. *Appl. Phys. Lett.* **89**, 063506 (2006). DOI: 10.1063/1.2335627.
- [130] Fohr, F., Serga, A. A., Schneider, T., Hamrle, J. & Hillebrands, B. Phase sensitive Brillouin scattering measurements with a novel magneto-optic modulator. *Rev. Sci. Instrum.* **80**, 043903 (2009). DOI: 10.1063/1.3115210.
- [131] Vogt, K., Schultheiss, H., Hermsdoerfer, S. J., Pirro, P., Serga, A. A. & Hillebrands, B. All-optical detection of phase fronts of propagating spin waves in a Ni<sub>81</sub>Fe<sub>19</sub> microstripe. *Appl. Phys. Lett.* **95**, 182508 (2009). DOI: 10.1063/1.3262348.
- [132] Cui, Z. *Nanofabrication*. Springer US (2008). DOI: 10.1007/978-0-387-75577-9.
- [133] Grigorescu, A., van der Krogt, M., Hagen, C. & Kruit, P. 10 nm lines and spaces written in HSQ, using electron beam lithography. *Microelectron. Eng.* **84**, 822–824 (2007). DOI: 10.1016/j.mee.2007.01.022.
- [134] Yan, M., Lee, J., Ofuonye, B., Choi, S., Jang, J. H. & Adesida, I. Effects of salty-developer temperature on electron-beam-exposed hydrogen silsesquioxane resist for ultradense pattern transfer. *J. Vac. Sci. Technol. B* **28**, C6S23 (2010). DOI: 10.1116/1.3504497.
- [135] "Nano PMMA and Copolymer Developer". <https://kayakuam.com/wp-content/uploads/2019/09/pmma-1.pdf> (2020). Accessed: 2020-11-24.
- [136] *Developed and distributed by GenISys GmbH. Available from: <www.genisys-gmbh.com/>*. Accessed: 2020-11-24.
- [137] Unal, N., Charlton, M. D., Wang, Y., Waizmann, U., Reindl, T. & Hofmann, U. Easy to adapt electron beam proximity effect correction parameter calibration based on visual inspection of a "Best Dose Sensor". *Microelectron. Eng.* **88**, 2158 – 2162 (2011). DOI: 10.1016/j.mee.2011.02.066.
- [138] Khitun, A., Bao, M. & Wang, K. L. Magnonic logic circuits. *J. Phys. D: Appl. Phys.* **43**, 264005 (2010). DOI: 10.1088/0022-3727/43/26/264005.

## Bibliography

---

- [139] Hertel, R., Wulfhekel, W. & Kirschner, J. Domain-Wall Induced Phase Shifts in Spin Waves. *Phys. Rev. Lett.* **93**, 257202 (2004). DOI: 10.1103/PhysRevLett.93.257202.
- [140] Kostylev, M. P., Serga, A. A., Schneider, T., Leven, B. & Hillebrands, B. Spin-wave logical gates. *Appl. Phys. Lett.* **87**, 153501 (2005). DOI: 10.1063/1.2089147.
- [141] Schneider, T., Serga, A. A., Leven, B., Hillebrands, B., Stamps, R. L. & Kostylev, M. P. Realization of spin-wave logic gates. *Appl. Phys. Lett.* **92**, 022505 (2008). DOI: 10.1063/1.2834714.
- [142] Demokritov, S. O., Serga, A. A., André, A., Demidov, V. E., Kostylev, M. P., Hillebrands, B. & Slavin, A. N. Tunneling of Dipolar Spin Waves through a Region of Inhomogeneous Magnetic Field. *Phys. Rev. Lett.* **93**, 047201 (2004). DOI: 10.1103/PhysRevLett.93.047201.
- [143] Haldar, A., Kumar, D. & Adeyeye, A. O. A reconfigurable waveguide for energy-efficient transmission and local manipulation of information in a nanomagnetic device. *Nat. Nanotechnol.* **11**, 437–443 (2016). DOI: 10.1038/nnano.2015.332.
- [144] Zhang, V. L., Lim, H. S., Ng, S. C., Kuok, M. H., Zhou, X. & Adeyeye, A. O. Spin-wave dispersion of nanostructured magnonic crystals with periodic defects. *AIP Adv.* **6**, 115106 (2016). DOI: 10.1063/1.4967334.
- [145] Demidov, V. E., Kostylev, M. P., Rott, K., Krzysteczko, P., Reiss, G. & Demokritov, S. O. Excitation of microwaveguide modes by a stripe antenna. *Appl. Phys. Lett.* **95**, 112509 (2009). DOI: 10.1063/1.3231875.
- [146] Demokritov, S., Hillebrands, B. & Slavin, A. Brillouin light scattering studies of confined spin waves: linear and nonlinear confinement. *Phys. Rep.* **348**, 441 – 489 (2001). DOI: 10.1016/S0370-1573(00)00116-2.
- [147] Bailleul, M., Olligs, D. & Fermon, C. Propagating spin wave spectroscopy in a permalloy film: A quantitative analysis. *Appl. Phys. Lett.* **83**, 972–974 (2003). DOI: 10.1063/1.1597745.
- [148] Bayer, C., Demokritov, S. O., Hillebrands, B. & Slavin, A. N. Spin-wave wells with multiple states created in small magnetic elements. *Appl. Phys. Lett.* **82**, 607–609 (2003). DOI: 10.1063/1.1540734.
- [149] Schneider, T., Serga, A. A., Chumak, A. V., Hillebrands, B., Stamps, R. L. & Kostylev, M. P. Spin-wave tunnelling through a mechanical gap. *EPL* **90**, 27003 (2010). DOI: 10.1209/0295-5075/90/27003.
- [150] Hämäläinen, S. J., Brandl, F., Franke, K. J. A., Grundler, D. & van Dijken, S. Tunable Short-Wavelength Spin-Wave Emission and Confinement in Anisotropy-Modulated Multiferroic Heterostructures. *Phys. Rev. Applied* **8**, 014020 (2017). DOI: 10.1103/PhysRevApplied.8.014020.
- [151] Botters, B., Giesen, F., Podbielski, J., Bach, P., Schmidt, G., Molenkamp, L. W. & Grundler, D. Stress dependence of ferromagnetic resonance and magnetic anisotropy in a thin NiMnSb film on InP(001). *Appl. Phys. Lett.* **89**, 242505 (2006). DOI: 10.1063/1.2405885.
- [152] Cherepov, S. *et al.* Electric-field-induced spin wave generation using multiferroic magnetoelectric cells. *Appl. Phys. Lett.* **104**, 082403 (2014). DOI: 10.1063/1.4865916.
- [153] Klingler, S., Pirro, P., Brächer, T., Leven, B., Hillebrands, B. & Chumak, A. V. Design of a spin-wave majority gate employing mode selection. *Appl. Phys. Lett.* **105**, 152410 (2014). DOI: 10.1063/1.4898042.



- 
- [154] Fangohr, H., Bordignon, G., Franchin, M., Knittel, A., de Groot, P. A. J. & Fischbacher, T. A new approach to (quasi) periodic boundary conditions in micromagnetics: The macrogeometry. *J. Appl. Phys.* **105**, 07D529 (2009). DOI: 10.1063/1.3068637.
  - [155] Bilzer, C., Devolder, T., Kim, J.-V., Counil, G., Chappert, C., Cardoso, S. & Freitas, P. P. Study of the dynamic magnetic properties of soft CoFeB films. *J. Appl. Phys.* **100**, 053903 (2006). DOI: 10.1063/1.2337165.
  - [156] Devolder, T., Kim, J.-V., Nistor, L., Sousa, R., Rodmacq, B. & Diény, B. Exchange stiffness in ultra-thin perpendicularly magnetized CoFeB layers determined using the spectroscopy of electrically excited spin waves. *J. Appl. Phys.* **120**, 183902 (2016). DOI: 10.1063/1.4967826.
  - [157] Dvornik, M., Kuchko, A. N. & Kruglyak, V. V. Micromagnetic method of s-parameter characterization of magnonic devices. *J. Appl. Phys.* **109**, 07D350 (2011). DOI: 10.1063/1.3562519.
  - [158] Mercier, D. & Lévy, J.-C. S. Roughness effects on spin waves. *J. Magn. Magn. Mater.* **163**, 207–215 (1996). DOI: 10.1016/s0304-8853(96)00300-9.
  - [159] Venkat, G., Fangohr, H. & Prabhakar, A. Absorbing boundary layers for spin wave micromagnetics. *J. Magn. Magn. Mater.* **450**, 34 – 39 (2018). DOI: 10.1016/j.jmmm.2017.06.057.
  - [160] Zeisberger, M. & Mattheis, R. Magnetization reversal in magnetic nanostripes via Bloch wall formation. *J. Phys.: Condens. Matter* **24**, 024202 (2011). DOI: 10.1088/0953-8984/24/2/024202.
  - [161] Leliaert, J., Mulkers, J., De Clercq, J., Coene, A., Dvornik, M. & Van Waeyenberge, B. Adaptively time stepping the stochastic Landau-Lifshitz-Gilbert equation at nonzero temperature: Implementation and validation in MuMax3. *AIP Adv.* **7**, 125010 (2017). DOI: 10.1063/1.5003957.
  - [162] Smith, N. Modeling of thermal magnetization fluctuations in thin-film magnetic devices. *J. Appl. Phys.* **90**, 5768–5773 (2001). DOI: 10.1063/1.1402146.
  - [163] Yoon, J., You, C., Jo, Y., Park, S. & Jung, M. Micromagnetic Analysis of Magnetic Noise in Ferromagnetic Nanowires. *J. Korean Phys. Soc.* **57**, 1594–1599 (2010). DOI: 10.3938/jkps.57.1594.
  - [164] Ng, K. K. *Resonant-Tunneling Diode*, chap. 8, 75–83 (John Wiley & Sons, Ltd, 2009). ISBN: 9781118014769. <https://onlinelibrary.wiley.com/doi/pdf/10.1002/9781118014769.ch8>.
  - [165] Maendl, S., Stasinopoulos, I. & Grundler, D. Spin waves with large decay length and few 100 nm wavelengths in thin yttrium iron garnet grown at the wafer scale. *Appl. Phys. Lett.* **111**, 012403 (2017). DOI: 10.1063/1.4991520.
  - [166] Tacchi, S., Madami, M., Gubbiotti, G., Carlotti, G., Goolaup, S., Adeyeye, A. O., Singh, N. & Kostylev, M. P. Analysis of collective spin-wave modes at different points within the hysteresis loop of a one-dimensional magnonic crystal comprising alternative-width nanostripes. *Phys. Rev. B* **82**, 184408 (2010). DOI: 10.1103/PhysRevB.82.184408.
  - [167] Zhang, V. L., Lim, H. S., Lin, C. S., Wang, Z. K., Ng, S. C., Kuok, M. H., Jain, S., Adeyeye, A. O. & Cottam, M. G. Ferromagnetic and antiferromagnetic spin-wave dispersions in a dipole-exchange coupled bi-component magnonic crystal. *Appl. Phys. Lett.* **99**, 143118 (2011). DOI: 10.1063/1.3647952.

## Bibliography

---

- [168] Gubbiotti, G., Zhou, X., Haghshenasfard, Z., Cottam, M. G. & Adeyeye, A. O. Reprogrammable magnonic band structure of layered permalloy/Cu/permalloy nanowires. *Phys. Rev. B* **97**, 134428 (2018). DOI: 10.1103/PhysRevB.97.134428.
- [169] Neusser, S. & Grundler, D. Magnonics: Spin Waves on the Nanoscale. *Adv. Mater.* **21**, 2927–2932 (2009). DOI: 10.1002/adma.200900809.
- [170] Röschmann, P. YIG filters. *Philips Tech. Rev* **32**, 322–327 (1971).
- [171] Manuilov, S. A., Fors, R., Khartsev, S. I. & Grishin, A. M. Submicron  $\text{Y}_3\text{Fe}_5\text{O}_{12}$  Film Magnetostatic Wave Band Pass Filters. *J. Appl. Phys.* **105**, 033917 (2009). DOI: 10.1063/1.3075816.
- [172] Vogt, K., Fradin, E. Y., Pearson, J. E., Sebastian, T., Bader, S. D., Hillebrands, B., Hoffmann, A. & Schultheiss, H. Realization of a spin-wave multiplexer. *Nat. Commun.* **5**, 1–5 (2014). DOI: 10.1038/ncomms4727.
- [173] Heussner, E., Nabinger, M., Fischer, T., Brächer, T., Serga, A. A., Hillebrands, B. & Pirro, P. Frequency-Division Multiplexing in Magnonic Logic Networks Based on Caustic-Like Spin-Wave Beams. *Phys. Status Solidi RRL* **12**, 1800409 (2018). DOI: 10.1002/pssr.201800409.
- [174] Wang, X.-g., Chotorlishvili, L., Guo, G.-h. & Berakdar, J. Electric field controlled spin waveguide phase shifter in YIG. *J. Appl. Phys.* **124**, 073903 (2018). DOI: 10.1063/1.5037958.
- [175] Dobrovolskiy, O. V., Sachser, R., Bunyayev, S. A. *et al.* Spin-wave phase inverter upon a single nanodot. *ACS Appl. Mater. Interfaces* **11**, 17654–17662 (2019). DOI: 10.1021/acsami.9b02717.
- [176] Wang, Q., Pirro, P., Verba, R., Slavin, A., Hillebrands, B. & Chumak, A. V. Reconfigurable nanoscale spin-wave directional coupler. *Sci. Adv.* **4**, e1701517 (2018). DOI: 10.1126/sciadv.1701517.
- [177] Chumak, A. V., Vasyuchka, V. I., Serga, A. A., Kostylev, M. P., Tiberkevich, V. S. & Hillebrands, B. Storage-Recovery Phenomenon in Magnonic Crystal. *Phys. Rev. Lett.* **108**, 257207 (2012). DOI: 10.1103/PhysRevLett.108.257207.
- [178] Collier, R. J., Edgar, D. L., Yip, J. *et al.* A Study of High Frequency Performance of Coplanar Waveguide as a Function of Substrate Thickness. In *2000 30th European Microwave Conference*, 1–3 (2000). DOI: 10.1109/EUMA.2000.338733.
- [179] Heinz, B., Brächer, T., Schneider, M. *et al.* Propagation of Spin-Wave Packets in Individual Nanosized Yttrium Iron Garnet Magnonic Conduits. *Nano Lett.* **20**, 4220–4227 (2020). DOI: 10.1021/acs.nanolett.0c00657.
- [180] Wintz, S., Tiberkevich, V., Weigand, M., Raabe, J., Lindner, J., Erbe, A., Slavin, A. & Fassbender, J. Magnetic vortex cores as tunable spin-wave emitters. *Nat. Nanotechnol.* **11**, 948–953 (2016). DOI: 10.1038/nnano.2016.117.
- [181] Dieterle, G., Förster, J., Stoll, H. *et al.* Coherent Excitation of Heterosymmetric Spin Waves with Ultrashort Wavelengths. *Phys. Rev. Lett.* **122**, 117202 (2019). DOI: 10.1103/PhysRevLett.122.117202.
- [182] Sluka, V., Schneider, T., Gallardo, R. A. *et al.* Emission and propagation of 1D and 2D spin waves with nanoscale wavelengths in anisotropic spin textures. *Nat. Nanotechnol.* **14**, 328–333 (2019). DOI: 10.1038/s41565-019-0383-4.

- 
- [183] Chang, L.-J., Chen, J., Qu, D. *et al.* Spin Wave Injection and Propagation in a Magnetic Nanochannel from a Vortex Core. *Nano Lett.* **20**, 3140–3146 (2020). DOI: 10.1021/acs.nanolett.9b05133.
  - [184] Gräfe, J., Weigand, M., Van Waeyenberge, B. *et al.* Visualizing nanoscale spin waves using MAXYMUS. In *Spintronics XII*, vol. 11090, 1109025 (International Society for Optics and Photonics, 2019). DOI: 10.1117/12.2530326.
  - [185] Förster, J., Wintz, S., Bailey, J. *et al.* Nanoscale X-ray imaging of spin dynamics in yttrium iron garnet. *J. Appl. Phys.* **126**, 173909 (2019). DOI: 10.1063/1.5121013.
  - [186] Förster, J., Gräfe, J., Bailey, J. *et al.* Direct observation of coherent magnons with suboptical wavelengths in a single-crystalline ferrimagnetic insulator. *Phys. Rev. B* **100**, 214416 (2019). DOI: 10.1103/PhysRevB.100.214416.
  - [187] Chen, J., Yu, T., Liu, C. *et al.* Excitation of unidirectional exchange spin waves by a nanoscale magnetic grating. *Phys. Rev. B* **100**, 104427 (2019). DOI: 10.1103/PhysRevB.100.104427.
  - [188] Yu, H., Kelly, O. d., Cros, V., Bernard, R., Bortolotti, P., Anane, A., Brandl, F., Huber, R., Stasinopoulos, I. & Grundler, D. Magnetic thin-film insulator with ultra-low spin wave damping for coherent nanomagnonics. *Sci. Rep.* **4**, 1–5 (2014). DOI: 10.1038/srep06848.
  - [189] Klingler, S., Amin, V., Geprägs, S. *et al.* Spin-Torque Excitation of Perpendicular Standing Spin Waves in Coupled YIG/Co Heterostructures. *Phys. Rev. Lett.* **120**, 127201 (2018). DOI: 10.1103/PhysRevLett.120.127201.
  - [190] Qin, H., Hämäläinen, S. J. & Van Dijken, S. Exchange-torque-induced excitation of perpendicular standing spin waves in nanometer-thick YIG films. *Sci. Rep.* **8**, 1–9 (2018). DOI: 10.1038/s41598-018-23933-y.
  - [191] An, K., Bhat, V., Mruczkiewicz, M., Dubs, C. & Grundler, D. Optimization of Spin-Wave Propagation with Enhanced Group Velocities by Exchange-Coupled Ferrimagnet-Ferromagnet Bilayers. *Phys. Rev. Applied* **11**, 034065 (2019). DOI: 10.1103/PhysRevApplied.11.034065.
  - [192] Silver, S. Circuit relations reciprocity theorems. In *Microwave Antenna Theory and Design*, 16–60 (McGraw-Hill, 1949).
  - [193] Chumak, A. V., Serga, A. A. & Hillebrands, B. Magnon transistor for all-magnon data processing. *Nat. Commun.* **5**, 1–8 (2014). DOI: 10.1038/ncomms5700.
  - [194] Sadovnikov, A. V., Grachev, A. A., Gubanov, V. A., Odintsov, S. A., Martyshkin, A. A., Sheshukova, S. E., Sharaevskii, Y. P. & Nikitov, S. A. Spin-wave intermodal coupling in the interconnection of magnonic units. *Appl. Phys. Lett.* **112**, 142402 (2018). DOI: 10.1063/1.5027057.
  - [195] Sadovnikov, A. V., Gubanov, V. A., Sheshukova, S. E., Sharaevskii, Y. P. & Nikitov, S. A. Spin-Wave Drop Filter Based on Asymmetric Side-Coupled Magnonic Crystals. *Phys. Rev. Applied* **9**, 051002 (2018). DOI: 10.1103/PhysRevApplied.9.051002.
  - [196] Schroeter, S. & Garst, M. Scattering of high-energy magnons off a magnetic skyrmion. *Low Temp. Phys.* **41**, 817–825 (2015). DOI: 10.1063/1.4932356.
  - [197] Garst, M., Waizner, J. & Grundler, D. Collective spin excitations of helices and magnetic skyrmions: review and perspectives of magnonics in non-centrosymmetric magnets. *J. Phys. D: Appl. Phys.* **50**, 293002 (2017). DOI: 10.1088/1361-6463/aa7573.

## Bibliography

---

- [198] Demokritov, S. O., Demidov, V. E., Dzyapko, O., Melkov, G. A., Serga, A. A., Hillebrands, B. & Slavin, A. N. Bose–Einstein condensation of quasi-equilibrium magnons at room temperature under pumping. *Nature* **443**, 430–433 (2006). DOI: doi.org/10.1038/nature05117.
- [199] Sandweg, C. W., Kajiwara, Y., Chumak, A. V., Serga, A. A., Vasyuchka, V. I., Jungfleisch, M. B., Saitoh, E. & Hillebrands, B. Spin Pumping by Parametrically Excited Exchange Magnons. *Phys. Rev. Lett.* **106**, 216601 (2011). DOI: 10.1103/PhysRevLett.106.216601.
- [200] Kurebayashi, H., Dzyapko, O., Demidov, V. E., Fang, D., Ferguson, A. J. & Demokritov, S. O. Spin pumping by parametrically excited short-wavelength spin waves. *Appl. Phys. Lett.* **99**, 162502 (2011). DOI: 10.1063/1.3652911.
- [201] Van de Wiele, B., Hämäläinen, S. J., Baláž, P., Montoncello, F. & Van Dijken, S. Tunable short-wavelength spin wave excitation from pinned magnetic domain walls. *Sci. Rep.* **6**, 21330 (2016). DOI: 10.1038/srep21330.
- [202] Poimanov, V. D., Kuchko, A. N. & Kruglyak, V. V. Magnetic interfaces as sources of coherent spin waves. *Phys. Rev. B* **98**, 104418 (2018). DOI: 10.1103/PhysRevB.98.104418.
- [203] Schlömann, E. Generation of Spin Waves in Nonuniform Magnetic Fields. I. Conversion of Electromagnetic Power into Spin-Wave Power and Vice Versa. *J. Appl. Phys.* **35**, 159–166 (1964). DOI: 10.1063/1.1713058.
- [204] Davies, C. S. & Kruglyak, V. V. Generation of Propagating Spin Waves From Edges of Magnetic Nanostructures Pumped by Uniform Microwave Magnetic Field. *IEEE Trans. Magn.* **52**, 1–4 (2016). DOI: 10.1109/TMAG.2016.2517000.
- [205] Stigloher, J., Taniguchi, T., Madami, M., Decker, M., Körner, H. S., Moriyama, T., Gubbiotti, G., Ono, T. & Back, C. H. Spin-wave wavelength down-conversion at thickness steps. *Appl. Phys. Express* **11**, 053002 (2018). DOI: 10.7567/apex.11.053002.
- [206] Madami, M., Bonetti, S., Consolo, G., Tacchi, S., Carlotti, G., Gubbiotti, G., Mancoff, F., Yar, M. A. & Åkerman, J. Direct observation of a propagating spin wave induced by spin-transfer torque. *Nat. Nanotechnol.* **6**, 635 (2011). DOI: 10.1038/nnano.2011.140.
- [207] Dubs, C., Surzhenko, O., Linke, R., Danilewsky, A., Brückner, U. & Dellith, J. Sub-micrometer yttrium iron garnet LPE films with low ferromagnetic resonance losses. *J. Phys. D: Appl. Phys.* **50**, 204005 (2017). DOI: 10.1088/1361-6463/aa6b1c.
- [208] Ping, C., Baumgaertl Korbinian, Kúkol'ová Anna, Dubs Carsten & Grundler Dirk. Supporting Informations for 'Efficient wavelength conversion of exchange magnons below 100 nm by magnetic coplanar waveguides' (2020). DOI: 10.5281/ZENODO.3633075.
- [209] Smith, K. R., Kabatek, M. J., Krivosik, P. & Wu, M. Spin wave propagation in spatially nonuniform magnetic fields. *J. Appl. Phys.* **104**, 043911 (2008). DOI: 10.1063/1.2963688.
- [210] Obry, B., Vasyuchka, V. I., Chumak, A. V., Serga, A. A. & Hillebrands, B. Spin-wave propagation and transformation in a thermal gradient. *Appl. Phys. Lett.* **101**, 192406 (2012). DOI: 10.1063/1.4767137.
- [211] Sadovnikov, A., Bublikov, K., Beginin, E. & Nikitov, S. The electrodynamic characteristics of a finite-width metal/dielectric/ferroelectric/dielectric/metal layer structure. *J. Commun. Technol. Electron.* **59**, 914–919 (2014). DOI: 10.1134/S106422691408018X.

- 
- [212] Sadovnikov, A. V., Grachev, A. A., Beginin, E. N., Sheshukova, S. E., Sharaevskii, Y. P. & Nikitov, S. A. Voltage-Controlled Spin-Wave Coupling in Adjacent Ferromagnetic-Ferroelectric Heterostructures. *Phys. Rev. Applied* **7**, 014013 (2017). DOI: 10.1103/PhysRevApplied.7.014013.
  - [213] Scheunert, G., Heinonen, O., Hardeman, R., Lapicki, A., Gubbins, M. & Bowman, R. M. A review of high magnetic moment thin films for microscale and nanotechnology applications. *Appl. Phys. Rev.* **3**, 011301 (2016). DOI: 10.1063/1.4941311.
  - [214] Seki, S., Okamura, Y., Kondou, K. *et al.* Magnetochiral nonreciprocity of volume spin wave propagation in chiral-lattice ferromagnets. *Phys. Rev. B* **93**, 235131 (2016). DOI: 10.1103/PhysRevB.93.235131.
  - [215] Jamali, M., Kwon, J. H., Seo, S.-M., Lee, K.-J. & Yang, H. Spin wave nonreciprocity for logic device applications. *Sci. Rep.* **3**, 1–5 (2013). DOI: 10.1038/srep03160.
  - [216] Yu, H., Brechet, S. D., Che, P. *et al.* Thermal spin torques in magnetic insulators. *Phys. Rev. B* **95**, 104432 (2017). DOI: 10.1103/PhysRevB.95.104432.
  - [217] Edmonds, D. T. & Petersen, R. G. Effective Exchange Constant in Yttrium Iron Garnet. *Phys. Rev. Lett.* **2**, 499–500 (1959). DOI: 10.1103/PhysRevLett.2.499.
  - [218] Demokritov, S. O. & Slavin, A. N. *From Fundamentals to Applications*. vol. 125 Springer-Verlag Berlin Heidelberg (2013). DOI: 10.1007/978-3-642-30247-3.
  - [219] Coey, J. M. D. *Magnetism and Magnetic Materials*. Cambridge University Press (2010). DOI: 10.1017/CBO9780511845000.
  - [220] Brown, W. F. Thermal Fluctuations of a Single-Domain Particle. *Phys. Rev.* **130**, 1677–1686 (1963). DOI: 10.1103/PhysRev.130.1677.
  - [221] Wernsdorfer, W., Orozco, E. B., Hasselbach, K., Benoit, A., Barbara, B., Demoncy, N., Loiseau, A., Pascard, H. & Mailly, D. Experimental Evidence of the Néel-Brown Model of Magnetization Reversal. *Phys. Rev. Lett.* **78**, 1791–1794 (1997). DOI: 10.1103/PhysRevLett.78.1791.
  - [222] Breth, L., Suess, D., Vogler, C., Bergmair, B., Fuger, M., Heer, R. & Brueckl, H. Thermal switching field distribution of a single domain particle for field-dependent attempt frequency. *J. Appl. Phys.* **112**, 023903 (2012). DOI: 10.1063/1.4737413.
  - [223] Yamaguchi, A., Ono, T., Nasu, S., Miyake, K., Mibu, K. & Shinjo, T. Real-Space Observation of Current-Driven Domain Wall Motion in Submicron Magnetic Wires. *Phys. Rev. Lett.* **92**, 077205 (2004). DOI: 10.1103/PhysRevLett.92.077205.
  - [224] Parkin, S. & Yang, S.-H. Memory on the racetrack. *Nat. Nanotechnol.* **10**, 195–198 (2015). DOI: 10.1038/nnano.2015.41.
  - [225] Hayashi, M., Thomas, L., Rettner, C., Moriya, R., Bazaliy, Y. B. & Parkin, S. S. P. Current Driven Domain Wall Velocities Exceeding the Spin Angular Momentum Transfer Rate in Permalloy Nanowires. *Phys. Rev. Lett.* **98**, 037204 (2007). DOI: 10.1103/PhysRevLett.98.037204.
  - [226] Weller, D. & Moser, A. Thermal effect limits in ultrahigh-density magnetic recording. *IEEE Trans. Magn.* **35**, 4423–4439 (1999). DOI: 10.1109/20.809134.

## Bibliography

---

- [227] Gao, K. Z., Heinonen, O. & Chen, Y. Read and write processes, and head technology for perpendicular recording. *J. Magn. Magn. Mater.* **321**, 495–507 (2009). DOI: 10.1016/j.jmmm.2008.05.025.
- [228] Thirion, C., Wernsdorfer, W. & Mailly, D. Switching of magnetization by nonlinear resonance studied in single nanoparticles. *Nat. Mater.* **2**, 524–527 (2003). DOI: 10.1038/nmat946.
- [229] Zhu, J., Zhu, X. & Tang, Y. Microwave Assisted Magnetic Recording. *IEEE Trans. Magn.* **44**, 125–131 (2008). DOI: 10.1109/TMAG.2007.911031.
- [230] Scholz, W. & Batra, S. Micromagnetic modeling of ferromagnetic resonance assisted switching. *J. Appl. Phys.* **103**, 07F539 (2008). DOI: 10.1063/1.2838332.
- [231] Nozaki, Y., Narita, N., Tanaka, T. & Matsuyama, K. Microwave-assisted magnetization reversal in a Co/Pd multilayer with perpendicular magnetic anisotropy. *Appl. Phys. Lett.* **95**, 082505 (2009). DOI: 10.1063/1.3213559.
- [232] Li, S., Livshitz, B., Bertram, H. N., Schabes, M., Schrefl, T., Fullerton, E. E. & Lomakin, V. Microwave assisted magnetization reversal in composite media. *Appl. Phys. Lett.* **94**, 202509 (2009). DOI: 10.1063/1.3133354.
- [233] Seki, T., Utsumiya, K., Nozaki, Y., Imamura, H. & Takanashi, K. Spin wave-assisted reduction in switching field of highly coercive iron-platinum magnets. *Nat. Commun.* **4** (2013). DOI: 10.1038/ncomms2737.
- [234] Kostylev, M. P., Serga, A. A., Schneider, T., Leven, B. & Hillebrands, B. Spin-wave logical gates. *Appl. Phys. Lett.* **87**, 153501 (2005). DOI: 10.1063/1.2089147.
- [235] Schneider, T., Serga, A. A., Leven, B., Hillebrands, B., Stamps, R. L. & Kostylev, M. P. Realization of spin-wave logic gates. *Appl. Phys. Lett.* **92**, 022505 (2008). DOI: 10.1063/1.2834714.
- [236] Gertz, E., Kozhevnikov, A. V., Filimonov, Y. A., Nikonov, D. E. & Khitun, A. Magnonic Holographic Memory: From Proposal to Device. *IEEE J. Explor. Solid-State Computat.* **1**, 67–75 (2015). DOI: 10.1109/JXCDC.2015.2461618.
- [237] Islam, R., Li, H., Chen, P.-Y., Wan, W., Chen, H.-Y., Gao, B., Wu, H., Yu, S., Saraswat, K. & Wong, H.-S. P. Device and materials requirements for neuromorphic computing. *J. Phys. D: Appl. Phys.* **52**, 113001 (2019). DOI: 10.1088/1361-6463/aaf784.
- [238] Fallarino, L., Madami, M., Duerr, G., Grundler, D., Gubbiotti, G., Tacchi, S. & Carlotti, G. Propagation of Spin Waves Excited in a Permalloy Film by a Finite-Ground Coplanar Waveguide: A Combined Phase-Sensitive Micro-Focused Brillouin Light Scattering and Micromagnetic Study. *IEEE Trans. Magn.* **49**, 1033–1036 (2013). DOI: 10.1109/TMAG.2012.2229385.
- [239] Topp, J., Heitmann, D. & Grundler, D. Interaction effects on microwave-assisted switching of Ni<sub>80</sub>Fe<sub>20</sub> nanowires in densely packed arrays. *Phys. Rev. B* **80** (2009). DOI: 10.1103/physrevb.80.174421.
- [240] Schultheiss, H., Vogt, K. & Hillebrands, B. Direct observation of nonlinear four-magnon scattering in spin-wave microconduits. *Phys. Rev. B* **86**, 054414 (2012). DOI: 10.1103/PhysRevB.86.054414.
- [241] Olson, H. M., Krivosik, P., Srinivasan, K. & Patton, C. E. Ferromagnetic resonance saturation and second order Suhl spin wave instability processes in thin Permalloy films. *J. Appl. Phys.* **102**, 023904 (2007). DOI: 10.1063/1.2756481.

- [242] Nozaki, Y., Tateishi, K., Taharazako, S., Ohta, M., Yoshimura, S. & Matsuyama, K. Microwave-assisted magnetization reversal in 0.36- $\mu\text{m}$ -wide Permalloy wires. *Appl. Phys. Lett.* **91**, 122505 (2007). DOI: 10.1063/1.2786593.
- [243] Podbielski, J., Heitmann, D. & Grundler, D. Microwave-Assisted Switching of Microscopic Rings: Correlation Between Nonlinear Spin Dynamics and Critical Microwave Fields. *Phys. Rev. Lett.* **99**, 207202 (2007). DOI: 10.1103/PhysRevLett.99.207202.
- [244] Schoen, M. A. W., Thonig, D., Schneider, M. L., Silva, T. J., Nembach, H. T., Eriksson, O., Karis, O. & Shaw, J. M. Ultra-low magnetic damping of a metallic ferromagnet. *Nat. Phys.* **12**, 839–842 (2016). DOI: 10.1038/nphys3770.
- [245] Wang, Y., Zhu, D., Yang, Y. *et al.* Magnetization switching by magnon-mediated spin torque through an antiferromagnetic insulator. *Science* **366**, 1125–1128 (2019). DOI: 10.1126/science.aav8076.
- [246] Eerenstein, W., Mathur, N. D. & Scott, J. F. Multiferroic and magnetoelectric materials. *Nature* **442**, 759–765 (2006). DOI: 10.1038/nature05023.
- [247] Parkin, S. S. P., Hayashi, M. & Thomas, L. Magnetic Domain-Wall Racetrack Memory. *Science* **320**, 190–194 (2008). DOI: 10.1126/science.1145799.
- [248] Kimura, T., Otani, Y., Tsukagoshi, K. & Aoyagi, Y. Spin-current-assisted domain-wall depinning in a submicron magnetic wire. *J. Appl. Phys.* **94**, 7947 (2003). DOI: 10.1063/1.1629150.
- [249] Yamaguchi, A., Ono, T., Nasu, S., Miyake, K., Mibu, K. & Shinjo, T. Real-Space Observation of Current-Driven Domain Wall Motion in Submicron Magnetic Wires. *Phys. Rev. Lett.* **92** (2004). DOI: 10.1103/physrevlett.92.077205.
- [250] Kronmüller, H. & Parkin, S. (eds.). *Handbook of Magnetism and Advanced Magnetic Materials*. Wiley (2007). DOI: 10.1002/9780470022184.
- [251] Zelent, M., Mailyan, M., Vashistha, V., Gruszecki, P., Gorobets, O. Y., Gorobets, Y. I. & Krawczyk, M. Spin wave collimation using a flat metasurface. *Nanoscale* **11**, 9743–9748 (2019). DOI: 10.1039/c8nr10484k.
- [252] Gräfe, J., Gruszecki, P., Zelent, M. *et al.* Direct observation of spin-wave focusing by a Fresnel lens. *Phys. Rev. B* **102** (2020). DOI: 10.1103/physrevb.102.024420.
- [253] Morgan, D. Surface acoustic wave devices and applications: 1. Introductory review. *Ultrasonics* **11**, 121 – 131 (1973). DOI: 10.1016/0041-624X(73)90608-2.
- [254] Vlaminck, V. & Bailleul, M. Current-Induced Spin-Wave Doppler Shift. *Science* **322**, 410–413 (2008). DOI: 10.1126/science.1162843.
- [255] Schütz, G., Wagner, W., Wilhelm, W., Kienle, P., Zeller, R., Frahm, R. & Materlik, G. Absorption of circularly polarized x rays in iron. *Phys. Rev. Lett.* **58**, 737–740 (1987). DOI: 10.1103/PhysRevLett.58.737.
- [256] Krichevtsov, B. B., Gastev, S. V., Suturen, S. M., Fedorov, V. V., Korovin, A. M., Bursian, V. E., Ban-shchikov, A. G., Volkov, M. P., Tabuchi, M. & Sokolov, N. S. Magnetization reversal in YIG/GGG(111) nanoheterostructures grown by laser molecular beam epitaxy. *Sci. Technol. Adv. Mater.* **18**, 351–363 (2017). DOI: 10.1080/14686996.2017.1316422.

## Bibliography

---

- [257] Groß, F., Träger, N., Förster, J., Weigand, M., Schütz, G. & Gräfe, J. Nanoscale detection of spin wave deflection angles in permalloy. *Appl. Phys. Lett.* **114**, 012406 (2019). DOI: 10.1063/1.5074169.
- [258] Venkat, G., Kumar, D., Franchin, M., Dmytriiev, O., Mruczkiewicz, M., Fangohr, H., Barman, A., Krawczyk, M. & Prabhakar, A. Proposal for a Standard Micromagnetic Problem: Spin Wave Dispersion in a Magnonic Waveguide. *IEEE Trans. Magn.* **49**, 524–529 (2013). DOI: 10.1109/T-MAG.2012.2206820.
- [259] Yu, H., Huber, R., Schwarze, T., Brandl, F., Rapp, T., Berberich, P., Duerr, G. & Grundler, D. High propagating velocity of spin waves and temperature dependent damping in a CoFeB thin film. *Appl. Phys. Lett.* **100**, 262412 (2012). DOI: 10.1063/1.4731273.
- [260] Wang, H. L., Du, C. H., Pu, Y., Adur, R., Hammel, P. C. & Yang, F. Y. Scaling of Spin Hall Angle in 3d, 4d, and 5d Metals from  $\text{Y}_3\text{Fe}_5\text{O}_{12}$ /Metal Spin Pumping. *Phys. Rev. Lett.* **112**, 197201 (2014). DOI: 10.1103/PhysRevLett.112.197201.
- [261] Griffiths, D. *Introduction to Electrodynamics*. Pearson Education (2014). ISBN: 9780321972101.



Korbinian Baumgärtl  
Rue de la Tour 37  
CH-1004 Lausanne

Phone : +41 78 8927859  
E-mail : korbinian.b@web.de  
[www.linkedin.com/in/KBaumgaertl](http://www.linkedin.com/in/KBaumgaertl)

## Education

---

4/2016- <i>Expected 9/2020</i>	PhD student in MATERIALS SCIENCE & ENGINEERING at <b>École polytechnique fédérale de Lausanne</b>
2016	Master of Science in CONDENSED MATTER PHYSICS, <b>Technische Universität München</b> GRADE 1.0* - Focus on semiconductor physics and magnetism - Academic exchange semester at EPFL and Royal Institute of Technology (KTH), Stockholm
2011	<b>General qualification for university entrance (Abitur)</b> , König Karlmann Gymnasium, Altötting (Germany) GRADE 1.5*

\*(1.0 being the highest, 4.0 the lowest passing grade)

## Technical skills

- 
- **Nanofabrication:** 4 years of experience in cleanroom work (ISO 6) with a focus on electron beam lithography (EBL), thin film evaporation and sputtering, ion beam etching (IBE) and wet etching.
  - **Material characterization:** Scanning electron microscopy (SEM), atomic and magnetic force microscopy (AFM & MFM), Brillouin light scattering (BLS), microwave spectroscopy with vector network analyzer, time-resolved scanning transmission X-ray microscopy (TR-STXM), magneto-transport measurements at room and cryogenic temperatures.
  - **Data Analysis:** Experienced in data analysis and visualization using Python, OriginLab and Microsoft Office.
  - **Laboratory safety:** 3 years of experience as security correspondent of a research group with a certificate in 'Basic knowledge of workspace safety and health protection for safety officer' following RS 822.116
  - **Experimental skills:** Maintenance of two Brillouin light scattering microscopy setups including microwave excitation and cryostation.
  - **Simulations:** Micromagnetic simulations using MuMax<sup>3</sup> and Nmag. High-frequency electromagnetic simulations using Sonnet and Comsol.

## Academic projects

---

- 2016-present      **Laboratory of Nanoscale Magnetic Materials and Magnonics (LMGN), EPFL**  
**"Magnonic crystals with reconfigurable magnetic defects for spin-based microwave electronics."**  
*Doctoral Thesis* | Supervisor: Professor Drik GRUNDLER. Funded by SNF grant 163016. Cleanroom fabrication of magnetic nanostructures. Characterization of dynamic magnetic properties by BLS microscopy, microwave spectroscopy and synchrotron based X-ray imaging techniques. Visualization and modeling of experiment data with Python and micromagnetic simulation software.

## Key publications

---

- "Nanoimaging of Ultrashort Magnon Emission by Ferromagnetic Grating Couplers at GHz Frequencies"; K. Baumgaertl *et al.*; *ACS Nano Letters* **10**, 7281–7286 (2020).
- "Efficient wavelength conversion of exchange magnons below 100 nm by magnetic coplanar waveguides"; P. Che\*, K. Baumgaertl\*, A. Kúkol'ová, C. Dubs and D. Grundler; *Nature Communications* **11**, 1445 (2020).  
\*equal contributions
- "Phase control of spin waves based on a magnetic defect in a one-dimensional magnonic crystal"; K. Baumgaertl, S. Watanabe, D. Grundler; *Applied Physics Letters* **112**, 142405 (2018)
- "Magnetization reversal in individual Py and CoFeB nanotubes locally probed via anisotropic magnetoresistance and anomalous Nernst effect"; K. Baumgaertl *et al.*; *Applied Physics Letters* **108**, 132408 (2016)

## Teaching experience

---

- **Teaching assistant** for 'General Physics 3' in 2018, 2017 and 2016 at EPFL.
- **Supervisor for Master thesis** 'Application and exploration of magnetic nanoparticles as magnetic scatterers in magnonic devices', Andrea Mucchietto (2018)
- **Supervisor for semester project** 'Magnetization reversal in ferromagnetic nanowires', Bin Lu, (2016)

## Additional skills

---

- Computer skills: Data Analytics with PYTHON, Graphic Design & Word Processing with ADOBE ILLUSTRATOR, L<sup>A</sup>T<sub>E</sub>X and MS Office, Programming of measurement routine with LABVIEW and PYTHON, Micromagnetic simulations with MUMAX3 and NMAG, 3D CAD with SOLID WORKS.
- Reviewing for *Applied Physics Letters* and *ACS Applied Nano Materials*
- Course certificate in "Management of Innovation and Technology Transfer" (EPFL, 2019)
- Driving license category B (cars)